Ruperto-Carola University of Heidelberg

Combined Faculties of Natural Sciences and Mathematics

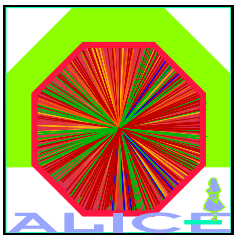

Development of the Readout Chamber of the ALICE Transition Radiation Detector and Evaluation of its Physics Performance in the Quarkonium Sector

Dissertation

Tariq Mahmoud

May 2004

Dissertation
submitted to the
Combined Faculties of Natural Sciences and Mathematics
of the Ruperto-Carola University of Heidelberg, Germany
for the Degree of
Doctor of Natural Sciences

presented by
Diplom-Physiker Tariq Mahmoud
born in Tammoun, Palestine

Oral examination: 19.07.2004

Development of the Readout Chamber of the ALICE Transition Radiation Detector and Evaluation of its Physics Performance in the Quarkonium Sector

Referees: Prof. Dr. Johanna Stachel
Prof. Dr. Franz Eisele

Entwicklung der Auslesekammer für den ALICE–Übergangsstrahlungsdetektor und eine Beurteilung seiner Leistungsfähigkeit in Experimenten zur Quarkoniumphysik

Im zentralen Bereich des ALICE–Detektors werden Resonanzen über ihre elektronischen Zerfälle nachgewiesen. Deren Identifikation wird allerdings durch die reichlich produzierten Pionen erschwert. Daher ist der Einsatz eines Elektronen und Pionen trennenden Übergangsstrahlungsdetektors (TRD) von entscheidender Bedeutung.

Diese Arbeit beschreibt die Entwicklung und den Bau eines maßstabsgetreuen Prototypen, ausgehend von den ersten theoretischen Überlegungen und der anschließenden Überprüfung auf mechanische und elektrostatische Stabilität bis hin zum Nachweis seiner Fähigkeit, zwischen Elektronen und Pionen zu unterscheiden. Bei einer Effizienz von 90% für die identifizierten Elektronen war der Prototyp in der Lage, gemäß der Vorgabe von ALICE, 99% der Pionen mit Impulsen von 2 GeV/c zu unterdrücken.

Die in Testmessungen gewonnenen Daten sind in einem Simulationspaket benutzt worden, das die drei zentralen Detektoren von ALICE beschreibt, und zwar den inneren Trackingdetektor, die Zeitprojektionskammer und den TRD. Auf der Basis von 0.38 Prozent der zentralen Ereignisse für ein Jahr ALICE–Messzeit wurde das Verhalten der Detektoren untersucht, wobei Pionen–Unterdrückungsraten mit und ohne TRD–Beitrag berücksichtigt wurden. Es zeigt sich, dass eine aussagekräftige Messung der Quarkoniumzustände nur unter TRD–Einsatz möglich ist. Die erreichbare Signifikanz beträgt 95% der Signifikanz für einen idealen Detektor, in dem Pionen vollständig unterdrückt werden.

Development of the Readout Chamber of the ALICE Transition Radiation Detector and Evaluation of its Physics Performance in the Quarkonium Sector

In the central barrel of the ALICE detector, resonances are proved through their electronic decays. Doing so, the abundantly produced pions make the electrons identification complicated. Therefore the adoption of an electron–pion separator, like the Transition Radiation Detector (TRD), is of particular importance.

This thesis went along with the first real dimension TRD prototype from the first theoretical considerations of its readout chamber over testing it for its mechanical and electrostatical stability up to determining its pion rejection capability. With an efficiency of 90% for identified electrons, the TRD allows to reject 99% of the pions with momenta of 2 GeV/c.

The gained data were implemented in a fast–simulations–package, which includes the three ALICE central detectors; the Inner Tracking System, the Time Projection Chamber, and the TRD. With $3.8 \cdot 10^{-3}$ of the central events recorded in one ALICE year, the detector physics performance was studied. The pion rejection was considered with and without a TRD contribution. It was found that only with the TRD it will be possible to detect the Quarkonium resonances significantly. The significance is at the level of 95% of the significance of an ideal detector where pions are perfectly rejected.


jenin جنين
al-fallujah الفلوجه
madrid مدريد

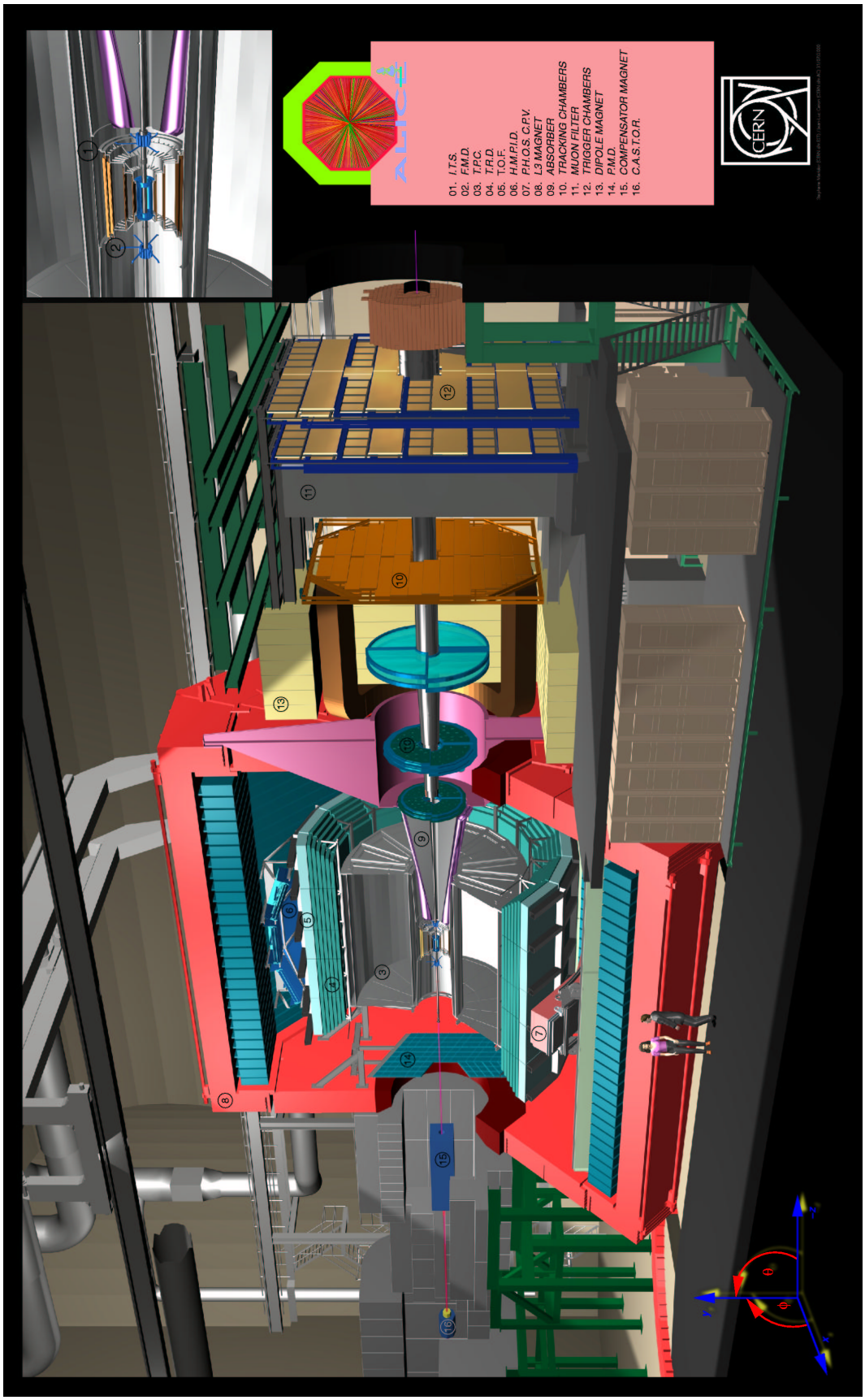

Figure 1: Layout of the ALICE detector. The subdetectors are listed on the right side.

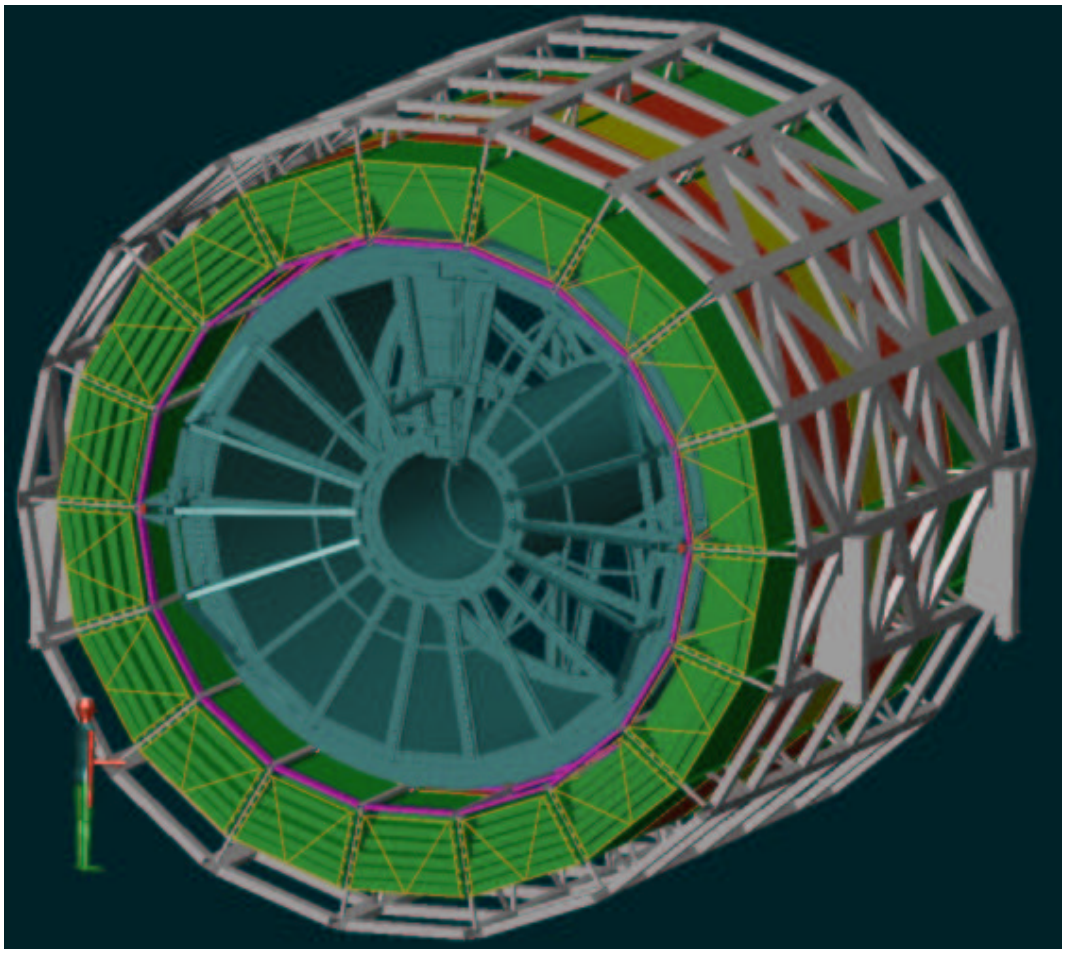

Figure 2: The ALICE space frame with the TRD mudules.

Contents

1 Motivation **7**

1.1 Introduction 7

1.2 Outline of the Thesis 9

I Generalities **11**

2 Ultra-relativistic Heavy-Ion Physics **13**

2.1 Quantum Chromo-Dynamics and Quark Gluon Plasma 13

2.1.1 QCD Properties 14

2.1.2 Lattice QCD 15

2.1.3 Quark Gluon Plasma and Critical Parameters 16

2.2 Heavy-Ion Collisions 19

2.2.1 Experimental Programs 19

2.2.2 Collision Dynamics 20

2.3 Signatures of Quark Gluon Plasma 22

2.3.1 QGP Diagnostic 22

2.3.2 Global Observables 23

2.3.3 Probes of Large Cross Section 28

2.3.4 Probes of Small Cross Section 30

2.4 Large Hadron Collider 33

2.4.1 LHC Event Features 33

2.4.2 New Physics at LHC 34

2.5 The ALICE Experiment 37

2.5.1 ALICE Sub-detectors 38

3 Ionization Energy Loss and Transition Radiation **43**

3.1 Ionization Energy Loss 43
3.2 Transition Radiation 46
3.2.1 Theory of Transition Radiation 46
3.2.2 TR Yield From a Stack of Foils and Gaps 48
3.2.3 Maximizing the TR Yield and Saturation 50
3.2.4 TR From Irregular Radiators 51
3.3 Gas Detectors 52
3.3.1 Drift Chambers 52
3.3.2 Effects in MWPCs 54

4 The ALICE Transition Radiation Detector **57**

4.1 Physics Motivation 57
4.1.1 Heavy-Ion Collisions 58
4.1.2 *pp* Collisions 59
4.2 Design Criteria 59
4.3 TRD Module 62
4.4 The Pad Plane 63
4.4.1 Pads Layout 64
4.4.2 Wire Grids 64
4.5 The Radiator 65
4.6 Principle of Operation 67
4.7 Front End Electronics 67
4.7.1 Electronics Overview 68
4.7.2 Electronics Design Requirements 68
4.7.3 Data Processing 70
4.8 Trigger Concept 70
4.9 The TRD in Numbers 70

II Development of the ALICE-TRD Readout-Chamber **73**

5 Readout Chamber **75**

5.1 Gas Mixture and its Properties 76
5.1.1 Electron Transport Properties 77

5.1.2 Gas Mixture in the TRD Drift Chamber . . . 80
5.1.3 Drift Velocity and Drift Field . . . 82
5.1.4 Lorentz Angle . . . 83
5.1.5 Diffusion and Electron Attachment . . . 85
5.1.6 Measured Properties of the Gas Mixture . . . 87
5.2 Pad Response Function . . . 88
5.3 Gas Gain . . . 90
5.3.1 Amplification Factor . . . 90
5.3.2 Amplification Factor in the ALICE TRD Chamber . . . 91
5.4 Wire Sag . . . 93
5.4.1 Theoretical View on Wire Sag . . . 94
5.4.2 Wire Sag in the TRD Chamber . . . 96
5.5 Gain Stability . . . 100
5.6 Field Shaping . . . 104
5.7 Ion Signal and Pad Coupling . . . 106
5.8 Isochronity . . . 107

6 Module Stability 111
6.1 Measurement Environment . . . 112
6.2 Deformation of the Read-Out Sandwich . . . 113
6.3 Deformation of the Radiator . . . 115
6.4 Deformation of the Chamber Frame . . . 116
6.5 Voltage Divider . . . 116
6.6 Gas Gain . . . 117
6.6.1 Gas Gain Uniformity . . . 118

7 Detector Performance 121
7.1 Measurements Setup . . . 121
7.2 General Signal Properties . . . 123
7.3 Tail Cancellation . . . 125
7.4 Signal and Noise . . . 128
7.4.1 Noise . . . 128
7.4.2 Signal-to-Noise Ratio . . . 129
7.5 Tracking and Position Reconstruction . . . 130
7.5.1 Pad Response Function . . . 130

7.5.2 Position Reconstruction Performance . . . 133
7.6 Signal Charge . . . 135
7.6.1 Qualitative Considerations . . . 135
7.6.2 Gas Gain . . . 137
7.7 Transition Radiation Performance . . . 138
7.7.1 Electron and Pion Distributions . . . 138
7.7.2 Quantitative Yield of the TR . . . 139
7.8 Pion Rejection . . . 142
7.8.1 Pion Rejection with one TRD Layer . . . 142
7.8.2 Pion Rejection with Six TRD Layers . . . 144

III Physics Capabilities 147

8 Di-electrons and Heavy Quarkonia in Heavy-Ion Collisions 149
8.1 Di-Leptons . . . 150
8.2 Quarkonia Systems . . . 151
8.3 General Features of Pb-Pb Collisions at LHC . . . 154
8.4 Count Rates of Quarkonia, Open Charm and Open Beauty . . . 156

9 Fast Simulation Package for the ALICE Central Barrel 159
9.1 Why Fast Simulation? . . . 160
9.2 Fast Simulation Strategy . . . 160
9.3 Slow Simulations . . . 161
9.3.1 Local Tracking . . . 161
9.3.2 Global Tracking . . . 162
9.4 Global Detector Response in the ACB . . . 163
9.4.1 Transverse Momentum Distribution . . . 163
9.4.2 Global Detector Efficiency in the ACB . . . 163
9.4.3 Global Detector Resolutions in the ACB . . . 166
9.5 Particle Identification . . . 167
9.6 Fast Simulation Package . . . 170

10 Physics Performance of the ACB **173**

10.1 Generators 173

10.2 Generators Properties and Acceptance 173

10.3 Simulation Environment 178

10.4 Qualitative Consideration of the Invariant Mass Spectra 180

10.5 Resonances Resolution 183

10.6 Calculation of the Signal 184

10.7 Quantitative Consideration of the Invariant Mass Spectra 185

10.8 Significance and p_t-Cut 187

10.9 Significance and Multiplicity 189

11 Conclusion **191**

11.1 Outlook 194

Chapter 1

Motivation

also lautet ein beschluss, dass der
mensch was lernen muss.
lernen kann man, Gott sei dank,
aber auch sein leben lang.
wilhelm busch

1.1 Introduction

The experimental programs of heavy-ion collisions at ultra-relativistic energies offer a unique opportunity to access the properties of strongly interacting many-body-systems, which are described by non-perturbative Quantum Chromo-Dynamics (QCD). Special attention is concentrated on the predicted formation of the so-called Quark-Gluon-Plasma (QGP) as a chirally symmetric system [1], if the temperature (energy) and/or the baryonic density in the colliding system exceeds a critical value. In this state of matter the nucleon constituents, i.e. quarks and gluons, move "freely" in the system. In nature this state may exist only in the core of neutron stars and collapsing supernovae. In the laboratory the strong interacting matter can only be studied by means of heavy-ion collisions at facilities like the Large Hadron Collider (LHC) [2] at CERN.

The physics program of LHC involves beside proton-proton collisions at a center-of-mass energy of $\sqrt{s} = 14$ TeV, an extensive heavy ion collisions program at a center-of-mass energy of $\sqrt{s} = 5.5$ TeV per nucleon pair. At these energies, QCD estimates the duration of the QGP to be around $\tau_{QGP} = 10$ fm/c[3]. The QGP system formed is first in a hot stage and is expected to be in local thermal equilibrium, but afterwards the system expands, cools down, and undergoes a confining transition where it finally freezes out into hadrons. At freeze-out time the expected volume of the plasma is on the order of 10^5 fm^3 (about 65 times greater than a lead nucleus volume) with an energy density of about $\epsilon = 500$ GeV/fm^3 (around 6000 times the energy density of a lead nucleus in its ground state). The relative long life and the large volume of the QGP allow to describe it according to the laws of hydrodynamics.

The existence of QGP authenticates the QCD theory and its properties offer valuable clues to the nature of the strong interaction. Furthermore, in its first microsecond after the Big Bang the early universe existed as a system in a QGP state. This makes the investigation of this state of great interest for astrophysics and cosmology communities.

Once the QGP is produced in a heavy-ion collision, the major challenge is then to prove it. Compared to typical detector dimensions, the life-time of the QGP state is very short making it impossible to observe the deconfined state directly in the laboratory. Therefore the plasma properties are studied through its signatures carried by those particles surviving the hadronization (leptons and photons) and those produced from hadronic decay (leptons, hadrons and photons).

A detector should be able to identify these particles and their properties and that in turn signals the existence of the QGP. ALICE (A Large Ion Collider Experiment)[4, 5] is an experiment at the LHC designed to study heavy-ion collisions and the properties of the QGP. Figure 1 shows the ALICE detector and in Subsection 2.5.1 the ALICE sub-detectors are briefly presented.

One of the most promising QGP signatures are the Quarkonium signals, J/ψ and Υ families. In particular the abundance of the produced Quarkonia in a QGP system relative to those produced in nucleon nucleon collisions is of special interest. The importance of the Quarkonia is not only related to the physics behind the production mechanism of heavy quarks under extreme conditions but also in the way how they are going to signal the formation of the deconfined QGP system. The predictions for LHC energies alternate between total suppression[6, 7] and enhancement relative to the Quarkonia production in nucleon-nucleon collisions[36, 113, 170].

The predicted production cross sections (extrapolated from nucleon-nucleon data) of the Quarkonia in heavy-ion collisions, are very small[8] which makes their detection, as all rare probes, a challenging undertaking. The only way to detect them are their di-leptonic decay channels; (e^+e^- and $\mu^+\mu^-$). This makes them difficultly accessible, due to the low branching ratios of 6% (J/ψ) and 2.5% (Υ) and the expected high background particle yields consisting mainly of pions. Therefore a robust and high performance pion-electron identification detector like the Transition Radiation Detector (TRD) is required.

In the ALICE experiment Quarkonia will be recorded in the muon arm via their di-muon decay channel, and in the ALICE Central Barrel (ACB) via their di-electron decay chanel. In addition to the TRD, the ACB consists of the Inner Tracking System (ITS) and the Time Projection Chamber (TPC). The electron identification among the abundant pions of underlying events, is one of the main tasks of the TPC via energy deposit. However this request becomes inefficient at particle momenta around 1 GeV/c and is practically not feasible for larger momenta. At best, the TPC pion electron separation capability enables a limited access to the J/ψ-region, but never to the Υ-region. Therefore an additional detector with efficient electron-pion separation is necessary to perform the di-electron (also high-p_t single electron) physics program. This was the main issue to propose the TRD[9, 130].

In addition to electron identification, the TRD will serve as a trigger for electrons with momenta higher than 3 GeV/c. A task that is not less important than electron identifica-

tion, especially in terms of the small production rates of Quarkonia. With the TRD the number of recorded J/ψs will be enhanced by a factor 4 and the number of recorded Υs will be enhanced by an order of magnitude[130]. The TRD will also improve the tracking capability of the TPC.

1.2 Outline of the Thesis

This thesis will deal with the readout chamber of the ALICE TRD and its physics performance in the Quarkonia sectors produced in heavy-ion collisions. As such, the thesis deals with two physics fields: Detector physics and heavy ion physics. From academic point of view these two fields are not related to each other therefore the thesis is subdivided into three parts.

In Part I generalities to both fields will be presented (restricted to purview which are related to the thesis). Chapter 2 gives a physics state on heavy-ion collisions, QGP, its properties and signatures and an overview on LHC and the ALICE experiment and its sub-detectors. Chapter 3 gives a summery on energy loss in gases and transition radiation, as the main processes on which the electron identification of the TRD relies. Chapter 4 contains a reference summery of the TRD parameters, physics motivations, and design criteria.

In Part II the read-out chamber of the TRD will be studied. Chapter 5 deals with electrostatic simulations of the chamber, aiming to determine the electrostatic and the geometric settings of the chamber and a drift gas mixture. In Chapter 6 the results of tests on the geometrical and electrostatic stability will be discussed. Chapter 7 covers the analysis of beam data with pions and electrons. In particular the pion-electron separation capability of the detector and its dependence on the particle momentum will be studied as well as the position and angular resolutions and their dependence on the signal-to-noise ratio.

Part III covers the simulated physics performance of the central barrel in the Quarkonia sector. In Chapter 8 an overview on the Quarkonia systems and their production rates in Pb-Pb collisions at LHC energies will be given. Chapter 9 shows the detector response of the ACB, its detection efficiency and transverse momentum resolution. Finally in Chapter 10 the capability of the ACB to detect Quarkonia systems will be discussed with special emphasize on the role of the TRD in this physics sector.

Although the TRD is now in the mass-production phase, some parameters which are given in this study could change in the future. For an updated set of parameters see the home-page of the TRD:
http://www-alice.gsi.de/trd/index.html.
and the home-page of the ALICE physics performance report[5]:
http://alice.web.cern.ch/Alice/ppr/.

Part I

Generalities

Chapter 2

Ultra-relativistic Heavy-Ion Physics

2.1 Quantum Chromo-Dynamics and Quark Gluon Plasma

In analogy to the *Quantum Electro-Dynamics* (QED), the theory which describes electromagnetically interacting systems, the *Quantum Chromo-Dynamics* (QCD) was developed to describe strongly interacting systems. The QED particles are electrically charged and the potential between them follows a $(1/r)$-law; $V_{QED} = -\alpha_{em}/r$, where r is the distance between the interacting particles and $\alpha_{em} = 1/137$ is the *fine structure constant* with which the interaction couples. The interaction between the particles is mediated through virtual, electrically neutral photons.

In the QCD the fields are quark and gluon fields with the associated particles quarks and gluons (*partons*). Quarks are spin-1/2 particles and carry in addition to the electric charge one of three different *color charge*s. This quantum number has been introduced to avoid the violation of the Pauli exclusion principle[1]. Quarks appear in six *flavors* denoted with *u,d,s,c,b*, and *t* which are respectively, the *up*, *down*, *strange*, *charm*, *bottom*, and *top* quarks. Gluons are the electric neutral gauge bosons which intermediate the strong interaction and carry themselves color charge and as such they can interact with each other. This is one of the main differences between QCD and QED. Another characteristic difference between both theories, is the weakness of the electromagnetic coupling which facilitates the application of *perturbation theory* to describe electromagnetically interacting systems. Based on an expansion in powers of α_{em}, this theory considers the properties of exchanging more than one photon in the interaction, the so-called *next-to-leading order(s)*. This allows to calculate the forces between the particles involved in the interaction with high accuracy. Since α_{em} is very small, higher powers can be neglected.
Contrary to the electromagnetic coupling constant the QCD coupling "constant" α_s is not really constant but it is rather a strongly varying function of energy and momentum

[1]Particles like Ω^- which consists of three quarks (*sss*), have a total spin of 3/2. This means that all three spins of the quarks are oriented parallel to each other. Therefore the quarks must have an additional quantum number to characterize their state.

transfer in the interaction $q^2)^2$ [10])[3]:

$$\alpha_s(Q^2) = \frac{12\pi}{(33 - 2n_f)\ln(Q^2/\Lambda^2_{QCD})}, \tag{2.1}$$

where n_f is the number of flavors, $Q^2 = -q^2$ with q^2 the momentum transfer which is inversely proportional to distance between the interacting particles,r, and Λ_{QCD} is the QCD energy scale. Λ_{QCD} represents the energy scale at which the strong interaction becomes strong [12]. The value of Λ_{QCD} was determined experimentally to be about 200 MeV [13].

2.1.1 QCD Properties

Confinement:

A third difference between the two theories is the phenomenological fact that single quarks were never observed in nature, only color singlet states exist in the *QCD vacuum* (hadronic world), represented by quark–anti-quark bound states (mesons) and three-quarks (anti-quarks) bound states (baryons). This suggests that the interaction between quarks and gluons must be strong at large distance scales. The potential between the quarks increases with the distance between them, so that it becomes energetically favorable to build a quark–anti-quark pair from the vacuum to create colorless mesons. This behavior is reflected in the potential of the strong interaction:

$$V_s = -\frac{4}{3}\frac{\alpha_s}{r} + kr. \tag{2.2}$$

The first term shows the Coulomb-like behavior of the strong interaction. It represents the exchange of one gluon between two quarks (leading order). The second term represents the gluons self-interaction. At large distances the energy kr reaches a value which is large enough to create a new quark–anti-quark pair. With this behavior, quarks and gluons possess the long-distance property of *confinement*.

In Equation 2.1 the confinement is reflected by the increase of α_s at small momentum transfer (large r), resulting in stronger forces between the partons at larger distances, which confines them within a small region on the order of hadron sizes ($\sim$ 1 fm[3]). This corresponds to an energy scale at the level of Λ_{QCD}.

Asymptotic freedom:

Since the quarks are confined, it is not possible to observe them directly. Their existence was inferred by deep inelastic-scattering of electrons on hadrons [14, 15, 16] and e^+e^- annihilation experiments [17]. This allowed to probe their momentum distribution within the bound hadronic state. It was found that with large momentum transfer from a scattering electron to a parton, the latter seems to behave as if it were free. In contrast to long scale distances, α_s approaches zero at short-distances and the potential becomes

[2]Therefore α_s is also called running coupling constant.

[3]Strictly speaking α_{em} is also a function of q^2 but the dependence is much weaker.

weak, the quarks are said to follow the short distance property of *asymptotic freedom*. As a function of Q^2, α_s was measured at LEP, for instance, by the DELPHI Collaboration of CERN's LEP [18]. The mentioned differentiating character of Λ_{QCD} between the confined (hadronic) world at the scale of $Q^2 \simeq \Lambda_{QCD}$ and the deconfined world at $Q^2 \gg \Lambda_{QCD}$, reflects the QCD asymptotic freedom property. It was one of the first perceptions which lead to the prediction of the QGP existence [19].

The asymptotic freedom property at small distances is a consequence of the self interaction of gluons. It makes QCD, as QED, accessible to perturbation theory which describes systems with large Q^2, *hard processes*, very well. On the other hand the study of interactions with small Q^2, *soft processes*, or the study of hadronic ground states, which require low momentum transfer, is not sufficient with power based perturbation theories of the strong varying coupling "constant". Systems with strong coupling, i.e. confined matter, must be treated *non-perturbatively*. At this limit the QCD observables can be calculated within the *Lattice QCD* formalism.

Chiral symmetry:

In the limit of vanishing quark masses, the QCD Lagrangian is chirally invariant due to the particles helicity conservation. *Right-* and *left-handed* quarks do not mix. Considering the *up* and *down* quarks, the lightest with *current* masses ($\simeq$ 5 MeV) much lower than Λ_{QCD}, this constitutes an $SU(2)_L \otimes SU(2)_R$ symmetry. In QCD vacuum where α_s is larger than zero, quarks can interact, leading to an increase of their masses up to the *dynamical* values of 300 MeV for the u and d quarks and 500 MeV for the s quark [20]. Since a massive quark cannot move with the velocity of light, it is always possible to find a reference system in which a right-handed quark has a spin antiparallel to the momentum. When a quark could appear to be right- or left-handed, depending on the reference frame, the chiral symmetry is broken. The vacuum is a condensate of scalar quark–anti-quark pairs which squeezes color fields in hadrons.

With Equation 2.1, α_s approaches zero when the transverse momentum becomes higher than Λ_{QCD}. This minimizes the quark interaction and their masses approach their current values and the chiral symmetry is "partially" restored.

2.1.2 Lattice QCD

A system of quarks and gluons with strong long-range (low momentum transfer) behavior cannot be described analytically since, according to Equation 2.1, α_s goes to infinity. It is, therefore, treated with the lattice gauge theory. A computer based simulation in which the QCD continuum is discretized on a lattice of space-time coordinate [21, 22]. It offers a reliable method to study strong forces between quarks and hadrons at low momentum transfer.
This theory possesses two advantages: First, with finite space-time intervals it offers a possibility to regularize terms with *ultraviolet (UV) divergence*. The distance between two nearest lattice points, a, is the shortest distance scale of the system. The UV divergences are regularized by giving a momentum cut-off on the scale of $\Lambda = 1/a$. Making

use of the discretization the second advantage is the possibility to employ numerical path integrals for the QCD Lagrangian. Monte-Carlo methods can be used to find out the equilibrium state of the system. With the two advantages, LQCD provides an approach to basic aspects of the thermodynamics of strongly interacting matter in equilibrium allowing non-perturbative aspects of the QCD to be studied.

Such LQCD calculation predicted that a strongly interacting matter will undergo a *phase transition* from hadronic state into a new strongly interacting system with high energy density where quarks and gluons are deconfined, if the temperature or the pressure of the system becomes comparable with Λ_{QCD} [1].

2.1.3 Quark Gluon Plasma and Critical Parameters

The confinement can be seen in the following way: In hadronic matter the vacuum outside the hadrons acts as a color isolator confining the colored quarks and gluons to colorless hadrons. The pressure of the vacuum acts on each hadron separately. This is one of two differences between a Hadron Gas (HG) of massless hadrons (pions for instance) and an ideal QGP gas with massless quarks. Assuming a vanishing baryon density n_B the vacuum pressure in the QGP gas is perturbative and external and it acts on the system as a whole whereas the pressure in the HG is not external since the vacuum is present between the hadrons.
The second difference between both gases is the number of degrees of freedom represented by the *degeneracy* factor g:

$$g = n_b + \frac{7}{8} n_f, \tag{2.3}$$

with n_b and n_f the number of boson and fermion degrees of freedom respectively.
Using thermal momentum distributions for bosons and fermions, the energy density ϵ, the pressure p, and the entropy density s in the ideal relativistic gas are given by [10]:

$$\begin{aligned} \epsilon &= \frac{g}{30}\pi^2 T^4, \\ p &= \frac{g}{90}\pi^2 T^4, \\ s &= \frac{2g}{45}\pi^2 T^3, \end{aligned} \tag{2.4}$$

where T is the temperature. With $n_b = 3, n_f = 0$ for the HG, its pressure is given by:

$$p(HG) = \frac{1}{30}\pi^2 T^4. \tag{2.5}$$

In a QGP state n_b and n_f are given by:

$$\begin{aligned} n_b &= 8(\text{color}) \times 2(\text{spin}) = 16, \\ n_f &= 3(\text{color}) \times 2(\text{spin}) \times 2(\text{flavour}) \times 2(\text{quark} - \text{antiquark}) = 24. \end{aligned} \tag{2.6}$$

The external pressure on the QGP can be estimated with the MIT *bag model* [10]. The model considers the quarks to be massless particles inside a bag of finite dimension and infinitely massive outside. Confinement is then the result of an inwards acting *bag pressure* B, which is balanced by the pressure arising from the thermal pressure (kinetic energy) of the quarks and gluons. The gluons are also confined in the bag leading to a colorless matter inside it. With Equations 2.4 and 2.6, the pressure in the QGP gas is given by:

$$p(QGP) = \frac{37}{90}\pi^2 T^4 - B. \tag{2.7}$$

The bag pressure B is given by [10]:

$$B^{1/4} = \left(\frac{2.04N}{4\pi}\right)^{1/4} \frac{1}{R}, \tag{2.8}$$

with R the bag radius at equilibrium and N the number of quarks in the system. Equations 2.5 and 2.7 indicate that low temperatures lead to a $p(HG)$ higher than $p(QGP)$. As the temperature increases, both pressures become equal at a critical value T_c. At temperatures grater than T_c and due to its larger number of degrees of freedom, the pressure of the QGP state overrules that of the HG. Since the state of the higher pressure is the stable one, the HG is stable at low temperatures whereas at high temperatures the QGP state is the stable one. Both pressures are equal under the critical temperature:

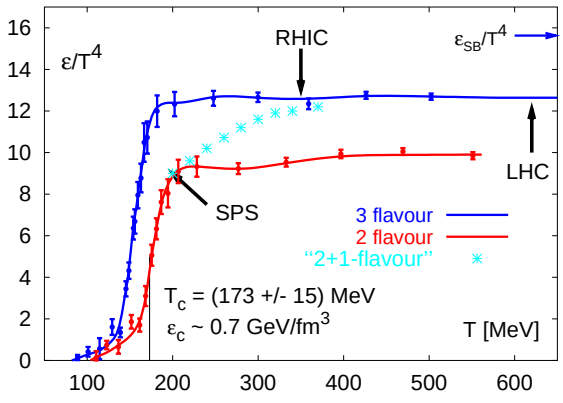

Figure 2.1: Energy density as a function of the temperature as calculated within LQCD for different compositions of quark flavors. The critical temperature is around 174 MeV, see [11]

$$T_c = \left(\frac{90B}{34\pi^2}\right)^{1/4}, \tag{2.9}$$

which characterizes the point where $p(HG)$ overrules B.

For a 3-quark system in a baryon with a confinement radius of 0.8 fm, Equation 2.8 results in a bag pressure of $B^{1/4} = 206$ MeV. With Equation 2.9 this leads to a critical temperature of about $T_c \simeq 144$ MeV. Once the temperature of the system exceeds T_c, the quark-gluon-plasma is expected to occur.

Depending on the number of included quark flavors and quark masses, lattice calculations deliver exact results for the critical temperature of the phase transition. Lattice calculations [1] show that this transition occurs with a sudden increase of the energy density as

a function of the temperature, within a narrow interval around T_c (compare Figure 2.1). For 2-flavor QCD the expected critical temperature is found to be $T_c = 173 \pm 8$ MeV [23] at a critical energy density of about $\epsilon_c = 0.7$ GeV ($T_c = 171 \pm 4$ MeV [24]). For 3-flavor QCD the critical temperature is about 20 MeV lower than the 2-flavor QCD case ($T_c = 154 \pm 8$ MeV [23]). Taking two light and one heavier quark (2+1-flavor) delivers comparable values. But it increases slower than the 3-flavor case. This means that the s-quark dose not take part at the thermodynamical evolution of the system directly at T_c but at about $2T_c$.

At vanishing temperature, the bag pressure can be overruled by the parton pressure at high baryon number density n_B. The Pauli exclusion principle allows only one quark (fermion) to populate one state. With increasing quark number in the bag, the quark gas acquires a pressure due to its degeneracy. At a critical baryon number density the *degeneracy pressure* exceeds the bag pressure and a QGP state becomes possible.
With the baryon density number of a quark $n_B(\mathrm{q}) = 1/3$, the critical baryon number density is given by [10]:

$$n_B(\mathrm{QGP}) = \frac{4}{3}\left(\frac{g_q}{24\pi^2}\right)^{1/4} B^{3/4}, \tag{2.10}$$

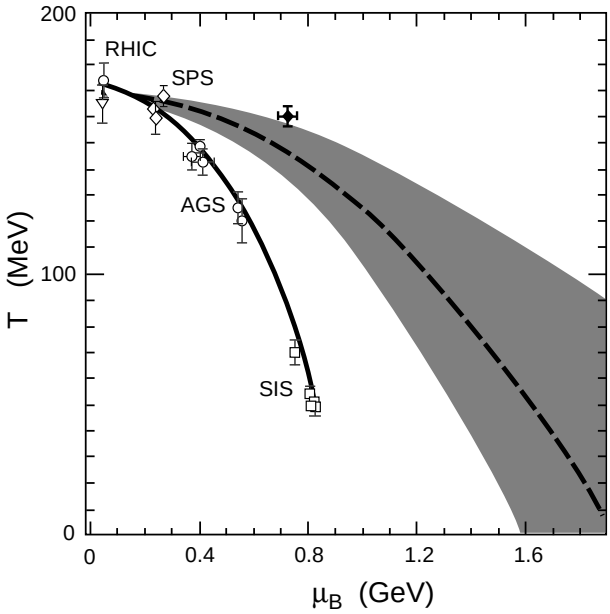

Figure 2.2: QCD phase boundary as calculated on the lattice, dashed line. The open symbols show the conditions of chemical freeze-out at different experiments as reconstructed from the data.The Figure is taken from [5] where the original references are given.

The formation of the deconfined matter occurs when the baryon number density exceeds a value of $3\rho_0$, where ρ_0 is the nuclear matter density. Theoretical lattice calculations for non-vanishing net baryon density are difficultly accessible because of the mentioned UV divergence in the LQCD.
Nonetheless, efforts in this sector delivered recently first results [25, 26, 27] where $T_c(\mu_B)/T_c(0) = 1 - 0.0065(\mu_B/T)^2$, where μ_B is the baryon chemical potential. It is related to n_B via $n_B = g\mu_B^3/6\pi^2$. The results show a rather low dependence of T_c on the chemical potential. The chemical potential characterizing the *freeze-out* (defined in next section) at RHIC, μ_B is found to be around 50 MeV [65]. Therefore the influence of a non-vanishing chemical potential will be much weaker at LHC.

The cases between the mentioned extreme situations ($T = 0$ and $n_B = 0$), are a sum of two contributions from both the thermal and the degeneracy pressure. Figure 2.2 shows the

phase diagram in the temperature and baryonic chemical potential plane represented by the dashed line, see Refs. 12-16 in [5]. The points represent the obtained pairs of variables (T, μ_B) at chemical freeze-out. The values are extracted from experimental data, taken within a large beam energy rang, using thermal fits of measured particle ratios [61]. LHC, which is not shown in the figure, enables closer approach to vanishing net baryon density, getting closer to the stage which is believed to have dominated in the early universe in its first few microseconds.

The order of the phase transition into the QGP state is still debated and only partially understood. One expects a *first order* transition at low temperatures and high baryon densities which would probably change to a *continuous crossover*transition at a critical point (T^{so}, μ_B^{so}), which is represented by the full point in Figure 2.2. The point shown in the figure is taken from early calculations [25] where it was found at $T^{so} \simeq 165$ and $\mu_B^{so} \simeq 700$ MeV. Recent calculations [30] show that the point is rather at $T^{so} \simeq 162$ MeV and $\mu_B^{so} \simeq 400$ MeV. For a recent review on LQCD results of the transition parameters see [11].

2.2 Heavy-Ion Collisions

2.2.1 Experimental Programs

The extreme conditions required to form the QGP state may be attained in laboratory by employing heavy-ion collider, where heavy nuclei ($A > 200$) collide head-on after being accelerated to ultra-relativistic energies. The established nuclear matter is highly compressed and excited, longitudinal beam energy is converted into transverse energy and other degrees of freedom, creating the best energetic conditions to form the deconfined state of matter. The investigation of the properties of such a matter is the field of ultra-relativistic Heavy-Ion Physics (HIP) which aims to detect and characterize the QGP. The field is quite interdisciplinary as it contains elements from particle physics, nuclear physics, particle kinetics, statistical field theory and fluid dynamics.

In the last fifteen years a series of experiments with *Nucleon-Nucleon* (pp), and *Nucleus-Nucleus* (AA) collisions started at different laboratories. At the Schwer-Ionen-Sychrontron (SIS) at the Geselschaft für Schwer Ionen (GSI), experiments were carried out with Au-Au and Ni-Ni at energies of $\sqrt{s} \simeq 1-2$ AGeV in the center of mass system (*cms*). At the Alternating Gradient Synchrotron (AGS) at Brookhaven National Laboratory experiments with Si, O, and Au beams were carried out at *cms* energies of about $\sqrt{s} \simeq 5$ AGeV.
The Super Proton Synchrotron (SPS) of CERN started at mid-eighties with O and S beams at *cms* energies of $\sqrt{s} \simeq 8$ AGeV. The facility was later upgraded to enable Pb-Pb beams at $\sqrt{s} \simeq 20$ AGeV. In 2000 the collider era started with the Relativistic Heavy-Ion Collider (RHIC) at a *cms* energy of 130 AGeV which is meanwhile extended to 200 AGeV. In 2007 LHC will start its program at a *cms* energy of $\sqrt{s} \simeq 5.5$ ATeV, see Section 2.4.

Non-vanishing baryonic number brings up complex quantities in the Feynman integrals, therefore lattice calculations are difficult accessible with $\mu_B \neq 0$. The most theoretically understood region of QCD matter is that of high temperature and low baryon density

($\mu_B/T \rightarrow 0$). This region is only accessible with machines like RHIC and LHC. But, the higher the energy, the larger is the number of final state particles, which is, however, very helpful when interpreting the data. For example when taking the ratios of neutral-to-charged low-p_t pions, which give information on chiral symmetry restoration and the ratio of kaons-to-pions which carry signatures of strangeness enhancement. The large number of particles is also helpful since the statistics is event-dependant which offers fluctuation studies.
In addition, the system from which the particles are generated, occupies a larger volume than in proton-proton collisions, for instance, which enables the system to be in thermal equilibrium, so that the principles of thermodynamic can be applied on the data. On the other hand, such high energy regimes are coupled to enhancement in the nuclear transparency and baryon density effects cannot be studied. Here, lower energies are required. The program of the SIS-200 at GSI will be carried out [31] to study this heavy-ion sector in more detail.

2.2.2 Collision Dynamics

Typically, in heavy ion collisions high energy nucleus collide with a fixed target (SPS) or head on at collider facilities. In the collision zone, the so called *participant region*, the nucleons from both nuclei which take part in the primary collisions are called *participants* and the non-interacting nucleons are called *spectators*. Since a nucleon can take part in more than one collision, the number of participants, N_{part}, can lead to a maximum value of N_{bin}, the number of binary collisions. N_{bin} and N_{part} depend on the *centrality* of the collision. That is the degree of the nuclei overlap. The only "access" to the geometry of the collision is the *impact parameter* b, which is defined to be the distance between the two nuclei centers. The maximal b value is then given by the nuclei radii.

During the collision the nuclear matter is extremely heated and compressed. Partons interact and scatter frequently in a region with high energy density where the best opportunity is achieved to form the QGP state. The system evolves in time and space and goes through several stages: initial conditions (or thermalization), formation of QGP, phase transition from QGP to hadron gas, chemical freeze-out and finally kinematic (or thermal) freeze-out.

Assuming that the system lives long enough and that a thermal equilibrium is attained within the formation time, $\tau_0 = \tau_{eq}$, compare Figure 2.3, the time evolution of the system's temperature can be described within hydrodynamical models [32]. The most physical scenario looks like follows: At the temperature T_{eq} the system is in its initial stage, the inelastic collisions of the partons in the nucleons create many secondary partons. It follows the pre-equilibrium stage in which the relevant degrees of freedom are partonic causing the secondary partons to undergo interactions with each other. At the time $\tau_0 = \tau_{eq}$ the partonic system reaches a thermal equilibrium. From this time on and up to the time τ_c where the temperature is at the critical value T_c, the system expands, due to its internal pressure, isentropically and adiabatically and strong re-interactions lead to collective phenomena and chemical equilibrium in the light sector. For the duration of $\tau_{mix} = \tau_h - \tau_c$ the system expands isothermally at constant temperature T_c, the heat is

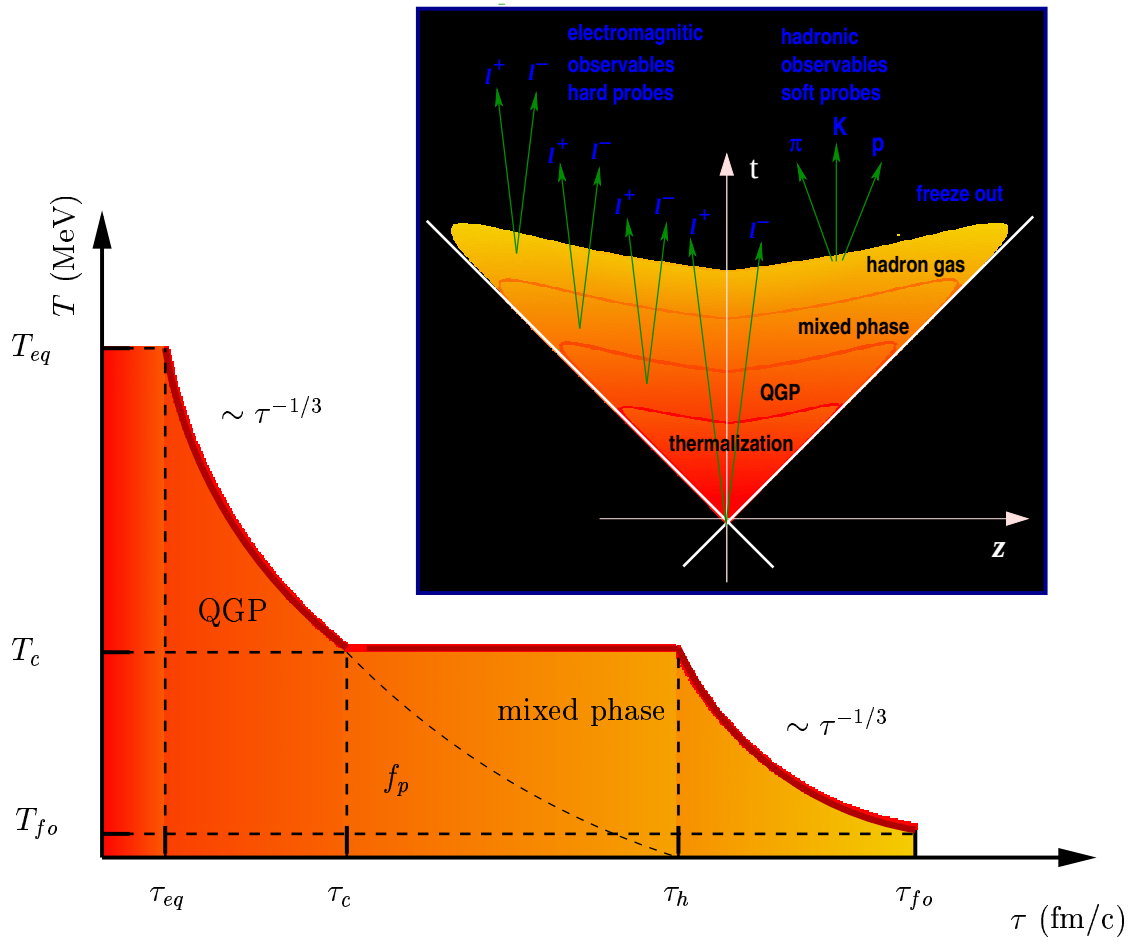

Figure 2.3: Sketch of the dynamical evolution in a heavy ion collision.

consumed in the conversion of the patrons degrees of freedom into those of hadrons. If the phase transition is of first order, then a co-existence of partons and hadrons will occur at this temperature. As the system expands it reaches a point in time where its energy is low for inelastic collisions. At this time point the particles distributions among the hadronic states is frozen and no flavor changes appear any more.
The hadronization process is then completed at the time τ_h resulting in a hadronic gas which starts to expand isentropically and to cool down. During this expansion the hadrons continue to interact with each other up to the thermal freeze-out time, τ_{fo}. At this point in time, the elastic collisions between the hadrons stop, due to the low density and they escape the system.

In order to compare the phenomena in the collision, its observables are presented in terms of Lorentz invariant and additive variables. The *rapidity*, y, which presents the velocity of the beam. $y = \frac{1}{2}\ln(\frac{E+p_z}{E-p_z})$ with E the total particle energy and p_z the momentum component in the beam direction. The transverse momentum p_t , which is perpendicular to the beam direction and Lorentz invariant under longitudinal transformations. These variables are measurable in experiments and can be used to estimate the energy density

ϵ, as given in Equation 2.4, reached in a collision.

The development of the system and the calculated energy density depend strongly on the *stopping power* of the collision which characterizes the kinetic energy loss that the nucleus suffer. It defines the prevailing energy and the particle density. The two extreme scenarios of total stopping and total transparency of the colliding nuclei are described by the *Landau model* of relativistic heavy-ion collisions [33] and the *Bjorken model* [34] respectively. In the Landau model the nucleons undergo many secondary collisions until they come completely to rest in the center of mass system. As all of the initial baryons are then concentrated at mid-rapidity the full stopping creates a baryon rich plasma. The critical energy density at which the plasma is established is given by:

$$\epsilon = 2\gamma^2\epsilon_0,$$

where $\gamma = 1/\sqrt{1-(v/c)^2}$ is the relativistic factor and ϵ_0 is the energy density of the ions at rest. ϵ is an upper limit for real values reached in experiments.
The Bjorken scenario assumes that the colliding nuclei pass through each other after the initial collisions and travel far away from the collision region such that no secondary collisions take place. This situation relates to a plasma with vanishing net baryon density (baryon free). In this scenario the energy density is given by:

$$\epsilon = \frac{dE_t}{d\eta}\frac{1}{\pi R^2 \tau_0},$$

where $\frac{dE_t}{d\eta}$ is the transverse energy per unit rapidity, η is the so-called *pseudo-rapidity* η , $\eta = -\log\tan(\theta/2)$ with θ the polar angle.R is the radius of the participant region and τ_0 as defined before. Since τ_0 is not measurable in experiments, it is generally taken to be $\tau_0 = 1$ fm/c following Bjørken's assumption [34].

2.3 Signatures of Quark Gluon Plasma

2.3.1 QGP Diagnostic

The theory does not deliver any definitive indicator of the predicted deconfined state of QGP, but numerous of observable signatures. In most cases one looks for anomalies which differ from those in hadronic states.
A serious problem is the short life time of the QGP state and its small size. Apart from LHC conditions the duration time of the deconfined matter is below 5 fm/c.
Nevertheless a notable number of ideas were proposed to accomplish the identification and investigation of the deconfined matter state despite its short life time. Thereby various signatures must be measured simultaneously as functions of the energy density, p_t, and the pseudo-rapidity in collisions at different *cms* energies.

One subdivides the nowadays adopted QGP signatures into three classes:

1. **Global observables** like the particle *collective flow*, the distributions of charged particle density per rapidity unit $\mathrm{d}N_{ch}/\mathrm{d}y$, energy density per rapidity unit $(\mathrm{d}\epsilon/\mathrm{d}y)$,

and *Hanbury-Brown-Twiss* (HBT) particle correlation function.
The collision evolution as sketched in Subsection 2.2.2 is justified by the assumption of thermal equilibrium. Equilibrium implies that collective effects should play an important role in the evolution of the system [35]. It is intuitive that the first thing to look at is whether an equilibrium occurs in the collision or not. The global observables try to answer this question.

2. **Probes of large cross section** like strangeness enhancement, particle abundances, baryon chemical potential at freeze-out (particles yield ratios)
These probes are also called hadronic probes which are easily accessible to detectors. But hadrons also take part on the evolution of the strong re-interactions of the system after their creation. Also after hadronization they keep interacting with each other both elastically and inelastically until they escape the system and can be detected. This makes them susceptible to momentum modifications which affect the particle composition in the final state. However, the ratios of produced hadrons offer keys to questions of particle production mechanisms and of the freeze-out points.

3. **Probes of small cross section** like J/ψ production, QGP thermal radiation, open charm and beauty, and jet quenching (which is rather an effect as a physical signature). These are the electromagnetic probes, due to their electromagnetic decay channels (apart from jet quenching). They are hard to detect due to their small production cross sections and their low di-leptonic Branching ratios combined with the largely abundant background. Their advantage is the "neutrality" in the evolution, due to their non-ability to interact strongly, such that they propagate through the system without any kinematic modifications. In addition, since leptons are produced at all stages of the collision, they carry information on the evolution of the system back to the very first moment.

Some of these signatures were observed experimentally like strangeness enhancement and J/ψ suppression. However the latter is still debated and the way how the J/ψ yield is related to the QGP state is seen in different ways by different communities of heavy-ion physics [6, 36, 37, 38].

In the following some of the topics listed above which are widely accepted and partially observed in experiments will be, rather not complete, presented. For reviews see for example [39, 40, 41].

2.3.2 Global Observables

1. **Collective Flow:**

   The hot and dense matter created in the participants region is presumably affected by the compression of the initial stage. The (an)isotropy of this matter is described by anisotropic flow which provides access to the equation of state [42]. Many other processes like thermalization, QGP formation, phase transition, and freeze-out point are accessible with the anisotropic flow.

Quantitatively the anisotropic flow is expressed through the Fourier coefficient of the particle distribution in the azimuthal angle of the emission ϕ.

$$F(\phi) = F_0(1 + \Sigma_{i=1}^{n} 2v_i \cos(i\phi)), \tag{2.11}$$

ϕ is measured with respect to the reaction plane[4] which is spanned between the impact parameter b and the beam direction z.

It turns out that [42] $\langle \cos i\phi \rangle = v_i$, in heavy-ion collisions the most used harmonics of Equation 2.11 are the di- and the quadrupole coefficients v_1 and v_2. They denote the *directed flow* and the *elliptic flow* respectively.
In general large values of collective flow are considered to be signatures of hydrodynamic behavior and therefore signal a QGP state.

Directed flow:

The directed flow affects particles at forwards or backwards rapidities. At very low energies where attractive nuclear mean fields are dominated, the nucleons of the projectile are reflected towards the target leading to a negative directed flow. At higher energies, nucleon-nucleon collisions dominate over mean field effects. The fragments of the projectile and target are deflected away from each other leading to positive directed flow.
At much higher energies the affected particles escape quickly the central region, i.e. the influence region of the transverse pressure. This means that the directed transverse flow pattern is established very early in the collision. Since the time scale in such a situation decreases, the directed flow decreases also but remains positive.

In [43] it is argued that the increase entropy density at the onset of QGP production should lead to a softest point in the nuclear equation of state. In [44] the softening process is predicted to reduce the directed flow making the phase transition visible as a minimum in its beam energy dependence. Therefore the study of directed flow enables answering the question if the system goes through a phase transition or not.

Elliptic flow:

The elliptic flow is generated by geometrical asymmetry of the reaction region in transverse plane. Immediately after the collision the system is expected to have the largest spatial anisotropy. As the system evolves this spatial anisotropy is converted into momentum-space anisotropy through multiple interactions.

Experimental evidence of both, the directed and the elliptic flow was observed at all energies studied up to now. As function of the beam energy the directed flow starts with negative values at SIS energies and crosses the zero level to reach a plateau at an energy of about 2 GeV in the AGS region [45]. At SPS energies it drops again [46, 47, 48, 49] and keeps decreasing at RHIC energies [50]. This decrease indicates indeed changes in the nuclear equation of state.

[4]The reaction plane is to be taken in the momentum space.

The elliptic flow was observed over all energy regimes between SIS and RHIC [48, 51]. Through the dominance of the attractive nuclear mean field at low energies, the target and the projectile form a rotating system. The established centrifugal force causes particles to escape the system in the rotation (interaction) plane. This positive elliptic flow is called *in-plane flow*. At high energies where the nucleon-nucleon collisions dominate over mean field effects, the participants which are compressed in the overlap region of target and projectile, cannot escape the system in the reaction plane any more because of the pressure of the spectators. The heated matter expands more rapidly in the exposed direction perpendicular to the reaction plane rather than in the "blocked" one. This elliptic flow is called *out-plane flow* and it is signed negative. At relativistic energies $\simeq 4$ GeV/c, the spectators of the colliding nuclei pass each other very quickly such that the direction of the interaction plane becomes also exposed and the in-plane flow component becomes dominant and the flow becomes positive again. Its value keeps increasing with increasing beam energy.

In [52] it is argued that a minimum of the collective flow excitation function will signal a first order phase transition. Recent results from the NA49 Collaboration [53] show a vanishing v_2 of protons in Pb-Pb collisions at $sqrts = 40$ AGeV at mid-rapidity and for all centralities. These results are remarkable because v_2 of protons at $\sqrt{s} = 11$ AGeV (AGS) and $\sqrt{s} = 160$ AGeV (SPS) is different from zero at mid-central and peripheral collisions [54, 53]

2. N_{ch} **and** E_t **Distributions:**

The thermodynamical variables, representing the initial conditions of the collision, are related to measurable observables, respectively: The energy density to dE_t/dy, the entropy density to dN_{ch}/dy, and T to the slope of the transverse mass m_t distribution.
From Equations 2.4 it is evident that the degeneracy g increases with growing temperature as a function of the pressure and the energy density.

Due to the large difference in degrees of freedom between QGP and HG states (27 and 3 respectively), if a QGP state is formed a rapid increase in the ratios ϵ/T^4 and p/T^4 would occur within a small temperature range.

Charged particles density:

The charged particle density is proposed to be sensitive to particle production mechanism [55]. Soft (hard) processes are believed to scale with N_{part} (N_{bin}), the knowledge on dN_c/dy will shed light on the debated issues in the particle production sector.
If a local equilibrium is established in the system, the entropy remains conserved during the dynamical evolution of the system [55]. Therefore the dN_c/dy distribution contains information on the equilibrium status.

Transverse energy density:

Measurements of dE_t/dy enable a direct estimate of the energy density ϵ via the Bjorken formula. At AGS, SPS, and RHIC, $dE_t/d\eta$ was found to be about 200 [56],

450 [57], and 578 [58] respectively. Using the Bjorken formula with an initial time of 1 fm, this results in energy densities of 1.3, 3.2, and 5.0 GeV/fm^3. With the critical temperature between 150 and 200 MeV, the energy density is between 0.6-2 GeV/fm^3, see Figure 2.1 which implies that already the SPS energy is in a critical region.

In general, the multiplicity (dN_{ch}/dy) and the transverse energy distributions, support all other QGP signals through the information which they provide on the initial conditions. The averaged transverse energy per produced particle ($[dE/d\eta]/[dN_{ch}/d/\eta]$) is found to be universal at a constant value 0.8 (within errors) as data from WA98 [59] and PHENIX show [60]. It dose not depend on the beam *cms* energy which implies that the increase in the energy leads to an increase in the number of produced particles rather than in increasing the transverse energy of produced particle.

The relation of the temperature to the m_t slope will be discussed in connection with the kinetic freeze-out.

3. **Freeze-Out:**
During the cooling down and the collective expansion of the system, particles decouple when their density gets low enough (low temperature). At two different stages two types of freeze-out occur: chemical and kinetic freeze-out.

Chemical freeze-out:

The chemical freeze-out denotes the point where the species of the particles are settled. The ratios of the resulting yield of the different particles are well described by statistical models [61]. With the grand canonical ensemble, the final particle production ratios are governed by two independent variables; the temperature T and the baryo-chemical potential μ_B [62, 63].

All data at all energy regimes from AGS to RHIC can be described within the thermal model [63, 64]. It delivers that the temperature and the baryo-chemical potential reached at SPS are in the order of $T_c = 165 \pm 5$ MeV and $\mu_B = \simeq 270$ MeV respectively [63]. At RHIC, T_c is found to be on the order of 175 ± 7 MeV and $\mu_B = 51 \pm 6$ MeV [66]. At both energy regimes the temperature seems to be in the same region but the net baryon density (characterized by μ_B) is much lower at RHIC. The SPS and RHIC points in the $T - \mu_B$ plane as reconstructed from the data are shown in Figure 2.2, they are close to the theoretical HG-QGP boundary which indicates that the system was, at least, in a mixed phase.

Kinetic freeze-out:

At the kinetic freeze-out the produced particles stop interacting with each other. The p_t-spectra of identified particles give information on the condition (temperature) where this point took place [67]. If the system is in thermodynamic equilibrium the transverse mass spectra ($m_t = \sqrt{m^2 + p_t^2}$) will have a slope inversely proportional

to the temperature T. If the particles in the transversely expanding system freeze out at the same temperature then the slope parameter will increase with the mass of the particles. This means that in addition to the thermal (chaotic) flow, the system features an additional collective flow component, β_t [68]. This component shifts the freeze-out temperature T_{fo} in the blue region such that the measured temperature is given by $T = T_{fo} + m_t \langle \beta_t \rangle^2$. This postulation enables to characterize the spectra only by two parameters, T_{fo} which is found to be around 130 MeV for all energy regimes up to RHIC and β_t which takes a value of about 0.4 at AGS and SPS and 0.6 at RHIC, see [40] and Refs. therein.

4. **HBT Correlation**
The copiously produced charged π-mesons in a collision are spinless particles and thus they are described by *Bose-Einstein quantum statistics*. They tend to cluster together in the momentum space at short range correlations.
The geometry and dynamics of the fireball source at the chemical and thermal freeze-out time determine the characteristics of the pion clustering. Consequently, studying of the clustering allows the extraction of the source geometry and delivers information on its dynamics. Due to its large degrees of freedom, an unusually long life time of a source can signal the formation of the QGP state.

The HBT interferometry is the technique which is used to carry out the clustering studies. It enables access to the thermal freeze-out through the size of the source, its life time, emission duration, and expansion (flow) velocity.

In addition to two-pion HBT analysis, kaon interferometry allows investigation of the time characteristics of the source, its geometry etc., under the kaon production conditions and at their production momentum, which is expected to occur earlier than the pions production time due to the larger mass of kaons.

The source geometry is characterized by three radii (R_{long}, R_{side}, and R_{out}). R_{long} describes the longitudinal expansion and the life time up to freeze-out τ_{fo} and longitudinal correlation length. R_{side} and R_{out} describe the radial expansion and their ratio gives the duration of particles emission from the source and transverse geometry.

HBT analysis programs have been successfully accomplished for pions, kaons and protons at SPS energies [69, 70, 71], and RHIC energies [72, 73].
The CERES HBT analyses have shown that the source radii depend only weekly on the SPS beam energy. Assuming a freeze-out temperature between 120 and 160 MeV at a beam energy of 158 AGeV, the analyses lead to measurements of the freeze-out time of $\tau_{fo} \simeq 7 - 8$ fm/c, a transverse velocity of about $\beta_t \simeq 0.4c - 0.6c$, an emission duration of $\Delta\tau \simeq 2$ fm/c [70]. The volume at freeze-out increases linearly with the centrality ($\langle N_{part} \rangle$) [71]. But for central events, V_{fo} does not show a monotonic behavior when considering it for beam energies between AGS over SPS up to RHIC. V_{fo} decreases at AGS energies and reaches a minimum between AGS and SPS, where it increases again. No evidence was observed for long-living hadronic phase.

First results from RHIC (STAR [72] and PHENIX [73]) show similar values of the radii as the SPS data. If a QGP state is established the ratio R_{out}/R_{side} should be

larger than 2 [74][5]. Such a behavior was not observed which means either one needs higher beam energies to establish the deconfined state or it was already established at SPS or the current perception of the space-time evolution of the heavy-ion collisions must be reconsidered.

2.3.3 Probes of Large Cross Section

1. **Strangeness Enhancement**
   The strangeness content is believed to be enhanced in a QGP state compared to HG state [75]. Due to new (different) production channels and lower production energy thresholds, high baryonic number and high temperature together or individually, cause a strange enhancement. At large baryon density there are many u and d quarks (fermions) abundant which occupy the collision volume if a QGP state is created. Due to the Pauli exclusion principle it becomes favorable to produce strange particles in spite of their larger mass.
   The extra mechanism of strange production due to Pauli in QGP leads a production rate 10 to 30 times higher than HG [76].

   At low temperatures the production of the strange quarks is suppressed due to their high dynamical mass (500 MeV). As strangeness is conserved in the strong interaction, a hadron with a strange anti-quark must be produced in the same reaction as a hadron with a strange quark. Which makes the production threshold for the strange pair at the level of 1 GeV. At high temperatures and due to chiral symmetry restoration the mass of the strange quark is reduced to its current value on the order of 150-350 MeV. With such, relatively, low mass the thermal strange production becomes possible, in other words, the threshold of s quakes production becomes lower by more than factor 2, leading to the same factor in the strange yield. The current mass is on the order of the expected critical temperature. Already in this temperature region, the gluon density is expected to be high in the plasma, see [77] and Refs. therein. Gluon fusion ($gg \rightarrow s\bar{s}$) as well as quark anti-quark annihilation ($q\bar{q} \rightarrow s\bar{s}$) offer more strange production channels.

   The enhancement might, however, occur in a purely hadronic state if the system lives long enough so that the hadrons can interact with each other. The abundance of strange quarks grows gradually in a chain of rescattering processes of inelastic collisions. This was observed at SPS [78] and even at AGS [79] in terms of the $\langle K^+ \rangle / \langle \pi^+ \rangle$ ratio[6]. The ratio is enhanced in AA collisions compared to pp collisions as a function of the center of mass energy per nucleon[7].

[5] The value is model dependent.

[6] The reason for using the positive charged particles rather than all states, is the suppression of K^- production at low energies /AGS) where the net baryon density is large. The K^+ mesons are produced in combination with a Λ meson: $N + N \rightarrow \Lambda + K^+ + N$.

[7] It is also found that the ratio $\frac{K^+/\pi^+(AA)}{K^+/\pi^+(pp)}$ is also dependant on $\sqrt{s_{NN}}$ [80]. It reaches values of about 9 at AGS and drops to about 2 at SPS. This behavior comes from the higher stopping power at low energies which increases the baryo-chemical potential, μ_B. and therefore the pion absorption increases. The large enhancement is caused by the reduction of pions number rather than the increase in the kaons number. In addition in pp collisions the available energy is below the required energy to produce kaons,

Since the enhancement of single strange particles like kaons is not unique to the QGP state, one looks for particles which are not likely to be produced by hadronic rescattering because of their large masses and small cross sections. The yield of particles such as $\bar{\Lambda}$ ($\bar{u}\bar{d}\bar{s}$) or multi-strange particles such as ϕ ($s\bar{s}$) and Ξ^- (dss) is expected to be enhanced, in first approximation, by a factor of about 6-9 if they are produced by a recombination of quarks from the QGP. By Ω^- which is a tri-strange state, one expects an enhancement factor between 15 and 25 [81]. Which means that the enhancement increases with the strangeness-content of the produced hadrons. Such an enhancement (order of magnitude) was observed in Pb-Pb collisions compared to pPb collisions, by the WA97 [78] and the NA57 [82] Collaborations of SPS.

The strangeness enhancement (Pb-Pb to pPb) increases with centrality so far $N_{part} \geq 100$ [78].

2. **Chiral Symmetry Restoration:**

Hadron masses could decrease compared to their values in HG, this is visible in the broadening of the resonances in the invariant mass spectrum, see Section 8.1.

The phase transition into the QGP is expected to restore the broken chiral symmetry, i.e., make the quarks behave as though they are mass-less. It is argued [83] that in the expanding hot matter, domains of the so-called *Disoriented Chiral Condensates* (DCC) could form, resulting in anomalous isospin fluctuations. The DCC would decay into neutral and charged pions, favoring a charged-to-neutral ratio different from the value expected from isospin symmetry [84].

The reduction of the quark mass could leave three signatures which probe the restoration of chiral symmetry: Firstly: Quarks with higher dynamical masses, as the strange quarks, can be produced in higher rates than in hadronic states when the temperature becomes comparable with a quark–anti-quark pair, see **Strangeness Enhancement**.
Secondly: Hadrons masses with strange content could decrease compared to their values in HG. The ϕ meson, for instance, decays via the di-kaon chanel or the di-electron chanel. If its mass shifts down due to symmetry restoration, it will quickly loose (at least partially) the option to decay into kaons due to their high mass. Studying both decay channels will verify whether the chiral symmetry is restored in a collision or not. Thirdly: The width of resonances such as the ρ meson is broadened.
Experimental results will be discussed in Section 8.1 in terms of di-leptonic signatures.

which is not the case in AA collisions (secondary collisions). These arguments tells that the factor 2 of SPS gives a reliable reference for the strange enhancement.

2.3.4 Probes of Small Cross Section

1. **Photon Production**:

   Photons are a useful tool to probe the thermodynamics of the fireball, as they interact only electromagnetically [85]. They have a mean free path much larger than the size of the reaction volume and, unlike hadrons, they do not undergo strong final state interactions. Photons survive therefore the hadronization phase and live long enough to reach the detectors and can be observed.
   However, photons are produced by different interactions in different stages throughout the fireball evolution. (i) *Prompt photons* are produced in the initial stage by hard parton scattering, (ii) *direct photons* are produced in a QGP state, and (iii) photons are also produced in the final hadronic stage. The first and the third sources produce background photons from which the direct photons are to be distinguished to signal the existence of the QGP state.

   Direct photons can be produced either by a quark–anti-quark annihilation ($q + \bar{q} \rightarrow \gamma g$) or from the QCD Compton process ($g + q(\bar{q}) \rightarrow \gamma + q(\bar{q})$) [86]. Since the gluon density is expected to be high in a QGP state the direct photons are expected to be enhanced via the gluonic channel. Once produced, direct photons carry information about the thermodynamics of the system. Their transverse momentum distributions are determined by those of the quarks, anti-quarks, and gluons in the plasma [10]. Since the temperature of the QGP state is high, the momentum distributions of direct photons are expected to show an enhancement at higher transverse momentum.

   The background signatures are a serious problem in detecting and identifying the direct photons. Prompt photons are produced through the same processes as direct photons. Their transverse momentum distributions will be determined by those of the colliding partons which are approximately in the same order as the direct photons ($p_t \gg 1$ GeV/c) [87] and therefore are difficult to be distinguish from the direct photons.
   Photons coming from the HG are produced via hadronic mechanisms such as: pion annihilation ($\pi^+\pi^- \rightarrow \rho^0\ \gamma$), Compton ($\pi^\pm\rho^0 \rightarrow \pi^\pm\gamma$), and the ρ decay ($\rho \rightarrow \pi^+\pi_-\gamma$). The momentum distributions of these photons are determined by those of the hadrons. Since the temperature of the hadrons is lower as that of the QGP, the momentum distributions of their photon production will be lower than those produced in the QGP, which enables to separate both and to signal the QGP [85].

   Experimental evidence for direct photons was reported by the WA98 Collaboration [88] in Pb-Pb collisions at $\sqrt{s} = 158$ AGeV/c. The collaboration measured the transverse momentum spectra of photons in central and peripheral collisions. Compared to calculations of annihilation (prompt) and decay (HG) background photons. The central photons show an enhancement of about 20% at high transverse momenta. Which again shows that at least a mixed phase of QGP and HG was established at SPS.

   Some efforts suggested that it is not necessary to reach a QGP state to reproduce the WA98 data [89, 90]. The references show that the WA98 results can be reproduced either by assuming a HG state or a QGP state. Anyway, a HG state which

reproduces the data requires an initial state temperature of about 230 MeV which is, according to LQCD prediction, much higher than the critical temperature of about 170 MeV for a phase transition. If one buys into the LQCD calculations, the HG of the cited models is in conflict with LQCD and thus does not describe a physical situation.

For an extended study on direct photons see [91].

2. **Di-leptons and Color Screening:**

   As photons, di-leptons are not subject to strong interactions and therefore probe the earliest and hottest phase of the evolution of the QGP without being affected by final state interactions. They give access to signatures like strangeness enhancement and chiral symmetry restoration as well as Quarkonia suppression. Di-leptons and Quarkonia probes will be subject of studies in Chapter 8 in connection with the fast simulations of the Quarkonia signals in the ALICE central barrel.

3. **Jet Quenching:**

   Jets are high-p_t partons, which can be produced in a collision at high beam energies (collider). Their propagation within the plasma offers a QGP probe which is sensitive to correlations in the plasma and retains its information during the intense hadronic scattering in the exit phase of the reaction.

   As leptons, jets are relatively insensitive to scattering in the exit hadronic phase. therefore in addition to probing the properties of the plasma, they leave the collision zone before the plasma hadronizes and are causally disconnected from the hadronic stage and hence retain any information they have on the QGP. Outside the collision zone the jets fragment into hadrons, and any energy-loss in the plasma will soften the hadronic spectrum, i.e. reduce the measured yield of hadrons at high-p_t, *jet quenching* [92, 93].

   The theory of parton propagation in the dense medium shows that energy loss is proportional to the initial gluon density in the system [94, 55]. Since the gluon density is expected to be higher in a QGP state, jet quenching will probe the first stages of the collision. It can be studied (and measured) by means of the *nuclear modification factor* $R_{AA}(p_t)$ which describes the ratio of particle yields in nucleus-nucleus collisions, n^{AA}, to particle yields in proton-proton collisions at an impact parameter b. R_{AA} measures the deviation of momentum distributions in an AA collision from the momentum distributions in a superposition of pp collision. It is scaled by the *Glauber nuclear overlap function*, $T_{AA}(b) = \langle N_{bin}(b)\rangle/\sigma^{pp}_{inel}$:

$$R_{AA}(p_t) = \frac{d^2n^{AA}/dp_t d\eta}{T_{AA}d^2\sigma^{pp}/dp_t d\eta},$$

   where η is the pseudo-rapidity, $N_{bin}(b)$ the binary collisions between nucleons, and σ^{pp} is the total production cross section in pp collisions. At low p_t the ratio scales with N_{part}, $R_{AA}(0) \simeq 0.5N_{part}/N_{bin}$.

If no nuclear effects occur at high p_t, $R_{AA}(p_t)$ should be equal to unity and at low p_t it does not scale with N_{bin}. First results from RHIC at $\sqrt{s} = 130$ GeV/c show the expected jet quenching effect of high-p_t particles. The STAR [95] data for negative hadrons show an increasing $R_{AA}(p_t)$ up to $p_t \simeq 2.5$ GeV/c where it drops again and reaches a value of $R_{AA}(p_t \simeq 5) \simeq 0.35$. The PHENIX results [96] include, in addition to the negative hadron results, also results from neutral pions. $R_{AA}(p_t)$ is found to flatteren at a value of $R_{AA}(p_t > 2) \simeq 0.5$ and $R_{AA}(p_t > 2) \simeq 0.3$ for charged hadrons and neutral pions, respectively.

For long time, jet quenching due to energy loss in the dense matter was believed to be absent in the SPS AA data. The ratio $R_{AA}(p_t)$ was found to overshoot unity and to saturate at high-p_t like in pA collisions [92, 93, 97] which is explained by the *Cronin effect* [98], where high-p_t particle production in pA collisions is enhanced beyond binary scaling.
Recently, the pion production at transverse momenta larger than 2 GeV/c in AA collisions at SPS energies ($\sqrt{s_{NN}} \simeq 20$ GeV), were re-evaluated and compared to all existing pp data in the same *cms* energy regime [99]. It was found that for central events (up to 8% centrality), the SPS data do not show strong enhancement of $R_{AA}(p_t)$, but rather a consistency with N_{bin} scaling. The reason for the early statements on the data is the lacking in $p + p \rightarrow \pi^0 + X$ reference data at high-p_t and mid-rapidity in the same energy regime.
One had to rely on pQCD calculations which add non-perturbative effects to bring the parton model analysis into agreement with available data. The non-perturbative effects cannot, however, be introduced in a model independent way such that different models lead to different yields in the final pion spectra. In the earlier analysis two models were taken into account [100, 97] which use different power laws. They were tuned to reproduce the available data at a *cms* energy of about 20 GeV. The results were disaccorded. The study in [99] compared the available SPS AA data systematically to all available pp data in the same energy range.
Furthermore the study found, that the yield in neutral pions around $p_t \simeq 3$ GeV/c and mid-rapidity is found to be suppressed by a factor of 1.6 in the first 1% of central events. This shows that final state energy loss of hard scattering partons in the dense medium took place already at SPS energies. The suppression is not observed for peripheral collisions.

In the same manner one defines $R_{CP}(p_t)$ which represents the yield of central collisions to the yield of peripheral ones. The advantage of this ratio is its independency of a pp reference measurement. Measurements show a suppression of high p_t particle yields in central events compared to peripheral ones

As mentioned earlier the saturation of the elliptic flow coefficient v_2 with p_t could be interpreted by jet quenching. High energy partons loose energy as they pass through the matter created in the collisions. Since the sources are asymmetric, the amount of energy loss depends on the direction which the particles travel. In this way the energy loss can lead to momentum-space anisotropy which reflects the initial spatial anisotropy of the source.

Event-by-Event Fluctuations:
In addition to the discussed QGP indicators there is still the possibility of employing the largely abundant particles in a collision. The statistics is event-dependant which offers fluctuations studies through the so-called event-by-event analysis.
The idea of event-by-event analysis is to compare the electric charge distribution in a QGP to that of ordinary hadronic matter. Carrying only a fraction of the electric charge unit, the quarks distribute the electric charge in a QGP more consistent than it is spread in ordinary matter. It is expected that this evenness survives the phase transition and leaves signatures in the spectra of the produced final state particles [101, 102].
For a review on event-by-event fluctuations see [103].

2.4 Large Hadron Collider

In 2007 the Large Hadron Collider will start up, an unprecedented acceleration machine, not only in the energy available but also in *luminosity* and complexity of the operating experiments. Four experiments will start taking data: ATLAS [104] and CMS [105]; two general-purpose *pp* experiments, LHCb [106]; a *pp* experiment dedicated for CP-violation and *b*-quark physics and ALICE the dedicated heavy-ion experiment [4, 5]. Recently CMS integrated also a heavy-ion part in its program [8].

2.4.1 LHC Event Features

Table 2.1 [3] contains the parameters of SPS, RHIC and LHC. In *pp* collisions the charged particle multiplicity $\mathrm{d}N_{ch}/\mathrm{d}y$ grows only slowly from SPS energies up to LHC ones, 1 : 1.33 : 2.77, and so does the average transverse momentum, 1 : 1.09 : 1.47.

In AA collisions, with the nuclear radius $R_A \sim A^{1/3}$ fm, there is a new qualitative aspect which makes it difficult to treat heavy-ion collisions within a unified theory [108]. During an AA collision, many different time and energy scales are involved in the creation and evolution processes of the system.

The charged particle multiplicity depends on the nuclear radius, i.e. nuclear number, and the available energy. Going from SPS over RHIC to LHC energies its values cover a higher range in AA collisions than in *pp* ones and scales as (1 : 2.5 : 7.5 - 20). At low *cms* energies (SPS) the charged particle multiplicity scales with A and at high *cms* energies (LHC) it grows with $A^{4/3}$. Due to *gluon shadowing* factors, final state *parton saturation*, and jet-quenching, calculations [3] lead to a smear in the multiplicity values expected for LHC. Most calculations used a power law when calculating the multiplicity as a function of the *cms* energy leading to multiplicities in the order of 8000. But since RHIC started up it became evident that this is not true. Figure 2.4 [107] shows data on dN_{ch}/dy at mid-rapidity for central collisions in the energy interval between AGS and RHIC energies. The solid line shows the prediction of the saturation model [109] which gives for LHC a value of about 2300. The dashed line represents a power law ($\sqrt{s}^{0.3}$) parameterization [107] which predicts a multiplicity of about 2000 for LHC.

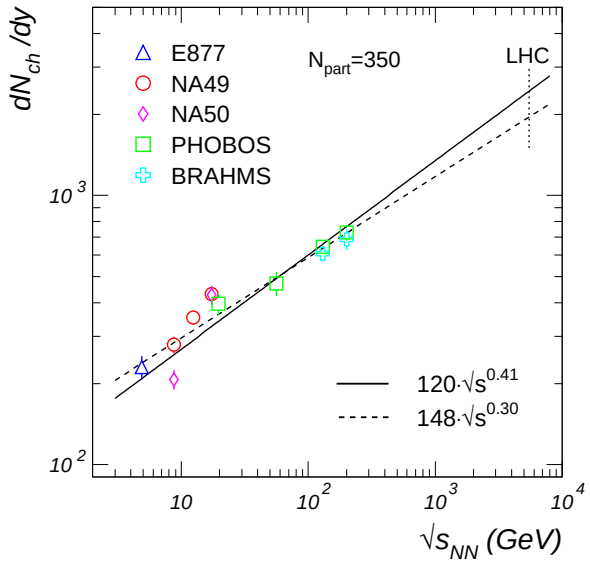

Figure 2.4: Charged particle multiplicity as a function of beam energy at mid rapidity for central collisions. The data points cover the beam energy range from AGS up to RHIC. Contrary to earlier expectations which overestimate the multiplicity for LHC energies, the nowadays extrapolations predict values between 2000 and 3000. The figure is taken from [107].

Throughout the discussion of the QGP signatures it became evident that the phase transition point was reached at SPS [110]. The RHIC data offer an extensive study of a system at, and beyond, the phase transition, but it is unique to LHC to investigate physics within the high temperature QCD phase.
With the LHC initial conditions given in table 2.1 the density of interacting particles increases leading to a rapid thermalization of hard probes (large p_t), i.e. a decrease of the formation time. This increases the energy density ϵ up to 20 times larger than at RHIC leading to an inertial temperature $T_0 = T_{eq}$ at LHC larger by factor two. This implies a longer QGP life time $\tau_{\mathrm{QGP}} = \tau_c - \tau_{eq}$, compare Figure 2.3, longer freeze-out time τ_{fo} and larger freeze-out Volume $\mathrm{V_{fo}}$ of the system, approaching the region where QCD is theoretically accessible.

2.4.2 New Physics at LHC

- **Hard Processes:**
  Studying the QGP state is achieved best via the hard probes like high-p_t jets, high-p_t photons, heavy Quarkonia, and $W^{\pm}$- and Z^0 mesons. The squared momentum transfer, Q^2, necessary for their production denotes the "hardness" character of these probes. At LHC, Q^2 is larger than 2500 GeV^2 [3] implying a large production cross section which enables detailed studies of these probes. The production time of hard probes is inversely proportional to the squared momentum transfer. With the Q^2 values of LHC, the production times are smaller than 0.01 fm/c. This is early enough to probe the classical chromo-dynamic stage of the fireball where the so called *gluon walls* decay, see below. Secondary particles materialize at a time of 0.2 fm/c during which and in their way out of the collisions environment the hard

	SPS	**RHIC**	**LHC**
		pp	
dN_{ch}/dy	1.8	2.4	5
p_t GeV	0.36	0.39	0.53
partons in p	4	10	30
		Pb-Pb	
$\sqrt{s}/A$ GeV	17	200	5500
dN/dy	$\propto N_{part}$	$\propto A \cdot N_{part} + B \cdot N_{bin}$ [111]	$\propto N_{bin}$
dN_{ch}/dy	400	1000	2-3$\times 10^3$
τ_0 fm/c	1	0.2	0.1
ϵ GeV/fm^3	3	35	500
τ_{QGP} fm/c	$\leq$2	2-4	$\geq$10
τ_{fo} fm/c	10	20-30	30-40
V_{fo} fm^3	few 10^3	few 10^4	few 10^5
shadowing	1	0.8	0.5

Table 2.1: Extrapolation of particle production from pp to AA and global features estimations [3].

probes explore the properties of the secondary matter through their scattering off it. The time available for the matter probing is given by the time needed of the probes to travel through the QGP, it can extent up to the QGP life time.

- **Gluon Walls and Low-x Physics:**
  The high density of the produced particles in heavy-ion collisions originate from collisions between the so called *gluon walls*. These are the densely packed two colliding nuclei approaching each other with velocities close to the velocity of light. The phase space density of low-momentum gluons saturates and the system become sensible to *gluon merging*. In Pb-Pb collisions the gluon saturation sets in at a momentum of around 2 GeV/c^2 where perturbative QCD (pQCD) is applicable. This enables the calculation of the particle production, the bulk of the transverse energy and the initial conditions for the following expansion of the hot matter within the pQCD formalism.

  Gluon saturation becomes visible through its effect on the production of secondary partons with p_t below 2 GeV. In the fireball many probes can be used to explore the consequences of gluon saturation and recombination on the nuclear structure functions. These are the distributions of the quarks, anti-quarks and gluons in the wave functions of the colliding nuclei in the *pre collision* environment. The effects of the wave functions on the density of the *post collision* environment and its evolution can also be studied.

  Pre-collision: The production of (*i*) direct photons, (*ii*) the $W^{\pm}$- and Z^0 mesons, and (*iii*) open charm and open beauty is suitable for studying the pre-collision environment with the wave functions of the nuclei. The first are sensitive for quarks and gluon distribution functions, the second for quark and anti-quark distribution

functions and the yield of the third is sensitive for the gluon distribution functions. Whilst the production of the $W^{\pm}$- and Z^0 mesons at RHIC are only in pp collisions measurable, at LHC this production is also accessible in AA collisions. These collisions allow to study the modification of the parton distribution in the nucleon by the nuclear matter, called *shadowing effect* in terms of its spatial dependence in the tranverse plane to the collision axis. This follows by studying the production of the mentioned hard probes as a function of the impact parameter.

Post-collision: Probes which are subject of strong final state interactions are suitable for the post collision environment. These probes are (*i*) the hadronic decay of $W^{\pm}$- and Z^0 mesons, (*ii*) high-p_t quark and gluon jets, and (*iii*) heavy Quarkonia. These probes hadronize very early after the collision and therefore they travel through dense soft secondary particles. The hard probes which will be produced abundantly at LHC, will carry the signatures of the soft matter and its evolution.

- Z^0 **and jets**:
  In general, quark jets of known energy are produced in processes such as $g+q \rightarrow q+\gamma$ and $g+q \rightarrow q+Z^0$. At LHC energies the Z^0 signal is particularly favorable because it is free from background contributions from hadronic decays to the direct photon spectrum. The Z^0 and the photon momenta can be measured and consequently the quark jet energy. The measured energy is a degree of the cross section between the partons in the medium and the hard probes, in other words for the transparency of the medium which represents an access to the parton density in it and the way how it is affected by the gluon saturation. The ratio of mono-jet to di-jet final states allows to study the energy loss as a function of the jet transverse momentum.

- **heavy Quarkonia**:
  Charmonium and Bottonium are screened in the partonic matter. This could lead to a suppression in the yield of J/ψ and Υ mesons [6]. According to their different radii these mesons are suppressed differently at different medium temperatures. This makes them a suitable indicator for the system temperature. Information on the Quarkonia resonances enable a scan of the medium and the suppression dependence on their tranverse momentum. However, many observations of the available data [36, 37, 112, 113] make this scenario questionable at high energies such as those of RHIC and LHC, so that the term "Quarkonia (J/ψ) suppression" implies a specific controversial interpretation of J/ψ data. The contradicting predictions make the study of all Quarkonia state of special interest. At RHIC energies only J/ψ is accessible with enough statistics but only at LHC the Υ resonances group can be studied with high statistics and in sufficient details. The di-electron channel of Quarkonia decay will be recorded in the ALICE central barrel. The efficiency and the significance with which these signals are recorded will be the subject in Part III of this thesis.

2.5 The ALICE Experiment

The LHC heavy ion physics program discussed above will be mainly studied by ALICE, a multi purpose experiment which was designed to deal with the challenges tied to the program. In general, the properties of strongly interacting matter and those of the QGP will be addressed. This is the first time where all the currently considered QGP signatures can be measured in a single experiment. Figure 1 shows the ALICE experiment with its sub-detectors.

For the duration of three years a run with Pb ions is planed [114]. An ALICE year extends about 10^6 s. The *cms* energy will be 5.5 TeV per nucleon pair. The ALICE running scenario was established and discussed at the LHC Performance Workshops in March 2003 [115]. During the first year ALICE will take *pp* data which will serve as reference data for later Pb-Pb collisions. Although at low luminosity, an early Pb-Pb program is also planed in the first year to established the overall properties of the collisions. During the second year both programs will continue but with higher luminosity in the Pb-Pb collisions program ($\mathcal{L} = 1{\cdot}10^{27}$ cm^{-2}s^{-1}). In the third year a pPb or alternatively deuteron- or alpha-lead program will be carried out to study nuclear modification of the parton distribution function. In the fourth year the rare observables will be studied. Lighter ion systems like Argon [116] will be used to study the dependence of the (rare) observables on energy density in the fifth year. The program of the following years will depend on the results achieved up to that point in time.

With the LHC maximal luminosity in Pb-Pb collisions, $\mathcal{L} = 1{\cdot}10^{27}$ cm^{-2}s^{-1}, the maximum event rate will be around 7800 events per second of which only 5 to 10% could be classified to be central. ALICE is designed to be able to deal with this multiplicity and to record the rare central events. The program after this period will be determined by the results achieved from the data during the first years of running.

ALICE has been designed to measure most of the particles which emerge from a heavy-ion collision. The experiment consists of three main parts: the central barrel which covers the central rapidity range of $|\eta| < 0.9$, where hadrons, electrons and photons will be detected providing excellent *tracking* and *Particle Identification* (PID). Charged hadrons which live long enough are identified through energy loss and time-of-flight measurements. Short living hadrons can be identified by their decay products. Electrons are identified through the transition radiation and photons through electromagnetic calorimetry. The particle momenta are obtained by tracking procedures within the L3 magnet with solenoidal field (0.3 - 0.5 T). The central barrel detectors are designed to record particles with transverse momenta extending from 100 MeV/c up to 100 GeV/c. This makes ALICE a powerful detector covering soft and hard physics processes in a heavy-ion collision.
The second part is the forward detector which covers a rapidity range of $2.5 < \eta < 4$, where muons will be registered.
The third part is responsible for the low *trigger* level and precise event time measurements.

For the overall description of the ALICE experiment cylindrical coordinates are used. The origin is located at the interaction point in the center of the detector. The beam direction characterizes the z-axis with the negative direction pointing towards the muon arm[8]. The angles ϕ and θ cover the azimuthal and the polar directions respectively. The

[8]In some references and ALICE document the muon arm direction is characterized by the positive

magnetic field runs parallel to the beam direction making the angle ϕ the deflection angle of charged particle under the Lorentz force.
Since the TRD chambers are flat objects, it is more convenient for tracking and resolutions discussion to use Cartesian coordinates. The y-axis run perpendicular to the earth surface with the positive direction upwards. The x-axis runs parallel to the surface of the earth with the positive direction pointing towards the center of the LHC ring. Throughout the thesis both coordinate systems will be used depending on the subject of discussion. The definition of the axis is indicated in Figure 1.
The ALICE central barrel covers a polar angle between $45° < \theta < 135°$, corresponding to a pseudo-rapidity range of $\mid \eta \mid < 0.9$, over the whole azimuth.
With this construction ALICE will be able to detect the most primary and secondary leptons, photons and hadrons produced in a collision enabling the mentioned measurements of the QGP signatures.

2.5.1 ALICE Sub-detectors

The requirements of QGP measurements and the LHC environment put certain constraints on ALICE and its sub-detectors and played the decisive role in their design. In the following these sub-detectors will be briefly presented. For more details see [5, 4] and the individual technical design report of each detector.

2.5.1.1 Inner Tracking System (ITS)

The ITS consists of six barrels of high resolution detectors. Starting from the innermost the first tow barrels, at radii of 4 and 7 cm are silicon pixel detectors, the following two, at radii of 15 and 24 cm are silicon drift detectors. In the high particle density these detectors enable a good impact parameter resolution (below 100 μm). The outermost two layers, at radii of 39 and 44 cm, are equipped with double-sided silicon micro-strip detectors. The ITS covers the nominal pseudo-rapidity region of the ALICE central barrel of $\mid \eta \mid < 0.9$ and an interaction diamond length of 10.6 cm along the beam direction.

The segmentation is optimized for efficient tracking. The outer radius is determined by requirement of matching tracks in the ITS with the TPC (see below). The inner radius is determined by the beam pipe (3 cm).

In addition to tracking, the ITS will reconstruct secondary vertices of the charmonic and hyperonic decays, and improve the momentum resolution of high-p_t particles. The detector will also improve the measurements of energy density per unit rapidity ($\mathrm{d}\epsilon/\mathrm{d}y$) as well as those of HBT correlation functions.

The ITS has a standalone capability as a low p_t particle spectrometer. Independent from each other, its layers will identify particles in the non-relativistic region via $\mathrm{d}E/\mathrm{d}x$.

z-axis. The coordinates given here are those adopted and used since May 2003.

2.5.1.2 Time Projection Chamber (TPC)

The TPC is the main ALICE tracking system which guarantees a reliable performance in a multiplicity environment up to 8000 charged particles per rapidity unit. It will also provide momentum measurements and particle identification via $\mathrm{d}E/\mathrm{d}x$ up to a transverse momentum of about 2 GeV/c, see Section 9.5. The TPC starts at a radius of 90 cm and extends up to a radius of 250 cm. The maximum acceptable hit density (0.1 cm^{-3}) determined the inner radius, the outer one is determined by the length required for $\mathrm{d}E/\mathrm{d}x$ resolution of $< 7\%$. This resolution allows the TPC to identify electrons of momenta up to 2.5 GeV/c. The design, read out and the gas parameters are optimized for a good double-track resolution: The gas mixture of Ne/CO_2 (90/10) is chosen to reduce the space charge and to minimize the electron diffusion. The read out consists of 72 pad-read out planes with a total of 570,000 channels. Each channel is read out with a preamplifier-shaper, a 10-bit ADC and a digital circuit for tail cancellation, data compression, multi event buffering and baseline restoration.

2.5.1.3 Transition Radiation Detector (TRD)

In the ALICE central barrel the TRD will identify electrons with momenta above 1 GeV/c and serve as a trigger for electrons with momenta above 3 GeV/c. In the next section the TRD is briefly introduced. The read out chamber of the detector and its performance are subject of studies in part I of this thesis.

The three detectors, ITS, TPC, and TRD establish the main tracking unit in the central barrel. Their combined efficiency and momentum resolution will be studied in Chapter 9. In Chapter 10 the physics of the three detectors will be discussed in terms of Quarkonia signals. The role of the TRD in this sector will be highlighted.

2.5.1.4 Time Of Flight (TOF)

The TOF sub-detector will identify pions, kaons and protons up to 2.5 GeV/c. To achieve this task the TOF must have an overall time resolution on the order of 100 ps. This challenging duty is overbeared through optimizing a simple but efficient device with excellent timing properties consisting of *Multi-gap Resistive Plate Chambers* (MRPC). These chambers consist of a double stack of resistive plates separated from one the other via a series of gas gaps, (2×5), of equal thickness of 250 μm. This small thickness is determined through the required time resolution. The uniformity of the gaps is guaranteed through the so-called *fishing wires*.
Electrodes are connected to the outer services of the stack. The intermediate plates are kept floating. Electrostatics in the system gives them their initial voltage then the flow of electrons and ions of avalanches perpetuates it. They are transparent for avalanche signals. The induced signal on the outer plates is the analog sum of signals in all gas gaps. This signal is read out with a single set of read out strips.
TOF reaches time resolution between 50 and 60 ps and an efficiency of 99% (better than anticipated), thus promising a good hadron identification.

2.5.1.5 High Momentum Particle Identification Detector (HMPID)

ALICE is also equipped with a *Ring Imaging Cherenkov Counter* (RICH) for particle identification in high-p_t regions. It is located at a radius of about 4.5 m from the beam axis. The HMPID consists of seven modules with an area of 1.5×1.5 m^2 each and a total number of read out channels of more than 160,000.
The used radiator is liquid C_6F_{14} (perfluorohexane) and the read out chamber is a multi-wire proportional chamber with pad read out. The pad plane is evaporated with a thin layer of CsI (Cesium iodide) as a photo cathode. In π/K (K/p) identification the RICH detector extends the 3 σ limit to 3 GeV/c (5 GeV/c).

2.5.1.6 Photon Spectrometer (PHOS)

Prompt and direct photons as well as those from high-p_t neutral meson decays are reconstructed and measured in PHOS, a high resolution electromagnetic calorimeter with a total area of 8 m^2 and 17,000 read out channels. It is located at a radius of about 4.6 m beneath the interaction point.
In the large particle density environment the accuracy of the photon spectra will be determined by the systematic errors on photon reconstruction efficiency of about 4% and the background. Low channel occupancy guarantees an acceptable systematic error which is achieved through filtering low momentum photons, thus the used crystal must posses a small *Moliére radius*, i.e must be dense enough, but it must also have a high light output. PHOS consists of dense scintillating $PbWO_4$ crystals which achieve the requirements. The acceptance is defined such that the statistical errors are kept below the systematic ones. Triggering on high-p_t photons is achieved through energy and time information provided through the read out electronics.

2.5.1.7 Forward Muon Spectrometer (FMS)

The FMS is designed to cover the complete spectrum of Quarkonia resonances and to allow their study via their di-muon decays. The detector covers a polar angle of $2° < \theta < 9°$, corresponding to $2.5 < \eta < 4$.
The FMS consists of a front absorber, small-angle absorber, dipole magnet, tracking chambers and muon filter. The 3.5 m long front absorber consists of carbon absorber covering the rapidity range of the FMS. A 10 mm tungsten layer covers the front end facing the ITS and the TPC. This reduces multiple scattering and particle leakage. An other 100 mm thick tungsten cover is located at 2 degrees in order to shield the detector from the beam pipe and the particles emitted at angles within this cone. The small-angle absorber shields the tracking chambers from the large flux of particle emitted from the beam pipe.
About 9.75 meters separate the center of the spectrometer magnet from the interaction point. This is a large dipole magnet with a 3 Tm field integral. The muon filter is a $5 \times 5 \times 2$ m^3 iron absorber located just behind the dipole magnet.

Ten chambers detect the muons, these are thin MWPC grouped in five sectors, two before, one inside and two after the dipole magnet.

The signals of $J/\psi, \psi', \Upsilon, \Upsilon'$, and Υ'', appear on a combinatorial continuum of Drell-Yan processes and **D** and **B** meson decays which require good efficiency and mass resolution. The FMS di-muons efficiency is 90%, the invariant mass resolution is 100 (70) MeV/c^2 for the Υ (J/ψ) family. The Quarkonia measurements in the FMS and in the central barrel complement each other such that a wide rapidity range is covered.
The FMS is read out with a *Dual-Threshold Front-end Chip* which was especially designed for the detector. It provides an excellent time resolution of below one nanosecond.

2.5.1.8 Forward Detectors

In addition to the central barrel detectors and the forward muon arm ALICE comes with other smaller forward detectors which determine the general properties of the event and serve as a *Level-0* trigger:

- Zero Degree Calorimeter (ZDC): located inside the LHC tunnel on both sides of the ALICE experiment, two calorimeters on each side. ZDC measured the impact parameter, i.e. the centrality of the collision.
- Forward Multiplicity Detector (FMD): measures the charged particle production.
- Photo Multiplicity Detector (PMD): measures non statistical fluctuations in the photon-to-charged-particles ratio. It determines the interaction plane and measures the flow and transverse energy of neutral particles.
- T0: measures the event time very precisely.

2.5.1.9 Performance of the ALICE Tracking System

Tracking in ALICE is provided through ITS, TPC and TRD. As first step and before starting with full tracking, primary vertices are found through combined information from the first two ITS layers. For a Pb-Pb event a precision of 5 μm and 15 μm is achieved in z and transverse plane respectively. The ITS is able to provide tracking and PID for low-p_t particles like hyperons.

Matching tracks from ITS, TPC and TRD delivers an excellent capability of disentangling close tracks and a momentum resolution better than 1.5% for momenta between 0.2 and 2 GeV/c. For momenta around 100 GeV/c the resolution is below 12%. The angular resolution is about 0.5 mrad.
The impact parameter resolution is about 60 μm at a transverse momentum of 1 GeV/c and increases at higher p_t values. With such resolutions the identification of short living mesons like **B** and **D** mesons is efficient. These tracking capabilities enable also good precision measurements of HBT radii for a source with a radius smaller than 10 fm.
The tracking procedure in the central barrel will be discussed in Section 9.2.

2.5.1.10 Particle Identification in ALICE

One of the most important design features of ALICE is its capability to identify many particles over a large part of the phase space in each Pb-Pb event. ALICE distinctive and robust PID system comes from using different (almost all known) identification techniques. The PID of each sub-detector and the momentum range in which it is valid are shown in Figure 2.5.

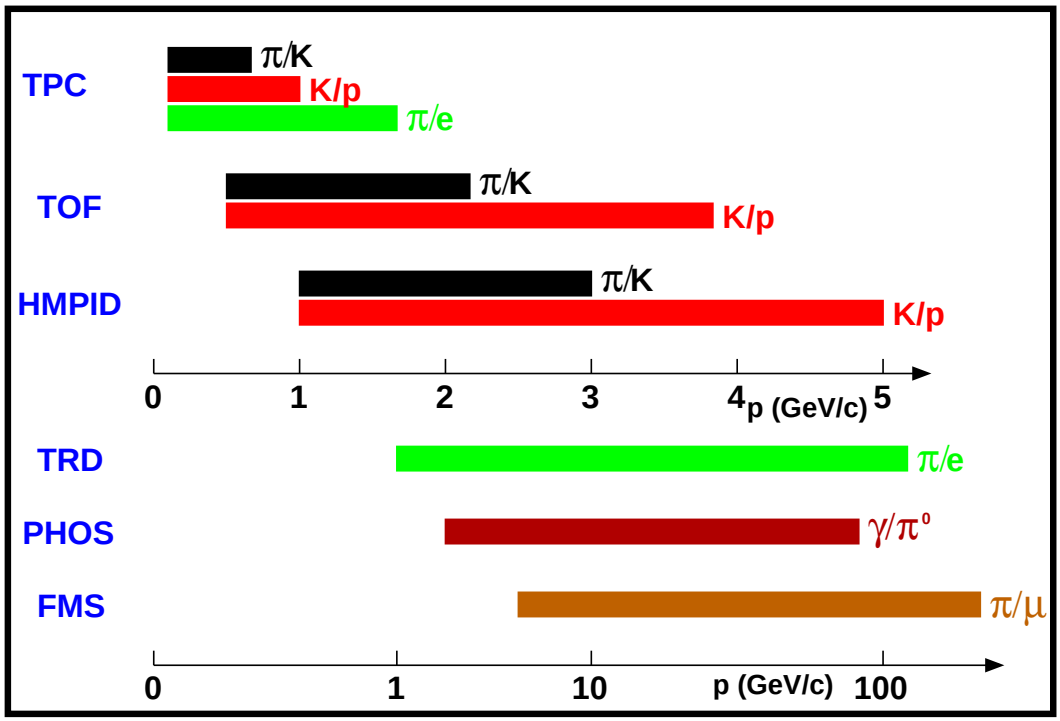

Figure 2.5: Particle identification capabilities of the ALICE central detectors.

In conjuction with ALICE good tracking system these PID techniques enable the measurements of hyperons and vector meson decays. The potency of the combined techniques of vertexing, tracking and PID enable the measurement of rare charmed meson. The **D** meson decay into $K\pi$, for instance, is measurable with a significance of about 37. This enables a direct study of the p_t dependence of charmed mesons production down to 1 GeV/c. The TRD pion-electron separation capability will be studied in Chapter 7 and the combined pion rejection capability of TPC and TRD will be discussed in Chapter 9.

Chapter 3

Ionization Energy Loss and Transition Radiation

Radiation is the only access to processes which occur on scales which are either too short, too tiny, or too far away to be observed directly. Radiation detectors, which are nowadays applied in many branches of science, were originally developed for particle, nuclear, and atomic physics. Their ongoing development, continual improvement, and performance-enhancing are along with the interplay of theory and experiment, one of the guarantees for progresses in science.
Radiation detectors take on many forms and sizes and thus they suit a wide range of applications. They consist of materials in individual aggregate states - solid, liquid, or gaseous - or in a combination of two or all three states. The main substances of the ALICE Transition Radiation Detector (TRD) are in solid (radiator) and gaseous (drift chamber) aggregate states.

In this chapter the physical processes are discussed on which the detection properties of an ALICE TRD gas chamber are based; the *energy deposit* $\mathrm{d}E/\mathrm{d}x$, Section 3.1 and *Transition Radiation* (TR), Section 3.2. In Section 3.3 the basic features of drift chambers are reviewed, which will play an important role by the construction of a TRD gas chambers.

3.1 Ionization Energy Loss

When a charged particle propagates through matter it loses energy through elastic and inelastic collisions with the electrons and nuclei of the medium's atoms. The processes through which the particle loses energy depend on its rest mass and its energy. Using this information one can trace the particle by following the impact of its interaction with the medium. Ionization processes which deliver electrons from atoms leading to *ion-electron pairs* play an important role. To free an electron, the energy of the propagating particle must be larger than the *ionization energy* of the material. An accurate and exact quantum-mechanical calculation which describes the energy deposit per unit length is given by the *Bethe-Bloch formula* [117]:

$$\frac{\mathrm{d}E}{\mathrm{d}x} = 4\pi N_{\mathrm{A}} r_e^2 m_e c^2 z^2 \frac{Z}{A}\frac{1}{\beta^2}\left[\ln\left(\frac{2m_e c^2\gamma^2\beta^2}{I}\right) - \beta^2 - \frac{\delta}{2}\right], \tag{3.1}$$

where N_A is the Avagadro constant, m_e and r_e are the electron mass and radius, Z and A are the atomic number and mass of the medium, z is the charge of the propagating particle in units of the elementary charge e, γ is the Lorentz factor and β is the particle velocity in units of the light velocity c.

The material characteristic constant I is the mean excitation energy of the absorber atoms. It depends on their molecular state. I is found to increase with the atomic number of a chemical element Z and can be estimated to $I \approx AZ$ [118]. For xenon (argon) it has a value of 482 (188) eV.

The charge density of the material atoms weaken the transversal electric field of the propagating relativistic particle leading to the so called *density effect* which stops the *relativistic rise*, discussed below. The parameter δ accounts for the density effect. It depends on β and the absorber material and its aggregation state.

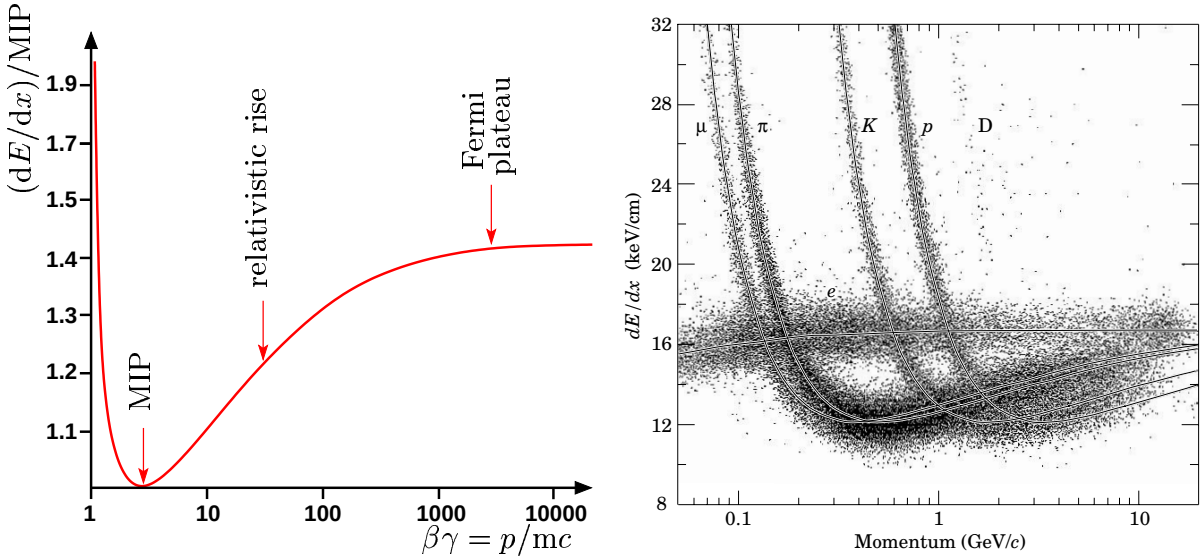

Figure 3.1: Left panel: Illustrative curve of energy deposit, see text. Right panel: $\mathrm{d}E/\mathrm{d}x$ measurements in multi-hadron events. With energy deposit, it is possible to separate electrons from pions at low momenta. Apart from the cross-over region pions and kaons can always be separated. The figure is taken from [119].

The left panel of Figure 3.1 illustrates the dependence of the $\mathrm{d}E/\mathrm{d}x$ on the Lorentz factor γ. With increasing particle velocity the interaction time between the particle and the medium decreases, leading to a decrease of the energy deposit. The curve falls with $1/\beta^2$ to a Lorenz factor of about $\beta\gamma \simeq 4$. A particle with a $\mathrm{d}E/\mathrm{d}x$ at this value is called a *Minimum Ionizing Particle* (MIP). The energy deposit of MIPs in light materials ($Z/A = 0.5$) can be approximated to be around 1-2 MeV·cm/g. For xenon (argon) this value is 1.24 (1.51) MeV·cm/g.

For $\beta\gamma > 4$ the curve shows a logarithmic rise which comes from the logarithmic term in Equation 3.1 which increases for large $\beta\gamma$. Its strength is given by the ionization potential I. Physically the rise is mainly generated from *δ-electrons*: with increasing $\beta\gamma$ the maximal energy that can be transfered from a crossing particle to an atom increases and so does the average energy deposit. A pion of 10 GeV, for example, can transfer 3.3 GeV to

an electron at rest [118]. Liberated electrons are the δ-electrons. They gain high energy from the primary particle and become able to ionize atoms.
Finally, the density factor δ, stops the relativistic increment in $\mathrm{d}E/\mathrm{d}x$ leading to the *Fermi plateau*. For low β values the density factor is negligible, whereas when β approaches unity the density factor approaches $\ln(\hbar\omega_\mathrm{p}\gamma/I)^2 - 1$, with, ω_p the *plasma frequency*, see Equation 3.3. As a linear function of $\ln(\gamma)$, the density factor cancels the relativistic rise [118].

Giving $\mathrm{d}x$ in g/cm^2 makes the formula independent of the density of the ionization material. The real distance over which the particle loses the energy $\mathrm{d}E$ is given by $\mathrm{d}s = \mathrm{d}x \cdot 1/\rho$, with ρ the density of the material. For a short $\mathrm{d}s$ the distribution of $\mathrm{d}E/\mathrm{d}x$ is not symmetric; it exhibits a tail generated from the so called *Landau fluctuations*. The probability that a charged particle loses energy between ϵ and $\epsilon+\mathrm{d}\epsilon$ falls with $1/\epsilon^2$. Following this rule the δ-electrons cause the Landau-tail. The effect is mostly pronounced in gaseous or thin absorbers. The tail can be canceled by *truncation techniques*. Figure 3.2 shows the $\mathrm{d}E/\mathrm{d}x$ distribution as measured by the ALICE TRD Collaboration [120] for pions at a momentum of 1 GeV/c in $\mathrm{Xe/CO_2}$ mixture.

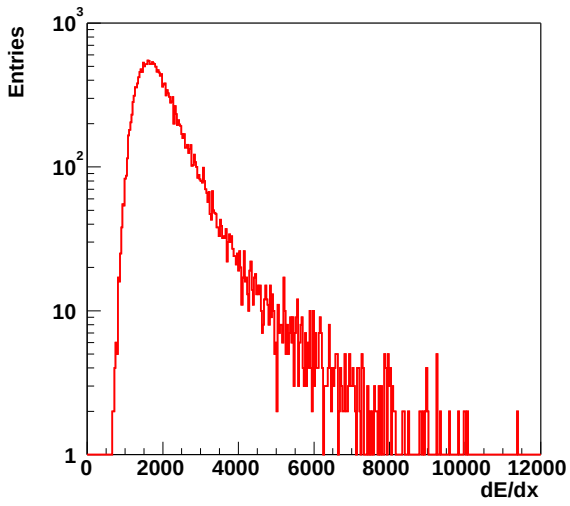

Figure 3.2: $\mathrm{d}E/\mathrm{d}x$ of pions, measured in a TRD chamber, at a momentum of 1 GeV/c in $\mathrm{Xe/CO_2}$ (85:15).

Equation 3.1 shows that $\mathrm{d}E/\mathrm{d}x$ depends only on the velocity of the primary particle and its charge. This makes it useful for particle identification as far as the propagating particle is still non-relativistic. But since the formula dose not depend on the particle's mass, it is not suitable for particle identification in the ultra-relativistic domain, Figure 3.1.
The minimal energy deposited in some materials which are relevant for detector chambers are given in Ref. [117]. For xenon and argon it has the values $7.3 \cdot 10^{-3}$ MeV/cm and $2.69 \cdot 10^{-3}$ MeV/cm respectively.

In addition to energy deposit through ionization, particles loose a part of their energy through excitation, bremsstrahlung, pair formation, and nuclear interaction. Apart from excitation, their contributions are proportional to the particle energy and appear at energies higher than 150 GeV [117]. Thus these processes can be neglected in particle identification at low momenta.

3.2 Transition Radiation

Transition radiation is an electromagnetic process involving charged particles propagating in matter. A charged particle traversing a medium emits radiation if either its velocity or the phase velocity of its electromagnetic field, i.e. the dielectric constant ϵ of the medium, changes. The first case characterizes the bremsstrahlung; the second is the transition radiation. Thus TR can be produced whenever the matter exhibits discontinuity in its dielectric constant ϵ for a constant particle velocity $v = \beta c$. It depends strongly on the Lorentz factor $\gamma = E/mc^2$ which implies dependency on the particle rest mass. Therefore it is an excellent way to identify ultra-relativistic particles where other methods like *Time of Flight*, $\mathrm{d}E/\mathrm{d}x$, and Čerenkov radiation fail.

3.2.1 Theory of Transition Radiation

A discontinuity in ϵ is realized at an interface between two materials of dielectric constants ϵ_1 and ϵ_2 as illustrated in Figure 3.3. The TR phenomenon can be illustrated by the following simple model. The moving charge $-q$ forms an electric dipole of a dipole momentum, $\vec{p}$, with its mirror charge beyond the boundary. The dipole creates an electric field $\vec{E}$ and *polarization* $\vec{P}$. Assuming Zone 2 to be vacuum with $\epsilon_1 > 1$ and $\epsilon_2 = 1$, the electric energy density of the dipole in the medium is given by:

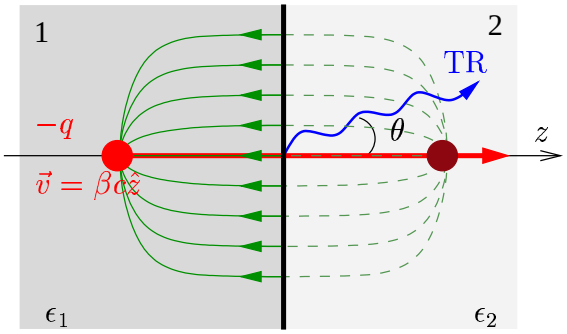

Figure 3.3: A charged particle traversing a boundary between two media of dielectric constants ϵ_1 and ϵ_2.

$$w_{el} = \frac{1}{2}\vec{P}\vec{E} = \frac{\epsilon_0}{2}\vec{E}^2 - \frac{1}{2}\vec{E}\vec{D}, \qquad (3.2)$$

where $\vec{D}$ is the electric displacement field.
The second term on the right hand side of Equation 3.2 is the energy density generated from the polarization.
Due to the particle movement towards the interface, the dipole moment, the polarization, and the electric displacement field are functions of time. The quantities decrease with the distance of the charge from the interface. At the moment when the charge traverses it, the polarization vanishes and its energy is emitted in form of transition radiation.

In general the dielectric constant is a complex quantity which varies with the energy of the interaction photon, $\epsilon = R(\epsilon) + I(\epsilon)$. The imaginary part is responsible for the absorption properties of the material. In the ultra-relativistic case where the Lorentz factor of the traversing particle is much larger than unity, the energy of the interaction photons is in the X-ray region (of the order of a few keV). In this high-frequency domain the absorption character of the material vanishes and the dielectric constant can be considered to be real. This material transparency allows to consider it as an electrically neutral system where the electrons of its atoms oscillate around a rest position, i.e. as in a plasma. The

oscillation frequency is called the *plasma frequency* of the medium, ω_p. The dielectric constant is close to unity and can be described by the *plasma formula*[1] [121]:

$$\epsilon(\omega) = 1 - \frac{\omega_p^2}{\omega^2} = 1 - \xi^2, \tag{3.3}$$

with $\omega_p^2 = 4\pi N_e e^2/m_e \simeq 830(Z\rho/A)$. Here N_e is the electron density and m_e is the electron mass. Z and A are the atomic number and mass number. $\xi = \omega_p/\omega$ determines the deviation of the dielectric constant from unity and ω is the energy of the particle.

Technically, transition radiation is the solution of a homogeneous Maxwell equation which must be added to fulfill the boundary conditions between two inhomogeneous Maxwell equations which represent the electromagnetic interactions in two adjacent media of different dielectric constant through which the charged particle passes. The TR field amplitude is a function of γ, ξ_i and the emission angle θ, such that the emitted TR is concentrated in a narrow cone of an angle $\theta \simeq 1/\gamma$ [122]:

$$\vec{e}_{TR}(\omega, \vec{\theta}) = \frac{\vec{\theta}}{\gamma^{-2} + \theta^2 + \xi_1^2} - \frac{\vec{\theta}}{\gamma^{-2} + \theta^2 + \xi_2^2}. \tag{3.4}$$

$\vec{\theta}$ of length θ is the difference between the unit vectors $\vec{k}/k$ and $\vec{v}/v$. $\xi_i = \omega_i/\omega$ with $\omega_i =: \omega_{p_i}$ for simplicity.

With this small emission angle and Equation 3.3, the energy density at the interface, that is the energy radiated per unit frequency and per unit solid angle, is proportional to the squared amplitude of the TR field given in Equation 3.4. The constant of proportionality is α/π^2, with $\alpha = 1/137$ the *fine structure constant.*

$$\left(\frac{d^2W}{d\omega d\Omega}\right)_{si} = \frac{\alpha}{\pi^2}\left(\frac{\theta}{\gamma^{-2} + \theta^2 + \xi_1^2} - \frac{\theta}{\gamma^{-2} + \theta^2 + \xi_2^2}\right)^2, \tag{3.5}$$

where $d\Omega = 2\pi \sin\theta d\theta \approx 2\pi\theta d\theta$. For simplicity we write $\xi_i = \omega_i/\omega$ in material $i = 1, 2$, with $\omega_i =: \omega_{p_i}$.

The integrated energy density over the solid angle for a single interface, $D_{si} = \frac{dW}{d\omega}$, increases logarithmically with γ if the charged particle traverses from a medium to vacuum where $\omega_2 = 0$. In a more realistic case where the second medium is a gas ($\omega_2 > 0$) the radiation saturates, compare Figure 3.4. The distribution is flat up to an energy value on the order of $\omega = \gamma\omega_2$, then it decreases logarithmically down to $\omega = \gamma\omega_1$, and finally it plunges for greater ω values. $\omega = \gamma\omega_1$ represents the *frequency cut-off* above which the radiation is negligible. The most radiation is emitted in the energy range $0.1\gamma\omega_1 \leq \omega \leq \gamma\omega_1$ [119].

The total energy radiated from the interface is obtained by integrating D_{si} over the whole energy spectrum:

$$W = \frac{1}{3}\alpha\gamma\frac{(\omega_1 - \omega_2)^2}{(\omega_1 + \omega_2)}, \tag{3.6}$$

[1] Assuming $\hbar = c = 1$.

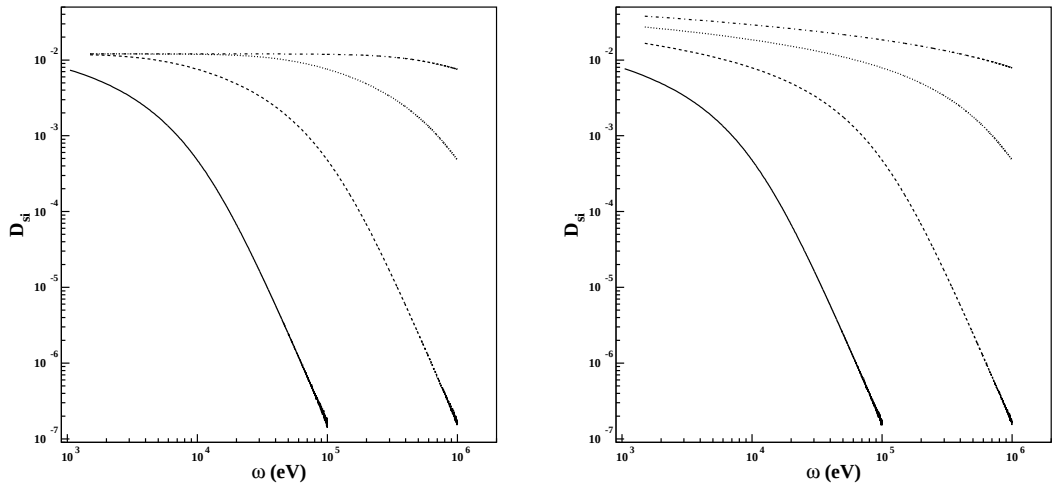

Figure 3.4: TR energy distribution of a single interface. Solid: $\gamma = 10^3$; dashed: $\gamma = 10^4$; dotted: $\gamma = 10^5$; dashed-dotted: $\gamma = 10^6$. Left: Lithium in Helium, right: Lithium in vacuum. The figure is taken from [122].

selecting $\omega_1 \gg \omega_2$ maximizes W:

$$W = \frac{1}{3}\alpha\gamma\omega_1. \tag{3.7}$$

Equations 3.6 and 3.7 contain the properties of the TR emitted from an ultra-relativistic charged particle at a single interface:

- The TR yield is on the order of the fine structure constant [122]. For example, on average only $5\alpha \approx 0.034$ photons are generated from an interface between *polypropylene* and air for $\omega = 1$ keV and $\gamma = 10^4$ [123]. Polypropylene is the main component of the ALICE TRD radiator, its plasma frequency is about 200 keV. The low yield of TR underlines the need of some hundreds of interfaces in order to be able to detect a charged particle with help of the transition radiation.

- W is proportional to γ, which makes TR favorable for particle identification. Particles with identical momenta but with different rest mass have different Lorentz factors. The rest mass differences between electrons and hadrons is large enough so that at the same momentum the Lorentz factors differ in some orders of magnitude. Up to 100 GeV/c relativistic electrons are the only particles which produce TR. In the ALICE experiment, the TRD will separate electrons from the abundant background of pions.

3.2.2 TR Yield From a Stack of Foils and Gaps

In order to intensify the TR photons flux, periodic arrangements of a large number of foils, (N), of identical thickness l_1 are in use. They are separated by gaps, usually also,

of identical thicknesses l_2, which are filled with a gas like helium or air for instance, as in the ALICE TRD case [2].

The TR energy distribution of this *radiator* configuration is a modified superposition of the TR yield from each of the interfaces. It is the coherent sum of contributions from the foils and gaps and it is given by:

$$\left(\frac{\mathrm{d}^2W}{\mathrm{d}\omega\mathrm{d}\Omega}\right)_N = \left(\frac{d^2W}{d\omega d\Omega}\right)_{si} \times 4\sin^2\frac{\phi_{1,m}}{2} \times I_N(\phi,\sigma). \tag{3.8}$$

The first modification factor, $4\sin^2(\phi_{1,m}/2)$, is an interference term generated from the phase retardation at the interfaces of the m-th foil [122]:

$$\phi_{1,m} \approx \frac{\omega l_1}{2}(\theta^2 + \gamma^{-2} + \xi_1^2). \tag{3.9}$$

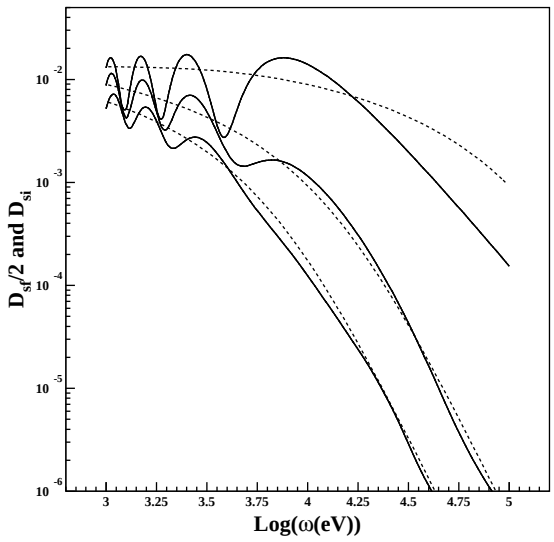

Figure 3.5: TR energy distribution of a single foil (solid) and single interface (dashed) for polyethylene/vacuum with $l_1 = 25\mu m$. From bottom to top the γ values are 500, 10^3, and 10^4. To enable a comparison with the single interface results, the distributions from the foil are divided by two. The figure is taken from [122].

The retardation is caused by the difference between $\vec{v}$ and $\vec{k}$, the particle velocity and the photon wave velocity respectively. In Figure 3.5 the TR distribution generated from a single foil is compared with those generated from a single interface at different Lorentz factors. Apart from the interference effect both distributions are consistent with each other.

The second modification factor, $I_N(\phi,\sigma)$, embodies the presence of the N foils. It accounts for the interference and absorption of TR photons in subsequent foils of the radiator, it is given by:

[2] As will be seen later, the radiator of the ALICE TRD does not consist of foils but irregular fibre and foam. Here only the material properties are meant.

$$I_N(\phi,\sigma) = \exp\left[\frac{1-N}{2}\sigma\right]\frac{\sin^2(N\phi/2)+\sinh^2(N\sigma/4)}{\sin^2(\phi/2)+\sinh^2(\sigma/4)}, \tag{3.10}$$

with $\phi = \phi_1 + \phi_2$ the sum of the foil and gap phases, and $\sigma = \sigma_1 + \sigma_2$ the sum of the corresponding absorption factors in a *foil-gap unit.*

The modification terms cause sharp peaks in the angular distribution ($\mathrm{d}^2W/\mathrm{d}\omega\mathrm{d}\theta$) which satisfies the condition $\phi = 2n\pi$, with n an integer. According to Equation 3.9 the spacing between the peaks is on the order of $\Delta\cos\theta \simeq \omega/(l_1+l_2)$ and thus it is too small to be measured. Therefore one picks up the TR yield as the flux integrated over angles ϕ_m [124]. It turns out that the TR distribution is similar to that of the single interface scaled by the *effective foils number*, N_{eff}. This is the upper limit of N which would lead to the same TR yield if absorption in the foils is set to zero. N_{eff} has the form:

$$N_{eff} = \frac{1-e^{-N\sigma}}{1-e^{-\sigma}}. \tag{3.11}$$

If $N\sigma \ll 1$, the gained radiation is proportional to N, as N increases, so does the absorption and after the threshold of N_{eff} there is as much radiation produced as absorbed. Saturation occurs at $N_{eff} \simeq 1/\sigma$. If the practical case of large N and small σ is considered, I_N can be approximated as a sum of delta functions [125]:

$$\begin{aligned} I_N(\phi,\sigma) &= 2\pi N_{eff}\sum_n \delta(\phi - 2n\pi) \\ &= \frac{\sin^2(N\phi/2)}{\sin^2(\phi/2)} \end{aligned} \tag{3.12}$$

The δ-character appears because the denominator $\sin^2(\phi/2)$ can vanish and I_N shows a maximum value of N^2 at $(\phi/2) = n\pi$. However the δ-character itself vanishes when the medium becomes irregular, see Subsection 3.2.4.

3.2.3 Maximizing the TR Yield and Saturation

Maximizing the TR yield is achieved by optimizing the type and thickness of the used materials. As indicated from Equation 3.7 a reasonable large difference between the plasma frequencies of both radiator materials maximizes the TR yield from each interface of the radiator foils. The second step is to determine N_{eff} and to minimize the absorption in the radiator materials. This can be achieved by choosing materials of low atomic number, Z, and by tuning and adjusting the thicknesses.

To determine the optimal foil thickness ${l_1}^{opt}$, for given radiator materials, the *formation length* z_1 of a foil is defined:

$$z_1 =: \frac{2}{\omega(\theta^2+\gamma^{-2}+\xi_1^2)} = \frac{l_1}{\phi_1}. \tag{3.13}$$

This is the depth of the foil for which the TR yield saturates as a function of thickness. In the m-th foil, if $l_1 \ll z_1$, the phase ϕ_1 approaches zero and it looks as if this foil does not exist and it does not contribute to the interference. The interference vanishes and consequently the TR is suppressed. This is the so-called *formation zone effect.*

The optimum total TR yield from the foil is achieved with a constructive interference between the photons emitted from its both interfaces. The enhanced case occurs if ϕ_1 is an odd multiple of π. This stipulates, for a given formation length z_1 (given material), the optimal foil thickness ${l_1}^{opt}$ at the so called detector *operation frequency* ω_0:

$${l_1}^{opt} = \frac{2\pi}{\omega_1^2 - \omega_2^2} \times \omega_0. \tag{3.14}$$

In terms of saturation, the radiation emitted from a single foil behaves like the TR which is emitted from a single interface. If the foil is placed in vacuum ($\omega_2 = 0$), the radiation increases logarithmically with γ otherwise if $\omega_2 > 0$ it saturates at [122]:

$$\gamma_{sat} = \frac{1}{2\pi} \frac{l_1 \omega_1^2}{\omega_2}. \tag{3.15}$$

In addition to the yield in the foil the TR is enhanced through a contribution from the adjacent gap. If the gap thickness, l_2, is smaller than its formation length z_2, then the TR yield is suppressed due to the formation zone effect in the gap. But if the opposite is true ($l_2 > z_2$) then the single gap yield will be roughly equal to the yield of a single interface.
If $\gamma \gg \omega/\omega_2$, then z_2 does not depend on γ anymore and the TR yield from the gap saturates at $\gamma_{sat} = \omega/\omega_2$.
The TR yield from a stack of N foil-gap units saturates under two conditions:

- If $l_2 < z_2$ the yield of N foils saturates as in the single gap case. Thus we have the saturation condition $\gamma_{sat} = \omega/\omega_2$.
- If $l_2 \gg z_2$ the yield has a cut-off as in the single foil case and consequently saturates according to condition 3.15.

The saturation in the radiator is then the minimum of these two conditions [122]:

$$\gamma_{sat}^N = \left\{ \begin{array}{ll} \frac{1}{2\pi}\frac{\omega_1^2 l_1}{\omega_2}, & \text{if} \quad \frac{l_2\omega_2}{l_1\omega_1} < \frac{1}{15} \\ 0.3\omega_1\sqrt{l_1 l_2}, & \text{if} \quad \frac{l_2\omega_2}{l_1\omega_1} > \frac{1}{15} \end{array} \right\} \tag{3.16}$$

3.2.4 TR From Irregular Radiators

The above mentioned material properties on which the TR yield depends help choosing the proper material for a TRD. Practical problems appear when the area of the radiator becomes large like in the case of the ALICE TRD. It is almost impossible to handle extensive thin foils. Moreover the mechanical stability of the radiator can not be guaranteed.

However, the main requirement for producing TR is the presence of boundaries between materials of different dielectric constants and with large differences between their plasma frequencies. These conditions are also satisfied in extreme irregular materials like fibres and foam. The point to be addressed is then the influence of the irregularity, i.e. the inequalities of the $(l_1)_i$ and the $(l_2)_i$, on the TR yield. More precisely, one must find out how the TR yield from the individual interfaces interferes. This question was first studied in the early seventies, by Garibyan *et al.* [125].

Considering an irregular radiator where $(l_1)_i$ and $(l_2)_i$ are random quantities, the TR yield generated in it, will also be a random quantity. Its distribution is determined by the distributions of the thicknesses $(l_1)_i$ and $(l_2)_i$ [125].

With extremely irregular thicknesses the absorption and interference factors of Equation 3.10 have the form $I = (1 - p^N)(1 + p)/(1 - p)$, with $p = \langle \exp(-2\mu(l_1)_i) \rangle$ the absorption term, where μ is the linear absorption coefficient. It is related to the absorption factor σ via the thickness: $\sigma = \mu l$. The TR yield is the additive sum of the radiation from the $2N$ interfaces.

Since the thicknesses are positive quantities and p has an exponential form it is convenient to take *Gamma-distributions* for them [126]. Calculations show that the main influence of the irregularity is the destruction of the interference between the radiation from different interfaces. At *irregularity degrees* above 15% the interference disappears. However below this value, when the irregularity becomes small, one observes the interference maxima and the irregular case approaches the regular one.
The irregularity degree is defined as $\eta = \langle \Delta l_i^2 \rangle^{1/2} / \bar{l}_i$ where $\bar{l}_i = \langle l_i \rangle$, and $\langle \Delta l_i^2 \rangle = \langle (\bar{l}_i - l_i)^2 \rangle$ [125] and $i = 1, 2$.

As noted in [125], only empiric results can give information about the TR yield from irregular radiators. The ALICE TRD Collaboration carried out a series of tests on different foam-fibre radiator configurations [127, 130]. In Chapter 7 the TR performance of a real dimension ALICE-TRD prototype will be addressed.

3.3 Gas Detectors

3.3.1 Drift Chambers

Ionization Chambers:
A ionization chamber utilizes the ionizing properties described in Section 3.1. They can be planar or cylindric. In the first case the chamber consists of two plates, an anode and a cathode, which comprehend a homogenous electric field in between. In the second type, a cylindric body acts as a cathode with a wire in its center acting as an anode. A typical wire diameter is on the order of 1 mm.
The ionization material in the chamber is gaseous. Mostly gas mixtures are in use, thereby electronegative components should be avoided to keep from *electron attachment*.

In both chamber types the current on the anode is read out through a resistance which creates a voltage signal. Ionization chambers are used to measure energy deposit or par-

ticles total energy if they are completely stopped in the chamber, like α-particles.

Proportional Chambers:
Since the field of the wire is inversely proportional to the wire radius, it is very strong for wire diameters on the order of some tens of micrometers. In this case the ionization chamber is called a *proportional chamber*.
Each ionization process (called *hit*) creates a *cluster* of one to three secondary electrons [118]. A secondary electron comes under the influence of a strongly gradient field and gains kinetic energy. If this energy is larger than the ionization energy of the gas atoms, it ionizes them and creates more secondary electrons and so on. The secondary electrons spawn avalanche like.

The avalanche starts at a threshold distance r_{th} from the wire center, with the threshold voltage U_{th}. From this point on, the amplification takes place and the first ionized electron is multiplied by the *amplification factor* A. Depending on the used drift gas, A is constant for a given anode wire voltage. The chamber is said to be operated in the *proportional mode*.

Multi-Wire Proportional Chamber:
A multi-wire proportional chamber (MWPC) works on the same principle of the proportional chamber but with many anode wires between two planar cathodes. In a simplified form it consists of two cathodes with an *anode-wires grid* in between. The distance between the grid and a cathode plane is called *wire gap* d. The distance between two neighboring wires is called *wire pitch* p, compare Figure 3.6.

In an MWPC one reads out the anode wires or one of the cathodes. In the first case the current of the wire is recorded, in the second the induced charge on the cathode.

In stand-alone mode, MWPCs operate as position measurement detectors. If a hit is recorded on a wire, the position of the particle in z-direction is determined, Figure 3.6. Therefore, in order to get a reasonable position resolution one must reduce the wire pitch, $\sigma = p/\sqrt{12}$. Best values are in the order of 600 μm. If better position resolution, or in addition a position reconstruction a long the wire is required, one reads out one of the cathodes and segments it into strips, *pads*. This allows a two dimensional position reconstruction within the pad area with resolutions down to 100 μm)[3].

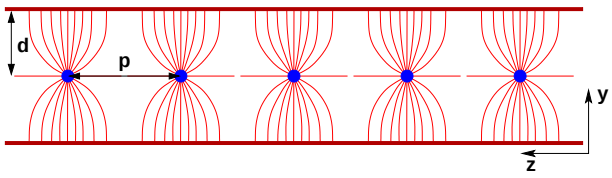

Figure 3.6: The MWPC chamber. The blue circles depict the anode wires, the brown lines symbolize the cathode planes and the red lines depict the field lines. p and d are the wire pitch and wire gap.

For momentum measurements of the propagating particle one puts a ionization chamber in a magnetic field. The Lorentz force curves the path of the particles, *tracks*. The curvature is a measure for the momentum of the particle. If a higher *Signal-to-Noise* ratio (S/N)

[3]Two dimensional position reconstruction is also achieved by two wire planes in which the wires are oriented perpendicular to each other. The advantages of pads is minimizing the occupancy in one chanel.

is required, a combination is used of a planar ionization chamber, for good tracking, and an MWPC, for amplification. This combination is the *Time Projection Chamber* (TPC). The ALICE TRD gas chamber can be considered as a "mini" TPC.

3.3.2 Effects in MWPCs

Once an avalanche has started in the amplification region, its development on its way towards the wire is enclosed within a few tens of microns (50 - 100) in longitudinal direction [118]. The processes in the avalanche are complicated and their description is beyond the scope of this work[4], but some unwelcome effects such as *space charge effect* and *Penning effect*, deserve more attention. In order to build a working counter, one must take these effects into account when choosing the drift gas and determining the chamber geometrical parameters.

Space Charge Effect:
If a primary particle crosses a gas chamber at high angles relative to the wire direction, the ionization electrons are collected over several centimeters of an anode wire. But if the incidence angle of the particle is small, the charge is collected only on a few millimeters of the wire. The field of the avalanche and the drifting ions reduces the amplification field. The gas gain of consecutive clusters is reduced and a signal distortion occurs. This is the so-called *space charge effect.*

With a large wire pitch the number of avalanches created per unit of wire length increases. This increases the avalanche charge density and it becomes comparable with the wire charge density. This enhances the space charge effect.

The effect can be eliminated if the anode wire grid in the counter is inclined with respect to the beam and/or the wire pitch is small.

The effect occurs also if the gas counter is exposed to high density particles flux, such as in experiments at RHIC and LHC. In this case the avalanches of different primary particles may accumulate. The field of such avalanches is high enough to arise the space charge effect.

Since one has no influence on incidence angles in these experiments, and a reduction of the wire pitch does not achieve the desired reduction of the effect, one operates the counters at low amplification factors (low anode voltage).

For reliable results on the space charge effect in a chamber, only empiric data of an individual detector can keep it under control. The ALICE TRD Collaboration investigated this effect in small area prototypes, but otherwise under nominal conditions. The results are presented in [128] and briefly discussed in Section 5.5.

Destroying the Proportional Modus:
In addition to the ionization processes in the avalanche, excitation processes take also place

[4]See for example Refs. [118] or [117].

resulting in the production of UV-photons. Up to a certain probability these photons escape the avalanche and create a ionization pair via photo effect outside the avalanche. A new avalanche arises. These effects cause a broadening of an avalanches-coat around the wire and deteriorate the position resolution capability of the detector. Some photons may even reach the cathodes or other chamber components and produce free electrons by the photo-electric effect.
These effects are avoided through the *quench gas* which is an additional gas component that keeps the avalanche region localized by absorbing far-traveling photons. A quench gas must have, therefore, many degrees of freedom with a large photo absorption coefficient which exceeds the wavelength range of a UV-photon. Organic (CH-) and inorganic (CO_2) compounds are usually in use.

Penning Effect:
Also within the avalanche, excitation processes influence the signal. An excited atom A^* could lead to an intermediate ionization with other atoms, either of the same species, A, or other atoms or molecules B like the quencher component, if available.

$$e^- A \rightarrow e^- A^*,$$

$$A^* B \rightarrow A B^+ e^-.$$

The electron production of the second reaction produces its own avalanche which does not belong to the signal of the primary particle. This leads to a *variation* in the gas gain. This is the so called *Penning effect*. The second reaction occurs only if the excitation energy of A is larger than the ionization energy of B.

gas	atomic weight	atomic number	ionization energy (eV)	excitation energy (eV)
CO_2	44	22	13.773	0.083-10.5
xenon	131.3	54	12.13	8.3-11.7
argon	39.9	18	15.7	11.55-14.0

Table 3.1: Ionization and excitation energies of the gases used in the ALICE TRD chambers. Ar/CO_2 in tests and Xe/CO_2 is the operation gas mixture.

Chapter 4

The ALICE Transition Radiation Detector

Although TRDs take on many forms to match a wide range of applications, there are common basic principles of designing the radiator and the adjacent detection unit. The development of such a detector system is an interdisciplinary mix of physics, electronics, and computer sciences. In addition to the physics of particle passage through matter, and due to limited budget, self made low-noise microelectronics are mostly used. These electronics must be able to record all possible signals coming from an interaction with thousands of charged particles. In addition, high-speed data transformation and powerful computer-based data acquisition systems are needed. All these considerations seem to be valid for the ALICE TRD.

In this chapter the design issues of a TRD detector unit will be discussed in terms of an ALICE TRD *module*. In Section 4.1 the physics issues accessible with the ALICE TRD will be discussed. Its design requirements are presented in Sections 4.2. The operation principle of the detector will be presented in Subsections 4.6, and finally an overview on the final construction of the radiator will be given in Section 4.5.

The readout chamber of a TRD module[1] will be a subject of investigation in the following chapters of this part of the thesis.

4.1 Physics Motivation

Electrons are produced through many processes; before, during and after the establishment of a fireball in heavy-ion collisions. They carry information about its dynamics and its development throughout all stages. It is of interest to inquire whether the electrons arise from QGP production or from other processes like resonances decays. Thus their identification and classification have a leading position of interest and belong to the biggest challenges in the ALICE experiment.

[1]The denotation *module* means the whole device including radiator and electronics, whereas the denotation *chamber* means the gas volume, the wires and the readout pad plane.

In [9] it is shown that under the LHC energy environment the expected di-electron spectrum in the mass range $0 < m_{e^+e^-} < 5$ GeV/c^2 is dominated by the combinatorial background of the π^0 and η Dalitz decays and of the semi-leptonic decays of **B** and **D** mesons. An additional background comes from underlying events, mainly charged pions and kaons , which are expected to be between 2000 and 8000 particles per unit rapidity. Nevertheless, all Quarkonia, which are expected to be states to QGP formation, are accessible, if a reasonable electron identification is ensured. In addition, since light mesons like ϕ and ω can only be measured with low *Signal-to-Noise* ratio (S/N), the TRD must have a good resolution to identify these narrow resonances with low S/N.
Carrying out these requirements, the following measurements are accessible with the TRD [130, 9].

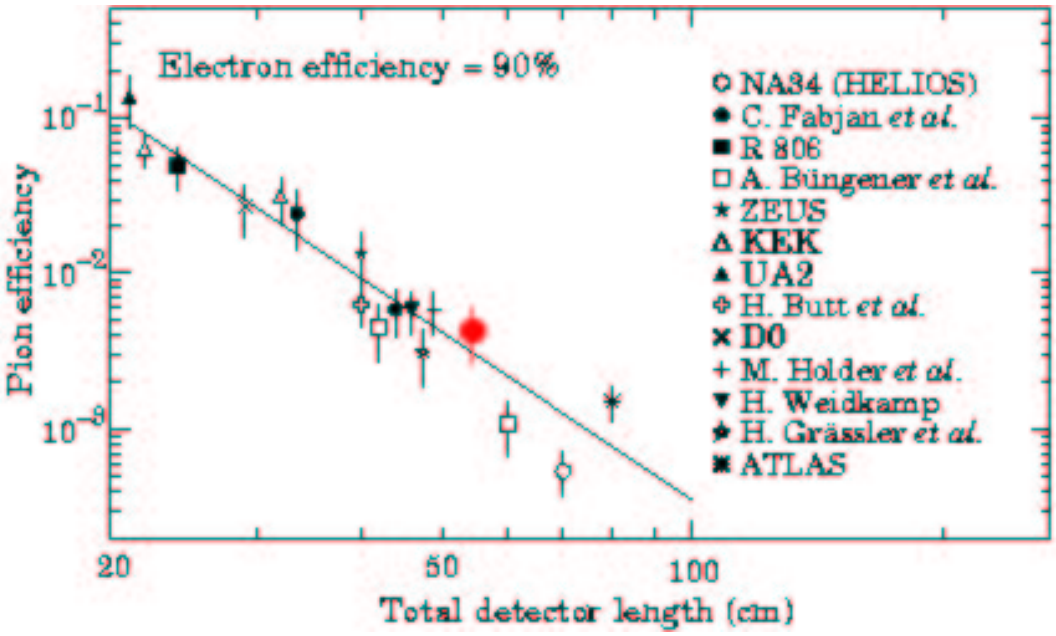

Figure 4.1: Pion efficiency, π_{eff}, for different TRDs as a function of the detector depth at an electron efficiency of 90%. The figure is taken from [119]. The red point, which we added, represents our results with ALICE TRD prototypes. Notice that the readout electronics which was used does not fulfill all requirements put on it. The results are expected to be clearly improved.

4.1.1 Heavy-Ion Collisions

- **Measurements of heavy and light vector mesons** at mid-rapidity, $y = 0$, where a baryon free environment is expected.

- **Via the di-electron channel** it is possible to :
  - distinguish between primary and secondary J/ψs using vertex information from the ITS.

  - achieve sensitivity at the Drell-Yan level which is expected to be screened by the open charm continuum. This requires a rejection of the electrons generated from **B** and **D** meson decays from the combinatorial background mentioned above.
  - address the thermal continuum radiation. The di-electron spectrum between J/ψ and Υ could be sensitive to the thermal continuum [131].

- **Via the single-electron channel** the semi-leptonic decay of hadrons with open charm or open beauty is accessible when requiring a vertex displacement (ITS information). This backs up the hadronic decay channel.

- **Electron-muon coincidences** information from the central barrel and the forward arm give access to correlated production of hadrons with open charm and open beauty in a rapidity range $0 < y < 4$, central barrel and forward arm rapidity.

In addition, the TRD will serve as a trigger for jets with high E_t. By requiring several (three or more) high p_t tracks in a TRD super-module, jets with high E_t can be selected at the trigger level. With three to five high p_t particles in the jet cone, a jet candidate can be identified. With the trigger regions of interest, high momentum electrons can be identified. This allows to determine the TPC sectors to which the electron candidates point and reduces the event size.
The importance of the TRD as a trigger is underlined by concerning the yield of high-p_t Quarkonia within the limited band-width of the DAQ and storage. Without the TRD trigger, about 2500 J/ψs with $p_t > 5.5$ GeV/c and about 160 Υs would be recorded per year in minimum bias collisions at an event rate of 200 Hz in the DAQ. The trigger enhances these numbers significantly to 10000 high-p_t J/ψs and about 2300 Υs.

4.1.2 *pp* Collisions

Proton-proton collisions are an important part of the ALICE running program. Information needed to compare the results achieved in the nucleus-nucleus collisions are collected in the *pp* program. Also topics of interest in elementary hadron interactions can be addressed. The detailed physics arguments for this program are discussed in [5].

4.2 Design Criteria

To achieve the physical requirements outlined in the previous subsection, the following considerations must be taken into account when designing the detector. All details and most of the figures are taken from [130].

1. **Pion rejection efficiency:**
   In order to be able to record significant Quarkonia signals in the abundant charged pions, a pion rejection factor of 100 is required [9].

Quantity	required value
gas gain	3000 - 8000
pion rejection efficiency	$\simeq$0.01
drift time	2 μs
spatial resolution	400 μm
angular resolution	1 degree
Quantity	**tolerated value**
gain variation	15%
gas overpressure	1 mbar
radiation length	$X/X_0 < 15\%$
pad plane flatness	200 μs

Table 4.1: Requirements and tolerances put on the TRD readout chamber.

Because of saturation effects in the TR yield, TRDs in general consist of a series of detector layers. The overall depth of the detector is the most important factor for the performance of any TRD. Figure 4.1 shows the measured (or extrapolated) *pion efficiency* (= 1/pion rejection factor, Section 7.8) for a variety of detectors at an electron efficiency of 90% [119]. The results presented cover a wide range of particle momenta, up to 40 GeV. The fit can be considered to be a universal curve for pion rejection.
Following it, the anticipated pion efficiency of 10^{-2} can be reached with a TRD depth of about 53 cm. The red point, which was added to the figure within this study, represents the performance of ALICE TRD prototypes. It shows the consistency of their performance results with the curve.

In the ALICE central barrel the space available for the TRD starts at 2.9 m radially from the interaction point and extends to 3.7 m. The correlation between the radiator height and the height of the detection chamber, see below, lead to a total number of 6 layers in the available overall depth.

2. **Mechanical stability and radiation thickness:**
Electrons with energies larger than 500 MeV lose energy primarily by means of *bremsstrahlung*. The radiation length, X_0, describes the amount of matter traversed until an electron loses all but $1/e$ of its energy through bremsstrahlung. X_0 is usually measured in g cm^{-2} and can be approximated by [117]:

$$X_0 = \frac{716.4 \cdot A}{Z(Z+1)\ln 287/\sqrt{Z}}, \tag{4.1}$$

where A and Z are the atomic weight and number respectively. Conversion probability and multiple scattering as well as electron energy loss through bremsstrahlung increase the pixel occupancy of the detector and degrade the electron measurements in the outermost TRD modules.To minimize these effects, light construction is required. The entire TRD should not represent more than 15% of radiative length. This implies the use of low Z materials.

Additionally the required mechanical stability of the chambers restricts the number of materials with high X_0 which are mutable to build the TRD. Both requirements of mechanical stability and high radiation length were compromised so that X/X_0 is still within tolerance levels.
Table 4.2 contains the radiation length of materials used in the ALICE TRD [117].

material	X_0/ **(g/cm^2)**
carbon	43
tungsten	6.8
copper	12.9
beryllium	65.2
xenon	8.48
CO_2	36.2
polypropylene	44.6

Table 4.2: Radiation length X_0 of the materials used in the TRD.

3. **Momentum resolution:**
The required TRD momentum resolution is driven by the one of ITS and TPC where the momentum resolution by a magnetic field of 0.4 T is as good as 100 MeV/c at the Υ mass level. The TRD must match these requirements: Simultaneously, the reconstructed track segments in the TRD must unambiguously find the elongation of the corresponding segments in the inner barrel detectors (ITS + TPC) and in the outer detectors (TOF). This requirement is constrained by the granularity (pad size or pixel) of the other detectors.

4. **Readout granularity:**
The high charged particle multiplicity expected at LHC energies requires the segmentation of the TRD readout pad plane in pads. The pad dimension in ϕ is determined by the momentum resolution required, the narrower the pad, the better the momentum resolution. In beam direction z the pad length is determined by the capability to identify and track electrons. The shorter the pad, the better the tracking capability of the TRD.
However a "very" small pad area deteriorates reconstructed pairs and increases the number of channels drastically, which would increase the electronics costs and overfill the limited space foreseen for services. A pad area between 590 and 730 mm^2 seems reasonable and gives an 80% tracking efficiency.

5. **Occupancy:**
At a maximal multiplicity of charged particles of 8000, the TRD readout pixel occupancy with a pad size of about 630 mm^2 and at central collisions is 34% (including secondary particles). The TRD works at this occupancy.

6. **Gas gain:**
The required momentum resolution corresponds to a position resolution on the order of 400 μm. This can be achieved with a S/N-ratio between 25 and 30. Thus the gas

gain should be large enough to enable this ratio, in particular around 3000. On the other hand and due to the space charge effect and ADC saturation, the gain should not exceed 8000. In addition, a large gain value decreases the pion rejection factor at small incidence angles of the primary particles [130].

7. **Gain variation:**
   The ADC, see later, is conceived to enable a hardware correction of the gas gain variation up to 15%. Gain variation can be caused by mechanical deformations of the readout sandwich, unevenness of the pad plane, or wire sag. All these effects together should not lead to gain variation larger than 15%.

These design requirements and those of the front end electronics, discussed in Section 4.7.2, are the fundamental basis of the simulations and prototype tests which will be subject of discussion in Part II of this thesis.

4.3 TRD Module

Each detector module is a large area drift chamber with radiator material in front. The chamber is a combination of a ionization drift chamber (DC) and a MWPC. A services unit including electronics and cooling elements, is part of each module.

Figure 4.2 shows a cross section of a TRD module. The body is made of G10 reinforced with aluminum profiles on the outside. The radiator is placed in the 48 mm of the module body radially inwards and adds to its mechanical stability. The drift electrode is glued to the radiator. The next 37 mm houses the gas volume. The DC depicts the so called *drift region* (30 mm) with uniform electric field of 700 V/cm, the MWPC depicts the *amplification region* (7 mm) with a sloped electric field. Both chamber sections are separated by a *cathode wire plane*. An *anode wire plane* is located halfway between the cathode wire plane and the *readout pad plane* at 33.5 mm from the drift electrode.

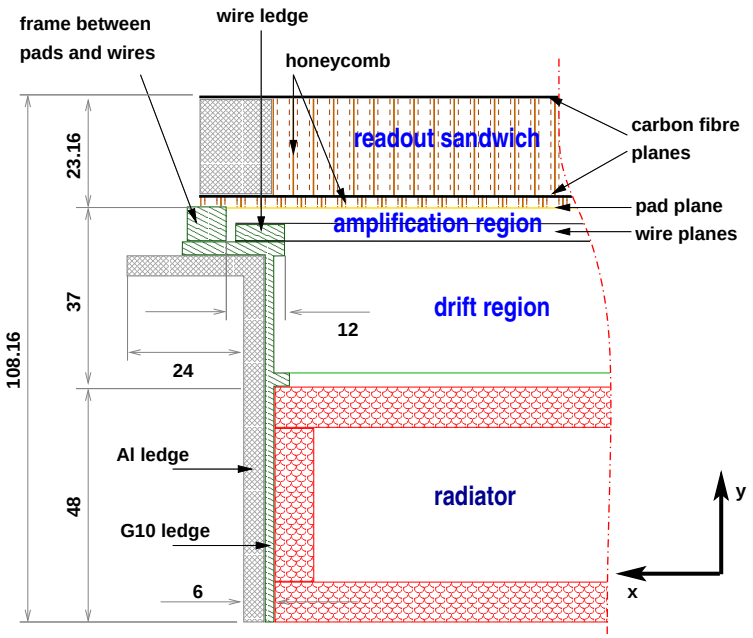

Figure 4.2: A cross section a long the TRD chamber.

The segmentation between the gas volume and the radiator was optimized [127] to fit in the space available (80 cm) with reasonable number layers such that the anticipated pion

efficiency of 10^{-2} is achieved. It is found that this value is obtained with 6 layers in radial direction.

The pad plane cathode is glued on a carbon fibre-honeycomb sandwich of 22 mm thickness. (A combination with acceptable X/X_0 value). The sandwich is divided into two parts of honeycomb with thicknesses of 20 mm and 2 mm. Both parts are separated through a carbon fibre plane of 200 μm thickness. A similar carbon fibre plane covers the outer side of the sandwich. On the inner side, the readout pad plane is glued directly on the 2 mm-honeycomb layer.
This layer construction reduces the cross-talk on the pad plane from about 52 pF to 16 pF. Furthermore glueing the pad plane on the flat honeycomb avoids fluctuations in the gap between the anode grid and the pad plane which are caused by air bubbles and glue mis-distributions when glueing the pad plane directly on the carbon fibre. The cross-talk would be decreased if a non-conductive material could be used instead of carbon. Suitable candidates, like glass-fibre, however have a low radiation length and the tolerated X/X_0 ratio would be exceeded.

The drift gas is a xenon/CO_2 mixture (85:15), This was found to enable a maximal photo absorption in the TR energy region such that the Lorentz angle is still acceptable. The anticipated drift velocity of 1.5 cm/μs is achieved at low drift field of about 700 V/cm, see Section 5.1.

Building small chambers is much simpler than building large ones. But, if the detector is assembled from many small modules, efficiency losses in the cracks between the modules become significant. Therefore the detector was segmented in 5 sectors along the beam direction, 18 super-modules in azimuth. With the radial segmentation of 6 layers, this configuration ensures an acceptance of about 80% within the nominal central barrel η acceptance and for momenta larger than 0.2 GeV.
One module is 13 cm deep, the lengths and widths of the modules vary according to their coordinate in space, Figure 2. The smallest (largest) module is 996 (1218 mm) wide and 1090 (1460 mm) long.

4.4 The Pad Plane

The TRD readout electrode is a 360 μm thick copper-FR4 plate with a surface flatness better than 50 μm. It is segmented into, in average, 630 mm^2 large pads. The thickness is constrained by the required radiation length, the readout sandwich provides nevertheless the necessary mechanical stability.
The flatness requirement is conditioned on the anticipated gain homogeneity, i.e. the homogeneity of the wire gap h. However, the detector is constructed to be able to deal with pad plane deflections up to 200 μm in- and outwards.
With the measured drift time, the pad segmentation allows a three dimensional position reconstruction of primary particles.
The main challenge of manufacturing such a pad plane is its large surface. The largest

plane producable in industry is not wide enough to cover even the smallest readout sandwich. Therefore two or three of pad plane segments are glued beside each other depending on the module size.

4.4.1 Pads Layout

The granularity of the pads, i.e. their shape and size, is determined by the required occupancy. In turn it determines the position and momentum resolution of the chamber. Two pad shapes were considered, chevron and rectangular. The advantages of the first is the low non-linearity of the pad response function, see Subsection 7.5.1, and the better position resolution achieved [132]. The linearity is defined to be the difference between the true position and the reconstructed position of the avalanche.

However, the non-linearity of rectangular pads is still negligible [133] and they achieve a position resolution down to 300 μm, Subsection 7.5.2. On the other hand, chevron pads give a wider PRF than rectangular ones and the border between two adjacent chevron pads is over three times larger than in the rectangular case leading to an increase in signal cross-talk.
For the reasons mentioned above, rectangular pads are used which give the required charge sharing. For detailed discussion of simulations and measurements with these two pad shapes see the mentioned Refs. and [134].

To enhance the position resolution in beam direction, the pads are tilted with respect to the beam direction. The tilt angle is 2 degrees.

4.4.2 Wire Grids

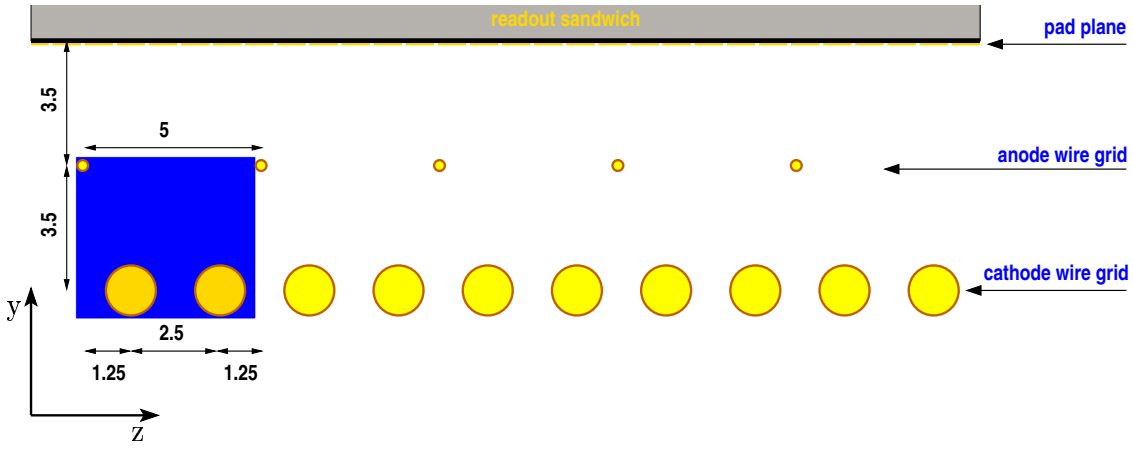

Figure 4.3: Wire geometry in a TRD module. Blue background indicates a wire unit. Dimensions are in millimeters.

Figure 4.3 shows the two wire grids in a TRD chamber. Per wire in the anode grid there are two in the cathode grid which are positioned in a staggered way. The three build a *wire unit* which is indicated by the blue background in the figure.

	anode wires	cathode wires
material	Au/W	Cu-Be
diameter (μm)	20	75
length (cm)	100 - 120	100 - 120
pitch (mm)	5	2.5
tension (N)	0.45	1.2
number/chamber	212 - 286	424 - 572
frame load (kg/150cm)	10 - 13	50 - 67

Table 4.3: Parameters of the wire grids in a TRD module.

With lengths up to 1200 mm the electrostatic stability of the wires deserves careful study. The choice of the wire materials as well as their parameters specifications will be studied and justified in the next chapter. They make the wire grids fulfill their tasks in the chamber.
The wires in the cathode plane consist of a copper-beryllium (Cu-Be) alloy. With their relatively large diameter of 70 μm, they isolate the amplification region with its high, inhomogeneous electric field from the drift region, where a lower and smoother drift field is required. It allows 99% of the electrons from the drift region to enter the amplification region, but only 26% of the ions produced around the anode wires to pass into the drift region. Ions in the drift region modify the drift field leading to deterioration of the gas drift properties.
The cathode wire grid is grounded and therefore it reduces the wire sag of the anode wires and thus reduces the gas gain variation. Each cathode wire is stretched to the chamber frame with a force of 120 g (1.2 N).
In the anode plane the wire diameter is 20 μm and the wire tension is 45 g (0.45 N). The wires consist of gold plated tungsten. For a given gap and drift voltage, the low diameter restricts the amplification field within the amplification region where the amplification voltage is 1.5 kV, and supports the separation between both chamber regions.
In the next chapter the specification procedure of the wire parameters given in Table 4.3 will be discussed.

4.5 The Radiator

The radiator is the generator of the TR. In general, its efficiency is limited by the effective number of the radiator layers, N_{eff}, which determines its thickness. Since only a few millimeters are necessary to detect the TR, the depth of the drift chamber is also determined.

Due to the large areas of the ALICE TRD chambers, regular radiators are prohibited. Therefore the TR yield of different irregular radiator types was systematically studied, in particular *Rohacell foam* and *polypropylene fibres*, which are easy to manufacture and available at reasonable prices.

Beside the best possible TR yield the radiator has to achieve the correlated and already mentioned requirements of mechanical stability and maximal radiation length X_0. The final radiator was optimized to provide these three requirements. It consists of polypropylene fibre mats of 32 mm total thickness sandwiched between two Rohacell foam sheets of 8 mm thickness each. The foam sheets are reinforced by carbon fibre sheets which are laminated onto the surface with a thickness of 100 μm each.

The measured radiator performance, with a pion rejection factor of 100 at an electron efficiency of 90%, is shown in Figure 4.4. The ratio $\langle PH \rangle_e / \langle PH \rangle_\pi$ is a quantitative measure for the transition radiation. The anticipated radiator design, $S - HF71$, is compared with pure foam and pure fibre. Pure foam, $HF71$, gives the best mechanical stability but decreases the radiation thickness. Pure fibre, $fibres17$, enables high radiation length but it is mechanically unstable. The considered design, $S - HF71$, gives reasonable TR yield and guarantees the required stability with a radiation length within tolerance levels.

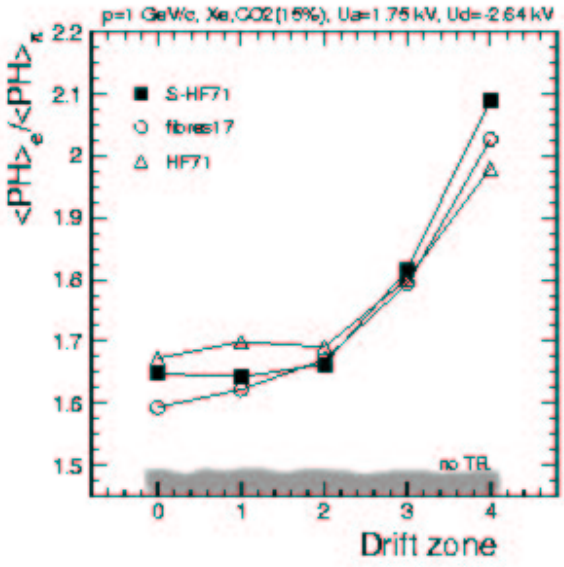

Figure 4.4: Comparison between three different radiator materials, foam, fibre and a combination of both. The ratio of electrons signal to pion signal in a TRD prototype. The figure is taken from [130].

The chamber drift cathode, a 25 μm thick aluminum-mylar foil, is glued onto the inner side of the radiator, in such a way that the chamber-radiator interface is leak tight. This yields two advantages: it avoids "expensive" xenon flows in the radiator, which would deteriorate the TR performance, and O_2-flow in the drift chamber, as this would enhance the electron attachment and consequently deteriorate the signal.
The flatness of the cathode is warranted through the radiator sandwich. In order to keep the drift field as smooth as possible, deflections in the radiator are only tolerable on a small scale. Thus, and due to the large chamber area, the radiator volume is segmented via Rohacell sheets of 8 mm thickness, into 20 to 25 cells. The cell walls stabilize the radiator mechanically.

The maximum overpressure allowed in the chamber is 1 mbar, deformation caused by this overpressure and the wire tension is within the tolerance of 1 mm, Section 6.3 and [135].

The drift voltage at the cathode is -2.1 kV.

4.6 Principle of Operation

When kaons, pions or electrons with momenta lower than 1 GeV/c transverse a TRD module they pass through the radiator without any appreciable effect[2]. In the drift region they create a trail of hits, each of which is a ionization event which creates ion-electron pairs.

But electrons with momenta around or larger than 1 GeV/c generate soft X-ray photons with energies between 5 and 30 keV in the radiator. The majority of these X-rays is absorbed in the first 10-15 millimeters of the gas volume, and create also ion-electron pairs in the entrance window of the drift region, compare Figure 4.5.
In both cases the liberated ionization electrons drift under the influence of the homogenous electric field towards the amplification region and create avalanches at the anode wires.
The electrons of the avalanche are quickly absorbed by the wires and the ions drift slowly away from them. During their movement they induce a signal on the pads. The TR signal provides a collateral signal superimposed on the ionization one. Within a certain Lorentz factor interval this addition signature distinguishes electrons from other charged particles, usually pions. In Chapter 7 the separation methods will be briefly discussed.

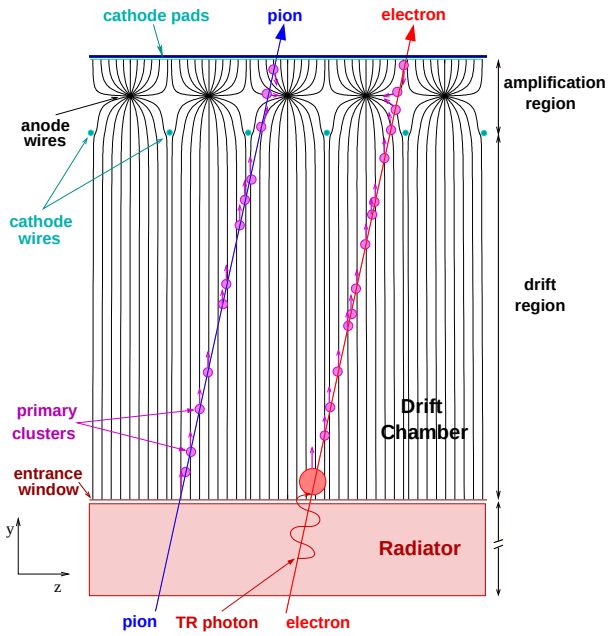

Figure 4.5: Sketch of an ALICE TRD module.

The hit position in the x and z-direction is reconstructed from the charge sharing among adjacent cathode pads. The drift time is segmented into 20 *time bins*. With the drift velocity, $v_d = 1.5$ μm, corresponding to the drift field and the gas mixture, and the drift depth the third spheric dimension y can be determined.

4.7 Front End Electronics

The TRD will serve as a *Level 1* (L1) trigger, see below, to select electron pairs with high transverse momenta. To do so one needs an accurate measurement of x-position, compare Figure 4.5. This space knowledge is selected from charge sharing between three adjacent pads. For tracking in the y-z-plane one needs measurements of the y-direction. This information is gained from the drift time. To get all that informations, a special

[2]except energy deposit for which such a narrow drift region is not appropriate especially with the presence of the TPC.

Front End Electronics (FEE) was designed for the (1.181.952) channels in the whole TRD. The requirements put on the FEE are determined through the parameters of read out chambers which influence the information mentioned before.

4.7.1 Electronics Overview

The FEE consists of two *Application Specific Integrated Circuits* (ASIC), compare Figure 4.6:

- One analog ASIC with 18 channels of charge sensitive preamplifier, shaper (PASA), and output driver. One channel has a shaping time of 120 ns at a conversion gain of 6.1 mV/fC, providing a maximum differential output of 1 V with a power consumption of 10 mW.
- One mixed analog/digital ASIC with 21 channels of 10 bits ADC, *Tracklet Pre-Processor* (TPP) and event buffer. All channels enter one single *Tracklet Processor* (TP). The last three layers are referred to as the Local *Tracking Unit* (LTU) and perform the on-line tracking in the TRD trigger mode.
- A *Global Tracking Unit* (GTU). This is a common processor for the LTU data coming from the 540 TRD modules.

Both ASICs, assembled in a *Multi-Chip Module* (MCM), are mounted directly on the readout chambers, in order to minimize the trigger latency. The combined tracking of all channels of the 540 chambers is done by merging all MCMs output into a single GTU, which processes information on the high-p_t track candidates.

4.7.2 Electronics Design Requirements

The working point of the FEE is set to an optimum according to the following considerations:

- The resolution of one detector hit is determined by the pad response function, Section 5.2, and by the signal-to-noise ratio. As defined for the lowest signal of a MIP, a reasonable point resolution is obtained at a 30:1 signal-to-noise ratio.
- The transition radiation energies are between 5 and 30 keV, much larger than the average ionization energy. Therefore the dynamic range is used more effectively if the signal (gas gain) is kept lower.
- Both previous requirements set a limit to the electronic noise of the preamplifier, which has been accepted at 1 *Least Significant Bit* (LSB), or 1000 equivalent electrons.

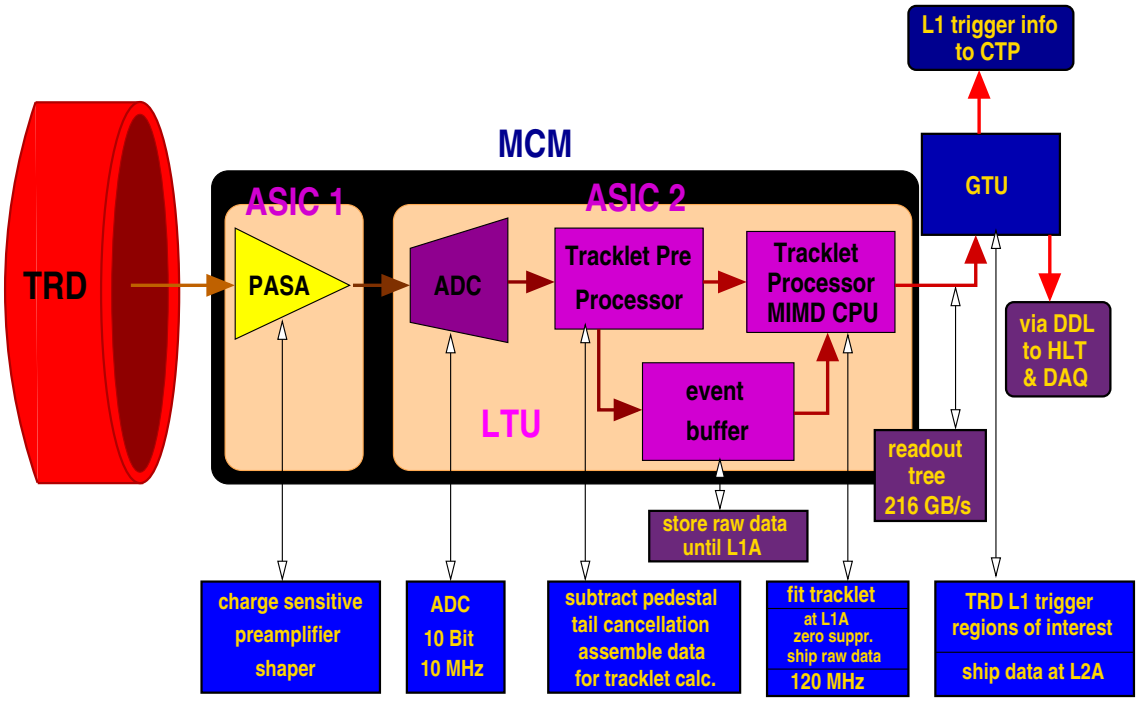

Figure 4.6: Basic components of the TRD front-end electronics. Everything except the GTU is mounted on the detector itself. The ADC, digital filter, TPP, TP and the event buffer are incorporated in a single chip. L1A, L2A refer to the different trigger levels of the Central Trigger Processor of ALICE.

The sampling frequency of the second ASIC, together with the high voltage setting, and the drift velocity in the gas chamber, define the number of reconstructed detector hits in one chamber. This number is a direct measure of the transverse momentum resolution which can be acquired. The total drift time has to be kept as small as possible, since it contributes to the latency of this trigger level. At the same time, the distance between two subsequent detector hits must not be much smaller than the shaping time of the PASA, since this will correlate the separated points. The shaping time is however limited by the electronic noise. By combining these opposite arguments, an optimum is found for a drift time of 2 μs and 10 MHz ADC sampling frequency, which implies having 20 spatial points in one chamber.

In addition to this, two other effects are present:

- The slower drift of the positive ions in the gas induces a long tail of the signal, which propagates from one detector hit to the next. Position and angular resolution are both affected.
- The capacitance between adjacent pads (6.5 pF) generates a channel-to-channel cross talk of about 6%, which distorts again the PRF.

These requirements and those of the detector design, discussed in Section 4.2, are correlated to each other, therefore we will often have to compromise between two or more parameters. Table 4.1 summarizes the design requirements. It tells on the limitations of the detector characteristic quantities and the parameters which influence these quantities.

4.7.3 Data Processing

During the drift time, the data processing is performed in the TPP. At the end of the drift time the TP processes the data of all time bins in order to determine potential tracklets, these are local track segments in a module. Selected tracklets are shipped to the GTU. The GTU combines and processes the trigger information from individual readout chambers and passes selected tracks on to the *Central Trigger Processor* (CTP).

4.8 Trigger Concept

The TRD trigger system is integrated in order to select high-p_t electron pairs by taking advantage of tracking and TR signature on a 6 μs time scale.
In the trigger mode, the TRD performs a fast tracking and selection of high-p_t particles, based on the short drift time of 2 μs and on the TR signature. The recording of the ADC data into the event buffers starts with each pre-trigger, L0. During the drift time the TPP accumulates the sums for the linear fit of the tracklets and combines the digits information into a local particle identification measurement. If the L0-Accept was issued, at the end of the drift time, the TP can already search, fit, and select the tracklets. The p_t is estimated by the tracklet deflection from the direction of a primary vertex particle with infinite momentum. With a p_t cut at 2 GeV/c, up to 40 tracklets per chamber are sent after 4.5 μs to the GTU. The GTU selects track candidates from matching at least 3 tracklets from different TRD layers, updates and applies a second cut in the transverse momentum at 2.7 GeV/c, and computes global PID information. If the TRD triggers on e^+e^- pairs, a further cut in the invariant mass can be applied. After 6 μs the TRD can contribute to the Level 1 of the CTP with a trigger signal, and to the more elaborate *High Level Trigger* (HLT) with regions of interest over a larger band width. The Level-1-Accept starts the reading of the FEE event buffers into the event buffer of the GTU, which is completed by putting the TRD electronics back into the stand-by mode. With a Level-2-Accept the event is forwarded to the HLT and to the data acquisition.

4.9 The TRD in Numbers

Taking the physics requirements and the design criteria into account the TRD parameters were optimized in a series of simulations and beam tests. The parameters of the readout chamber are gained from a set of simulations, Chapter 5, and prototype tests [130]. Results from tests on a real dimension prototype are presented in Chapters 6 and 7.

pseudo-rapidity coverage	$-09 < \eta < 0.9$
azimuthal coverage	2π
radial position	$2.9 < r < 3.7$m
length	maximal 7 m
segmentation in ϕ	18 folds
radial segmentation	6 layers
segmentation in z	5 folds
modules total number	540
largest module	$120 \times 145\text{cm}^2$
total active area	750 m^2
total thickness in the radial direction	15% X_0
radiator	a 4.8 cm thick fibres-foam sandwich
module segmentation in ϕ	144 pads
module segmentation in z	12-16 pad rows
pad geometry	between 590 and 730 mm^2
time samples in drift direction	20 time bins
number of readout channels	$1.18 \cdot 10^6$
number of readout pixels	$2.36 \cdot 10^7$
gas mixture	Xe/CO_2, (85:15)
gas volume	27.2 m^3
drift region depth	30 mm
amplification region depth	7 mm
nominal magnetic field	0.4 T
drift field	0.7 kV/cm
drift velocity	1.5 cm/μs
longitudinal diffusion	253 $\mu\text{m}/\sqrt{\text{cm}}$
transversal diffusion	186 $\mu\text{m}/\sqrt{\text{cm}}$
Lorentz angle	8°
occupancy (full multiplicity)	34%
position resolution	μm
in $r\phi$	low multiplicity required 400μm, measured 300μm high multiplicity required 600μm
in z	pad length/$\sqrt{2}$: 1 layer pad length/$\sqrt{12}$: 6 layers
momentum resolution	3%
pion suppression	10^{-2}

Table 4.4: Abstract of the TRD parameters [130].

Part II

Development of the ALICE-TRD Readout-Chamber

Chapter 5

Readout Chamber

In the previous chapter an overview on the ALICE TRD and the components of one of its individual module was given. The simulations which lead to those parameters will be discussed in this chapter. The geometrical and electrostatical settings as well as those of the gas mixture in the drift volume will be tuned. The task is to optimize a viable operation point set of parameters so that the design criteria, discussed in Section 4.2 are simultaneously met. Doing so, the following strategy will be followed:

- Determination of the drift gas mixture, its components and their fractions, Section 5.1.
- Determination of the gap between the anode wire grid and the pad plane such that a charge sharing between two to three adjacent pads of width $W = 7.5$ mm is accomplished, Section 5.2.
- Determination of an anode voltage and a wire pitch intervals, such that the gas gain in the chamber is within the anticipated gain interval dG between 3000 and 8000, Section 5.3.
- Studying the wire sag within the determined intervals and restricting them, such that the anode and cathode wire sagitta are minimized, Section 5.4.
- Settling the rest of the parameters by minimizing the gain variation such that it is within tolerances level of $\Delta G/G \simeq 15\%$, Section 5.5.
- Determination of the parameters of the voltage divider (field cage) and smoothen the drift field at the edges of the chamber, Section 5.6.
- Studying the ions signal in the chamber and its influence on the drift field, Section 5.7.
- Studying the isochron properties of the chamber with the determined parameters, Section 5.8.

The simulations were carried out with two programs:

- MAGBOLTZ [136]: This program computes electron-transport properties for a large variety of gas mixtures. The calculations are based on the numerical solution of the *Boltzmann transport equation.*
- GARFIELD [137]: This program simulates two and three dimensional drift chambers. With an interface to MAGBOLTZ, it computes electron and ion drift lines as well as drift and arrival time distributions in a gas mixture. In addition it computes the signals on different electrodes in a chamber and the electrostatical and gravitational forces acting on each component of a chamber.

optimized parameters	
gas mixture	Xe/CO_2 (85:15)
anode wire voltage U_{an}	1.5 kV
drift cathode voltage U_{dft}	- 2.1 kV
anode pitch p_{an}	5 mm
cathode pitch p_{cath}	2.5 mm
anode tension T_{an}	45 g (0.45 N)
cathode tension T_{cath}	120 g (1.2 N)
anode material	Au/W
cathode material	Cu-Be
wire gap h	3.5 mm
last resistor R_{last}	850 kΩ
number of resistors	6

fixed parameters	
cathode wire voltage U_{cath}	ground
chain resistors R	1 MΩ
drift velocity v_d	1.5 cm/μs
relative gain variation $\Delta G/G$	15%
gain interval dG	3000-8000
anode diameter d_{an}	20 μm
cathode diameter d_{cath}	70 μm
wire length L	120 cm
pad width W	7.5 mm
mag. field B	0.4 T

Table 5.1: Parameters of the ALICE TRD read out chamber.

The simulations, presented in this chapter, and measurements [127, 128, 138, 139], have lead to the *nominal parameters set* given in Table 5.1. If not explicitly specified, these are the parameters of the simulation environment. "Fixed" parameters are given by the ALICE experiment, by the space available for a TRD chamber, by the electronics capability, or practical aspects. In the simulations the largest module with a length of 120 cm is considered. This worse case length is taken to be fixed. The anode wire diameter of $d_{an} = 20$ μm and that of the cathode wires, $d_{cath} = 70$ μm are also taken to be fixed. At the end of Section 5.5 this diameters choice will be justified.

5.1 Gas Mixture and its Properties

The gas mixture is the main part of any drift chamber where the drift of ionization electrons and the amplification of the signal take place.

Under the influence of the electric field $E = |\vec{E}|$ and the magnetic field $B = |\vec{B}|$, liberated electrons start drifting towards the anode wires. The drift behavior of the electrons is described by the gas drift properties: drift velocity $v_d = |\vec{v}_d|$, Lorentz angle α_L, longitudinal and transverse diffusion D_l and D_t, and the electron attachment. These quantities are

functions of E, B, the gas composition, the temperature T, and the pressure p. In this section the relevant dependencies of the properties mentioned above on the electrostatical and geometrical parameters of the TRD drift chamber will be discussed.

Usually the electric drift field is normalized to the gas density, n, which is a function of the pressure, p, and the temperature, T, of the gas: $E/n = ETp_0/T_0p$ where p_0 and T_0 are the pressure and the temperature in a reference situation. Since the TRD will be operated at atmospheric conditions, $p_0 = 760$ Torr and temperature $T = 300$ K, simulations on the drift properties will be carried out under these conditions. E/n is replaced by E. To avoid fluctuations in T and p a sufficient cooling system is developed to compensate any heat generated from the electronics units of the chamber.

5.1.1 Electron Transport Properties

Drift velocity:
According to the classical theory of electron drift in gases, the movement of free electrons drifting in a gas volume is a random process. The basic of this behavior is the electrons scatter off the molecules in the gas. The direction which an electron takes after a random collision can be considered to be uncorrelated to its direction before the collision. The number of collisions, N, within a drift distance y is related to the average drift velocity (diffusion velocity) v_0 via the mean time between two collisions, τ:

$$N = \frac{y}{v_0\tau}. \tag{5.1}$$

τ is given by $\tau = (m/e)\mu$, where e and m are the electron charge and mass, and μ is the electron mobility in the gas. The electron velocity, v_0, is non-directed and its average energy is given by the temperature of the gas; $\epsilon = 3kT/2$, with k the Boltzmann constant. This energy is referred to as the *thermal limit.*

Under the influence of an electric field, E, a free electron possesses a macroscopic mean drift velocity, v_d, along the field direction. v_d is the average drift velocity, $\langle v \rangle$, which is determined by the average drift distances $\langle y \rangle$ over τ:

$$v_d = \langle v \rangle = \frac{\langle y \rangle}{\tau} = \frac{e}{m} E\tau = \mu E. \tag{5.2}$$

Due to the influence of E the electron extracts extra energy. This energy is, on average, lost in collisions through recoil or excitation such that an equilibrium is reached between the energy gain in the field and the energy loss in the collisions.

If in addition to E a magnetic field is applied with a component perpendicular to $\vec{E}$, $\vec{v}_d$ is not parallel to $\vec{E}$ anymore. The electron will have a velocity component in the direction of $\vec{E} \times \vec{B}$ and its trajectory forms the so-called *Lorentz angle*, α_L, with the electric field. The tangent of α_L is given by the ratio of the transverse component of the drift velocity, $v_d\perp$, to the longitudinal one, $v_d\|$, which translates in the cyclotron frequency of the electron, $\omega = (e/m)B$, and the mean time between two collisions, τ:

$$\tan \alpha_L = \frac{v_{d\perp}}{v_{d\parallel}} = \omega\tau. \tag{5.3}$$

Considering the case where both fields are perpendicular to each other, as the case in the TRD chamber, the macroscopic directed drift velocity is given by [117]:

$$v_d = \frac{\mu E}{\sqrt{1+\omega^2\tau^2}}, \tag{5.4}$$

It is related to the random drift velocity v_0 via τ and the fractional energy loss per collision λ [118].

$$v_0^2 = \left(\frac{1}{\lambda} - 1\right) 2v_d^2 + \frac{2kT}{m}. \tag{5.5}$$

τ can be expressed through the effective cross-section of the collision σ_{col}, the number density n, and the non-directed velocity v_0:

$$\frac{1}{\tau} = n\sigma_{col}v_0. \tag{5.6}$$

λ takes values between zero and unity. Approaching zero, the equilibrium energy is mainly caused by the electric field. The thermal energy can be neglected and Equation 5.5 gets the form:

$$v_0^2 = \frac{2}{\lambda}v_d^2. \tag{5.7}$$

This is the case in the so-called *hot gases* such as noble gases which are commonly used in particle detectors.
Approaching unity, λ causes v_0 to approach the thermal limit:

$$v_0^2 = 2kT/m. \tag{5.8}$$

This is the case in the so-called *cold gases* such as CO_2 and organic compounds. Their vibration and rotational degrees of freedom enhance λ. Therefore the addition of a cold gas (quencher) fraction to a hot gas (noble gas) increases the macroscopic drift velocity v_d of free electrons and decreases the diffusion velocity v_0 at a given drift field, temperature, and pressure as can be seen in Equation 5.7.

Diffusion:
The total electrons current in the drift gas is given by the sum of the drift current which is characterized by v_d and the diffusion current which is characterized by the random motion, i.e. by v_0. In a simple approximation the electrons distribution is isotropic. This means that a point-like cloud of electrons at time $t = 0$ will create a Gaussian density distribution after a time t through which it has drifted the distance y:

$$\frac{\mathrm{d}N}{N} = \frac{1}{\sqrt{4\pi Dt}} \exp\left(-\frac{y^2}{4Dt}\right) \mathrm{d}y. \tag{5.9}$$

Herein is dN/N the fraction of the electrons in the cloud which is located within the distance dy after the electrons have drifted a total distance of length y.
From Equation 5.9 the linear diffusion[1] width of the distribution is given by:

$$\sigma_y^2 = 2Dt. \tag{5.10}$$

The proportionality factor D is the *diffusion coefficient*. σ_y represents the width of the point-like cloud after it has drifted a certain distance, usually 1 cm.

Without any field influence the diffusion coefficient is related to the mean time between two collisions τ via the random velocity v_0 and the mean free path l_0 [118]:

$$D = \frac{l_0^2}{3\tau} = \frac{v_0 l_0}{3} = \frac{v_0^2 \tau}{3} = \frac{2}{3}\frac{\epsilon}{m}\tau, \tag{5.11}$$

with $\epsilon = 3kT/2$.
If an electric field is applied, Equation 5.10 gets the form:

$$\sigma_y^2 = 2Dt = \frac{2Dy}{\mu E} = \frac{4\epsilon y}{3eE}, \tag{5.12}$$

and the diffusion coefficient is given by:

$$D = \sqrt{\frac{mv_0^2}{eE}}. \tag{5.13}$$

With Equations 5.4 and 5.5, in the thermal limit D has the form:

$$D = \sqrt{\frac{2kT}{eE}}, \tag{5.14}$$

and in hot gases, where kT can be neglected, D follows (with a magnetic field):

$$D = \sqrt{\frac{2}{\lambda}\frac{eE\tau^2}{m(1+\omega^2\tau^2)}} \tag{5.15}$$

The field cancels the assumed isotropy. The diffusion in the direction of the E-field, D_l, has a different value than the diffusion perpendicular to it, D_t. This anisotropy is caused by the different mobility of the electrons located at different positions inside the electrons cloud, mainly the difference between the leading and the trailing edges. The electron energy eE/m dependence on the mobility, makes all properties which are related to it, be functions of the electron position in the cloud. Therefore the electron energy should be kept as small as possible at high drift field as seen in the Equation 5.12. This reduces both, D_l and D_t. Depending on the drift gas and the drift field, D_t could be larger or smaller than D_l.

The magnetic field alters the transverse diffusion and reduces it such as:

$$D_t(B)/D_t(0) = 1/(1+\omega^2\tau^2),$$

[1]The volume diffusion is $\sqrt{3}\sigma_y$.

but it does not affect D_l:

$$D_l(B) = D_l(0).$$

Electron attachment:
Encountering the molecules of the gas, free electrons could be captured by them, either through electro-affinity or molecular dissociation. This, electron attachment depends in first order on the mean energy of the free electron, eE/m. If this energy exceeds the threshold for molecular dissociation (4.6 eV for $O_2 \rightarrow O^+ + O^-$, 5.5 eV for $H_2O \rightarrow H^+ + OH^-$ and between 4 and 10 eV for CO_2), they are easily absorbed by the positive ions and a rapid increase of the attachment cross section is observed with increasing electric field. This process dominates therefore in the amplification region where the field is very high.

In noble gases and in most organic molecules negative ions can only be formed at collision energies of several electron-volts (which is higher than the energy reached during most of the drift processes in drift chambers). Nevertheless there are some molecules that are capable of attaching electrons at much lower electron energies. The largest electro-affinities are found with the halogenides and oxygen, therefore, contamination with air and water should be minimized, but also drift gas components like CF_4 and CO_2 can attach free electrons. The latter will be used in the TRD drift chamber.
Due to electron attachment the number of electrons falls exponentially with the drift time, the pressure p, and the partial pressure of the contamination p_{cont}:

$$N(t) = N_0 \cdot \exp\left(p \cdot p_{cont} \cdot R_{att} \cdot t\right), \tag{5.16}$$

where R_{att} is the electron attachment coefficient.

5.1.2 Gas Mixture in the TRD Drift Chamber

The essential component in a drift chamber is usually one of the noble gases such as argon, xenon or krypton. The second component is the quencher which could be any other gas with large number of degrees of freedom (cold gas), such as poly-atomic or organic compounds or pure gases.

In the TRD chamber the main criteria of the drift gas is the ability to absorb as much as possible of TR photons in the X-ray region (between 5 and 30 keV). As main component, although argon is inexpensive, xenon and krypton are much better suited due to their better ionization properties. The first ionization potential of xenon (Krypton) is at 12.1 eV (14.0 eV) and reaches a ionization cross section of $6 \cdot 10^{-16}$ cm^2 ($4 \cdot 10^{-16}$ cm^2) for electrons with an energy of about 100 eV [117].
Figure 5.1 shows that xenon possesses better X-ray absorption than krypton. The absorption length for a 10 keV photon is about 10 mm in xenon and 40 mm in krypton. Due to saturation effects in the radiator, the achievement of the anticipated pion separation efficiency requires several TRD layers. Combined with the limited space available for the TRD in the ALICE central barrel, the saturation effect makes **xenon the only possible candidate to the main component in the TRD drift gas mixture**.

The second component is the quencher gas. As denoted in Subsection 3.3.2, it must have many degrees of freedom with a large photo absorption coefficient to enable a stable amplification through absorbing photons which escape the avalanche and to avoid photoelectric effects at the surfaces of the surrounding electrodes.
Without a quencher the drift velocity would be very low, and a very high drift voltage would be required to achieve the anticipated drift velocity in a hot gas like xenon, see Equation 5.7. This would increase the electrostatic instability and encourage discharge in the chamber, and the inhomogeneity of the drift field. Furthermore, according to Equation 5.15 the quencher with higher fractional energy loss per collisions, λ, decreases the diffusion in the gas and improves the position resolution.

For the TRD, organic gases such as CH_4 are excluded, not only because of their flammable properties[2] but also because they accelerate ageing effects. Nitrogen compounds are excluded because nitrogen is able to capture neutrons, which will be abound at LHC, and emit photons of about 10 MeV. For the previous two reasons pure hydrogen is also excluded and oxygen because it causes electron loss through electron attachment. Carbon dioxide does not exhibit many of the properties listed above and it enables a larger fractional energy loss per collision (for Xe (CO_2) λ is on the order of $10^{-6}(10^{-1})$), therefore it accelerates the gas in small amount. As a consequence, **CO_2 has been chosen to be the quencher component in the TRD gas mixture**.

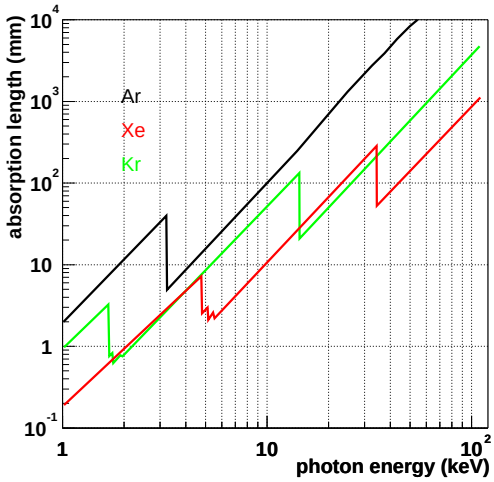

Figure 5.1: Absorption length of photons in xenon, krypton and argon as a function of photon energy. Only xenon is able to absorb photons with the energy of 10 to 30 keV within the first 10 to 20 mm.

Once the mixture is established, the right proportions of both components are to be fixed such that the anticipated drift velocity of 1.5 cm/μs is attained at a low drift field. In addition, the gas mixture must exhibit a low transverse diffusion in order to enable the anticipated position resolution of 400 μm. It should posses a low electron attachment coefficient in order to avoid capturing ionization electrons, and a high ion mobility to reduce pile-up in the signal and to keep the Lorentz angle, α_L, as small as possible, see Equation 5.3.

In the following it will be shown that the Lorentz angle, α_L, is the main criterium after which the CO_2 content in the mixture will be fixed. Since it depends on the drift velocity, Equation 5.3, the latter will be discussed first as a function of the drift field. Once the composition is fixed, it will be shown that the chosen ratios are characterized by adequate

[2]Meanwhile the usage of such gas compounds is subject to restrictions at CERN because of the mentioned flammability.

diffusion and electron attachment coefficients. Notice that the depiction in Section 5.1.1 is based on simplifications. MAGBOLTZ calculations follow realistic considerations.

In addition to the operation gas mixture, some contaminations of other contents such as oxygen and water vapor are not avoidable. They can come from leaks in the gas system, from impurities in the gas bottle, or from the gas system materials where the gas streams. They influence the drift velocity and the attachment. In the following simulations these contaminations will not be considered. There influences on the drift properties in the chamber will be discussed at the end of this section in terms of measurements in TRD prototypes.

5.1.3 Drift Velocity and Drift Field

Figure 5.2 shows the calculated drift velocity as a function of the drift field E for different Xe/CO_2 mixtures. For all CO_2 contents the drift velocity rises at low E-values and it falls at high E-values. The maxima (saturation regions) appearing in between, depend almost linearly on the CO_2 content in the mixture.

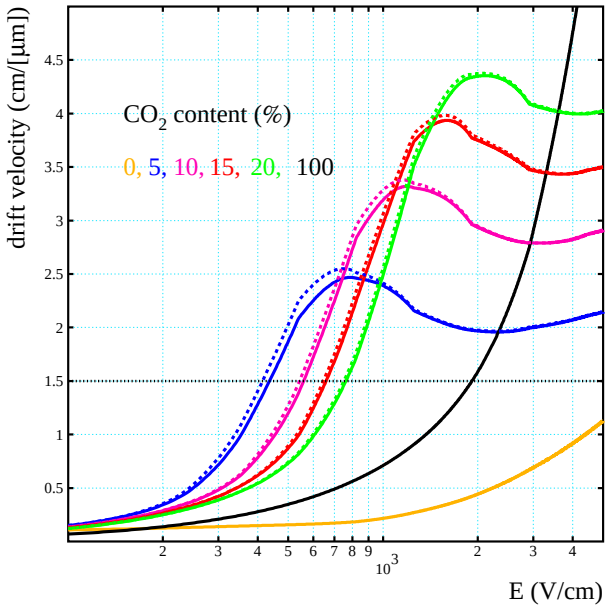

Figure 5.2: Drift velocity for different Xe/CO_2 gas mixtures. Solid lines represent v_d with a magnetic field of 0.4 T perpendicular to the electric field and the anode grid. The curves show the v_d component parallel to the electric field. The dashed lines are the results of simulations without a magnetic field. Notice how the presence of the magnetic field reduces the drift velocity at electric fields below 2 kV/cm. The reason is the electrons movement in a helical trajectories.

According to Equations 5.6 and 5.7, the drift velocity depends inversely on the effective cross-section, σ_{col}. As a function of the electron energy, σ_{col} has a minimum value at about 0.5 eV in xenon [140][3]. This is the point where the maximum in the v_d-E curve appears.

[3]This is the so called Ramsauer minimum. It occurs at an energy of about 0.25 eV, 0.5 eV, and 0.65 eV for argon, xenon, and krypton respectively [118, 140].

In pure xenon (yellow line in Figure 5.2) the drift velocity is very low at electric fields below 4 kV/cm and it increases rapidly with any small supply of CO_2 to the mixture. At a field of 0.7 kV/cm the drift velocity in a mixture with 5% CO_2 is 24 times higher than in pure xenon, whereas at a CO_2 fraction of 20%, v_d is 12 times higher.
The additional CO_2 degrees of freedom mean an increase in the fractional energy loss per collision in the gas mixture, as a consequence of that the maximum of the drift velocity curve goes to higher drift field values.

Regarding the drift velocity, the most preferable operation point is within a v_d-saturation region at one of the extrema in the v_d-curve. Within this region only minimal v_d fluctuations occur if the drift field gradient grows. This guarantees coordinate measurements in the chamber which are independent of the unavoidable E gradients.

Because the minima of all mixtures are located at too high drift fields they are excluded and the same is true for the maxima. The blue line presents the drift velocity with a CO_2 fraction of 5%. With about 2.5 cm/μs its maximum is much higher than the anticipated value of 1.5 cm/μs. Since the maximum point grows with the CO_2 content, only the left-hand side of it can be considered to determine an operation point. This choice means the loss of the stability condition and therefore requires a good control on the drift field and such that its gradients are minimal. The smoothness of the field at crucial edges of the chamber is controlled by a field cage which will be discussed in Section 5.6.

For CO_2 content of 5%, 10%, 15%, and 20% the required drift velocity of 1.5 cm/μs is achieved with fields of 0.43, 0.58, 0.67, and 0.8 kV/cm respectively. The 5%-mixture requires low drift field and guarantees an electrostatically stable chamber. However according to Equation 5.15, this means also higher diffusion coefficient and, much more important, a higher Lorentz angle as can be seen in Equations 5.3 and 5.6.

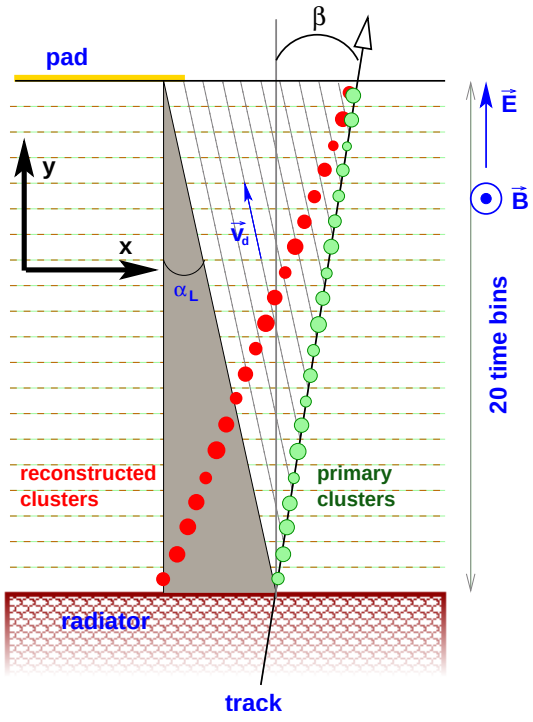

Figure 5.3: Lorentz angle leads to a faked angular reconstruction. To correct for this error, a precise knowledge on α_L is required.

5.1.4 Lorentz Angle

The ALICE magnetic field is perpendicular to the surface spanned by the electric field in a TRD chamber and its wire grids. According to Equation 5.3, the ionization electrons form the Lorentz angle, α_L with the electric field $\vec{E}$, causing the so-called $\vec{E} \times \vec{B}$-effect. The Lorentz angle is tainted with disadvantages: firstly, the effect delays the electrons and

reduces the drift velocity as seen from Figure 5.2 and Table 5.2. The arrival times of the clusters in a track segment are spread out. However the drift velocity variation which is correlated to this delay is lower than 3.5% for $0° \leq \alpha_L \leq 8°$. Compared to time variation which originates from non-isochronity, this value can be neglected, see Figure 5.23.
Secondly, the Lorentz angle fakes the reconstructed position of a hit leading to a deterioration of the point and momentum resolution, as illustrated in Figure 5.3. Therefore a priory knowledge of the Lorentz angle is very important to correct for it by the detector calibration.
Thirdly, the Lorentz angle influences also the primary charged particles. The reconstructed transverse momentum at a given magnetic field, drift distance, and drift depth, is proportional to $1/\sin(\beta)$, where β is the incidence angle relative to the normal incidence to the wire grids. Any inclination of the primary particle worsens the position and angular resolution, since it spreads the signal over more than three adjacent pads, see below. The Lorentz angle can degrade the resolutions (if it adds to the tilting angle). Therefore it is very important to keep it as low as possible.

Furthermore the TRD trigger concept is designed to work with charge sharing among three neighboring pads. If the charge is shared between more pads, the trigger capability will be degraded. Such a situation appears if the inclination of a track with a transverse momentum of 3 GeV/c, exceeds a total value of $\beta_{tot} = 28$ degrees [130]. In the reference it is shown that the trigger concept will still be valid if the contribution of the Lorentz angle to β_{tot} is less than 14 degrees.

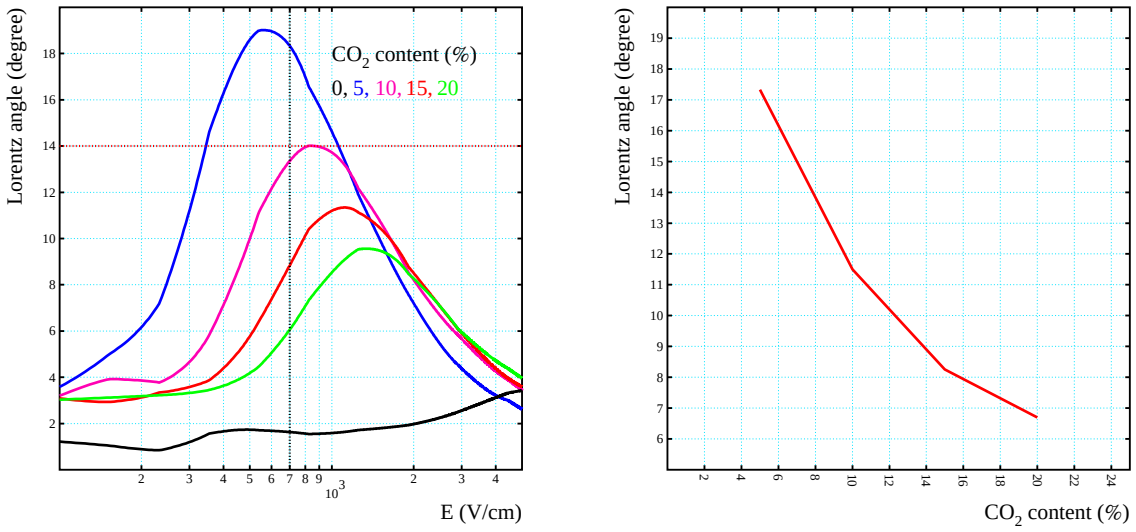

Figure 5.4: Left panel:Lorentz angle α_L as a function of the drift field and the CO_2 content in the gas mixture. At reasonable field values only CO_2-fractions above 10% guarantee a low α_L. Right panel: α_L as a function of the CO_2 content at fields which correspond to a drift velocity of 1.5 cm/μs.

Equation 5.3 indicates that the Lorentz angle can be reduced by reducing ω and/or τ. $\omega = eB/m$ depends only on the magnetic field and therefore it is fixed by the ALICE field. τ is proportional to the electron mobility, which can be reduced by increasing the drift field (for given particle energy and pressure). But for a given gas mixture, this implements a decrease of the drift velocity which would increase the trigger latency and deteriorates its capability.
Another possibility to reduce τ is to increase the CO_2 content in the mixture. The left panel of Figure 5.4 shows the Lorentz angle as a function of the drift field and the CO_2 content. Obviously neither the 5%- nor the 10%-mixture are suitable for the TRD since they are correlated with a Lorentz angle of about 18 and 12 degrees respectively. The first value exceeds the tolerated of 14 degrees and the second is close to it as can be seen in the left panel of Figure 5.4.

The right panel of Figure 5.4 shows the Lorentz angle as a function of the CO_2 content at drift fields corresponding to a drift velocity of 1.5 cm/μs.
With α_L of about 8.5 degrees, the mixture with 15% CO_2 content was chosen to be the operation gas mixture in the TRD chamber.

To summerize: the required high ionization potential of the drift gas and the space available for the TRD in the ALICE central barrel lead to the choice of xenon as the main component of the drift gas mixture. The second component was chosen to be CO_2 which does not exhibits disadvantages like flammability and ageing effects. To reduce the Lorentz angle in the chamber a CO_2fraction of 15% was chosen. It is still to be verified that this choice is justified in terms of diffusion and electron attachment.

5.1.5 Diffusion and Electron Attachment

Diffusion:
The position resolution of the chamber is determined by the distribution width of the electrons in a cloud, σ_y. Equation 5.12 shows that σ_y is proportional to the drift distance y. Since y is short in a TRD chamber, both the transversal and the longitudinal diffusion are only on the order of a few hundred microns for all gas mixtures studied here.

The left panel of Figure 5.5 shows both, D_l and D_t, as functions of the drift field in the adopted gas mixture Xe/CO_2 (85:15). The highest longitudinal diffusion is about 280 μm for 1 cm at a field value of about 750 V/cm. and the highest transverse diffusion is about 340 μm for 1 cm at a field of 3000 V/cm. Both field values occur in the amplification region which spreads the avalanche. At most, this leads to a wider spread of the avalanche over adjacent pads. In the drift region, indicated by the dotted vertical line, D_l is about 260 μm for 1 cm. For the whole drift distance, D_l is $260 \times \sqrt{3} \simeq 450$ μm for 3 cm. More important in the TRD chamber is D_t with a value of about 185 μm for 1 cm (320 μm for 3 cm). To evaluate the contribution of these values to the position resolution in the chamber, consider the number of the electrons which reach the wires under one pad for 1 cm drift distance, n_e. In xenon this number is about 115/cm and in CO_2 it is 50/cm [140]. In the TRD gas mixture, it is a linear superposition of both,

$0.15 \times 50 + 0.85 \times 115 \simeq 105$. The position resolution is on the order of $D/\sqrt{n_e}$ which translates in a longitudinal contribution around 25 μm and a transverse around 15 μm to the position resolution in the chamber.

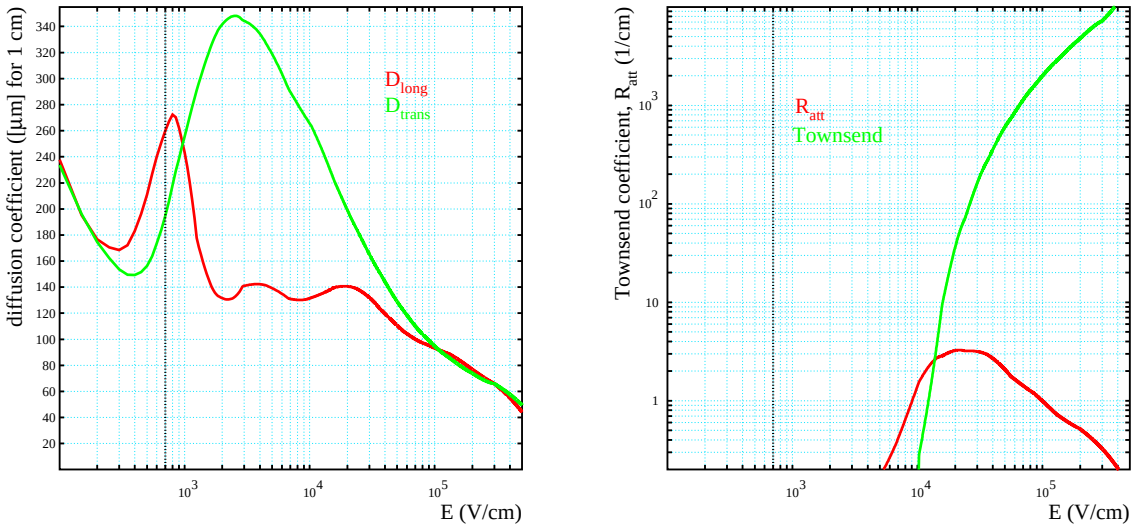

Figure 5.5: Left panel: Longitudinal and transverse diffusion as functions of the electric field in a Xe/CO_2 (85:15) mixture. Right panel: Electron attachment and Townsend coefficients in the same mixture.

Attachment:
As in all noble gases, the attachment coefficient, R_{att} defined in Equation 5.16, is vanishing in xenon. But CO_2 can attach electrons if their energy is between 4 eV and 10 eV [140]. The basic argument are the large number of low-lying excitation levels of CO_2. In the chosen gas mixture, these energy values are reached at a field values larger than 5 kV/cm as shown in the right panel of Figure 5.5. Therefore the electron attachment is negligible in the drift region. This is true for all gas mixtures studied here.

The highest attachment of about 2.5 cm^{-1} is at a field of about 22 kV/cm in the amplification region which means that an avalanche can lose some of its electrons but no signal will be lost since the Townsend coefficient overrules the attachment coefficient. The region where the attachment coefficient is dominant (5.5 kV/cm $< E <$ 11 kV/cm), spans over about 180 μm which makes the losses very low.

The contributions of contaminations in the gas mixture to the attachment will be studied in Subsection 5.1.6.

Table 5.2 shows calculated values of the diffusion and attachment coefficients of different gas mixtures at the nominal ALICE magnetic field of 0.4 T and the drift velocity com-

ponent in the electric field direction of 1.5 cm/μs. Values at vanishing B-field are also indicated in the table[4].

B field (T)	0.0				0.4				
CO_2 fraction (%)	5	10	15	20	0	5	10	15	20
attachment ($\frac{1}{cm}$)	0.0 for fields below 10 kV/cm.								
long. diffusion (μm for 1 cm)	411	331	252	236	280	382	311	253	210
trans. diffusion (μm for 1 cm)	350	238	185	158	399	365	239	186	160
$\Psi_L(^\circ)$	0	0	0	0	2.21	17.33	11.49	8.26	6.7
E_d ($\frac{\mathrm{V}}{\mathrm{cm}}$)	414	543	646	751	6809	436	560	659	763
v_d ($\frac{\mathrm{cm}}{\mu\mathrm{s}}$),at $E_d = 700\ \frac{\mathrm{V}}{\mathrm{cm}}$	2.53	2.36	1.75	1.32	0.49	2.42	2.24	1.67	1.29

Table 5.2: Electron Attachment, longitudinal and transversal diffusion coefficients, Lorentz angle, and drift fields at the required drift velocity of 1.5 cm/μs in several Xe/CO_2 mixtures. The last horizontal cell gives the drift velocity in the gas mixtures at a drift field of 0.7 kV/cm.

5.1.6 Measured Properties of the Gas Mixture

All the values of the gas mixture properties discussed above, are only valid in contamination free mixtures. In reality leaks in the gas system cannot be excluded. Due to the large volume of the TRD and the high costs of xenon, the drift gas will be recycled. For the gas recirculation a recycling system was designed. Nevertheless a certain fraction of contamination (O_2, N_2, H_2O) comes through into the system through leaking. Oxygen and water vapor which enhance the electron attachment and reduce the drift velocity [118], are easy to be filtered out, whereas Nitrogen is not easy to remove with known methods. Its filtering leads to additional loss of xenon and to composition modification.

Throughout the operation time nitrogen piles up and its content in the system increases with time. In eight months of operation the nitrogen content rises up to 8% [138]. This can be cryogenically distilled and removed during shut down periods with moderate loss of xenon.

During the running time the increasing amount of nitrogen influences the drift velocity. This could be crucial since the drift velocity in a TRD chamber does not lie within a saturation region. The ALICE TRD Collaboration carried out systematic measurements on drift velocity in different argon- and xenon based mixtures [138]. For the Xe/CO_2 (85:15)-mixture it is found that at drift fields larger than 1.2 kV/cm the drift velocity changes by 12% when going from nitrogen free mixture to a nitrogen content of 20% [5]. For drift fields below 0.8 kV/cm the influence of the same range of nitrogen contamination

[4]The anticipated drift velocity of 1.5 cm/μs is achieved at adrift field of 660 V/cm. With $E = 700$ V/cm the drift velocity is about 1.67 cm/μs.

[5]A Xe/CO_2 (85:15) mixture with 20% N_2 content results in Xe(68%),CO_2 (12%), and N_2(20%)

on the drift velocity is negligible. Therefore no crucial drift velocity variation is expected in a TRD chamber with a drift field of 700 kV/cm.

Measurements were also carried out to investigate the influence of the particle incidence angle β on the position and angular resolutions in a TRD drift chamber [139]. The tests were carried out with and without applying a magnetic field in the nominal TRD drift gas mixture.
Without a magnetic field, the deterioration of the position resolution is below 8% when increasing the incidence angle from zero to 15 degrees (relative to the beam which is perpendicular to the wire grids). The angular resolution worsens by almost 35% but is still below 1 degree. The resolutions behave similar for pions and electrons. Due to the emission of transition radiation, the position resolution for electrons is not as good as that of pions, see Chapter 7.
In the measurements the position resolution is found to be better than 300 μm at an incidence nominal incidence angle and degrades to about 400 μm at an incidence angle of 15 degrees. No significant changes in the angular resolution were observed when increasing the magnetic field from 0 to 0.56 T.

In [128] results on the space charge effect in an ALICE TRD chamber are reported. It is found that the space charge effect influences the signals of pions and electrons in the drift region. Going from an incidence angle of $\beta = 0$ degrees to $\beta = 15$ degrees, the space charge effect disappears. The effect is larger at higher gas gain and degrades the pion rejection power of the TRD. Therefore the detector should be operated at the lowest possible gas gain which enables a signal-to-noise ratio between 25 and 30.

5.2 Pad Response Function

The measurement of an avalanche coordinate along an anode wire is reconstructed by the pulse heights on the pads. In order to locate the center of the avalanche, one requires that the induced signal is distributed between more than one pad. On the other hand the number of pads should be few enough to enable reasonable S/N-ratio. The ideal choice of the number of pads on which the charge is distributed, is therefore two to three. The charge distribution among those pads is described by the *Pad Response Function* (PRF).

Neglecting the influence of the wires, the total induced charge density on a cathode plane is given by [118]:

$$\rho(x) = -\frac{\lambda}{2d} \cdot \frac{1}{\cosh(\pi x/h)}, \tag{5.17}$$

where λ is the positive charge density in an avalanche and h is the wire gap. The pad response function is the integral of ρ over the pad area [118]:

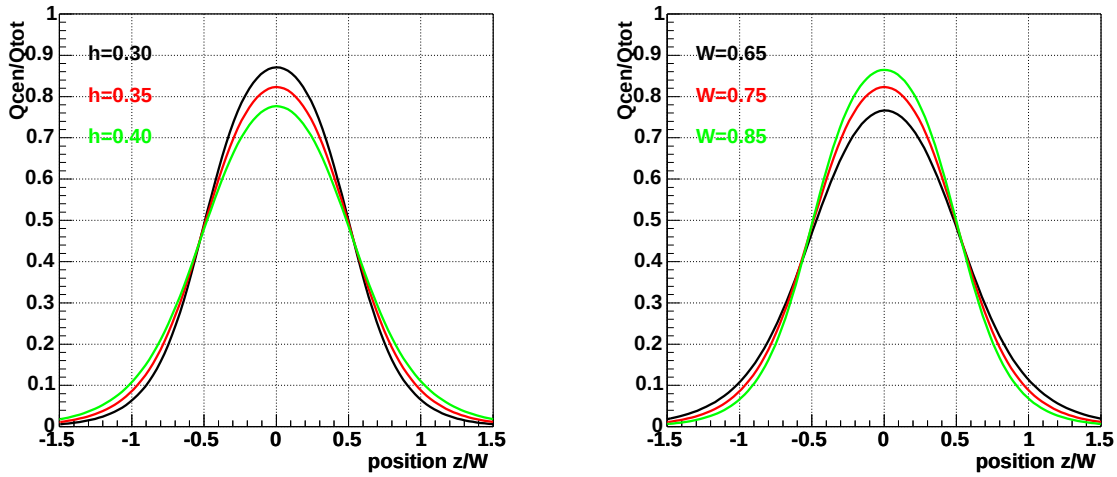

Figure 5.6: Left panel: Simulated PRF as a function of h at $W = 7.5$ mm. Right panel: PRF as a function of W at $h = 3.5$ mm.

$$\mathrm{PRF}(x) = \int_{x-W/2}^{x+W/2} \rho(x')\mathrm{d}x', \tag{5.18}$$

with W the pad width. The determination of the PRF and its dependence on the track parameters (wire geometry) and on the gas properties is the first important step to be taken when designing a chamber with pad readout. Two requirements are to be considered: First, Equation 5.18 shows that the PRF depends on both, the gap, h, and the pad width, W. Thus it is important to choose the ratio W/h such that the signal is spread on two or three adjacent pads. Considering the three pads case, an avalanche induces a large signal on the center pad and two smaller signals on the adjacent ones.

In the ALICE TRD it is aimed to have about 80% of the signal on the central pad and 10% on each of the other two. The large surface of the detector makes the total number of pads very large which requires that many electronics channels. Due to financial aspects (also practical ones in terms of the available space), this number should be minimized without reducing the S/N-ratio significantly. These requirements determined the pad width, W. The radial composition of the TRD (y-direction) causes discrepancies between the pad widths in different layers. Going from the innermost to the outermost layer, the pad width grows like $W = 6.65 + (n-1) \times 0.31$ mm, where $n = 1, ..., 6$ is the layer number. with pad lengths between 7.5 cm and 9.0 cm and the total TRD active area of about 720 m^2, this leads to a total number of pads (channel) of 1.181.952.
For an approximated average width of 7.5 mm the calculated PRF is shown in the left panel of Figure 5.6 as a function of the hit distance from the center of the central pad in units of W. The calculations were carried out following [141] for three h-values. The results obviously favor a gap value of 3.5 mm. A lower value increases the amount of induced charge on the central pad up to 88% for the averaged width and up to 90% in the outer most layers with $W \simeq 8.5$ mm. A larger h-value of 4 mm leads to the opposite effect. It reduces the induced charge on the central pad down to approximately 71% in

the innermost layers with $W \simeq 6.65$. The right panel of Figure 5.6 shows the PRF as a function of W at $h = 3.5$ mm.
The discussion above shows that the PRF for the given pad width(s) requires **a wire gap of $h = 3.5$ mm**.

The second requirement on the PRF is its linearity which will be discussed in Section 7.5.1.

5.3 Gas Gain

5.3.1 Amplification Factor

The characteristic term of the amplification region is the amplification factor A, which is ruled by the *first Townsend coefficient*, α. α is the number of ion-electron pairs created in an avalanche per unit length:

$$A = \frac{\mathrm{N}(y)}{\mathrm{N}(y_0)} = \exp\left(\int_{r_{th}}^{r} \alpha(y)\mathrm{d}y\right) = \exp\left(\int_{E(r_{th})}^{E(r)} \frac{\alpha(E)}{\mathrm{d}E/\mathrm{d}y}\mathrm{d}E\right). \tag{5.19}$$

$$\alpha = \sigma_{ion} \times \frac{N_A}{V_{\mathrm{mol}}}, \tag{5.20}$$

with N_A the Avogadro number, V_{mol} is the mole volume, and σ_{ion} is the ionization cross section. At a given ionization cross section the Townsend coefficient is a characteristic quantity of the drift gas[6]. In Figure 5.7, MAGBOLTZ calculations of the Townsend coefficient for several (Xe/CO_2) mixtures are shown as a function of the electric field.
Under the influence of an increasing electric field in the vicinity of an anode wire, a number of primary electrons at point y_0, $N(y_0)$ is amplified to $N(y)$ at point y after traveling a distance $y - y_0$:

The integral in the exponent of Equations 5.19 reflects the dependence of α on the amplification field, i.e. the distance from the anode wire. The amplification factor A is the constant which one gets by integrating between r_{th}, the point just where the field is high enough to produce secondary electrons, i.e. where the avalanche starts, and the anode wire radius, r:

Equation 5.19 shows the dependence of A on the gas mixture and the electrostatic parameters (through the Townsend coefficient) and the geometry of the chamber (wire diameter

[6]From now on the appellation *first* will be abandoned. For $A > 10^6$, which is called the streamer region, the contribution of excitation photons to the ionization is accounted for through the *second Townsend coefficient* γ. The amplification factor is modified to $A_\gamma = A/(1 - \gamma A)$. For more details see Ref. [118].

and r_{th} which is determined by the distances of other electrodes from the anode wire). In terms of these chamber parameters the amplification factor is given by [117]:

$$A = \exp\left[2\sqrt{\frac{kLC\mathrm{U}_a r}{2\pi\epsilon_0}}\left(\sqrt{\frac{\mathrm{U}_a}{\mathrm{U}_{th}}} - 1,\right)\right] \tag{5.21}$$

where C is the capacitance per unit wire length. In a MWPC, C can be approximated to:

$$C = \frac{4\pi\epsilon_0}{2\left(\frac{\pi h}{p} - \ln(\frac{2\pi r}{p})\right)}, \tag{5.22}$$

with p and h the wire pitch and gap respectively. L is the gas molecule number per volume unit ($N_A/V_{\text{molecule}} = 2.69 \times 10^{19}/\text{cm}^3$) at atmospheric conditions, $k = \frac{\alpha e}{L\epsilon}$ is a gas dependant constant where ϵ is the averaged electron energy between two collisions, and e is the elementary charge. U_{th} is the voltage at the point r_{th}.

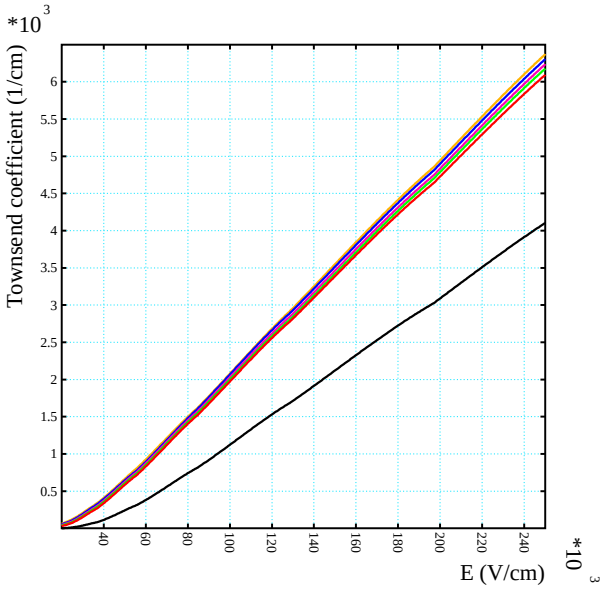

Figure 5.7: Townsend coefficient for several Xe/CO_2 gas mixtures. From top to bottom the curves present a CO_2 fraction of 5% (blue), 10% (purple), 15% (green), 20% (red), and 100% (black).

5.3.2 Amplification Factor in the ALICE TRD Chamber

Equations 5.19, 5.21, and 5.22 express the gas gain amplification factor A in terms of α, the electrostatical, and the geometrical parameters of the anode wire on which the amplification factor depends. α is determined by the gas mixture. The other parameters will be determined in the following.

Figure 5.8 shows the gas gain as a function of the anode wire voltage and the wire gap h. The highlighted area indicates the gain interval dG within which the gas gain in a TRD chamber is to be fixed. For the determined gap of 3.5 mm, dG is achieved within

an anode wire voltage interval between 1.51 and 1.61 kV.
For comparison the same calculations for gaps of 2.5 and 3 mm are also shown in the figure.

The left panel of Figure 5.9 shows the gas gain as a function of the number of cathode wires n_{cath} per wire unit and the anode wire voltage. To attain the gain interval dG at an anode voltage of $U_{an} = 1.5$ kV or below, at least two cathode wires are needed (or higher pitch, see later). With one cathode wire per wire unit, dG can only be attained with anode voltages above 1.55 kV. There is no possibility to be within dG without any cathode wires and adequate anode voltage (1.6 kV).

As discussed in Subsection 5.1.6, to reduce the space charge effect, it is preferable to operate the chamber at the lowest gas gain possible within dG. **This is achieved either with $U_{an} = 1.55$ kV and $n_{cath} = 1$ or with $U_{an} = 1.5$ kV and $n_{cath} = 2$.** Both cases are still suitable.

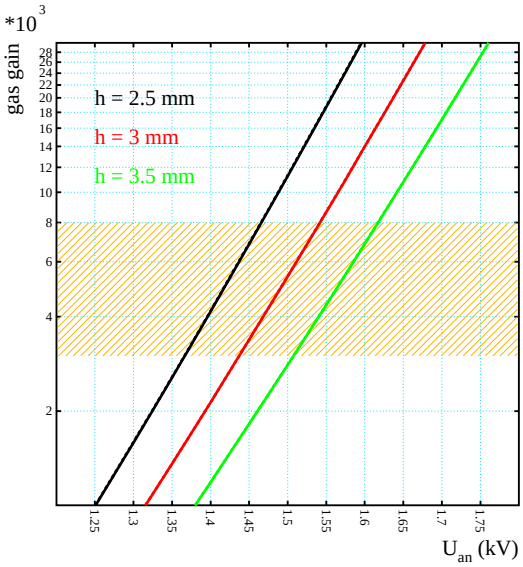

Figure 5.8: Gas gain as a function of the drift voltage and the wire gap. For $h = 3.5$ cm, the anticipated gain interval is achieved within an anode voltage interval between 1.51 and 1.61 kV.

The solid lines in Figure 5.9 represent a *staggered wire configuration*, where the cathode z-position of the cathode wires is symmetrically shifted relative to the z-position of the anode wire. The dashed lines show the gas gain for the *non-staggered* configuration, where a cathode wire is located at the same z-position of the anode wire. The results show that **staggering does not affect the gas gain** except a slight different at $n_{cath} = 1$ and U_{an} higher than 1.5 kV. The gas gain independency on the wire configuration is especially demonstrated in Figure 5.8 where the curves of staggered and non-staggered configurations overlap.

h	3.5 mm
CO_2 fraction	15% $\rightarrow U_{dft} = -2.1$kV
p_{an}	5-6 mm
n_{cath}	≥ 1
U_{an}	1.51-1.61 kV

Table 5.3: Intervals of the geometrical parameters and voltages within which the required gain interval dG.

The right panel of Figure 5.9 shows the gas gain as a function of the wire pitch p and n_{cath}. The dashed lines represent the staggered configuration and the yellow background

highlights again the interval dG. With anode voltages below 1.55 kV and low gas gain, p must be at least 5 mm for $n_{cath} > 1$. For $n_{cath} = 1$ the pitch must be at least 5.8 mm, which can be set as an upper limit, as large values of the wire pitch increases the position resolution ($\sigma = p/\sqrt{12}$ [117]).

But small pitch means high wire occupancy in the grids which increases the *frame load*. This is the mechanical force with which the wires pull the chamber frame inwards, leading to deformations in many parts of the chamber, see Chapter 6. Therefore the lower limit of the pitch is set to 5 mm, i.e. **the pitch should be between 5 and 6 mm**.

The values or values intervals of the parameters in the chamber which were determined in the last three sections are summarized in Table 5.3.

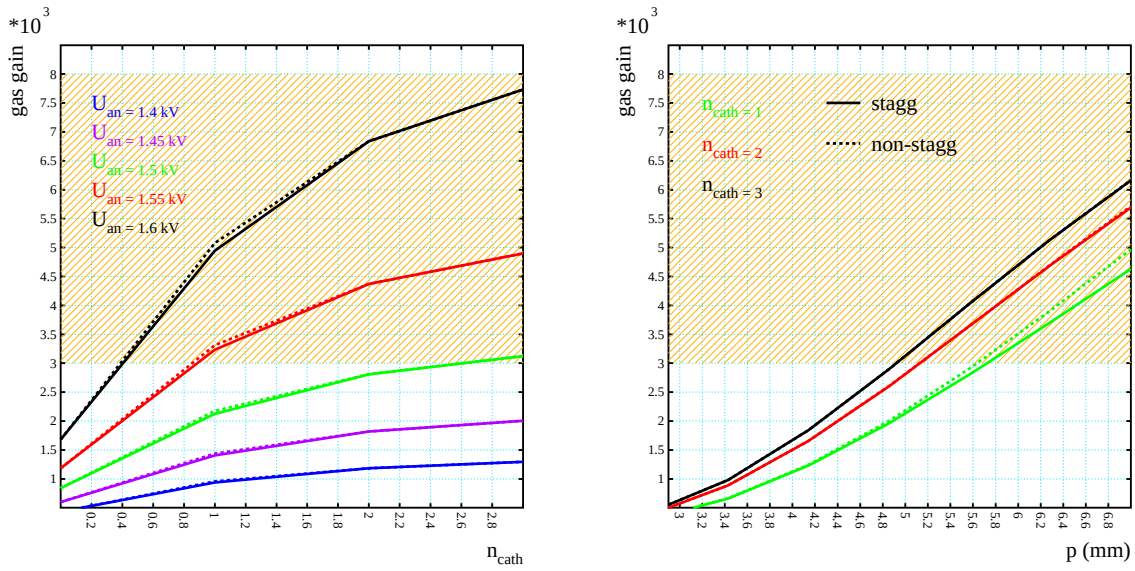

Figure 5.9: Left panel: Gas gain as a function of the number of cathode wires per anode wire and the anode voltage. With $U_{an} \leq 1.55$ kV at least one cathode is needed per anode wire. Right panel: Gas gain as a function of the wire pitch and the number of cathodes. The pitch must be between 5 and 6 mm to keep the gas gain within the interval dG.

5.4 Wire Sag

The decision on the operation parameters set within the intervals, which were established in the previous section, will be taken according to the mechanical and electrostatic stability of the chamber, and the gas gain stability in it. These reference points are directly related to the wire materials, wire geometry, and wire voltages which rule the wire stability and

wire shift under gravitational and electrostatic forces. In this section, after a theoretical overview on wire sagitta in drift chambers, the total (electrostatical and gravitational) wire sag in the TRD chamber will be studied and the unsettled parameters will be determined or the parameters intervals will be restricted.

5.4.1 Theoretical View on Wire Sag

Under gravitational and electrostatic forces the wires in a chamber are shifted off-axis. Major contributions to this shift could come from misalignments of the wires and the ledges on which they are aligned. In the following only the gravitational and the electrostatical sag sources will be studied. The misalignments will be discussed in the next subsection.

The maximal deflection, Δy, of a wire with length L is at $L/2$. This shift modifies the amplification and provokes amplification variation between the different points in the chamber. For high anode voltages and/or low gaps, the anode wire could even touch the pad plane.

Three forces act on each point of the wire; The gravitational, the electrostatical, and the restoring force which results from the tension of the wire. The latter is equivalent to the force which stretches the wires to the chamber walls.
The differential equation which describes the wire shift under equilibrium of the three forces is given by [117]:

$$T\frac{\mathrm{d}^2(\Delta y)}{\mathrm{d}^2 x} + f(y) + g\rho\sigma = 0. \tag{5.23}$$

The first term represents the restoring force with T, the mechanical tension applied to the wire in order to stretch it to the anticipated position. $\Delta y(x)$ is the shift perpendicular to the wire direction, x)[7].
The second term, $f(y)$, represents the electrostatic force. For a symmetric chamber where the anode wire grid is located at half-width between two continuous cathode planes, $f(y)$ is proportional to Δy [118] [8]:

$$f(y) = k\Delta y = \frac{U_{an}^2}{2}\frac{\mathrm{d}C}{\mathrm{d}y}. \tag{5.24}$$

This force is caused by the capacitance variation $\mathrm{d}C$ per unit length due to the shift. C is given by Equation 5.22, it expresses the dependency of the wire sag on the geometrical parameters, gap, pitch, and wire diameter. U_{an}, is the anode wire voltage.

The gravitational part of the force is represented by the third term of Equation 5.23 with g the gravity acceleration, ρ the wire density, and σ its cross section.

The solution of Equation 5.23 is achieved with the boundary conditions $\Delta y(0) = 0$ and $\Delta y(L) = 0$, the joints of the wire where the sag vanishes. At the wire center ($x = L/2$) it has the form:

[7] Remember, the notation of the ALICE Cartesian coordinate is used.

[8] Actually in a symmetric case, where the anode wires are exactly centered between two cathode planes, the wire sag vanishes. This ideal case is not realistic and never occurs in reality. Manufacturing inaccuracy and the gravitational force on the wires, destroy the symmetry.

$$\Delta y(\frac{L}{2}) = \frac{8 s_g T}{L^2 k}\left(\frac{1}{\cos\left(\sqrt{k/T}(L/2)\right)} - 1\right) = s_g \frac{2}{q^2}\left(\frac{1}{\cos q} - 1\right), \tag{5.25}$$

with the gravitational sag

$$s_g = \frac{L^2 g \rho \sigma}{8T} \quad \text{and} \quad q = \sqrt{k/T}(L/2). \tag{5.26}$$

The gravitational sag increases with the squared wire length and with decreasing wire tension. For a given wire length and material the gravitational sag can only be reduced with a large T, however, at a critical tension T_c the wire reaches its elastic limit. Furthermore a large wire tension bends the chamber walls on which the wires are fixed. Two effects one would like to avoid and therefore they must be compromised with the wire sag. T_c depends linearly on the wire cross section, σ, such that the ratio T_c/σ is constant.

With assumable voltages, the largest contribution to the sagitta of thin wires ($r \leq 30$ μm) is caused by the electrostatic forces. The wire becomes unstable if q in Equation 5.26 approaches $\pi/2$. Therefore the following stability condition must be fulfilled:

$$q^2 = \frac{kL^2}{4T}\left(\frac{U_{an} L}{p}\right)^2 \times \frac{4\pi\epsilon_0}{4T}\left(\frac{\pi h}{p} - \ln(\frac{2\pi r}{p})\right)^{-2} \leq 1. \tag{5.27}$$

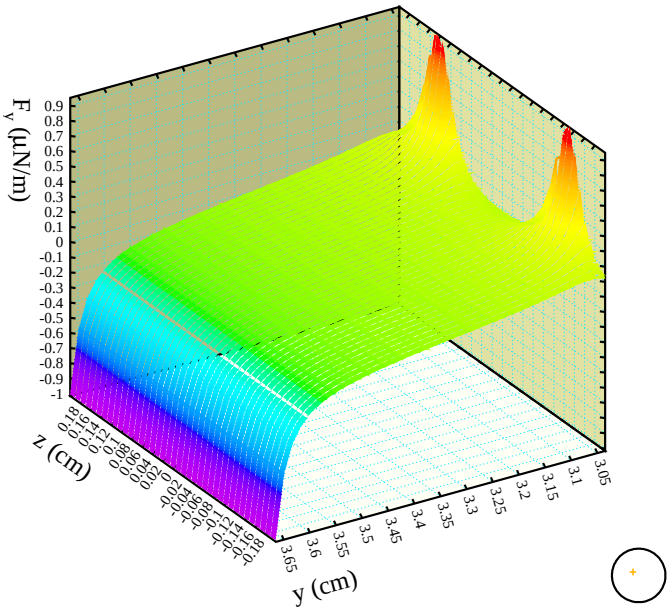

Figure 5.10: Electrostatic force acting on the anode wires as a function of displacement of the wire.

Designing a stable chamber requires a balance between the quantities in Equation 5.27. k expresses the capacity of Equation 5.22 and therefore the gas gain. For given material,

wire length L and wire diameter $d_{an} = 2r$, the gain is a function of U_{an}, h, and p. These quantities should be compromised with T in order to minimize the electrostatical wire sag and the gain variation.

The description of the sagitta carried out above is only valid for wires which are located symmetrically between two continuous plane conductors. In most practical cases the chamber configuration is not symmetric or, as in the case of the ALICE TRD, the anode wire grid faces a continuous plane only on one side. In such a configuration the electrostatic force on the wires, $f(y)$, is only for small displacements approximately linear as given in Equation 5.24.
GARFIELD calculations account for any modification from the simple symmetric case. Figure 5.10 shows $f(y)$ as a function of z and y in the TRD chamber under nominal conditions. It is calculated analytically by removing the considered anode wire and computing the force acting on a unit charge placed at various locations in the space. With the boundary conditions $\Delta y(0)$ and $\Delta y(L)$, the solution of $f(y)$ is calculated numerically using a *multiple shooting* method in which each shot is traced with a *Runge-Kutta-Nystroem method*, see [137] for details[9].

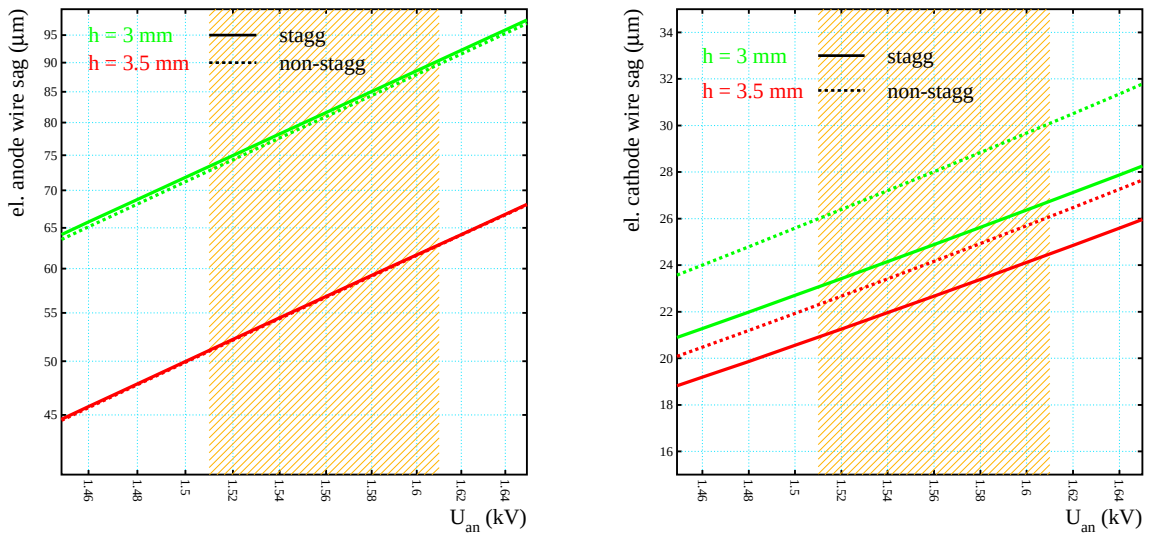

Figure 5.11: Electrostatical anode wire sag (left panel) and cathode wire sag (right panel) as functions of the anode wire voltage for staggered and non-staggered wire configurations. Yellow background highlights the voltage interval within which dG is achieved with $h = 3.5$ mm.

5.4.2 Wire Sag in the TRD Chamber

The total, electrostatic and gravitational, tolerable wire sag in a chamber is determined by the mechanical wire stability and the variation in the gas gain. However the first

[9] See also [142]

becomes crucial at a wire sag value where the second is already transcended. Thus only the gain variation will be considered as reference.

Figure 5.11 shows the anode wire sag (left panel) and the cathode wire sag (right panel) as functions of the anode voltage. The anode wire voltage interval which corresponds to dG is highlighted by the yellow background.
Going from $U_{an} = 1.51$ kV to 1.61 kV, the anode wire sag at a gap of 3.5 mm arises from 51 μm to 63 μm by about 26%. In the same interval, the cathode wire sag increases by about 17%. For comparison the results at a gap of 3 mm are also shown in the figures.

The dashed lines show the results achieved for the non-staggered wire configuration. At the gap values under consideration, staggering does not affect the anode wire sag. However, this is only true for large gaps.
In the non-staggered case, a cathode wire which is placed directly under the anode wire, compensating a certain fraction of the electrostatic force between the anode wire and the pad plane. Exceeding a threshold value of the gap, weakens the force between the wire grids and cancels the staggering influence. In the TRD chamber the gap threshold value is about $h = 2.7$ mm.

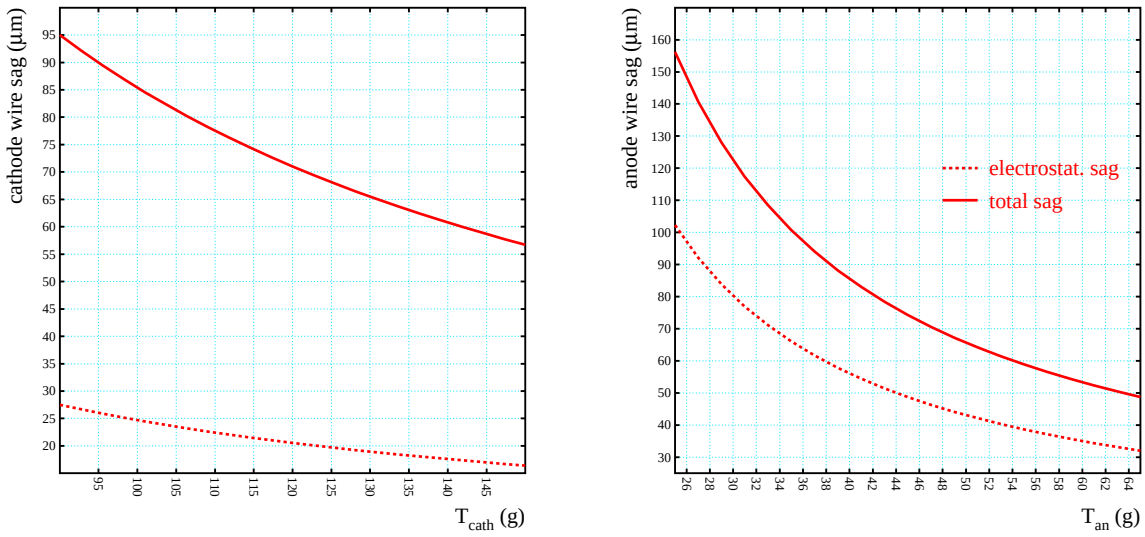

Figure 5.12: Cathode wire sag (left panel) and cathode wire sag (right panel) as functions of the corresponding wire tension. An anode tension of 45 g is a suitable compromise between total wire sag ($\simeq$ 74 μm) and mechanical stability. In the same way, a cathode wire tension of 120 g is a suitable compromise, where the total cathode wire sag is around 70 μm.

In the cathode wire case the staggering influence is still perceivable. In the non-staggered case the perpendicular force component between the cathode wire and the anode wire enhances the electrostatical cathode wire sag.

Neither the gas gain nor the wire sag[10] favor any of the two configurations. In the following the staggered one is adopted.

Equations 5.23 and 5.25 show that for a given length, material, and diameter the wire sag is inversely proportional to $(\cos[\mathcal{C}/\sqrt{T}])$ with $\mathcal{C}$ a constant, and the gravitational wire sag is inversely proportional to T.
To minimize the total wire sag of the "thin" anode wire, one must apply a high tension. In other words a high T_c/σ ratio is required. In turn, this requires a viable strength of the wire material to maintain its stability.

Gold-plated tungsten (Au/W) as well as the 98/2-copper-beryllium alloy (Cu-Be) are common used wire materials. The strength of tungsten makes it suitable for the anode wires. A tungsten wire with length $L = 100$ cm can be stressed up to a T_c/σ ratio between 180 and 410 kg/mm^2 [118]. The corresponding sagitta are between 6 and 13 μm. Although the radiation length of pure tungsten is of about factor two lower than pure copper and its atomic number is 2.9 times larger (heavier) [117], **(Au/W) will be used as anode wires in the TRD chamber** because of the strength priority.

In the cathode wire case there is no need for small diameters, in the contrary, with receivable large diameter the cathode wires balance the electrostatic forces between the anode grid and the pad plane. But large diameters imply large gravitational sag. In order to minimize it, cathode wires should be made from light material. This is in accordance with the requirement of high radiation length. Therefore a **(Cu-Be) alloy will be used for the cathode wires**.

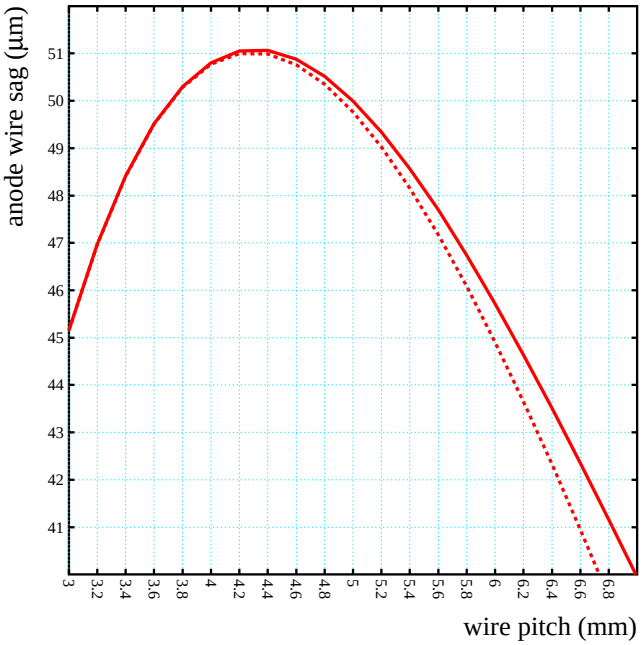

Figure 5.13: Anode wire sag as a function of the anode wire pitch. The sag increases up to a pitch of 4.2 mm where it drops again, see text.

Up to now only the electrostatic wire sag was considered. Depending on the azimuthal location of a TRD module in the ALICE central barrel, the gravitational wire sag contribution acts towards, away from, or parallel to the pad plane or any linear combination of these situations. The highest total wire sag is in the six-O'clock position where electrostatical and gravitational sagitta add up to the total wire sag. This worst scenario case is considered in Figure 5.12.

[10] Except a slight, negligible dependence of the electrostatical cathode wire sag.

The left panel shows the cathode wire sag as a function of the cathode wire tension. The right panel is the corresponding combination for the anode wires. Since the gravitational sag is proportional to d^2/T, the cathode wire sag, with $d_{cath} = 70$ μm, is very high for $T_{cath} < 120$ g. As noted earlier, a large T increases the frame load, therefore **a value of 120 g for the cathode wire tension will be considered**. The total cathode sag at this diameter-tension combination is 70 μm.

With a T_c/σ ratio of 300 kg/mm^2 and a diameter of 20 μm, a maximal tension of about 350 g can be applied to a tungsten wire of length between 1100 and 1300 mm)[11]. However, such a high tension enhances the frame load enormous, see Section 6.4.
The anode wire tension could take values around 50 g, Figure 5.12 shows that the total anode wire sag at an anode wire tension of with this value is about 61 μm. With T_{an} of 45 g the total wire sag is less still below 75 μm. As will be illustrated below, the gain variation caused by this sag is on the order of some percent. But since there are other potential sources of gain variation such as pad plane flatness, **the anode wire tension is set to 45 g**.

The influence of the anode wire pitch on the electrostatical wire sag is mainly maintained by the configuration symmetry around the anode wires. Two kinds of symmetries are to be distinguished; the first is the gap-symmetry where the distances from the anode wire grid to both cathode levels are equal. The second is the "plane-symmetry" where both cathode levels are continuous planes. In case of the plane-symmetry the electrostatic wire sag slopes with increasing pitch as far as the configuration is not gap-symmetric. Remember, in a gap-symmetric case the sag vanishes.
The TRD configuration is gap- but not plane-symmetric, smaller pitch means larger wire density in the grids and "larger" plane-symmetry ($p_{an}/2n_{cath}$). To study the dependence of the electrostatical wire sag on p, consider the mechanism of putting an anode wire on a certain potential. This is equivalent to providing the wire with charge. The charge induces mirror charge on the pad plane, which leads to forces between both electrodes. To keep the wire at the same potential but with larger pitch, more charge must be provided to the wire and consequently the force between the wire and the pad plane increases and so does the wire sag. On the other hand, the pad plane area on which the mirror charge of each wire is distributed, also increases with increasing wire pitch. This leads to a reduction of the perpendicular force component between the wire and the plane, and consequently the wire sag drops.
Figure 5.13 shows this behavior in a TRD chamber. The last effect dominates for pitch values exceeding 4.2 mm. From this point on the difference between staggered (solid line) and non-staggered (dashed line) configuration becomes visible.

From the results discussed in this section Table 5.3 can be updated.

CO_2 fraction (%)	15 ($\rightarrow U_{dft} = -2.1$kV)
anode material	Au/W
cathode material	Cu-Be
d	3.5 mm
T_{an} (g)	45
T_{cath} (g)	70
p_{an} (mm)	5-6
n_{cath}	≥ 1
U_{an} kV	1.51-1.61

Table 5.4: Updated Table 5.3.

5.5 Gain Stability

Due to the limitation in the dynamic range of the ADCs, the gain variation should not exceed 15%. Gain variation may be caused by inaccuracies in the chamber body or fluctuations in the pad plane flatness. Also electrostatic origins such as the space charge effect and wire sag contribute to the gain variation.

The space charge effect depends on the incidence angle of the primary particles, on the wire pitch, and on the gas gain. Since one has no influence on the incidence angles of primary particles, the space charge effect can be minimized with the proper choice of the gas gain and the wire pitch.
The dependence of the space charge on the gas gain (and the incidence angle) was studied with small TRD prototype[12]. Figure 5.14 shows the relative signal $R_{\langle PH \rangle}$ as a function of the drift time and the gas gain [128]. $R_{\langle PH \rangle}$ is a quantitative measure of the space charge at nominal incidence. It is defined as the ratio of the average signal at nominal incidence angle ($\beta = 0°$) to the average signal at an incidence angle of $\beta = 15°$ where the space charge effect is negligible, see Figure 5 in [128].
In the reference it is shown that $R_{\langle PH \rangle}$ is close to unity in the amplification region which indicates the absence of the space charge effect. This is well understood, since an avalanche is not screened by other proceeding avalanches in this region. This behavior is contrary to the observed ratio in the drift region where it decreases with the drift time (longer drift distance), indicating the influence of signal screening through the space charge effect.
The effect increases with increasing gas gain. At a gas gain of 3900 the effect reduces the pion signal by about 12% and the electron signal by about 18%. Measurements were also carried out with gas gain values of 6200 and 9600. Taking the effect at the considered gain values as a reference, the gas gain reduction at a gain of 3000 can be roughly extrapolated. Approximately it is around 9% for pions and 13% for electrons respectively. These results obviously favor the lower gain value of 3000 within dG.
As shown in Figure 5.8, such a gain value sets the **anode wire voltage to 1.51 kV**. Setting U_{an} to 1.5 kV, the gas gain is more than 2800 which is still giving a S/N-ratio

[11] Following the approximation given in Table 3.3 in [118]
[12] Small is related to the area of the chamber but not to the wires and pads dimension and geometries.

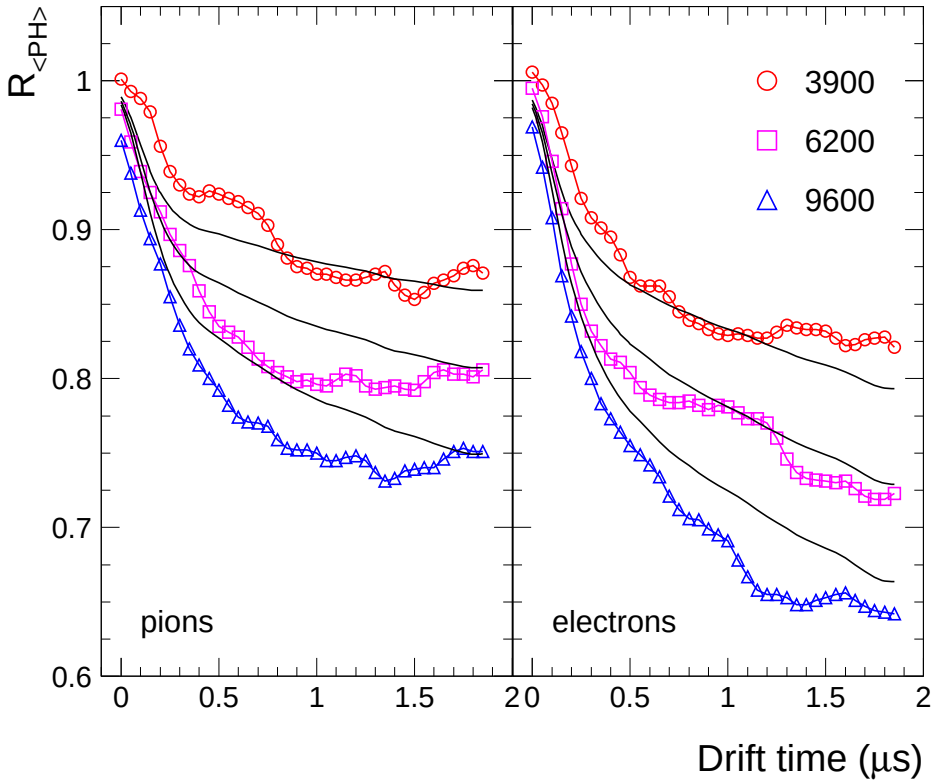

Figure 5.14: Relative signal as a function of the drift time and gas gain. The data are normalized to an incidence angle of 15° where the space charge is negligible. The symbols are the results of prototype measurements and the lines represent calculation results.

within tolerances ($25 < \mathrm{S/N} < 30$) as will be seen in Chapter 7.
According to Figure 5.9, this choice of U_{an} **sets the number of cathodes per wire unit to** $n_{cath} = 2$.

The dependence of the gas gain on the wire pitch, p, was demonstrated in Figure 5.9. The avalanche density on each anode wire increases with p which brings about a rise in the space charge leading to signal reduction as described above. Therefore p should take a small value which is in accordance with the anticipated low position resolution in the chamber ($\sigma = p/\sqrt{12}$) and, as will be seen later, small p values reduce the ion current into the drift region. With the chosen anode voltage and the number of cathode wires per wire unit, the wire pitch must **take an operation of value of** $p = 5$ **mm**. which conforms with the requirements listed above. In the next chapter it will be shown that the arising frame load, with this pitch value is still adequate.

Equations 5.21 and 5.22 show an exponential dependence of the gas gain on the distances of the anode wire to other electrodes (p and h). Therefore any small variation in these distances leads to a large variation in the gas gain. Variations in the wire position emerge

if mechanical imperfections occur in the ledges which carry the wires or in the pad plane. Also the total wire sag contributes to the position modifications.

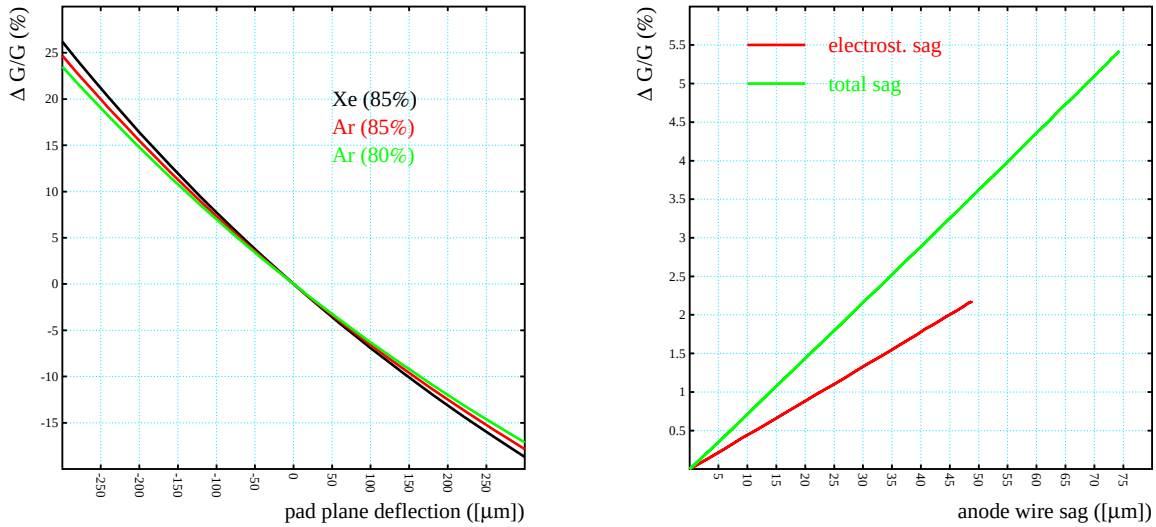

Figure 5.15: Left panel: Relative gas gain as a function of the pad plane deflection dy_{pp}. $dy_{pp} < 0$ indicates an inwards deflection of the plane. Calculations for argon based mixtures are also included. Right panel: Gas gain variation as a function of the total wire sag. The total wire sag contributes to the gain variation by less than 6%.

Ledge imperfections are on the order of 10 μm and therefore no major gain variations are expected from this source. The main contribution comes from unevenness in the pad plane. The difficulty of handling the thin pad plane is the main source of unevenness in the readout surface. The thin honeycomb layer which was added to the readout sandwich reduces variations in the pad plane which can occur during the gluing procedure, compare Figure 4.2. Nevertheless a safety factor of up to 200 μm is taken into consideration when designing the detector.

The left panel of Figure 5.15 shows the relation between the relative gas gain variation, $\Delta G/G$, as a function of the pad plane deflection dy_{pp}. Negative dy_{pp} indicates a pad plane deflection towards the anode grid (inwards). At a $dy_{pp} = -200$ μm the gain variation is around 15% and at $dy_{pp} = +200$ μm, $\Delta G/G$ is about 13%.

The right panel of Figure 5.15 shows how the gas gain varies under the influence of the total wire sag. The green line shows that the total wire sag of about 74 μm causes a relative gain variation of $\Delta G/G \simeq 5.5\%$. The red line represents the gain variation caused only by the electrostatic wire sag.

A worst scenario occurs in chambers located in the six-O'clock position -within the ALICE space frame- where the total wire sag in the middle of the chamber is 74 μm towards the pad plane. and decreases when getting closer to the chamber wall.

Assuming the maximal pad plane deflection of 200 μm outwards, both displacements, total wire sag and plane deflection, are in the same direction such that the total gain variation in the middle of the pad plane is less than 8% and in any case less than 10% elsewhere in the chamber. Note that under such conditions both displacements decrease when going from the middle of the chamber towards its frame. Therefore the gap variation remains more or less constant.

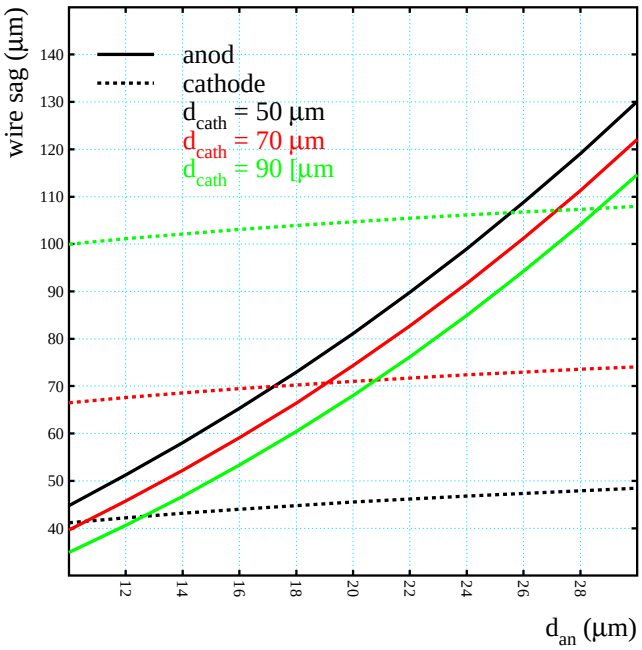

Figure 5.16: Anode (solid) and cathode (dashed) wire sag as a function of the anode wire and cathode wire diameters.

Assuming a maximal pad plane deflection of 200 μm inwards resulting a gas gain variation of about 15%. This situation appears only locally, i. e. within a small area of the pad plane. During the gluing procedure of the pad plane, it happens that air bubble become confined under the pad plane which reduces the gap locally. Assuming an area of 10 pads to be affected ($= 2(lengths) \times 5(widths)$)[13], the contribution of the wire sag to the gain variation is less than 1%. However, under such conditions the bubble in the plane decreases the wire gap and therefore increases the wire sag leading to a gain variation contribution of less than 1.5%. Although the gain variation is exceeding the tolerated value by about 1.5%, the situation is not crucial since it appears only locally and seldom.

Finally, since the ionization energy of CO_2 (13.773 eV) is higher than the excitation energy of xenon (8.3-11.7 eV), a gain variation due to the Penning effect is not expected.

From the results discussed in this section Table 5.4 can be again updated which results in Table 5.1. In the following sections some electrostatical properties of the readout chamber will be discussed under the determined parameters set. In some cases, excluded parameters values will be considered for comparison purposes.
To get the whole picture of Table 5.1, the choice of the wire diameters is justified in Figure 5.16 which shows the total anode and cathode wire sagitta as functions of the cathode wire and anode wire diameters. The cathode wire sag does not depend on the anode diameter but strong on the cathode diameter due to the gravitational wire sag. The anode

[13] This was observed.

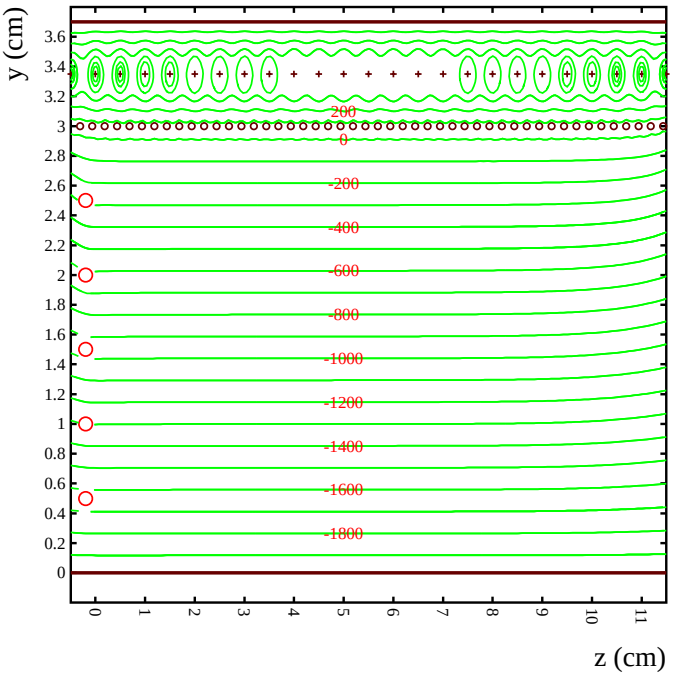

Figure 5.17: Equipotential lines in the chamber with (without) field cage on the left-hand (right-hand) side of the plot.

wire sag depends on both, d_{an} and d_{cath}. A large d_{cath} offers a larger surface towards the anode wires, i.e. more mirror charges which compensate more of the electrostatical force between the pad plane and the anode wires. The chosen wire diameters are a good compromise between the wire sag and the wire tension.

5.6 Field Shaping

Field shaping is the art of achieving a desired electric field by placing electrodes and adjusting their potentials. In this sense the cathode wire grid is a field shaping grid which separates the drift field from the amplification one and defines the zero potential level between them.

If one does not take any precautions, the drift field at the chamber edges is not uniform, as seen in the right-hand side of Figure 5.17, where the equipotential lines in a chamber with 25 wire units are shown under nominal conditions.

Consider the drift field at a distance of 5 mm from the chamber wall, $z = 11$ cm in Figure 5.17. Going from the vicinity of the drift electrode at $y = 2$ mm up to $y = 29$ mm close-by the cathode wire grid, the field varies between 695 V/cm and 770 V/cm. The black solid line in the left panel of Figure 5.18 shows this inhomogeneity. This non-uniformity remains visible up to a distance of 35 mm inside the chamber ($z = 8$ cm, green

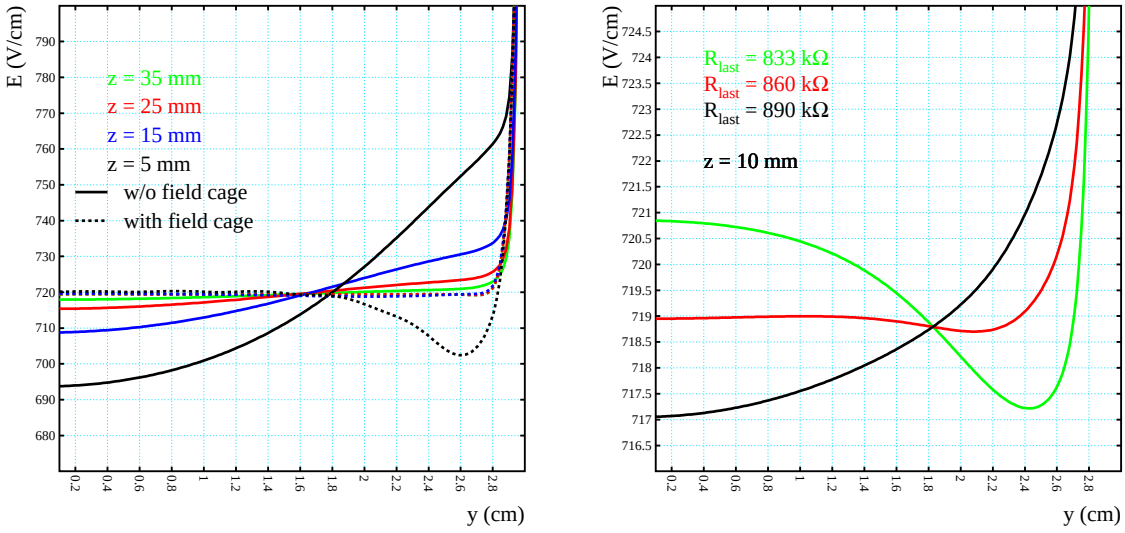

Figure 5.18: Left panel: Electric field at different z-positions from the edge (field cage). Solid lines with field cage, dashed without. Right panel: Electric drift field as function of chamber depth, y, and last resistor in the voltage divider R_{last} at $z = 10$ mm.

line). The blue and red lines represent the drift field at distances of 15 and 25 mm from the frame of the chamber.

The field inhomogeneity at the edge can be corrected with the so called *field cage*. This is a circuit board with conductive potential strips running along the inner side of the chamber walls, as illustrated in Figure 5.19.

A resistive *voltage divider* allows to obtain the desired potential on the strips. The impact of the voltage divider is seen on the left-hand side of Figure 5.17, where the equipotential lines are smoother. The dashed lines in the left panel of Figure 5.18 correspond to the same-colored solid lines but with the presence of the field cage. They show how the field cage smoothes the field. Its variation at a distance of 5 mm from the chamber wall is below 1%.

The voltage on each strip is chosen to smoothen the equipotential lines at the strip position. Starting from the drift voltage of -2.1 kV on the drift cathode, a resistor chain between the drift cathode and the cathode wire grid assigns the right voltage value on each strip. The number of strips is chosen such that a resistor of about 1 MΩ between two strips is called for. The value of the last resistor is chosen to smoothen the field between the amplification and the drift region.

The right panel of Figure 5.18 shows the drift field as function of y, the depth of the chamber at $z = 10$ mm from the cage for three values of the last resistor. A resistor of about R= 850 kΩ seems to be the right choice. For the TRD drift chamber depth of 30 mm these considerations lead to five voltage strips on the wall.

In Section 6.5 the performance of the voltage divider will be discussed.

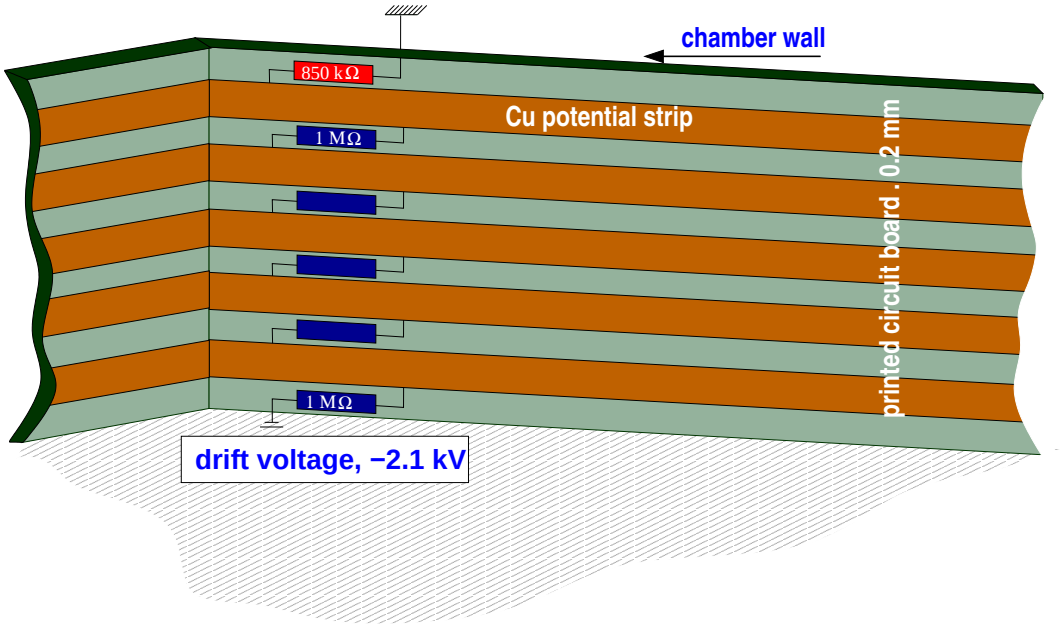

Figure 5.19: Sketch of the voltage divider and field cage on the chamber wall.

5.7 Ion Signal and Pad Coupling

The left panel of Figure 5.21 shows the drift lines and the isochronity levels of positive ions drifting from an anode wire. They induce signals on all electrodes around it. In this context two aspects are important for the signal and the electric fields in the chamber. First the fraction of the ions which passes the cathode wires into the drift region and secondly the fraction of the ions which drift towards the pad plane.

For given voltages and drift gas the ion currents depend only on the number of cathodes per wire unit. The right panel of Figure 5.21 shows the fractions of ions in an avalanche which drift towards different directions as a function of n_{cath}. The red line presents the ions which drift through the cathode wire grid into the drift region (multiplied by factor 2). The green line represents the ions which drift towards the pad plane. With $n_{cath} = 2$ only 25% of the ions pass into the drift region and more than 53% of them drift towards the pad plane. The remnants are attracted by the cathode wires. With respect to the one cathode wire case, in addition to reducing the electrostatic wire sag, this wire occupancy improves the signal on the pad plane by a factor of 4% and reduces the total ion current into the drift region by 5%. Although the numbers are not large, they confirm the choice of 2 cathode wires in a wire unite.

Under nominal conditions the ions that penetrate into the drift region create an ion feedback current of about 0.5 μA in it [130]. The created charge density in the drift volume is below 10^5 ions/cm^3.
The total resistance of the voltage divider at the chamber wall is 5.85 MΩ. The current through this chain between the drift voltage (-2.1 kV) and the ground potential at the cathode wire grid is about 360 μA. This current is large enough to draw out the low ion feedback current. Under the influence of the 25% of the ions, the drift field suffers only a

deterioration on the order of 10^{-3} of the nominal field of 700 V/cm.

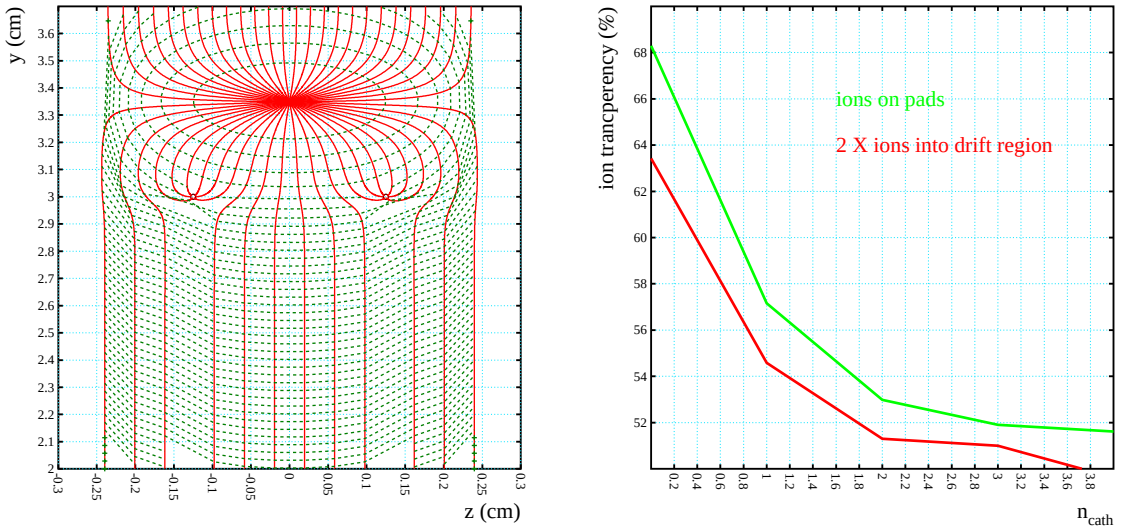

Figure 5.20: Left panel: Ion drift paths away from an anode wire. Right panel: Ion fraction which drifts towards the pad plane and into the drift region as a function of n_{cath}. To keep the ion current low in the drift field, at least one cathode wire is required per anode wire. At $n_{cath} = 2$ only 25% of the ions drift into the drift region and more than 53% drift towards the pad plane.

The fractions of the signal on different electrodes are shown in Figures 5.21. The left panel shows the induced charge as a function of the angle between the ion drift direction and the positive z axis within the first 500 ns. Obviously the signal on the pads is maximal when the ions drift towards the pad plane (90°) and minimal when they drift towards the cathode wire plane (−90°). In this sense the mentioned induced fraction on the pads is to be understood as an average of values between both extrema. This means that at the adopted gas gain value of 3000, one can not consider the avalanches to be isotropic around the anode wires. This is only true at gain values above 10^4 [118].

The right panel of Figure 5.21 shows the induced charge as a function of the ion drift time. The message of this figure is the constance of the induced signal on all electrodes within the first 100 ns, the deviation of the constant value is less than 10% if the signal is considered within the first 1 μs.

5.8 Isochronity

The influence of an anode wire in z direction extends up to $\pm p/2$ left and right from its position. Electrons starting their drift path at different z positions need different arrival

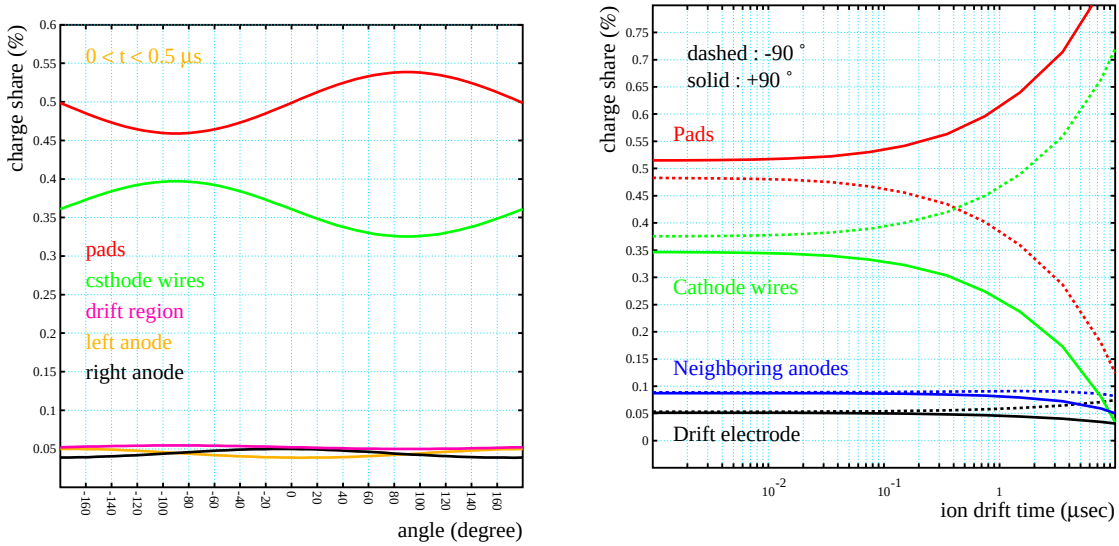

Figure 5.21: Left panel: Charge fraction which is induced on the different electrodes by the ions drifting away from the anode wire as a function of the angle under which the ions leave the wire vicinity relative to the z axis. Right panel: Charge fraction induced on the electrodes as a function of the drift time. On all electrodes the charge is approximately constant in the first 100 ns and varies by about 10% in the first 1 μs.

(drift) times to reach the anode wire, as seen in Figure 5.22. This time variation affects the measured drift time and therefore the determined hit position; a potential source for deterioration in the chamber position resolution.
The left panel of Figure 5.23 shows the drift time dependence of the z position. The anode wire is located at $z = 0.25$ cm. Electrons which start their drift path at $z = 0$ cm or $z = 0.5$ cm, need 0.18 μs longer (around 10%) than electrons which drift at $z = z_{anode}$ to reach the anode wire. Also those electrons drifting at z values in the vicinity of the cathode wires are delayed. Simulations show that these drift time differences are still small in terms of position resolution [130].

The right panel of Figure 5.23 shows the drift time distribution; most electrons spend in average 1.71 μs to reach the anode wire. The r.m.s. of the distribution is around 62 ns. The origin of the second peak is the delay of electrons by the cathode wire grid, see Figure 5.22.

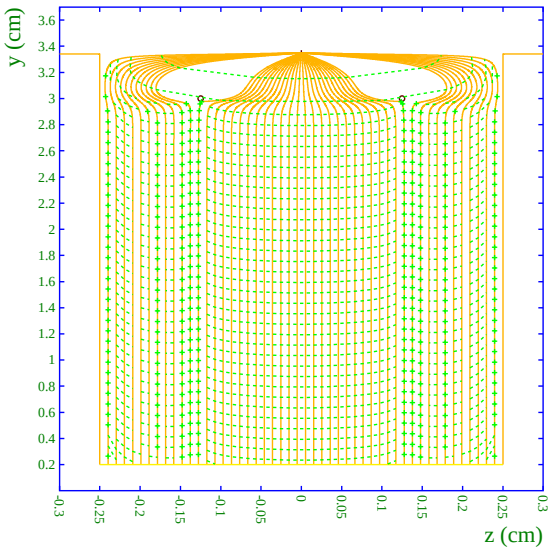

Figure 5.22: Electron drift lines from a track at $y = 2$ mm from the drift electrode. Electrons at $z = z_{anode} = 0$ drift a shorter path to the anode wire than those at $z = \pm p = 25$ mm

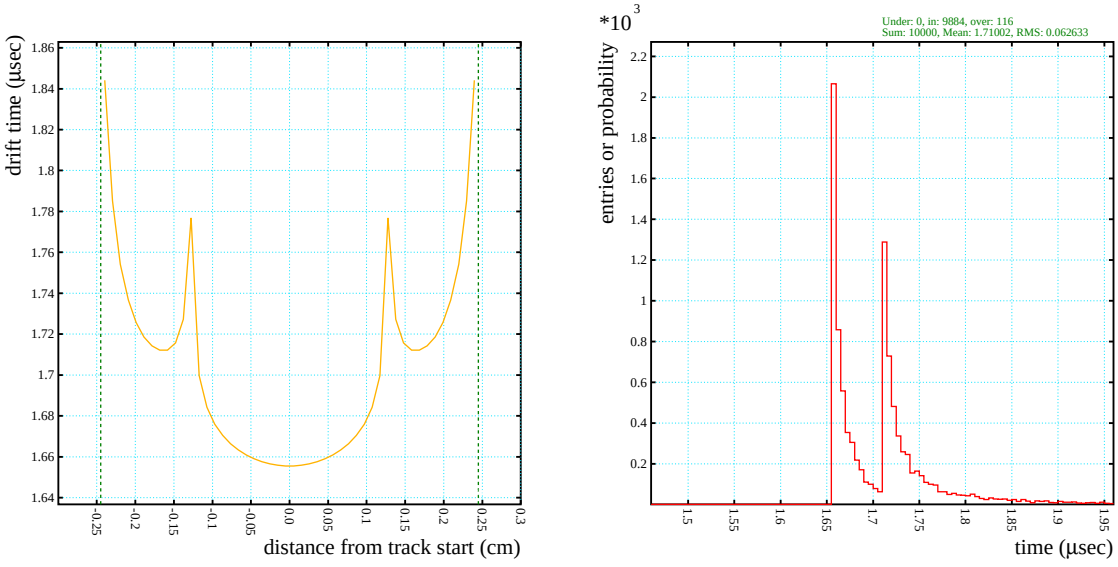

Figure 5.23: Left panel: Drift time as a function of z. Electrons starting their drift at $z = z_{anode} \pm p/2$ need around 10% longer as those which start at $z = z_{anode}$. Right panel: Drift time distribution.

Chapter 6

Module Stability

The TRD design requirements listed in Subsection 4.2 can be grouped in three classes which must be fulfilled simultaneously: Firstly, it must perform in a way that the physical requirements put on it are well satisfied. Secondly, it must be mechanically stable so that deformations of the components of its module -body frame, radiator, and readout sandwich- are still within tolerances, and thirdly, the TRD must not represent more than 15% of a radiative length.

The final design was a compromise between those three requirements. A real dimension prototype (largest) was built with the parameters and specifications described in Section 4.3 and summarized in Table 5.1, for test purposes concerning its mechanical and electrostatical stabilities. The results will be presented in this chapter.

The mechanical stability has to be maintained for the lifetime of one module of more than ten years. Apart from this, mechanical deformations of the individual components affect its performance. Mainly, there are two sources for mechanical instability in a TRD module: the first is the overpressure which pushes both, the readout sandwich and the radiator outwards, see Figure 6.1. The second is the wire tension which makes the radiator bulge supplementary outwards and pulls the frame ledges along the chamber inwards. Thereby the wires should not be stretched beyond their elasticity limit and their tension should not be decreased by the deformation of the frame.

Deformations on the radiator modify the drift field leading to a nonuniform drift time (i.e. drift velocity) and consequently to deterioration of the position resolution. The concavity of the readout sandwich contributes to the total gain variation, and any bump in pad plane implicates a "local" gas gain variation.

Keeping the demand of simultaneous fulfillment of the three requirements in mind, these deformations can not be entirely eliminated, but they must be kept within certain tolerances and as low as possible. Drift field variations are still acceptable if the radiator does not deviate more than 1 mm in y direction [135]. Deflections of the readout sandwich are tolerated as far as they are still below 200 μm as discussed in Section 5.5.

In terms of the mechanical, electrostatical and gain stability the following points will be verified after an overview of the measurement environment.

- Deformation of the readout sandwich and their impact on the gas gain, Section 6.2.
- Deformation of the radiator, Section 6.3.
- Deformation of the chamber's frame and its impact on the wire sag, Section 6.4.
- Voltage divider and drift field uniformity, Section 6.5.
- Gas gain and its dependence on the anode voltage and overpressure in the chambers volume, Section 6.6.
- Gas gain uniformity, Section 6.6.1.

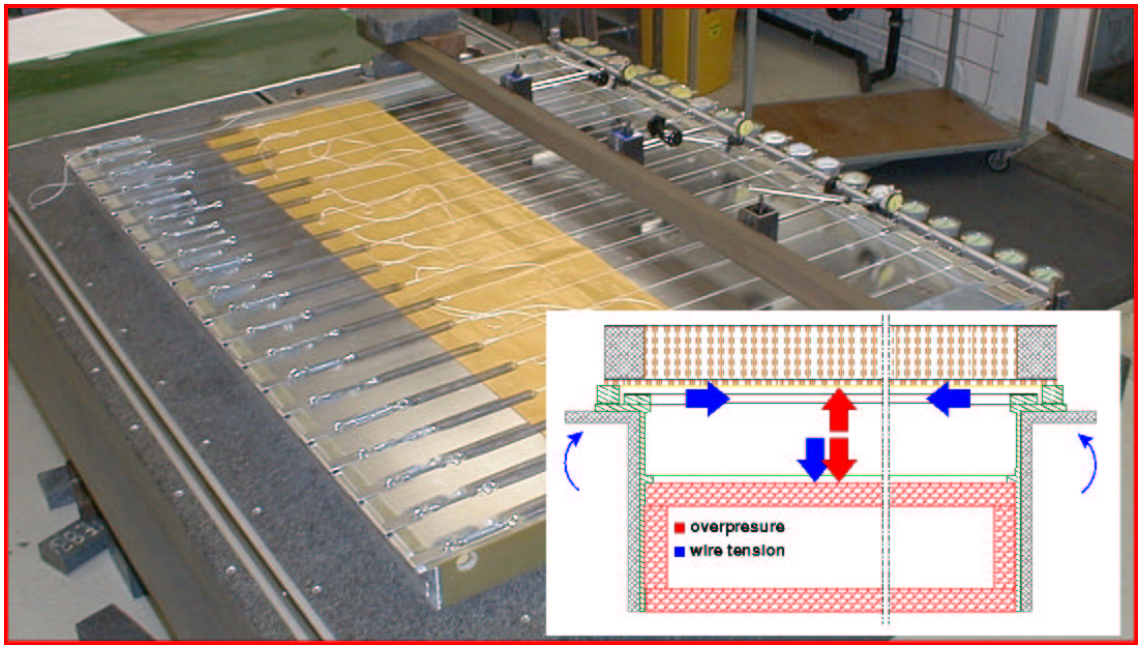

Figure 6.1: Photographic of the chamber with stretched spring scales. The scheme illustrates the forces acting on the individual parts of the chamber.

6.1 Measurement Environment

Tests of mechanical stability:
The module is 1590 mm long, with a wire unit width of 5 mm (anode wire pitch). This sums up to 318 anode and 636 cathode wires. Each wire is stretched with a tension of 45 g and 120 g respectively, leading to a total force on each frame side which is equivalent to a weight of 90 kg, (the force will be given in weight units).

The chamber length (y-direction) was segmented into 20 sections. On each section the acting force is 4.5 kg which was replaced by a spring scale. The deformation was measured at each joint to the frame. During the measurements the chamber was lying on a granite table with flatness at the level of micrometer, Figure 6.1.

The deformations of the read-out sandwich and the radiator were measured in the center, where the maximal deflection arises. The radiator was glued to the chamber frame, whereas the readout sandwich was only taped and clamped to the frame.
Note that the readout sandwich does not contain the 2 mm thick honeycomb layer.

In the overpressure measurements a simple, "home-made" bubbler device was used. It consists of a bottle half-filled with water. It was connected to the chamber volume such that the overpressure causes a rise at the water surface which was read out.

Tests of electrostatical and gain stabilities:
After completion the mechanical stability tests, the wire grids were glued to the frame. Also in this test series the pad plane sandwich was not glued to the chamber frame but carefully and tightly closed with tape. This gave the freedom to open the chamber when necessary and to test different types of pad plane sandwiches.
The drift gas was an argon/CO_2-mixture with a CO_2 content of 15% and 20%. The gas flow through the chamber volume was 32 l/h.
The pad plane cathode and the cathode wire grid were put to ground voltage. If not scanned in a measurement, the anode voltage was put to 1.5 kV and the drift voltage to -2.1 kV. The sources used were ^{55}Fe and ^{90}Sr. The first source emits photons in the energy range of transition radiation (around 5.5 keV), the second emits β electrons of the energy of 200 MeV. The current of the anode wires was read out.

The measurements took place in "usual" non-dust-clean laboratory room which does not satisfy the required cleanness. Since the chamber had to be opened several times for testing several types of read-out sandwich, dust in the chamber was not avoidable. The consequence was a large dark current which varied within 10 nA during one measurement. For the mass production a so called "clean room" (dust free room) was built. The dark current measured in later built chambers below 1 nA.

6.2 Deformation of the Read-Out Sandwich and its Influence on the Gas Gain

The read-out sandwich consists of 2 cm thick honeycomb sandwiched between two carbon fibre sheets of 400 μm thickness each.

An overpressure between 0.5 and 3 mbar was applied to the closed chamber in steps of 0.5 mbar and the deformation was measured in the middle of the sandwich.

The results are shown in the left panel of Figure 6.2. At high overpressure the data are consistent with theoretical calculations for the materials of the sandwich which are represented by the solid black line. At low overpressure the measurements are about 120 μm higher than the calculation.
This behavior could come from the used bubbler where the surface tension of the water causes a large read error. Since the measurements should only give a trend, this error was not accounted for.

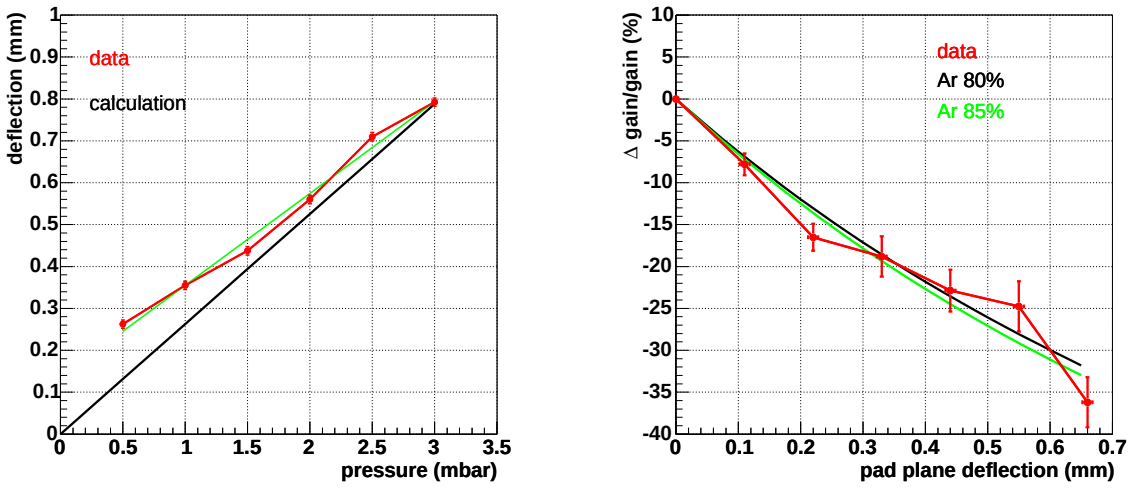

Figure 6.2: Left panel: Deflection in the mid-point of the read-out sandwich under the influence of the overpressure in the chamber. It concaves by about 220 μm/mbar. Right panel: Gain variation as a function of pad plane deflection. Garfield calculation underestimate the measured data by about 6%.

The slope of the linear fit exhibits a deformation of about 210 μm per millibar. This corresponds to a measured relative gain variation about 17%, as shown in the right panel of Figure 6.2. At such a deflection, GARFIELD calculations show a gain variation of about 14%. However within errors the measurement agrees with the simulation. Discrepancies could be triggered by the overpressure, since the Townsend coefficient depends on the gas density (pressure). However, in [140] it is shown that the gain variation is below 1%/mbar in Ar/CO_2 (90:10). Also temperature variation leads to a gain variation of about 1.5%/K. GARFIELD simulations are derived at atmospheric conditions.

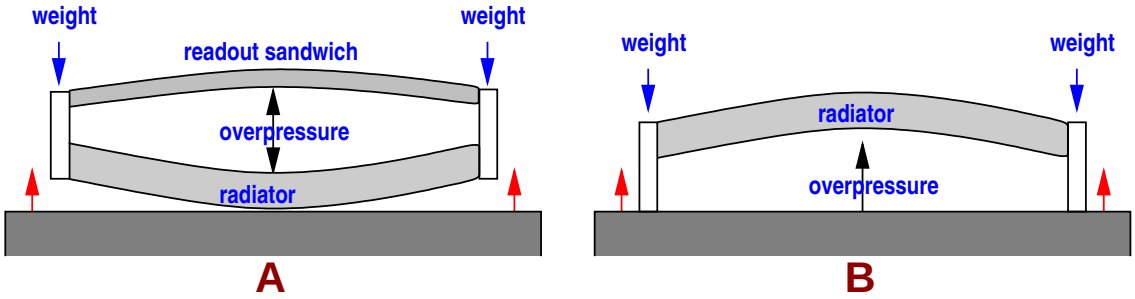

Figure 6.3: Schematic illustration of the deflection of the read-out sandwich (A) and the radiator (B) under overpressure in the chamber.

6.3 Deformation of the Radiator

The radiator was subject to the same measurement procedure. The open chamber (without the sandwich) was put upside-down, as illustrated in Figure 6.3 B. The edges were pinned down leak-tightly and overpressure was applied. The deflection was measured at the center of the radiator. The results are shown in the left panel of Figure 6.4. Under a pressure of 1 millibar, the radiator is deformed by 400 μm as exhibits by the slope of the fit curve. Also in this case there is an offset at zero overpressure at about 0.2 mm.

In addition to the deformation caused by the pressure, the radiator suffers an additional deflection under the influence of the wire tension. With the procedure described in Section 6.1 a tension interval between 3 and 8 kg per section was scanned in steps of 1 kg. This results in a total load of 60 to 240 kg for the whole chamber. These are 33% below and 265% above the nominal tension. For each load the radiator bulge was measured, the results are presented in the right panel of Figure 6.4. The slope of the curve shows a radiator camber of 5.2 μm per kilogram load. For the nominal total force of 90 kg this gives an additional 450 μm to the radiator deflection. Both the overpressure and the wire tension add up to a total radiator deflection of about 950 μm.

In [135] it is shown that with such a radiator concavity, the drift velocity of secondary electrons generated from two primary particles which drift at a distance of 1 cm of each other, does not change by more than 0.004 μs (0.2%).

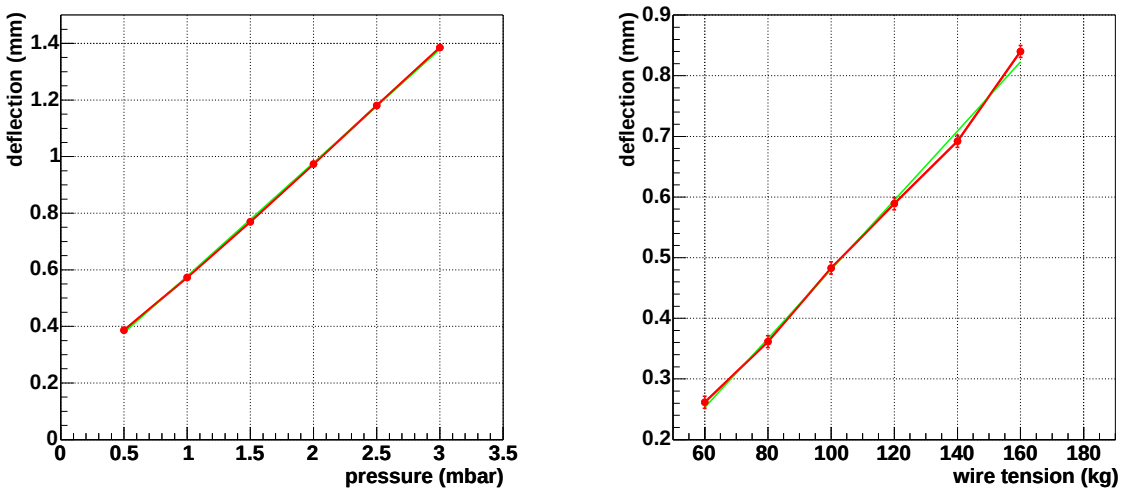

Figure 6.4: Deflection in the mid-point of the radiator caused by the overpressure (left) and the wire tension (right). Both sources add up to 950 μm which is within tolerances and causes no serious drift field modification.

6.4 Deformation of the Chamber Frame

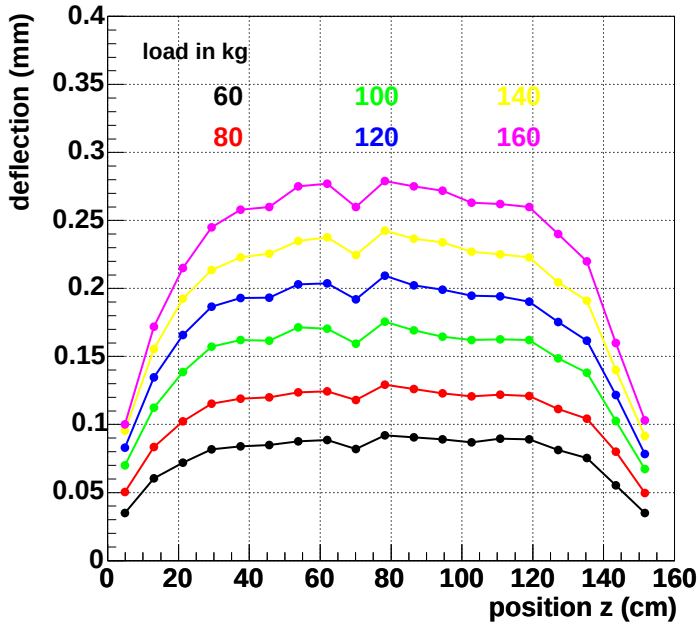

Figure 6.5: Frame binding under the influence of the wire tension as a function of the wire location and the wire tension.

The wire tension pulls the chamber frame ledges inwards with a force equivalent to 90 kg weight. The same load scan as described above was carried out for the frame deflection measurements. The results are presented in Figure 6.5, at mid-length of each side, the walls are deflected by about 140 μm under the nominal load of 90 kg.
Even under a force of 160 kg the deflection is still below 300 μm which is still within a tolerable domain.
After putting the chamber frame under a total load of 240 kg for the duration of 24 h, the interval was scanned backwards down to vanishing load (zero kg). At this point the measured deflections are between " -1 μm" and 2 μm, which is compatible within the precision of the measurement and allows to state the elasticity of the deformation.

6.5 Voltage Divider

As discussed in Subsection 5.6 the voltage divider is added to dominate the ion current which crosses the cathode wire grid into the drift region and to ensure the drift field uniformity at the edges of the chamber. It consists of four copper strips running along the chamber frame. The potential on the strips is determined by resistors such that the current is 360 μA. Each resistor amounts 1 MΩ. The resistor of 850 kΩ, between the last strip and the cathode wire grid is optimized to smoothen the field at this point, Figure 5.19.

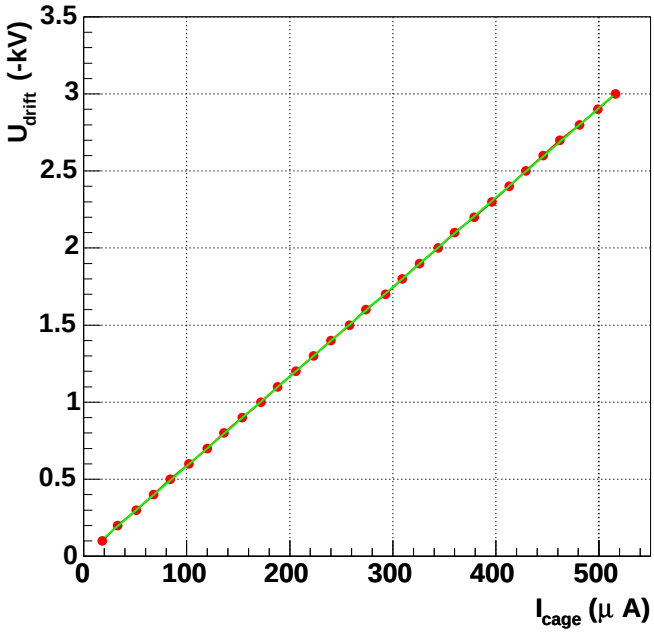

Figure 6.6: Field cage current as a function of drift voltage. The slope of 5.811 MΩ is in good agreement with the design value of 5.85 MΩ.

The current through the resistor chain was measured as a function of the drift voltage. The results are shown in Figure 6.6. With a slope of 5.811 MΩ the resistor is within tolerances in a good agreement with the design value of 5.85 MΩ, which affirmed the linearity of the voltage divider.

In mass production, which started in early 2004, the resistors values are doubled in order to halve the current and relieve the power supply. The ion feedback current of 0.5 μA is still by a factor 300 lower than the resistor chain current.

6.6 Gas Gain

In addition to the gain variation resulting from the deformation of the cover sandwich under overpressure, a gain variation occurs if the pad plane exhibits any local bulges which could come from problems during the gluing procedure. Also gap modification between the wire levels and the pad plane are a serious potential source of gain variation. These modification could be caused by deformations or inaccuracies in the frame, which carries the wires, and by the total wire sag.

Figure 6.7 shows the gain as measured with a ^{55}Fe source in an Ar-CO_2 (80:20) gas mixture as a function of the anode voltage. The gas gain increases by a factor of 1.7 per 50 V increase in the anode voltage. Whereas GARFIELD simulations show an increase by about 1.45 per 50 V. Such discrepancies between GARFIELD and measurements were observed

in an earlier measurement with a small prototype with Ar-CO_2 (80:20) gas mixture at GSI [130]. The referred measurements are in good agreement with the measurements discussed here.

6.6.1 Gas Gain Uniformity

To enable a gain measurement all over the chamber, the cover sandwich was divided into 16 sections in z- and 12 sections in y-direction. On the cross points of the so established grid a source was positioned and the anode wire current was measured. The gas mixture in this measurement was argon/CO_2 (80:15), the anode and drift voltages were put to their nominal values of 1.5 kV and -2.1 kV respectively.

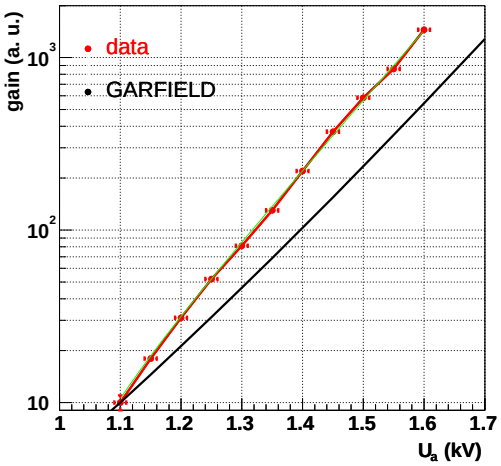

Figure 6.7: Gas gain as a function of the anode voltage. Measurements do not agree with GARFIELD simulations.

The results are shown in the left upper panel of Figure 9.6 as a function of the wire direction, y, and the "beam direction", z. The source was not collimated, therefore a certain fraction of the radiation escaped the active area of the chamber at its edges leading to reductions of the measured values there. Apart from this, the gas gain shows variations which grow inter-regionally. This comes from gluing mis-distributions. Such a problem was solved by the addition of the thin honeycomb layer to the read-out sandwich. The results as measured in a chamber with such a construction are shown in the right upper panel of Figure 9.6 where the fluctuation are minimized. The low gain at $z = 68$ cm originates possibly from bad grounding in this pad row.

Relative to the middle of the chamber at $z = 70$ cm, the gain variation in the upper left panel is shown in the lower left panel of Figure 9.6 (the edges are excluded). The values vary between 15% at $(z = 90, y = 10)$ cm and -22% at $(z = 150, y = 110)$ cm. Their distribution is given in the lower right panel of Figure 9.6 where the occurrence of a certain variation is given relative to the row at $z = 68$ cm. At most locations in the chamber, the gain variation is lower than 10%.

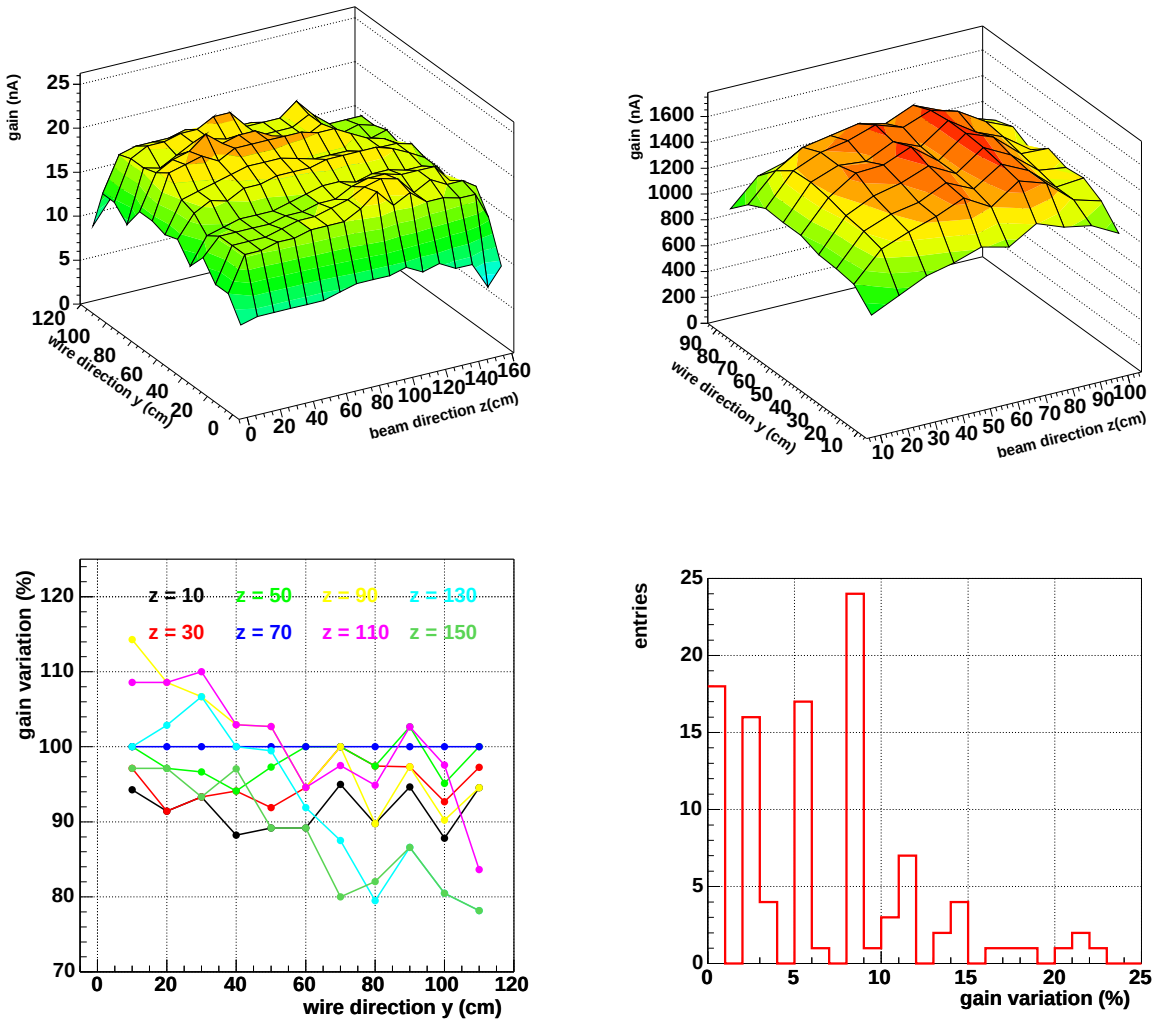

Figure 6.8: Upper row: Gas gain along the chamber length and width. The left panel as measured in the first real dimension prototype where gain variation between different points are seen. This is illustrated in the lower left panel. The highest variation is about 20%. The updated read-out sandwich reduces the gain variation to about 12%.

Chapter 7

Detector Performance

In the previous chapter the overall detector performance in terms of mechanical stability, drift field, gain uniformity, and gain variation were discussed. Based on beam tests this chapter evaluates the detector performance as such. The tests were carried out within 14 days of beam time in fall 2002 at the CERN PS facility. The task is to evaluate a real dimension prototype in terms of the following aspects:

- General properties and the drift velocity, Section 7.2.
- Signal and noise, Section 7.4.
- Position and angular resolution, Section 7.5.
- Gas gain, Section 7.6
- Transition radiation yield, Section 7.7.
- Pion rejection, Section 7.8.

7.1 Measurements Setup

The real dimension TRD prototype chamber was placed in a beam of electrons and pions with momenta between 1 and 6 GeV/c. For certain momenta, anode voltage intervals between 1.5 and 1.7 keV and a drift voltage interval between -3.0 and -1.9 keV were scanned.

Figure 7.1 shows the beam setup: In addition to the real dimension prototype (DC5), four small detectors (DC1-DC4) with a 20×20 cm^2 active area each were tested. The chambers were operated with a Xe-CO_2 mixture, the CO_2 content was around 15%. The O_2 and H_2O contents were 170-200 and 910-1000 ppm respectively.
The radiators of the small detectors were detachable from the entrance windows of the drift chambers, this enabled performance tests of different fibre-foam radiator compositions and the measurement of energy deposit of electrons in the chambers without the contribution of transition radiation. The radiator of the fifth detector was glued to the

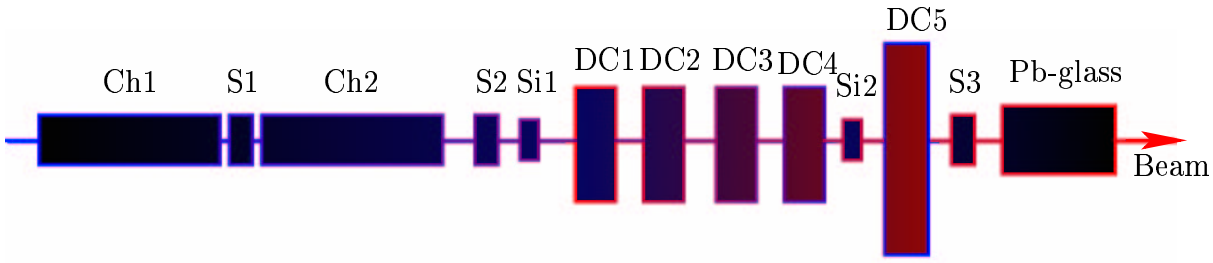

Figure 7.1: Schematic of the test setup, not to scale.

entrance window and consisted of polypropylene fibre and Rohacell foam sheets as described in Subsection 4.5.

The plane spanned by the wire direction and the beam direction laid in the horizontal plane. In case of the small chambers the angle between the beam and the wire directions was variable (but identical for all four chambers). For the large chamber this angle was fixed at 12 degrees for all runs. With the small detectors an angle interval between zero and 15 degrees was scanned in 5 degrees steps in order to measure the space charge effect and the dependence of the position and angular resolution on the incident angle of the beam particles. In this work the performance of the big chamber will be presented. Results from the small prototypes will be taken into account only for comparison reasons where needed. Their performances are discussed in Refs. [143, 120].

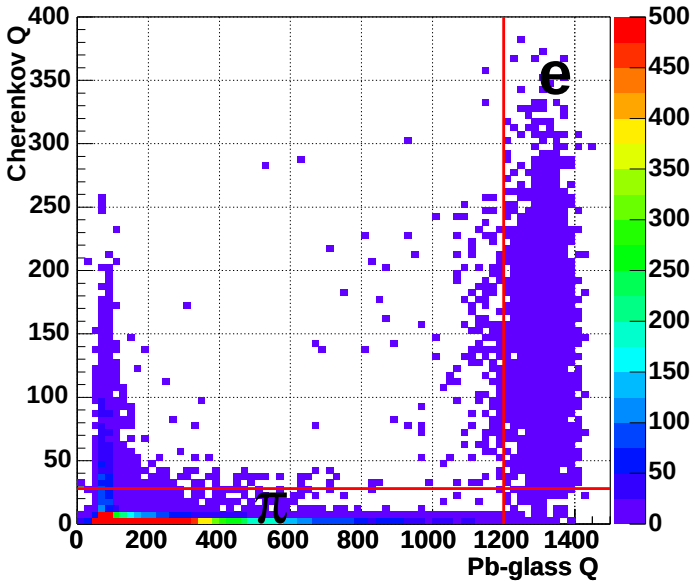

Figure 7.2: Correlated Cherenkov - Pb-glass signals. A good electron-pion separation is obtained with the cuts indicated by the red lines. The data were taken at a momentum of 6 GeV/c.

For Data Acquisition (DAQ) a *Multi Branch System* (MBS) [144] which was developed for experiments at the GSI, was used. In each detector eight pads were read out with a preamplifier/shaper (discrete PASA) and a *Flash ADC* (FADC) with a sampling frequency of 20 MHz.

In addition to the TRD modules the following detectors were used to obtain Particle Identification (PID), trigger and position reconstruction.

- Three scintillator counters (S1, S2, S3), with an area of 5×10 cm^2 each. The coincidence of the scintillators defined the beam trigger.

- Two Cherenkov detectors (Ch1, Ch2), each detector 2 meters long, read out via a mirror by photomultipliers.
  Ch1 was used in earlier tests at the beam facility at GSI Darmstadt, Ch2 was build in Dubna and used for the first time in the setup.

- A lead-glass calorimeter (Pb-glass), used also for electron-pion separation.

- Two silicon strip detectors (Si1, Si2) with an area of 32×32 mm^2 each. Both detectors have strips with 50 μm pitch in x and y direction adding up to 1280 channels per detector. The detectors are used for position reconstruction.

In a Cherenkov detector a charged particle emits Cherenkov light if its velocity, $v = \beta c$, is larger than the light velocity in the medium, c/n, where n is the medium refractive index. This electromagnetic process depends on the particle mass, m, and momentum, p, of the propagating particle, $\beta = \sqrt{1/(1 + \frac{m^2c^2}{p^2})}$.
In Pb-glass calorimeters electrons generate electromagnetic showers and produce higher signals, while pions lose energy only by ionization. For more details on these detectors see [118, 117].

Correlated electrons and pions signals at a momentum of 6 GeV/c of both detectors are shown in Figure 7.2 which indicates a good electron-pion separation.

7.2 General Signal Properties

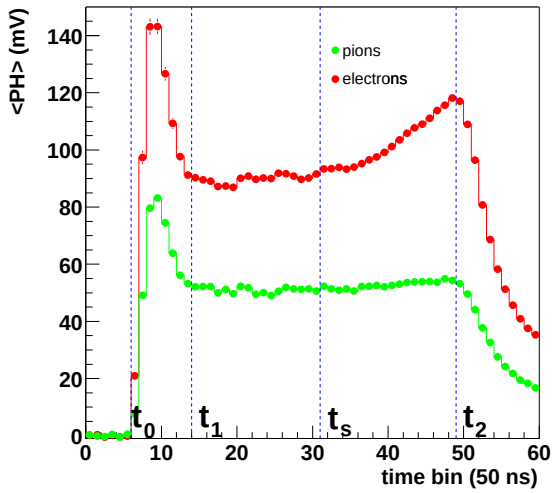

Figure 7.3: Average pulse height of electrons and pions as function of the drift time. The signal is measured at a momentum of 3 GeV/c, U$_a$ = 1.54 kV and Ud = −1.92 kV in Xe/CO$_2$ (86:14). The dashed vertical lines indicate the time intervals defined by t_0, t_1, t_2 and t_s.

Figure 7.3 shows the average pulse height, $\langle \mathrm{PH} \rangle$ of electrons and pions as functions of the drift time, which is measured in 60 bins of 50 ns each. The data were taken at a momentum of 3 GeV/c, an anode voltage of 1.54 kV, and a drift cathode voltage of -1.92 kV.
The starting point of the signal is assigned to bin number 6 (0.3 μs), labeled as t_0. At this time the amplification region starts and extends up to t_1, which separates the amplification region from the drift region. The latter ends at t_2. Due to the *ion tails*, Section 7.3, there is some ambiguity in determining t_2. It is set to be the time just where the drift plateau ends. The time $t_s = (t_1 + t_2)/2$ is also marked. It represents the time corresponding to the mid point of the drift region where the signal (S/N) is defined.

The average signal of electrons exhibits an evident increase towards longer drift time, this peak carries the signature of the transition radiation which is superimposed on the energy deposit by ionization in the gas. The peak around t_2 shows that most of the TR is absorbed in the vicinity of the entrance window of the chamber.
The peak has a tail through out the drift region towards shorter drift times, indicating that a certain fraction of the TR penetrates beyond the entrance region due to their higher energies, Section 7.7.

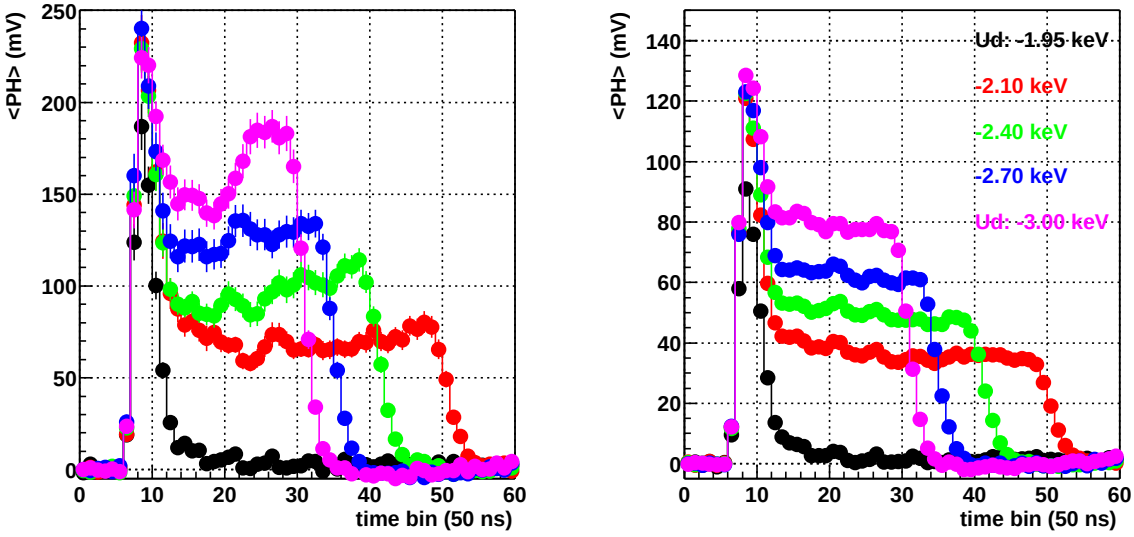

Figure 7.4: Average pulse height of electrons (left) and pions (right) as functions of the drift time for several drift voltages at an anode voltage of 1.6 kV and a momentum of 3 GeV/c.

The pion average signal, which originates from ionization energy loss, exhibits a slight increment towards later drift times. This effect comes from the build-up of currents in the chamber caused by the already mentioned ion tails in an avalanche around the anode wire.
The ions drifting away from the wires are slow due to their relatively large mass (xenon) and low mobility and therefore their average signals stretch over a time interval longer

than the duration of a time bin. In the next section, two methods of *tail cancellation* will be presented and their influence on the characteristic quantities of the detector will be discussed.

In coming sections the dependence of the average signals on the amplification voltage and the beam momentum will be studied, here only the influence of the drift voltage, U_d, on the pulse height is discussed by means of Figure 7.4.
Going from U_d = -1.95 to -3.0 keV the drift time gets shorter and the plateau gets higher (charge conservation). Also the amplification peak grows slowly due to cathode plane transparency.

From the signals in Figure 7.4 the drift velocity dependence on the drift field in the chamber can be calculated. The drift distance, Δs can be calculated from the angle $\alpha = 12°$ and the drift region depth $D = 30$ mm. With the measured drift time, $t_2 - t_1$, the drift velocity $v_d = \Delta s/\Delta t$ can be determined.
Despite the difficulty of establishing the right time corresponding to the chamber entrance, t_2, the calculated drift velocities are in good agreement with the GARFIELD simulation as can be seen in Figure 7.5.

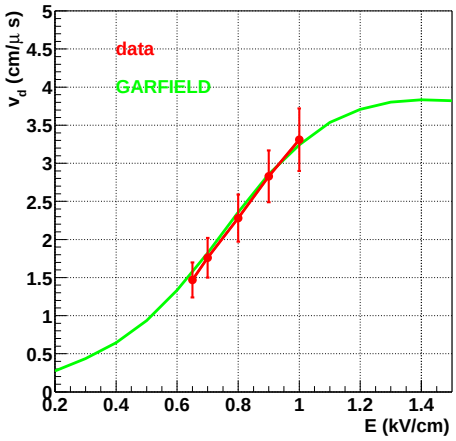

Figure 7.5: Drift velocity as a function of the drift field. The results (red) are compared to GARFIELD simulations.

7.3 Tail Cancellation

The signal tail observed in Figure 7.3 is a result of the slow movement of the ions drifting away from the anode wires. This slow movement induces a slowly rising signal on the pads. The signal of a time bin outlasts into the next time bin causing a tail. This correlation between the time bins makes the position and angular resolution performance sensitive to Landau fluctuations of the charge deposit [130].

The tail effect is shown in Figure 7.6 giving an example of the correlation between reconstructed angles and the shape of the signal. In the left panel the signals of two single events are shown. In the first case, green histogram, the signal weight is at the entrance of the chamber (large drift time). In the second case, red histogram, it is shifted towards the end of the chamber (low drift time). In each case the time averaged charge position, $t_{\langle Q \rangle}$, is marked by an arrow. The right panel shows the corresponding displacement from

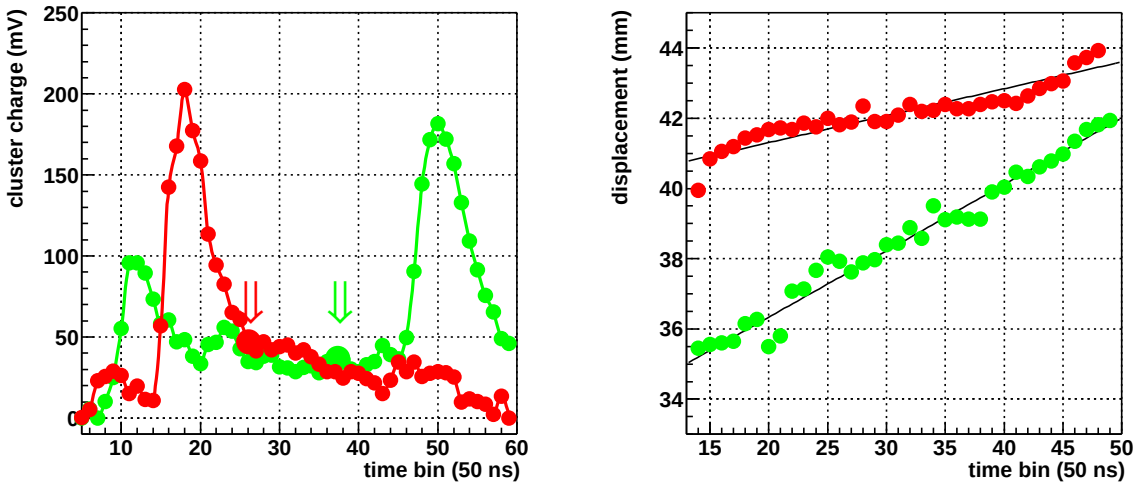

Figure 7.6: Left panel: Two examples of pulse heights integrated over all pads in the drift region. The time averaged charge position $t_{\langle Q \rangle}$, is indicated with arrows. The corresponding displacements are shown in the right panel. The lower is $t_{\langle Q \rangle}$, the shorter is the displacement, i.e. the smaller is the reconstructed angle. This effects results from ion tails in the signal.

the pad center. The reconstructed angles are smaller for events with larger clusters at the end of the drift time and vice versa.

The left upper panel of Figure 7.7 shows how the reconstructed angle distributions depend on the time of the average signal. The mean values of the reconstructed angles are shown by the symbols. For low $t_{\langle Q \rangle}$, i.e. at low drift times. the reconstructed angles are about 6 degrees, factor 2, smaller than the real one, 12 degrees. With increasing $t_{\langle Q \rangle}$ the reconstructed degrees approach this value.

In order to get rid of the systematic effect of the ions tail the so called *tail cancellation* is applied to the signal as an off-line software procedure which filters out the ion tail from it. By data taking it will be applied at the PASA level.
There are two levels of filtering: *one-exponential filter* (Filter1) and *two-exponential filter* (Filter2) [145]. The effect of the filters on the signals is illustrated in the bottom row of Figure 7.7. The filters eliminate the tail effects leading to a smooth drift plateau, apart from signal fluctuations, but they also cause a loss in the signal; up to 34% and 50% of the average signal are eliminated by Filter1 and Filter2 respectively.
Translated in detector performance these two effects mean good tracking and, as will be shown later they mean an enhancement in position and angular resolution, but deterioration of pion rejection factor.

Figure 7.8 shows the angular and position distributions for the three cases at a momentum of 3 GeV/c, U_a = 1.69 kV. The first filter improves the position resolution by 20% and

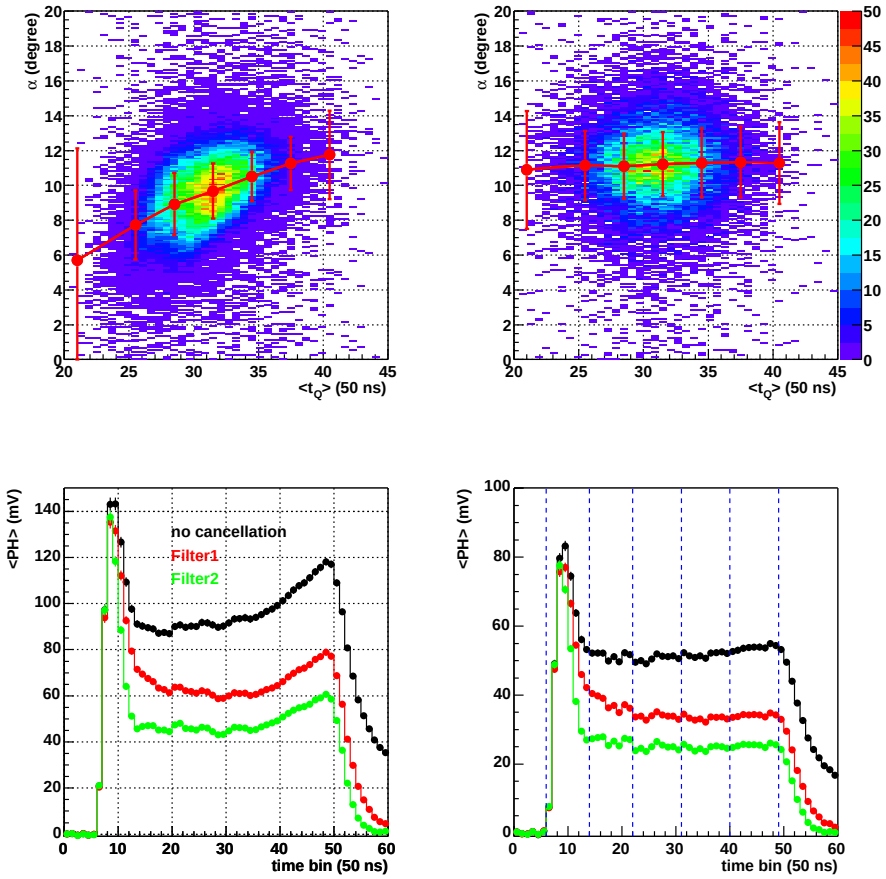

Figure 7.7: Upper row: The reconstructed angle as a function of the average charge position $t_{\langle Q \rangle}$. Left panel: before tail cancellation, right: after applying Filter2. Bottom row: The average pulse height of electrons (left) and pions (right) as function of drift time. The signal is measured at a momentum of 3 GeV/c, $U_a = 1.54$ kV and $Ud = -1.92$ kV in Xe/CO_2 (86/14). The black histogram shows the data before applying tail cancellation filters, the red histogram is the output of Filter1 and the green one results from Filter2.

the angular resolution by about 40%.
By the second filter the values worsen again, due to the signal loss and the consequent deterioration of the signal-to-noise ratio, see below.

The right panel of the upper row in Figure 7.7 shows the effect of the filter on the reconstructed angles. It shows the same angular distributions as in the left panel after applying Filter2. The reconstructed angles at low $t_{\langle Q \rangle}$ become closer to the real value. Due to the signal loss, a slight decrease is observed at high $t_{\langle Q \rangle}$ values.

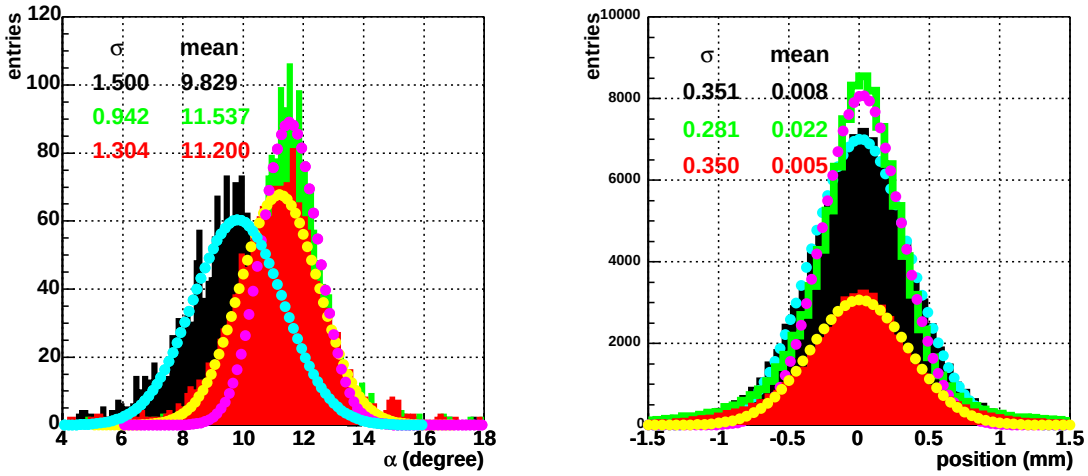

Figure 7.8: Angular and position distributions without filters (black) and with filters, green and red for Filter1 and Filter2 respectively. The incident angle is 12°, the data were taken at $p = 3$ GeV/c, U_a= 1.69 kV.

7.4 Signal and Noise

The signal is defined to be the *Most Probable Value* (MPV) of the Landau distribution which represents the charge deposited within the time bin corresponding to t_s, see Figure 7.3.
The noise is defined to be the standard deviation of the Gaussian fit applied to the noise distribution. This distribution presents the recorded pulses around the baseline in the drift time interval between 0 and $t_0 = 0.3$ μs where the signal starts. Figure 7.9 illustrates the definitions of signal and noise.

7.4.1 Noise

The left panel of Figure 7.10 shows the noise on eight pads of DC1, DC4, and DC5. The noise in DC5 is on average 3.5 times higher than in the other two chambers. Later investigations have shown that this large comes from insufficient shielding and grounding. Later tests, which aimed to repair for the observed noise by adequate shielding and grounding, have lead to a reduction of the noise to a value slightly below 1 mV.

Shielding screens sensitive electrodes in the detector from frequencies above 20 MHz. In shielding tests the read out sandwich was covered with metallic foils and achieved a decrement of the noise down to $\simeq$ 2.2 mV. In the final configuration the inner carbon fibre layer will be used as a grounded shielding plate, Section 4.3. The practicability of the method was prove in is extensive tests. The dark current (noise) in prototypes, which were built later, is below 1 nA. Note that the readout sandwich which is used in the chamber does not include the 2 mm thick honeycomb layer. Nevertheless, the cross talk noise between the

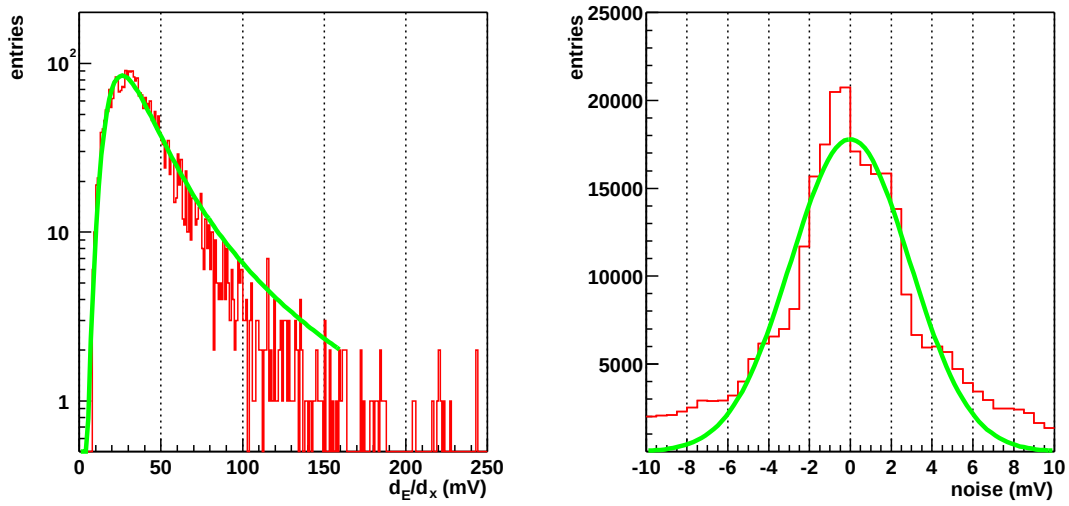

Figure 7.9: Signal and noise distributions at $U_a = 1.54$ kV, $U_d = -1.92$ kV and $p = 3$ GeV/c. The signal distribution, left, is recorded at $t = t_s$ and the signal value is the MPV of the Landau fit. The noise distributions, right, is the distribution of hits recorded in the time between $t = 0$ ns and $t = t_0$. The noise value is the standard deviation of the Gaussian fit.

pad plane and the sandwich inner side is negligible since the later consists from glass-fibre.

The grounding tests were aimed to define a suitable reference point for the PASA ground level. They have shown that the reference point on the detector should be as close as possible to the electronics unit. This reduces the inductivity of the detector and therefore the pick-up noise from the environment.

The right panel of Figure 7.10 shows the influence of the tail cancellation on the noise. The ion tails have low frequency, therefore the filters are designed to be efficient in this sector. Since the noise has a high frequence, it is not much affected by the filters.

7.4.2 Signal-to-Noise Ratio

Figure 7.12 shows the signal-to-noise ratio (S/N) as a function of the anode voltage for a 3 GeV/c pions at $U_d = -1.92$ kV. The highest S/N ratio at a given anode voltage is achieved without applying any signal filter. Due to signal loss, the ratio decrease by 34% and 50% under the influence of Filter1 and Filter2 respectively.

In all cases the high noise reduces the ratio down to a value below 6 at our nominal operation anode voltage of 1.5 kV. Since the filters do not affect the noise considerably but reduce the signal, they reduce the ratio considerably.
The dashed lines show the S/N ratio, with colors corresponding to the solid lines, which we would attain with the low noise achieved from reasonable shielding and grounding. At

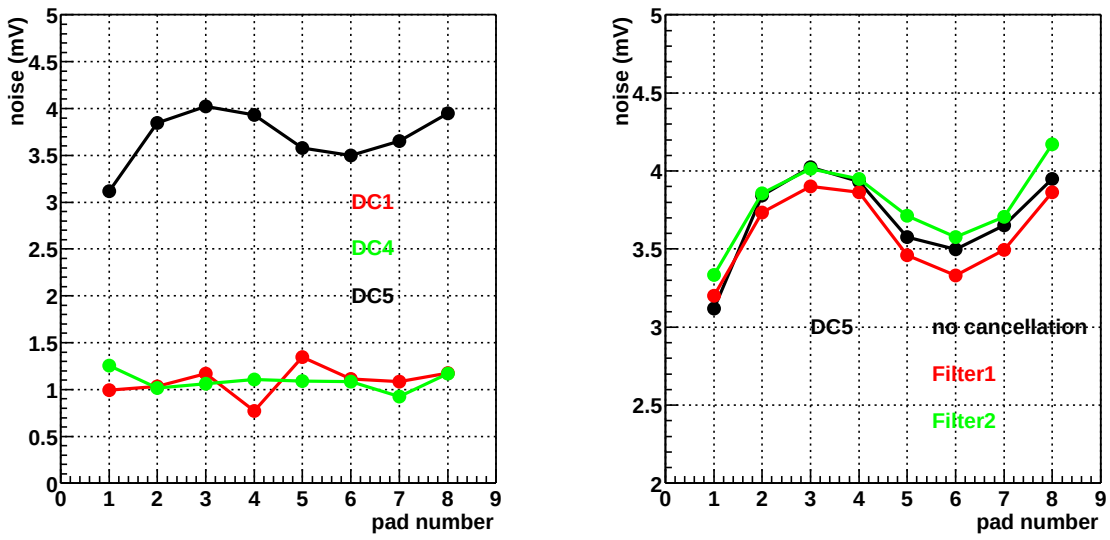

Figure 7.10: Left panel: Noise on each of the eight readout pads of three chambers On average the noise in the big chamber is 3.5 times higher than the noise in the small chambers. Right panel: Due to its high frequence the noise is not affected by the filters.

$U_a = 1.5$ kV we would reach a S/N ratio around 20 for pions. For electrons, and due to the TR signal, it reaches 28, which is within the anticipated regime.

7.5 Tracking and Position Reconstruction

7.5.1 Pad Response Function

Consider an avalanche inducing mirror charge over three adjacent pads of width W, a center one at coordinate x_i with the largest pulse height p_i and two neighboring pads at coordinates $x_i - W$ and $x_i + W$ with pulse heights p_{i-1} and p_{i+1} respectively. The pulse heights are normalized to the total pulse height, $p_{tot} = p_i + p_{i-1} + p_{i+1}$.

The *displacement* of the avalanche position, $\Delta x = x - x_i$ from the center of the central pad can be reconstructed by three methods: the *Center of Gravity* method (CoG), the *First Pad Response Function* method (PRF1) where a Gaussian shape of the pad response function is assumed and the *Second Pad Response Function* method (PRF2). In [130] it is shown that the CoG method gives the worst position resolution especially at low S/N ratio. Although the PRF1 leads to a higher number of reconstructed points, and thus to a better angular resolution, it can not describe measured PRFs, see below. The PRF2 method is a good compromise between noise sensitivity and number of reconstructed points, thus it was used to analyze the data.

Considering a Gaussian to describe the PRF (PRF1) gives:

$$\mathrm{PRF}(x) \simeq \mathrm{e}^{-x^2/\sigma^2}, \tag{7.1}$$

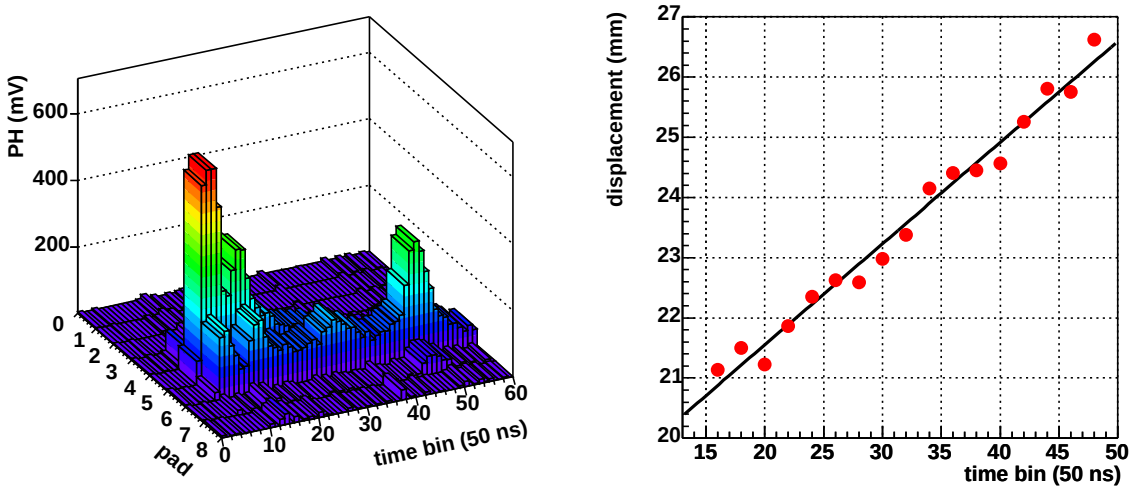

Figure 7.11: Left panel: pulse height of a single electron event in the drift and amplification region on eight pads in connection with the drift time. Right panel: the displacement as calculated according to Equation 7.4.

where σ is the FWHM of the PRF distribution:

$$\sigma^2 = \sigma_0^2 + \sigma_{\mathrm{diff}}^2(z, \mathbf{B}) + \alpha^2 l^2/12.$$

The last two contributions to σ^2 are caused by the diffusion in the gas and the track inclination respectively. Both are negligible for the ALICE TRD, σ_{diff}^2 because of the negligible diffusion in the TRD gas mixture, compare Table 5.2, and the last because of sampling the drift time in 20 time bins. For each bin, α, the angle between the track and the perpendicular to the pad plane, is very small. l is the considered track segment within one time bin.

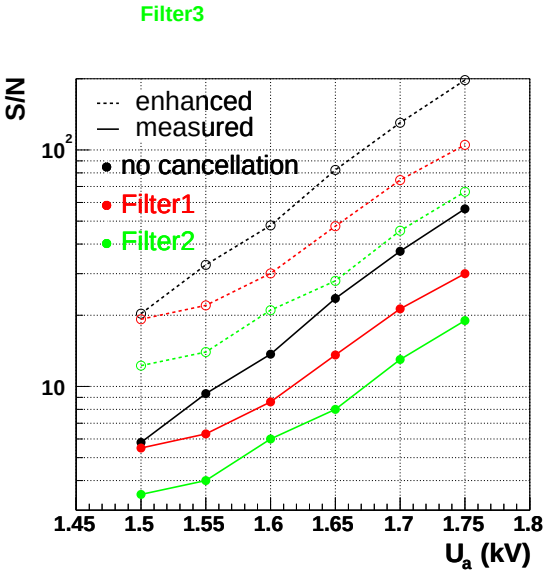

Figure 7.12: Signal-to-noise ration as a function of U_a.

With equation 7.1 (PRF1) the pulse heights of neighboring pads, see above, are correlated to the positions via:

$$\begin{aligned} p_{i-1} &= A\mathrm{e}^{-(\Delta x - W)^2/2\sigma^2}, \\ p_i &= A\mathrm{e}^{-(\Delta x)^2/2\sigma^2}, \\ p_{i+1} &= A\mathrm{e}^{-(\Delta x + W)^2/2\sigma^2}, \end{aligned} \qquad (7.2)$$

with the amplification factor A. Solving equations 7.2 for Δx gives the displacement without a priori knowledge of the pad response function, i.e. the parameter s and A.

$$\Delta x = \frac{W}{2}\frac{\ln(p_{i+1}/p_{i-1})}{\ln(p_i^2/p_{i-1}p_{i+1})}. \tag{7.3}$$

With the silicon strips Δx is measured and related to the pulse heights on the pads of the chamber. Figure 7.13 shows the results of the relative pulse height on the central pad as a function of Δx normalized to the pad width, $W = 8.25$ mm. It is evident that the shape of the measured PRF is not exactly described by a Gaussian fit (red points) and thus Equation 7.3 does not describe the hit position in the chamber. Compared to the calculated PRF in Figure 5.6, the measured one is wider. It was found [130] that this broadening effect is a result of the capacitive cross-talk between adjacent pads.
From the figure it is seen that about 80% of the signal are induced on the center pad. The FWHM of about 0.8 implies a good position and angular resolution capability of the chamber.

With the determination of σ, the displacement of the hits from the center of the central pad, can be determined either from the ration $(p_i/p_{i-1}) = \exp[(2xW + W^2)/2\sigma^2]$ or the ratio $(p_{i+1}/p_i) = \exp[(2xW - W^2)/2\sigma^2]$. The results achieved from the combination of both are much better:

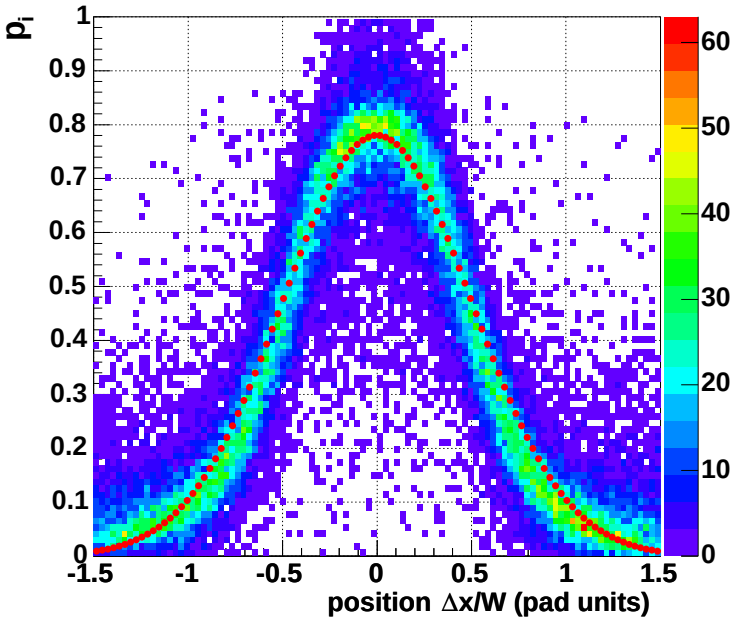

Figure 7.13: Measured PRF with pad width $W = 8.25$ mm, as a function of x in units of W. The red symbols represent a Gaussian fit to the mean pulse height ratio at given position.

$$\Delta x = \frac{1}{w_1 + w_2}\left[w_1\left(-\frac{\mathrm{W}}{2} + \frac{\sigma^2}{\mathrm{W}}\ln\frac{p_i}{p_{i-1}}\right) + w_2\left(\frac{\mathrm{W}}{2} + \frac{s^2}{\mathrm{W}}\ln\frac{p_{i+1}}{p_i}\right)\right], \tag{7.4}$$

where w_1 and w_2 are the weights of two measurements, the first done with the central pad and pad $i-1$ and the other with the central pad and pad $i+1$. The measurement error is roughly proportional to the pulse heights on the neighboring pads, thus w_1 and w_2 can be considered to be equal to p_{i-1}^2 and p_{i+1}^2 respectively [118].

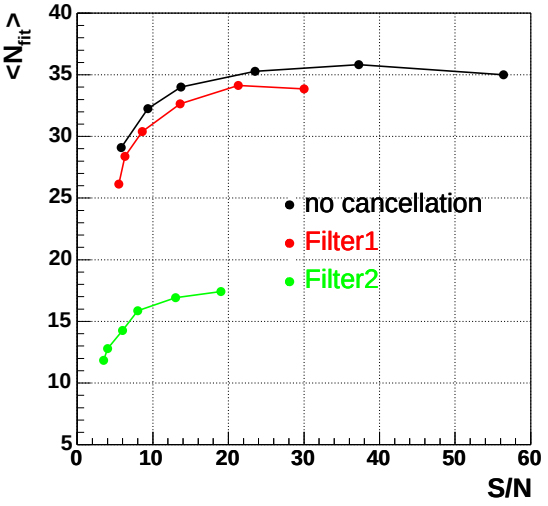

Figure 7.14: The average number of the reconstructed points which are used to calculate the reconstructed angles, as function of the S/N ratio.

For an electron event the displacement for all time bins is calculated corresponding to times greater than t_1 according to Equation 7.4. Since the drift velocity in the drift region is constant the displacement is a linear function with v_d representing its slope. For the 30 mm deep drift region and the incident angle of 12° along the anodes, a deflection of 6.4 mm is expected. The data reproduce this value as shown in the right panel of Figure 7.11. Notice that only after applying the filters the measured displacement reproduces the real displacement, see Figure 7.6.
The right panel shows the pulse height of the same event over all time bins and over the 8 readout pads. Both, the TR and the amplification peaks are observable.

7.5.2 Position Reconstruction Performance

The quality of the tracking in the chamber is characterized by the number of independent points, N_{eff}, which one can reconstruct along the trajectory of the particle. Usually the hits are statistically dependant and the number of points one gets by fitting the track N_{fit} is larger than N_{eff}. Evidently this is a consequence of the ions tail which smears the points so that many of them can not be considered independent.
Figure 7.14 shows N_{fit} as a function of the S/N ratio. With non filtered data, N_{fit} increases up to 35 and saturates at S/N of about 20. With Filter1, N_{fit} is slightly lower than the non filtered case and saturates at about 34. Finally, N_{fit} is much lower in the case of Filter2. It does not saturate in the measured region.
The decrease of N_{fit} with the filters results from the loss of the signal amplitude. The cluster charge in many points falls below the filter threshold of 10 mV.

The reduction of the reconstructed points is the result of compromising between S/N ration and the enhancement of the position and angular resolution.

7.5.2.1 Position Resolution

The anticipated position resolution in the bending direction x in a TRD module is 400 μm at a S/N ratio of about 25.

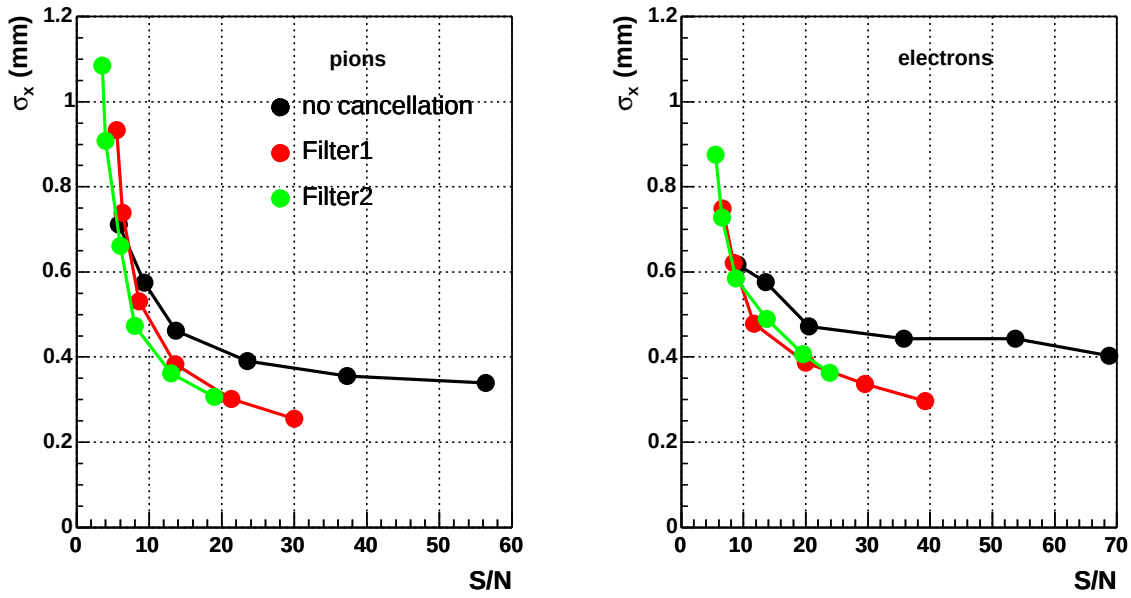

Figure 7.15: Position resolution as function of S/N ratio pions and electrons, with and without tail cancellation.

Figure 7.15 shows the position resolution as a function of the S/N ratio for pions and electrons, with and without tail cancellation. In the non filtered pion results the position resolution tends to saturate by S/N of about 30 (U_a = 1.65 kV) at 360 μm. The signal loss caused by the filters shifts their curves towards low S/N. None of the filtered data saturate but they reach, due to the enhancement of the independency degree between the points (N_{eff}), lower position resolutions. In both filtered cases the anticipated position resolution is reached already at S/N below 11 - 13.
Due to TR signals and bremsstrahlung, the non filtered electrons data saturate at lower values of S/N ratio ($\simeq$ 20). Only the filters enable an approach of the anticipated value.

At the TRD nominal anode voltage of 1.5 kV the S/N was 6 (8) for pions (electrons). The position resolution at these values is higher by more than factor 2 than the anticipated value. Recalling the high noise in the chamber and the proven possibility of its reduction, the S/N ratio can be enhanced by up to 20 for pions and 28 for electrons where the position resolution is about 300 μm for pions and 380 μm for electrons.

7.5.2.2 Angular Resolution

Figure 7.16 shows the angular resolution under the same conditions as in the position resolution case.

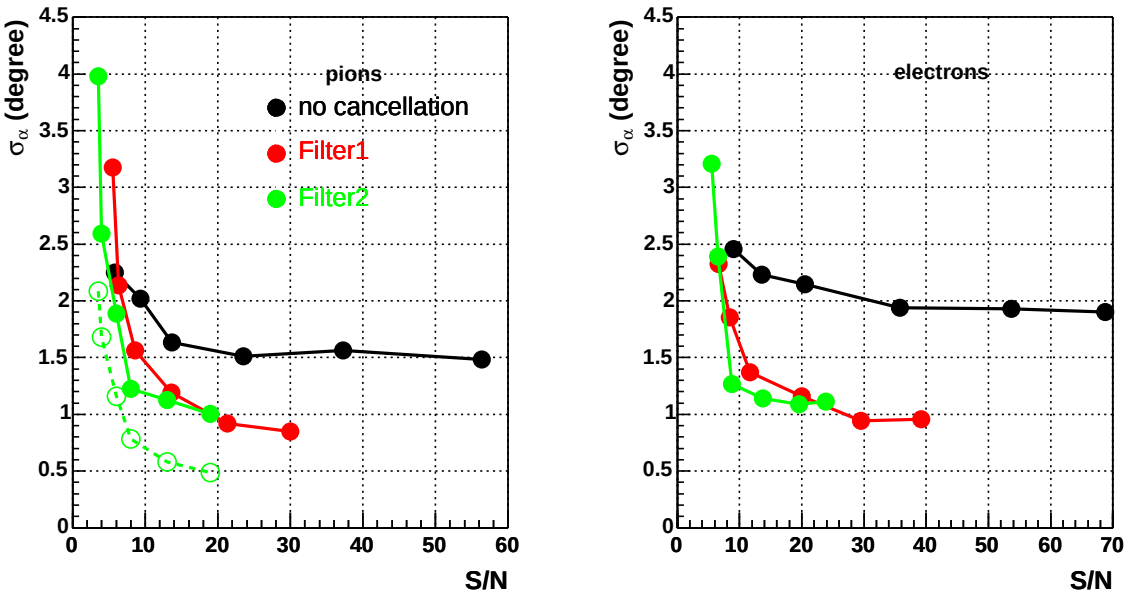

Figure 7.16: Angular resolution as function of S/N ratio pions and electrons, with and without tail cancellation.

Also the angular resolution of non filtered data saturates above relatively low S/N ratios. The filters enable resolutions around 1 degree already at S/N values of 15-20 for both pions and electrons. They reduce the resolution values by more than 30% for pions and 50% for electrons.

The angular resolution σ_α is related to the position resolution σ_x via N_{eff}:

$$\sigma_\alpha \simeq \sqrt{\frac{12}{N_{eff}}} \cdot \frac{\sigma_x}{D}, \tag{7.5}$$

where D is the depth of the detector. The N_{fit}-S/N curve saturates at $N_{fit} \simeq 35$ in the non filtered case and at 34 (19) in the first (second) filtered case, compare Figure 7.14. The pion data in Figure 7.16 show that this relation does not agree with the data, the dashed line represents σ_α as calculated from Equation 7.5 for the second filter case. The measured data are worse by factor 2 than the calculated ones. N_{fit} is taken as in Figure 7.14. This means that there is still some correlation between the time bins ($N_{eff<N_{fit}}$).

7.6 Signal Charge

7.6.1 Qualitative Considerations

Figure 7.17 shows the pulse heights of electrons and pions as functions of the drift time for different values of the anode voltage U_a.

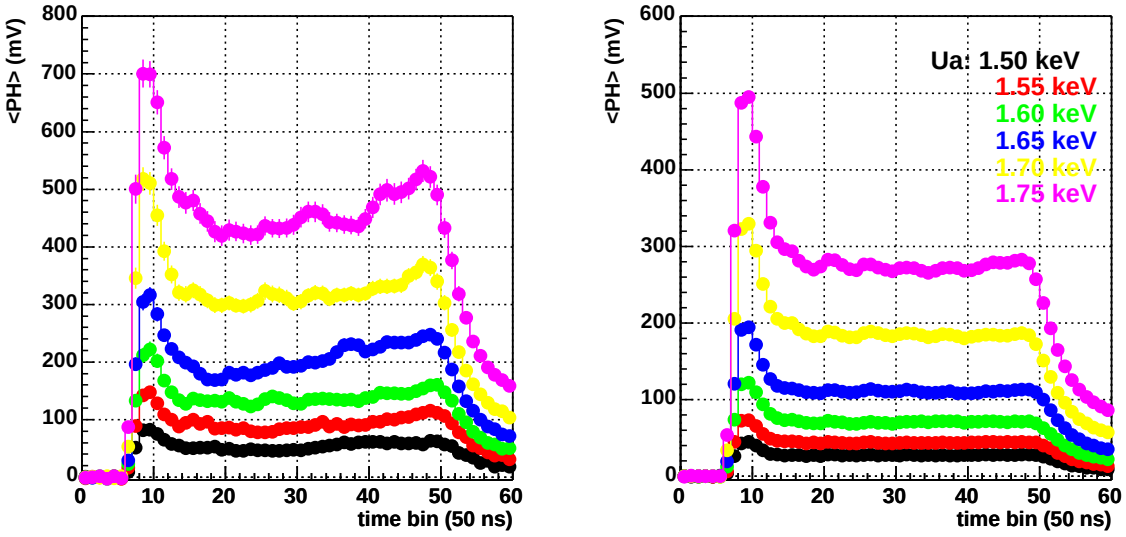

Figure 7.17: Pulse heights of electrons (left) and pions (right) as functions of the drift time for several anode voltages at drift voltage of -2.25 kV and a momentum of 6 GeV/c.

Denoting the charge recorded in the amplification region with $Q_a = \int_{t_0}^{t_1} \langle PH \rangle dt$ and that recorded in the drift region with $Q_d = \int_{t_1}^{t_2} \langle PH \rangle dt$, their ratio $Q_{ratio} = Q_d/Q_a$ and their sum $Q_{sum} = Q_d + Q_a$ can be defined.

Figure 7.18 shows Q_{sum} and Q_{ratio} as functions of U_a. Q_{sum} gives an impression of the gas gain dependence on U_a. Q_{ratio} tells of the influence of the space charge on U_a. In Section 5.5 this effect and its dependence on the chamber parameters were briefly discussed and Figure 5.14 showed how it depends on the incident angle and the gas gain (U_a): at zero degree it reaches a maximal value and decreases with increasing angle.

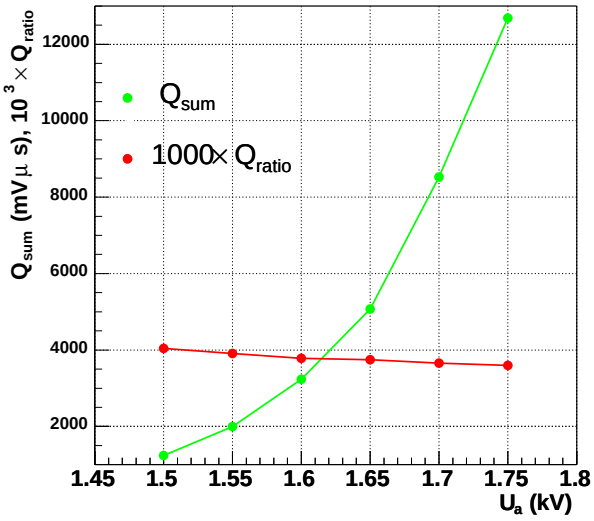

Figure 7.18: $1000 \times Q_{ratio}$ and Q_{sum} as functions of U_a. Q_{sum} gives a qualitative impression on the gas gain in the chamber. Q_{ratio} shows a gain reduction which could be an indication of the space charge effect.

At a certain angle this effect is apparent at higher anode voltages where the avalanches frequency increases. After a certain

point the avalanches screen subsequent signals from being amplified.
In this case only a qualitative study of the effect is possible.
For the big chamber one could study the last case, one angle with varying amplification voltage, via Q_{ratio}. It falls slightly but systematically with U_a. Since all measurements were performed under the same conditions, this reduction points to a gain saturation in the chamber.

Relative to Q_{ratio} at 1.5 kV the effect makes about 6% at 1.6 kV and 9% at 1.7 kV. Notice that the beam is at 12 degrees with respect to normal incidence. Lower angles would increase this value.
The effect as a function of the incident angle was studied in detail for the case of the small prototypes. The results are discussed in [128].

7.6.2 Gas Gain

In Subsection 6.6.1 the uniformity aspect of the gas gain all over the chamber and its dependence on the overpressure were discussed. The gain variation is acceptable under the operating conditions. With the taken data absolute gain values can be calculated.

Figure 7.19 compares the measured gas gain with GARFIELD calculations as a function of the anode voltage. The measurements agree with the GARFIELD simulation.

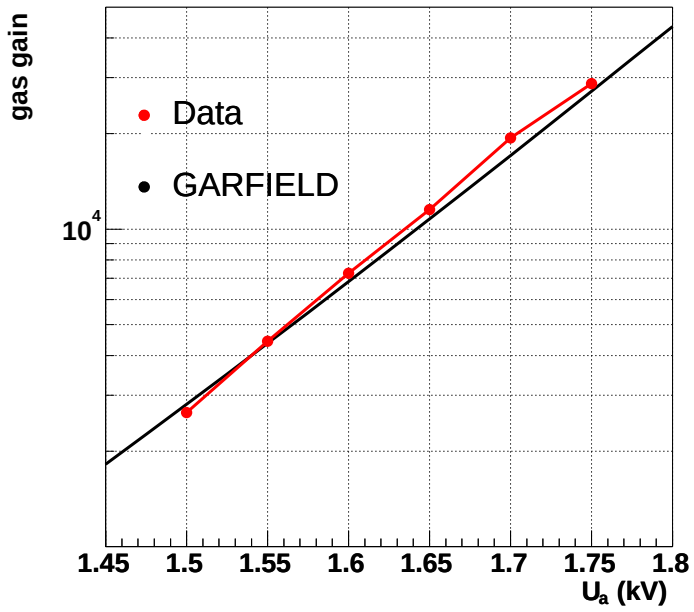

Figure 7.19: Measured gas gain as a function of U_a (red) is in good agreement with GARFIELD calculations (black). Q_{sum} is also shown.

7.7 Transition Radiation Performance

The main task of the ALICE TRD is to identify electrons with momentum above 1 GeV/c and to separate them from pions. The anticipated pion efficiency, π_{eff}, is around 10^{-2}. In this section the π_{eff} of the real dimension prototype will be discussed, the results will be compared to those of the small chambers and to the "universal" curve in Figure 4.1.

7.7.1 Electron and Pion Distributions

Consider the bottom row of Figure 7.7 again and subdivide the drift region in four time intervals with a width of $(t_2 - t_1)/4$ each. The amplification region represents a fifth interval. The intervals are indicated with the blue vertical dashed lines in the figure (going from the amplification region to the chamber entrance the regions are denoted by 1 to 5). In each interval the ratio of the electrons pulse height to that of the pions is build in each time bin and the average is taken;

$$Q_{ratio} = (\sum_{bin} Q_\pi/Q_e)/n_{bin}$$

. Figure 7.20 shows Q_{ratio} for all chambers DC1 - DC5, operated with the same radiator type.

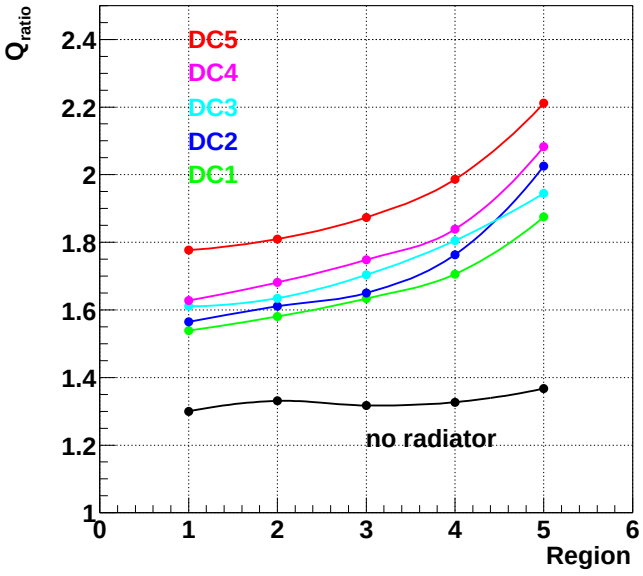

Figure 7.20: Electrons to pions signal ratios in four regions of the chamber, see text, The TR signature is evidently seen in region five which represents the entrance of the chamber in the neighborhood of the radiator. Compared to non-radiator measurements, the date show that the TR signal extends into the whole chamber depth, also in the amplification region.

The figure contains the following information:

1. Consider the curves which represent DC1 and DC5. The TR signature is in region five at the entrance of the chambers, where most of the TR is absorbed and thus enhancing the electrons signal. Both curves decrease down to a value of 1.55 (DC1) and 1.78 (DC5) in region one (amplification).

2. This behavior reproduces the already mentioned propagation of some high energy TR photons deeper in the drift and even in the amplification region causing an enhancement in the electrons signal of about 11% (DC1) and 35% (DC5). This is seen by comparing the curves with the black one which represents the ratio in DC1 when operated without radiator.

3. Including the other three chambers, the ratios, i.e. the electrons signal, increases when going from DC1 to DC5. This increment could be the consequence of some high energy TR photons which penetrate through the layers. Some of them propagate even through more than one layer, otherwise all the last four chambers would have more or less the same ratio.

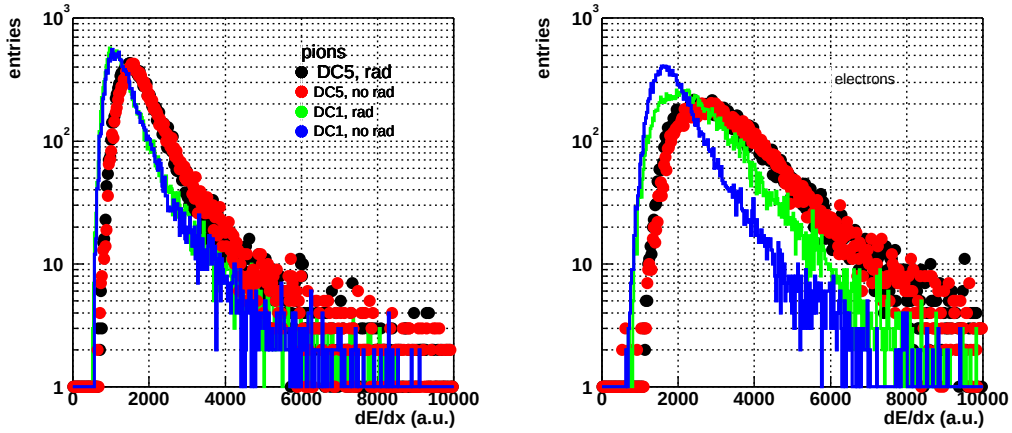

Figure 7.21: Electron and pion energy deposit distributions in DC1 and DC5. The difference in the electron signal of DC1 originates from TR.

7.7.2 Quantitative Yield of the TR

Up to now the TR signature was described qualitatively. To get a quantitative idea of its yield the electron signal is considered in drift chambers without radiator which include only ionization signals of the primary particles, $E_{tot} = E_{ion}$, and that of a detector with a radiator in front of its entrance window. This signal includes the TR signal in addition, $E_{tot} = E_{ion} + E_{TR}$. Theirin is E the MPV of the electron distribution and P is the corresponding signal of the pions. The TR yield is simply the difference between these two quantities. This simple way works only for the small detectors which were operated with and without radiator. The radiator of the big detector was permanently attached to

its entrance frame and another detector must be taken as a reference to calculate the TR yield.

To achieve this goal two situations were considered: Situation I describes runs where all chambers were operated with the nominal TRD foam-fibre radiator, and situation II describes runs where only the big chamber was operated with a radiator. Apart from these differences, the running conditions where the same. The left panel of Figure 7.21 shows the pions energy deposit distributions of DC5 and DC1 in both situations. In both cases, the spectra of each chamber agree with each other ($P_{1,I} = P_{1,II}$ and $P_{5,I} = P_{5,II}$). In the right panel shows the corresponding electron distributions. The electrons signals recorded in DC5 agree with each other but not those of DC1. The difference between them originates from the TR signal.

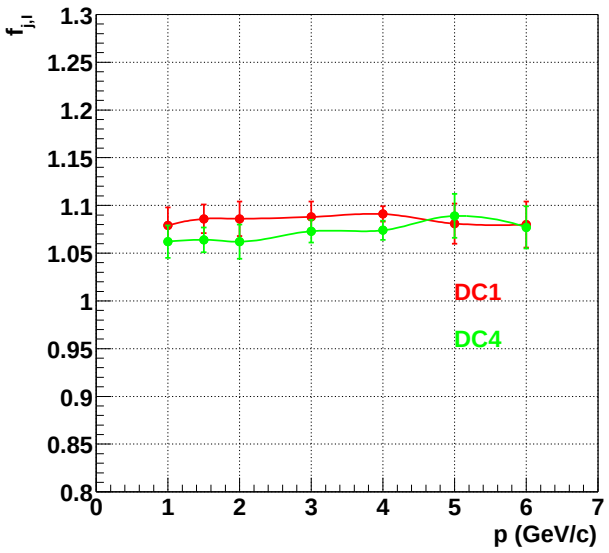

Figure 7.22: The factor $f_{j,I}$ as defined in Equation 7.6 as a function of the beam momentum for the chambers DC1 and DC4. It can be considered to be equal for all chambers and momenta. Notice that it is above unity due to the TR yield.

Define the factors $f_{j,I}$ to be:

$$\frac{E_{j,I}^{tot}}{E_{5,I}^{tot}} = f_{j,I} \cdot \frac{P_{j,I}}{P_{5,I}} \Rightarrow f_{j,I} = \frac{E_{j,I}^{tot} \times P_{5,I}}{P_{j,I} \times E_{5,I}^{tot}}. \tag{7.6}$$

Considering situation I and denoting the individual small chambers with $j = 1, 2, 3, 4$. The subscript 5 stands for the big chamber and tot denotes the whole recorded charge as described before.

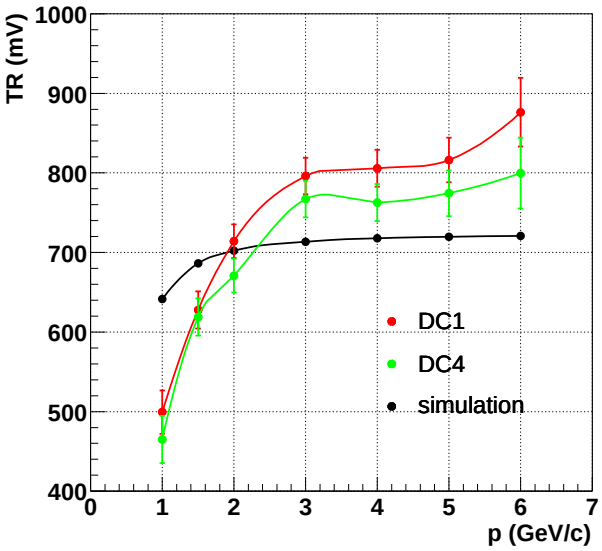

Figure 7.23: TR yield in DC5 as function of beam momentum. The green and red curves show the results when referring to DC4 and DC1 respectively. The black curve shows simulated TR yield which is detected in an ALICE TRD chamber, see text.

In all chambers and for all momenta the factor which relates the signals of two chambers to each other, can be considered to be equal under all conditions. As an example $f_{1,I}$ and $f_{4,I}$ are shown as functions of the beam momentum in Figure 7.22.
It can be concluded that the factors should behave as well in runs without radiators (also in situation II) therefore the subscript I can be rejected, $f_4 =: f_{4,I}$. Applying Equation 7.6 to the signals of DC4 and DC5 in situation II results in:

$$E^{ion}_{5,II} = \frac{E_{4,II}P_{5,II}}{f_4 P_{4,II}}, \tag{7.7}$$

with E^{ion}_5 being the electron signal which one would get if DC5 were operated without radiator. Subtracting E^{ion}_5 from the measured electrons signal in DC5 gives the TR yield:

$$E^{TR}_5 = E^{tot}_{5,II} - E^{ion}_5. \tag{7.8}$$

These results are shown in Figure 7.23 as a function of the beam momentum. The green curve represents the TR yield in DC5 if DC4 is taken as a reference and the red curve results if referring to DC1.
The results are also compared to simulations of a regular radiator from [129].
In the simulations the foil thickness of the radiator is 10 μm and the gap between two foils is 80 μm.

The effective number of foils is 270, see Equation 3.11. The parameters were tuned to reproduce the spectra of a non-regular foam-fibre radiator of the same type as the radiator used DC5, but with a Rohacell sheet thickness of 6 mm and 8 fibre mats in between. Notice that The DC5 radiator consists of 8 mm thick Rohacell sheets and 7 fibre mats in between.

Since the simulations in the reference are given in energy units, keV, and we do not aim to make a quantitative comparison to them here, we multiplied them with factor 75 to enable a qualitative estimate of the data behavior.
In the reference the simulated results are compared to data of the small chambers of our tests. It is shown that the simulations overestimate the TR yield at low momenta and underestimate it at high momenta. This effect is also seen here, indicating that the behavior of DC5 in terms of TR yield shows the same trend.

7.8 Pion Rejection

This section will give a quantitative description of the ALICE TRD's capability to discriminate electrons from pions. The discrimination is done by means of the distributions of the particles energy loss in the chamber. The left panel of Figure 7.24 shows these distributions of both particle species. The electrons are represented by the green and the blue areas and the pions by the black and the red areas.

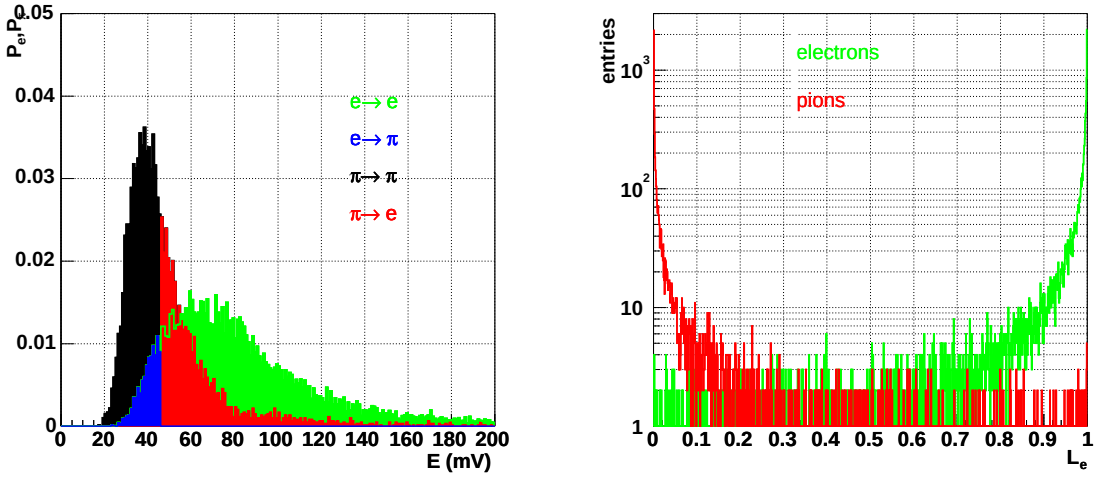

Figure 7.24: Left panel:Probability to detect an electron, red, or a pion, blue, of amplitude E. Right panel: The likelihood for a particle to be an electron.

7.8.1 Pion Rejection with one TRD Layer

The pion rejection factor is defined by $R_{\pi/e} = e_{eff}/\pi_{eff}$, where π_{eff} and e_{eff} are the detection efficiencies of the TRD for both particle species. e_{eff} is defined by a cut in the electron distribution at the boundary between the green and the blue areas in the left panel of Figure 7.24. The area of the pion distribution beyond this cut (red) defines the contamination of the electrons by the pions. Usually e_{eff} is fixed to 90% and $R_{\pi/e} := 1/\pi_{eff}$. In [130] the results of studies on the pion efficiency are shown for e_{eff}

values down to 80%. Going from $e_{eff} = 90\%$ to $e_{eff} = 80\%$, the π_{eff} is reduced by factor 2. However losing 20% of the electrons reduces the probability of recording enough Quarkonia. In addition, with $e_{eff} = 90\%$ one is still on the safe side as the referred tests show. This study therefore fixes e_{eff} to 90% for all results presented in this section.

There are several methods to analyze the data and separate electrons from pions. In all studies by the ALICE TRD group three of them were considered [130]: truncated mean of integrated energy deposit, likelihood on integrated energy deposit (L-Q) and two dimensional likelihood on energy deposit and position of the largest cluster found in the drift region of the detector (L-QX).

In the first method the highest signals are excluded from the calculated mean of the energy deposit. In this way one eliminates the δ-electron contributions in the signal. The cut should be fixed carefully to avoid loosing high TR-signals. Usually up to four pulses out of ten are excluded [122]. Earlier studies [130] showed that this method delivers the worst pion rejection.

In the L-Q method one normalizes the pulse height distributions to a unity area and considers it to be a probability distribution, $P(E)$, for the corresponding particle to generate a certain signal in a TRD chamber. In this sense the distributions in Figure 7.24 are the probability distributions, $P_e(E_1)$ and $P_\pi(E_1)$, of electrons and pions as measured in DC5. E_1 is the signal amplitude and the subscript 1 denotes that only one chamber was considered.

The L-QX method is an extended version of the L-Q and is considered to be one of the most promising procedures to analyze the TRD data. It enhances the results of the L-Q method by 15% to 20%. Since this thesis aims to study the TRD's capability of identifying electrons, the L-Q method was considered which is a lower limit of what will be the outcome when using the L-QX method.

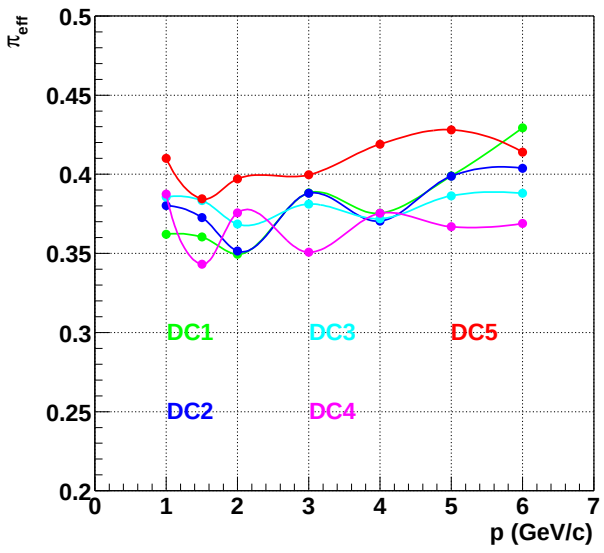

Figure 7.25: Pion efficiency as a function of the beam momentum for all five chambers.

The likelihood of recognizing a particle as an electron is given by:

$$L_e = \frac{P_e}{P_e + P_\pi}. \qquad (7.9)$$

When the detected particles are electrons, the L_e distribution peaks at unity and drops with a tail towards zero. Calculating L_e for pions gives the probability for them to be

misidentified as electrons. This distribution peaks at zero and has a tail towards unity. The right panel of Figure 7.24 shows the likelihood of a detected particle being an electron.

Figure 7.25 shows pion efficiency of each of the five chambers which result from applying the described method to the data.

In all chambers there are statistical fluctuations, but nevertheless one observes a general trend of the pion efficiency dropping between 1 GeV/c and 2 GeV/c where it starts to increase due to the pion relativistic rise. All chambers reach a pion efficiency between 0.35 and 0.42 over the whole momentum range in consideration. Recalling that the chambers are of a depth of 8.5 cm and referring to Figure 4.1, this is a good performance. Due to larger noise, the big chamber performs slightly worse compared to small prototypes.

7.8.2 Pion Rejection with Six TRD Layers

The atomic weight of the radiator material and the consequent TR photons absorption, makes it necessary to use a multi layer detector. This is evident from Figure 7.25. The values of π_{eff} can be enhanced considerably by combining the chambers performances.

The electron likelihood of Equation 7.9 is also valid for the multi layer case. From the probabilities $P_e(E_i)$ and $P_\pi(E_i)$ of the electrons and pions in a single layer, one gets the total probabilities $P_e(E)$ and $P_\pi(E)$.

$$P_e = \Pi_{i=1}^{N} P_e(E_i), \qquad P_\pi = \Pi_{i=1}^{N} P_\pi(E_i). \tag{7.10}$$

Figure 7.26 shows the pion efficiency attained from the four small chambers and how DC5 enhances it by approximately factor 2.

In Figure 7.27 the pion efficiency is shown as a function of the total depth of the chambers at 2 GeV/c. For the final ALICE TRD status (6 layers) the data were extrapolated. With $\pi_{eff} = 0.0105$ the anticipated value is reached.

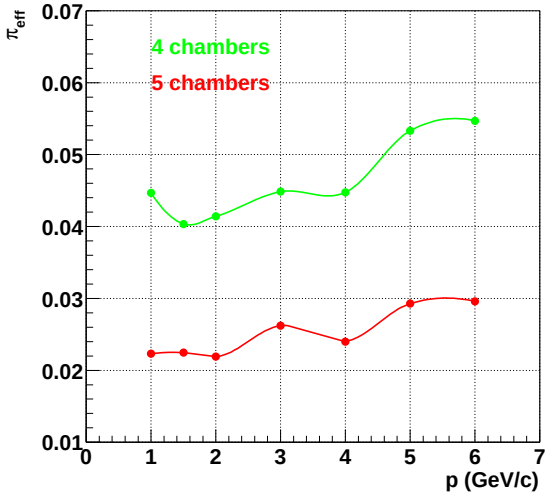

Figure 7.26: Pion efficiency of the combined small chambers, green, and the enhancement generated from DC5, red.

In the left panel of Figure 7.28 π_{eff} is shown as a function of the momentum, the values are extrapolated for 6 layers. Also in this case the tendance of

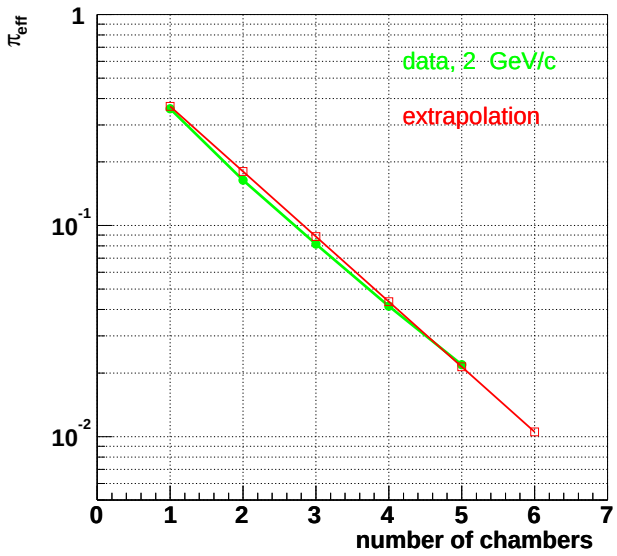

Figure 7.27: Pion efficiency as a function of detector depth for particles momentum of 2 GeV/c.

π_{eff} to drop for momenta below
2 GeV/c and to rise for higher momenta is observed.

The right panel of Figure 7.28 shows the extrapolated pion efficiency data up to $p = 50$ GeV/c where 96% of the pions can still be rejected. The extrapolation results in the following $\pi_{eff}(p)$ parameterization, which will be used in the physics performance simulations in Part III:

$$\pi_{eff} = \left\{ \begin{array}{lll} 0.015197 - 0.002345 \cdot p, & : & p < 2 \text{ GeV}/c \\ 0.008082 + 0.001198 \cdot p, & : & p \geq 2 \text{ GeV}/c \end{array} \right\}. \tag{7.11}$$

Finally the pion efficiency increases with the amplification voltage at low particle incidence angles [130]. With increasing angles π_{eff} drops and an enhancement of 2% is achieved when going from 1 to 17 degrees. The results of the big chamber are obtained at an incidence angle of 12 degrees. At zero degree, π_{eff} would not deteriorate more than 2%. The increasing of the pion efficiency with higher gain and lower incidence angle is related to the space charge effect in the chamber [130, 128].

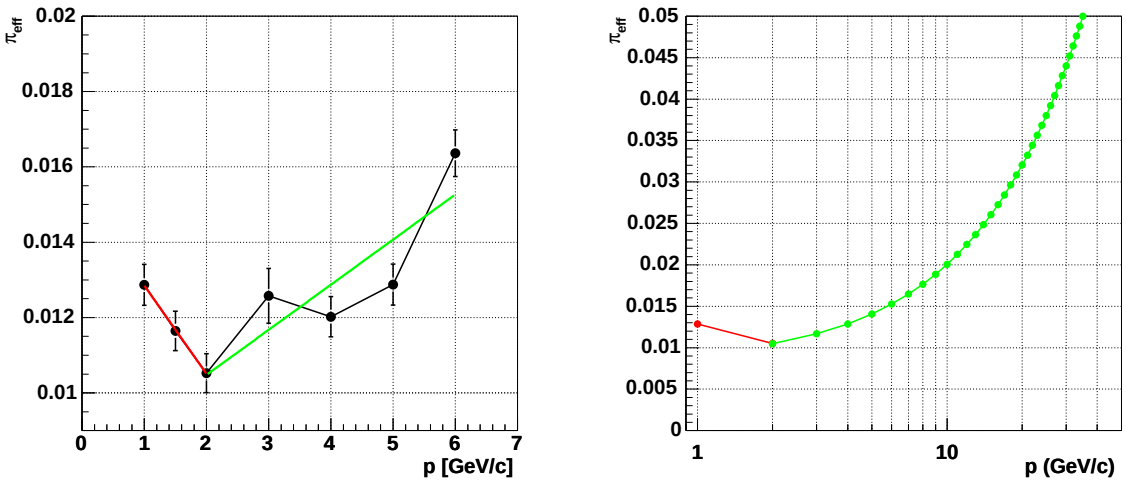

Figure 7.28: Left panel: Pion efficiency as a function of the beam momentum extrapolated from five to six layers. The green (red) lines give the fits of the data in the indicated ranges. Notice that the results are achieved from analyzing the pulse height in the drift and the amplification regions only (between t_0 and t_2, compare Figure 7.3). The results in Figure 7.27 include data beyond t_2 (tail). Right panel: The extrapolated data of the left panel up to a momentum of 50 GeV/c where one is still able to reject 93% of the pions.

Part III

Physics Capabilities

Chapter 8

Di-electrons and Heavy Quarkonia in Heavy-Ion Collisions

Two reasons make di-lepton measurements one of the most powerful tools to study physics of heavy-ion collisions. Firstly: Like photons, they are not subject to strong final-state interactions and therefore they are only slightly perturbed after their production. Compared to photons, di-leptons have the advantage of being massive and therefore their production processes can be determined by calculating invariant mass spectrum. Secondly: Depending on this invariant mass, and since di-leptons are emitted throughout the entire collision evolution, they can probe different stages of the collision.
Thereby the di-lepton channel of heavy Quarkonia decays plays a key role, because heavy Quarkonia are expected to be sensitive to QGP formation and, as hard probes, they allow an access to the initial state of the interaction.
However, specific detectors are needed to enable the identification and collection of interesting di-leptons with their small cross sections among a huge amount of background particles. Detectors such as the ALICE TRD which identify and trigger on electrons, are of certain importance in this sector.

In this part of the thesis, Quarkonia di-electron decays will be studied in the ALICE Central Barrel (ACB). Three detectors are involved in these studies; ITS, TPC, and TRD. Comprehensive statements will be made and it will be shown that a satisfying study of the J/ψ family is only possible with the TRD contribution as an electron-pion identifier - apart from its trigger capability. In addition, without the TRD no access to the Υ family is possible.

In this chapter the following topics will be discussed:

- Di-electron invariant mass spectrum, as reconstructed from heavy-ion collisions, Section 8.1.
- Some important data findings in the Quarkonia sector, mainly J/ψ, and the models, triggered by these data, and their predictions for LHC energies, Section 8.2.
- General properties of Pb-Pb collisions at LHC, Section 8.3.

- Calculation of the production rates of Quarkonia, open charm and open beauty, Section 8.4.

8.1 Di-Leptons

The importance of di-leptons (e^+e^- and $\mu^+\mu^-$) has two aspects; The first is the continuum di-lepton spectrum and the second is the di-lepton decay channel of vector mesons. In a QGP state leptons are produced via the *Drell-Yan process* ($q + \bar{q} \rightarrow l^+ + l^-$); in a hadronic gas, lepton pairs are produced via vector mesons decays, such as ϕ, η, ω, and ρ as well as from J/ψ and Υ. Although the branching ratios of the leptonic decays of these particles are small, they represent a large source of lepton pairs. They are also present in systems where no QGP state is expected to be established such as nucleon-nucleus collisions. Modeling the sources with Monte Carlo (MC) simulations and calculating their invariant mass allows a comparison with data findings.

The di-lepton invariant mass spectrum in heavy-ion collisions is rich in physics information on both the chiral symmetry properties and the deconfinement. Therefore it is subdivided into three mass intervals, see Figure 8.1; the *Low Mass Region* (LMR) with $m_{l^+l^-} < 1$ GeV/c, the *Intermediate Mass Region* (IMR) with $m_{l^+l^-}$ between 1 GeV/c and 2.5 GeV/c, and the *High Mass Region* (HMR) with masses from the J/ψ mass level upwards.

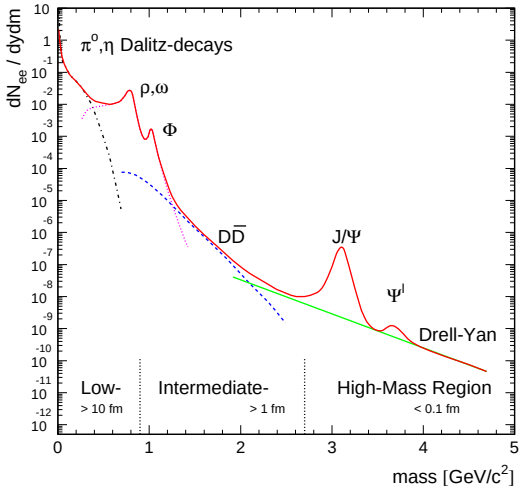

Figure 8.1: Schematic di-electron invariant mass spectrum.

The LMR di-electrons are produced at late collision stages and therefore they probe the soft processes. They carry information on in-medium modification of hadron properties such as the mass, the width, and the spectral functions. Already in the early eighties, calculations have shown [146] that if a QGP state is established, the di-leptons yield in the LMR would be enhanced by almost an order of magnitude relative to the yield from a hadronic gas.
The CERES Collaboration has carried out measurements with p-Be and p-Au collisions [147, 148] at SPS energies (450 GeV/c covering the LMR and a part of the IMR). The data could be reproduced by MC simulations.

The CERES Collaboration also carried out a number of systematic studies on nucleus-nucleus collisions -(S-Au) and (Pb-Au)- at energies of 200 GeV/c [147] and 158 GeV/c [149, 150] respectively. In the S-Au collisions there is an evidence for an excess in the di-electron yield within the mass window between 0.2 GeV/c^2 an the ρ and

ω resonances. In the Pb-Au data a clear enhancement is observed with an enhancement factor of about 2.3 [151]. The enhancement is relative to the mentioned Monte Carlo models which describe the p-Be data but scaled for Pb-Au collisions. The effect is found to depend linearly on the yield of charged particles per unit rapidity [151] and to increase with centrality [149].

The enhancement effect is explained by modifications of the ρ meson properties in the hot medium. Theoretical efforts ascribed it to a drop of the ρ mass in the medium of high baryonic density [152] where the ρ mass is shifted towards lower masses due to partial chiral symmetry restoration. It has been also shown that the enhancement can be related to a collisional broadening of hadronic spectral functions [153], where the changes are related to *in-medium* ρ–hadron interactions.

In later runs with Pb-Au collisions at 40 GeV/c [154], the CERES collaboration investigated the influence of the baryon density on the effect. The enhancement factor is found to be larger and amounts to 5.9. However the significance of these results is at 1.8σ and therefore one can consider them as a tendency to stronger dependence of the effect on the baryon density in the system than on its temperature. Also at this energy, the data can not favor any of the models mentioned above.

In the IMR, an enhancement is also observed in the di-muon invariant mass spectrum. HELIOS/3 [155] and NA50 [156] reported an enhancement factor of about 2.1 for most central events in the nucleus-nucleus di-muon spectrum. The enhancement is found to increase linearly with N_{part}, the kinematical distributions of the di-muon is compatible with the distributions expected from open charm decay [156]. Many theoretical efforts tried to interprete the observation. The most successful explanations are a thermal dilepton production [131] and the assumption of an open charm contribution via its semileptonic channel [157, 158, 159]. The situation is still ambiguous and an upgraded NA60 at CERN [160] should clarify the picture.

An important source of the di-leptons in the LMR and the IMR is the thermal radiation. They could come from the QGP or from the hadronic stage. The plasma contribution is provided by quark–anti-quark annihilation and they could be identified once the hadronic contributions are precisely evaluated. Anyhow, at T_c the thermal di-leptons from both sources are comparable. The plasma contributions can identify deconfinement only at high temperatures.

The HMR is dominated by the Drell-Yan electrons and the Quarkonium decay electrons.

8.2 Quarkonia Systems

During the last three decades heavy Quarkonia were, and are still, a challenging objective for QCD. These systems build a privileged way into the QCD world and they play a special role in heavy-ion collisions. On one hand, the charm quark, for instance, carries a mass of about 1.3 GeV/c^2 which is large enough to make its production be dominated by primary (early) nucleon-nucleon collisions. This makes them a good probe for the initial

stage of the collision. On the other hand, this mass is small enough to allow interactions with the surrounding reservoir of light quarks and gluons. This last property provides a direct probe of the hot and dense matter during its evolution.

Quarkonia state	J/ψ	ψ'	χ_c	Υ	Υ'	χ_b
m (GeV/c^2)	3.1	3.7	3.5	9.6	10.0	9.9
r (fm)	0.22	0.56	0.35	0.12	0.25	0.20
T_{diss}/T_c [7]	1.1	0.74	0.2	2.31	1.1	1.13

Table 8.1: Masses and radii of the Quarkonia states as well as their dissociation temperature in units of T_c. Note that recent lattice calculations have shown much higher dissociation temperatures. For instance the J/ψ state survives up to temperature of $1.5T_c$ [7, 161].

Quarkonia states ($J/\psi, \chi_c, \psi', \Upsilon, \Upsilon', \Upsilon'', \chi_b$) differ in their mass and their binding energy and as such they represent a multi-scale system, compare Table 8.1.
If a deconfined state of free quarks and gluons is formed, the color force between the heavy quarks is matter of attenuation under the influence of Debye screening, where its binding potential becomes screened by the bulk of color charges and consequently the interaction between the charm quark pairs could vanish. If the potential range, represented by the *Debye radius* λ_D, is smaller than the bound state radius, the heavy $q\bar{q}$ pairs are no longer in a bound state. But they dissolve and diffuse from each other in the medium. The dependence of λ_D (i. e. binding energy) on the temperature ($\propto 1/T$) suggests a dissociation temperature T_{diss} at which a bound state is dissolved.

The Debye screening formulation of charm quark pairs was motivated by Matsui and Satz [6], consequence of which is a suppression in the J/ψ yield coming from a heavy-ion collision if a QGP state is formed. In the suppression approach the dissolved heavy quarks and anti-quarks most likely form a final hadronic state with one of the largely abundant light quarks and anti-quarks. The total number of J/ψs coming from the collision, subsequently decreases relative to those which were produced initially in the collisions. This can probe the deconfinement state in two ways: firstly a significant suppression indicates the existence of the QGP state and secondly the different excited states (multi scale) have different binding energies and therefore the dissociation occurs at different temperatures leading to a sequential suppression. The relative ratios of the Quarkonia yields to each other give information on the temperature of the system. Table 8.1 shows the masses, the radii and the dissociation temperatures of the different Quarkonia states. Recent lattice calculation [161, 163] have shown that T_{diss} is higher than earlier results, given in the table. For instance, the J/ψ state survives up to temperatures on the order of $1.5T_c$, drops to about 50% of its intensity at $T = 2.25T_c$ and finally it disappears at about $3T_c$.

However, a suppression in the J/ψ yield was observed in experimental data in nucleon-nucleus and light nucleus-nucleus collisions, where no QGP state is expected to be formed. This suppression, called nuclear absorption, is understood to come from normal inelastic hadronic interactions [164].

Going from pA collisions to AA collisions an additional suppression was observed in experimental data taken at SPS energies by the NA50 Collaboration [162]. The results are shown in Figure 8.2. Although the temperatures is believed to be below the dissociation temperature of the J/ψ meson, the suppression is believed to be a consequence of the dissociation of χ_c and ψ' which dissolve at lower temperatures. Only about 60% of the J/ψs are expected to be produced directly. The rest comes from χ_c radiative decay and ψ' feed-down which contribute approximately by 20% and 8% respectively. The anomalous suppression is therefore explained by their disappearance which causes a suppression in the J/ψ yield.

In addition to the suppression, two observations were made in the SPS data. In [37] it was ascertained that the J/ψ yield per charged nucleon is constant, within errors, regardless the collision centrality. The authors made the hypothesis of statical production of the dominant fraction of the J/ψ produced in the system. The second observation was made by Shuryak and Zahed [112]. It is found that the ratio ψ'/ψ is independent of energy and its value in pA collisions is the same as in pp collisions. As function of centrality the ratio decreases in Pb-Pb collisions and approaches its thermal value at about 4% [113]. Braun-Munzinger and Stachel introduced the statistical hadronization model [36, 113] for Quarkonia production in heavy-ion collisions. The model explains the findings by assuming that all charm quarks are produced in the initial hard collisions. They reach thermal equilibrium in the plasma but not a chemical one. At hadronization the heavy quarks and anti-quarks are distributed in hadrons according to the same thermal equilibrium parameters that fit the light hadron abundances. The production of open and hidden charm mesons at chemical freeze-out, follows statistical laws.

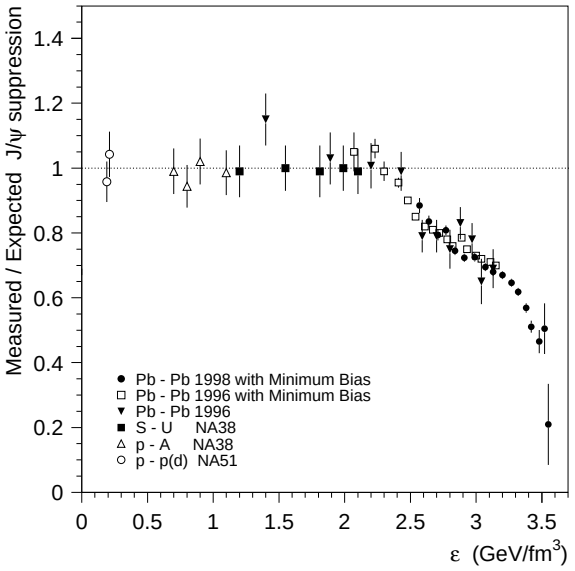

Figure 8.2: J/ψ anomalous suppression as a function of the energy density. The suppression is obtained by dividing the measured cross section by the values expected from nuclear absorption. Up to an energy density of about 2.2 GeV/fm^3 J/ψ is suppressed according to normal nuclear absorption. Beyond 2.2 GeV/fm^3 a non-normal suppression is observed. The figure is taken from [162].

Applying the framework of canonical thermodynamics [165], numerical calculations show that the relationship between the number of produced J/ψs, $N_{J/\psi}$, and the number of the produced charm pair, $N_{c\bar{c}}$ is quadratic:

$$N_{J/\psi} \propto \frac{N_{c\bar{c}}^2}{N_{ch}}.$$

The model calculation underestimates the SPS data [107] of NA50 Collaboration [162, 166]. The authors refer to the alternative open charm enhancement explanation for the enhanced di-lepton spectrum in the IMR. Their calculation shows that the underestimation factor (2.8) of the data is similar to the factor needed to explain the IMR enhancement. For collider energies the model predicts a production enhancement of J/ψ in the mid-rapidity density of $dN_{J/\psi}/dy = 0.011$ for RHIC and $dN_{J/\psi}/dy = 0.226$ for LHC. The prediction for the RHIC energy regime were compared [107, 167] to first results from the PHENIX Collaboration [168]. Within the large data errors, the results agree with the predictions

The enhancement scenario is also predicted by the *kinetic model* [169, 170]. Contrary to the statistical model, this model considers the possibility of direct formation of Quarkonia in the deconfined matter. A charm quark–anti-quark pair forms a color octet state which then emits a color octet gluon to become a color singlet bound state. As such, this picture is the opposite of the suppression picture where the bound Quarkonia state is dissolved by colliding with free gluons in the deconfined medium. As in the statistical hadronization model, the kinetic model suggests a quadratic growth of the Quarkonia population with $N_{c\bar{c}}$. The number of produced Quarkonia depends strongly on the considered rapidity window at mid-rapidity. Its expectations for RHIC and LHC are in the same order as the statistical hadronization model [167]. Differences appear in the centrality dependence which is due to the assumed momentum distribution of the resulting J/ψ. The RHIC data [168] seem to rule out cases with small rapidity windows.

A third suggestion to describe the J/ψ data is given by the *two-component model* which combines both, the suppression approach with the statistical hadronization model [171]. It predicts a suppression in the Quarkonia yield at low beam energies and an enhancement at high energies. This refrains from invoking any open charm enhancement in the IMR which is taken by the statistical model to describe the underestimation of the data.

How Quarkonia are going to signal a QGP state is still an open issue and the immediate future (RHIC) and all the more at LHC will allow clear statements in this sector.

8.3 General Features of Pb-Pb Collisions at LHC

At LHC the energy per nucleon pair will be 5.5 TeV in Pb-Pb collisions. For one experiment taking data the luminosity is expected to be between $\mathcal{L} = 0.85 \cdot 10^{27}$ cm^{-2}s^{-1} and $\mathcal{L} = 1.8 \cdot 10^{27}$ cm^{-2}s^{-1} [172]. For two experiments taking data this value can be reduced by factor 3. In this study a value of $\mathcal{L} = 1 \cdot 10^{27}$ cm^{-2}s^{-1} will be considered which is nevertheless to be seen as an upper limit, especially because CMS will share the heavy-ion running time with ALICE. ATLAS anticipates to adopt a heavy-ion program.

The total reaction cross section in a Pb-Pb collision, σ_{PbPb}, can be determined from the extrapolated nucleon-nucleon cross section of σ_{NN}= 60 mb. The anticipated σ_{PbPb} is

7.8 b [5]. With the considered luminosity this leads to a minimum bias interaction rate of 7.8 kHz. An ALICE data taking year amounts to 10^6 s [5] leading to a total number of primary events in the order of $7.8 \cdot 10^9$.

In an AA collision the number of binary collisions, N_{bin}, depends on the collision geometry through the impact parameters b. Taking a Woods-Saxon density profile for the colliding nuclei, N_{bin} can be calculated as function of b by the *Glauber nuclear overlap function*, $T_{AA}(b)$. For a Pb-Pb collision the relation is given by:

$$N_{bin}(b) = \sigma_{PbPb} \times T_{PbPb}(b). \tag{8.1}$$

In Figure 8.3 N_{bin} is plotted as a function of b.

From the point of view of the di-electron identification, the most important quantity in a Pb-Pb collision is the multiplicity of secondary charged hadrons, $\mathrm{d}N_{ch}/\mathrm{d}y$ as function of b. As discussed in Subsection 2.4.1, there are large uncertainties in the calculations of $\mathrm{d}N_{ch}/\mathrm{d}y$. The ALICE sub-detectors are design to perform at multiplicities up to 8000 for central events ($b = 0$). In this study three values are considered: 2000 (low multiplicity), 4000 (half multiplicity), and 8000 (full multiplicity). Meanwhile ALICE has adopted a value of 6000 for the full multiplicity.

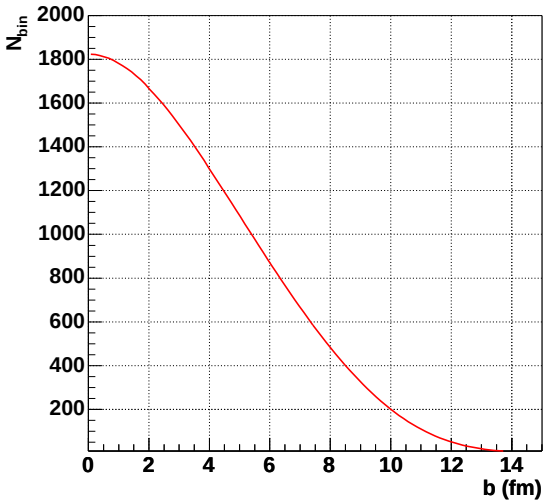

Figure 8.3: Binary collisions as a function of the collision geometry in a Pb-Pb collision at LHC.

Assuming that the multiplicity scales with N_{bin} and $\mathrm{d}N_{ch}/\mathrm{d}y$=6000, the multiplicity distribution, this is the number of collisions at a given multiplicity, can be obtained from the Glauber model. The distribution is shown in the left panel of Figure 8.4. The entries are scaled to the particle rate in one ALICE year. In average a Pb-Pb collision produces about 1100 charged particles, mostly pions and kaons [1].
The most central events are in the high multiplicity region. Considering 10% of the cross section to be central, the most central events start at a multiplicity of 3570. An average central Pb-Pb collision produces 4600 charged pions and kaons. The central events are indicated by the red area in Figure 8.4.

[1] Actually charged pions and kaons make a fraction of about 80% of the total charged particle multiplicity [8]. Taking all the charged particles to be pions and kaons offers a safety factor between the simulations and the real data taking.

8.4 Count Rates of Quarkonia, Open Charm and Open Beauty

Quarkonia Count Rates:
The integrated production cross section of J/ψ in $p\bar{p}$ collisions was measured by the CDF collaboration[2] for $p_t^{J/\psi} \geq 4$ GeV/c and $\mid \eta \mid < 0.6$ and was found to be 29.1 nb [174]. Correcting for the p_t-cut and extrapolating to LHC energies [8], the production cross section in $p\bar{p}$ collisions is expected to be about 400 nb.
The production cross section for the Υ family was measured in $p\bar{p}$ collisions at $\sqrt{s} = 1.8$ TeV/c. Including the branching ratio for di-muon decays, the cross section can be approximated to be about 1 nb [173]. For pp collisions at LHC energies, a linear extrapolation results in a cross section of 3 nb for all Υ states.

In AA collisions the production cross section of Quarkonia is derived from the $p\bar{p}$ data via the scaling law [8]:

$$B_r \left(\frac{\mathrm{d}\sigma(AA)}{\mathrm{d}y} \right)_{y=0} = A^{2\alpha} B_r \left(\frac{\mathrm{d}\sigma(p\bar{p})}{\mathrm{d}y} \right)_{y=0}. \tag{8.2}$$

where the parameter α counts for in-medium effects [176] such as shadowing, jet quenching, gluon saturation, and enhancement due to thermal production. α is about 0.9 for charmonium and 0.95 for bottonium states [175]. B_r is the branching ratio of the di-lepton decay (6% for J/ψ and 2.5% for Υ). Assuming that α is p_t-independent, the scaling law leads to a production cross sections of:

$$B_r \sigma_{\text{charmonium}}(AA \to q\bar{q}) = 59.4 \text{ mb}, \tag{8.3}$$

$$B_r \sigma_{\text{bottonium}}(AA \to q\bar{q}) = 571.0\ \mu\text{b}. \tag{8.4}$$

Quarkonia are hard probes, which are produced in the hard scattering of partons (first scattering generation) where the available *cms* energy of a parton-parton collision is still high enough to overcome the charmonium (bottonium) production threshold. At low energies their production scales with the number of participants N_{part}. At SPS and RHIC energies their yield is a linear combination between N_{part} and N_{bin} as shown in [111]. Whereas at LHC energies the yield can only estimated. The less favorable scenario is a proportionality to N_{bin}. Since this study aims to evaluate the ACB Quarkonia detection capability under worst case conditions, the N_{bin} proportionality is considered in the simulations of di-electron invariant mass.

Scaling the number of collisions in the multiplicity distribution (left panel in Figure 8.4) with N_{bin}, gives the Quarkonia differential production. The resulting distribution is shown in the right panel of Figure 8.4 for J/ψ as a prototype for the Quarkonia. The entries

[2]This study follows the argumentation of the CMS Collaboration in [8]. The given Quarkonia production cross sections are taken from the reference. For detailed discussion see also the references [173, 174, 175]

are scaled for one ALICE year. Notice that the assumed N_{bin}-dependence causes a slight drop in the J/ψ yield at high multiplicities. This can be explained by the behavior of the central event rate (left panel in Figure 8.4) and N_{bin} as functions of the multiplicity. The calculation assumes a linear dependence of the multiplicity and the central event rate is found to drop exponentially. This behavior changes (no drop in the yield [130]) if one assumes a yield scale with the number of participants.

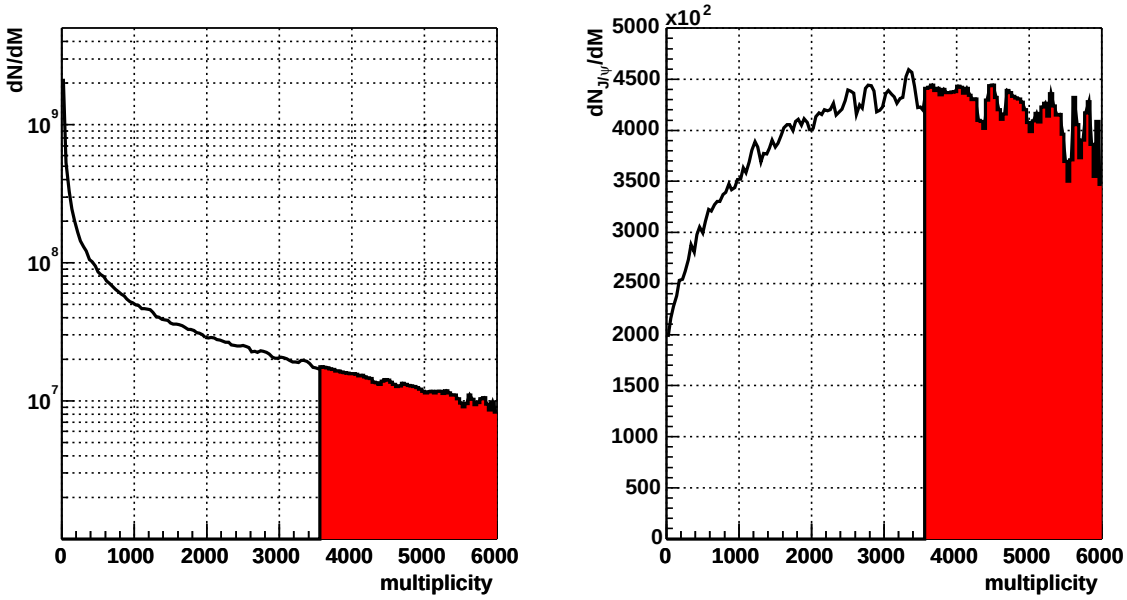

Figure 8.4: Multiplicity distribution (left) and J/ψ differential yield (right) as functions of the multiplicity. The results are scaled to one ALICE running year (10^6 s). In both cases the red area represents the most central 10% of the events.

Scaling the results with the cross section ratio $\sigma_{J\psi}/\sigma_{PbPb}$, $\sigma_{J\psi} \simeq \sigma_{\text{charmonium}}$, gives the minimum bias J/ψ yield within one ALICE year which is on the order of $5.94 \cdot 10^7$. With the total event rate of 7.8 kHz this leads to a minimum bias number of J/ψ per event of $7.6 \cdot 10^{-3}$.
Integrating the J/ψ differential cross section for the central events, red area in the right panel of Figure 8.4, results in 43.3% of the produced J/ψ coming from central events. This is equivalent to a total of $2.55 \cdot 10^7$ J/ψ particles coming from central events. Dividing by the total event rate results in 0.033 J/ψ per central event and di-electron chanel. In the same way with $\sigma_\Upsilon \simeq \sigma_{\text{bottonium}}$, the total number of produced Υs per central event and di-electron chanel is about $4 \cdot 10^{-4}$.

D and B Mesons Count Rates:
The charm and beauty production cross sections for LHC energies were extrapolated

from measurements at low energies from pp collisions [176] at next-to-leading-order. It is reported that, depending on the extrapolation parameters, quark mass, factorization, and renormalization scales, the uncertainties in the total production cross section reach a factor 4. Taking these factors as given in [176], the results lie in the middle of the theoretical uncertainties.

The extrapolation for nucleus-nucleus collisions, averaged over all impact parameters, follows the law:

$$\sigma_{AB} = \sigma_{pp}(AB)^{\alpha} \tag{8.5}$$

with α as defined in Equation 8.2.

Using the total cross sections σ_{NN} and σ_{PbPb} as given above and 5% centrality [176] leads to a charm production cross section of 6.64 mb for pp and 45.0 b for Pb-Pb collisions, and respectively 0.21 mb and 1.79 b for the beauty production cross section. The Pb-Pb cross sections lead to a total number of of 115 $\bar{c}c$ and 4.56 $\bar{b}b$ in each central event at LHC energies [176].

Chapter 9

Fast Simulation Package for the ALICE Central Barrel

ALICE is concepted to verify all QGP signatures accepted nowadays and it is capable to record particles with momenta down to some hundreds of MeV/c. This wide spectrum of physics topics makes detailed simulation compulsory to appreciate the detector's capability for each potential QGP probe.

AliRoot[177], an object oriented framework was developed to describe the ALICE detector. It enables interfaces to GEANT3[178], GEANT4[179] and PYTHIA[180] and includes detailed description of the geometry of all ALICE sub-detectors. Simulations can be carried out with each sub-detector system in stand-alone modus. Each sub-detector component can be manipulated and new ones can be added if required. Since many of the proposed QGP signatures require information from two or more sub-detectors -as the ϕ mass modification and Quarkonia signals for instance-, AliRoot is concepted to enable information exchange between the ALICE sub-detector systems.

In order to simulate the response of each sub-detector and the entire ALICE experiment, AliRoot has to overcome many challenges. For instance the large multiplicities expected at LHC and multiplicity variations put demanding requirements on the code and the computer power used. In addition to the software challenges, uncertainties in physics inputs make the simulations difficult, such as the unknown but low cross sections of promising probes like J/ψ and Υ resonances. These difficulties require a large number of generated events. Therefor parameterized generators for background and Quarkonia events were developed which will be briefly discussed in Section 10.1.

One of the main units of ALICE is its Central Barrel (ACB). It consists of three sub-detector systems: ITS, TPC, and TRD. Among others, the ACB will investigate the Quarkonia via their di-electron decay channel. Fast simulations in this sector are subject of study in this thesis. In this chapter the following topics will be discussed:

- Why fast simulation? Section 9.1.
- Fast simulation strategy, Section 9.2.

- Slow simulations with local and global tracking, Section 9.3.
- Global response (efficiency and resolutions) in the ACB, Section 9.4.
- Global particle identification, Section 9.5.
- Simulation Environment Section 10.3.

9.1 Why Fast Simulation?

In order to evaluate the detector efficiency of recording interesting signals, reliable and extensive simulations are necessary. A common challenge in the Pb-Pb collisions at LHC energies is the expected high multiplicity. For rare probes like Quarkonia, the small production cross sections lead to low total particle yields per central event. This requires simulation of a huge amount of central events to gather enough statistics to address the physics of these probes.
One event produces around 14000 tracks in the TPC alone which requires about 1 GB disc space. The tracking procedure in slow simulations consumes at least one hour CPU time on modern processors, to follow the clusters of each track.

To illustrate the situation, consider the production cross section of the Υ particle given in Equation 8.4. As discussed in the previous chapter, only $4 \cdot 10^{-4}$ particles are produced per central event. With half multiplicity, only 6.3% of this number is within detector acceptance and passes the PID and a p_t-cut of 1 GeV/c. Therfore in average, only $2.52 \cdot 10^{-5}$ Υs are accepted per central event. This means that one has to simulate, on average, about 40.000 events to record one Υ particle which consumes at least 4.5 years of CPU time.

These numbers show that it is impossible to carry out reliable simulations with conventional methods. Therefore event analyses packages were developed by ALICEs' individual Collaborations which rely on *Fast Simulation Modus* (FSM) like the muon-arm collaboration and the ACB. The latter is the subject of this part of the thesis.

9.2 Fast Simulation Strategy

In the FSM the following strategy is followed:

- Generate a small but significant number of events for a given running condition (given multiplicity and magnetic field) and apply a global tracking procedure within the three detectors ($\rightarrow$ slow simulation).
- Store all information about the kinematics quantities (transverse momentum p_t , azimuthal angle ϕ, and pseudo-rapidity η) of each particle in a data base within numerical *Look Up Tables* (LUTs) such as the resolutions of the quantities.

- Calculate the combined detection efficiency of the three detectors and include it in the data base.
- Include the TPC and TRD electron-pion separation efficiency in the data base.
- Generate a significant number of events including signal particles and background sources and apply the information of the data base to each particle.
- Combine each electron candidate (also misidentified pions) with each positron candidate and calculate the combinatorial invariant mass spectrum.

In the following sections these steps are presented.

9.3 Slow Simulations

The spacial granularity of a detector defines the number of the electronics digits which is represented by the total pad number in the TRD and the TPC. They are distributed according to a detector response function. The best possible hit position is determined by the inverse of this function which can be either an analytical or a numerical one. In the ALICE TRD online modus the numerical inverse of the Pad Response Function (PRF) will be used, see Section 5.2 and Subsection 7.5.1. Offline, both the numerical and the analytical inverse PRF will be used.
Each cluster of digits responds to an extended point in the detector.

9.3.1 Local Tracking

Due to the high density of occupied clusters at the innermost side of a detector (closer to the vertex), one starts the tracking procedure at its outermost side. In the TPC the clusters are distributed according to the pad rows, in the TRD they are distributed according to the drift time bins (radial y-direction in the ALICE coordinate system).
The tracking procedure in the ACB is based on the *Kalman filter* algorithm[181], see also [182] for a detailed description. In this technique the track is identified by a state vector of five parameters which defines the track and its *covariance matrix*. The Kalman procedure can be summarized in two parts. The first is the track initiating part, where clusters (also called track seeds) and position errors are determined according to the digits distribution function, PRF. The second part is the track following.

In the first part, starting from a cluster at the outermost row ($R0$) of a detector, one chooses a suitable window in the next row ($R1$) towards the vertex according to the precision of the cluster position. For all clusters within a chosen window, the χ^2-increment is calculated. The cluster which gives the minimal χ^2-increment is chosen and part two of the procedure starts. For primary particles, the chosen clusters in $R0$ and $R1$, the vertex as a third point, and the magnetic field, allow a track momentum determination. With the momentum information a window determination in the next row ($R2$) is achieved with a precise cluster position and so on. If no clusters are found so that the tracking

procedure can not be continued, the procedure is aborted and part one is initiated anew. During the tracking the energy loss and the multiple scattering in the detector material are taken into account. The state vector and the covariance matrix of the track are updated after each step. A successfully reconstructed track is fitted and the fit parameters are stored.
The found, local, tracks in each detector are matched together to give a global track. In the ACB, the matching between the individual detector tracks is a complex procedure, since the distances between the detectors are sufficiently large. The distance between the TRD-TPC and TPC-ITS amounts to about 40 cm[5]. In addition, the high track density in the ITS makes matching to the TPC tracks more complicated.

9.3.2 Global Tracking

The global tracking procedure aims to reconstruct a global track in all three detectors of ACB. One starts the procedure at the outermost side of the TPC and chooses the stiffest tracks first and proceeds as described above in the local tracking procedure. By and by one moves to the softer tracks. separately a tracking procedure is done in the ITS. To match the TPC tracks to those of ITS, for each reconstructed track in the TPC a "tree" of potential track candidates is built through all ITS layers by means of the local tracking procedure. The state vector and the covariance matrix of the matched track is then updated.

Reaching the innermost point of the ITS, one propagates back through the ITS and TPC to the outermost point of the track. Again the track fit parameters are updated. Reaching the last point at the outermost side of the TPC, one propagates towards the TRD entrance. Note that local track segments are not available in the TRD yet. Using the momentum information of the track gained from the TPC and the ITS, one extrapolates to the point location which the track would reach at the outermost side of the TRD. In the region of this point, one searches for potential seeds.

From this point on, one starts the Kalman filter tracking procedure in the TRD back to its innermost side. With a successful TRD local tracking, a global track is reconstructed. The track is then re-fitted back towards ITS and usually, better fit parameters are achieved compared to local tracking parameters. The so found track is labeled **back**.

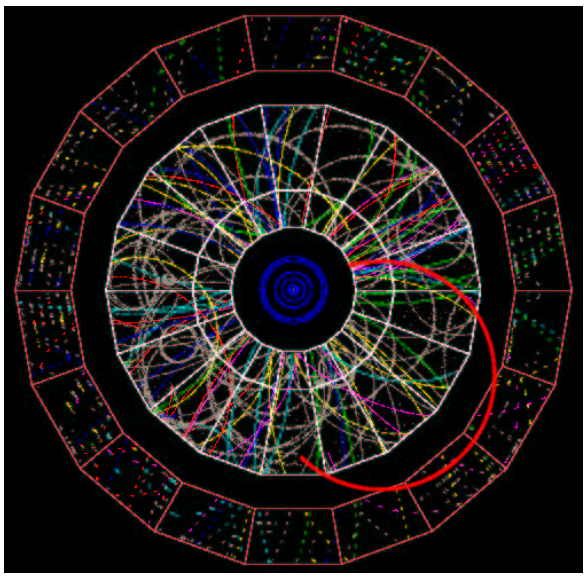

Figure 9.1: The tracks of a Pb-Pb event as simulated within the AliRoot framework. For illustration purposes the full multiplicity is scaled by factor 1/500.

A successful global tracking up to the outermost point of the TRD implies that the particle has propagated through all the TRD layers and left the ACB towards other sub-detectors.

The failure of finding a cluster on the outermost side of the TRD which matches to the ITS-TPC track implies that the track, either stacks (ends) in the TRD or if its momentum is low enough, its inclination radius under the influence of the magnetic field is small, such that it leaves the TRD at its innermost side towards the TPC, see the thick red track in Figure 9.1. The exit point is found according to the momentum information of the reconstructed ITS-TPC track.

Finally, the number of reconstructed tracks can be enhanced if one considers those clusters at the TRD's outermost side which still do not belong to any of the found tracks. From there on, new tracks are followed throughout the three detectors. This procedure is called **TRD-add-seeds** and increases the number of reconstructed tracks by about 10%.

9.4 Global Detector Response in the ACB

To evaluate the global detector response in the ACB Monte-Carlo simulations were performed by Thomas Kuhr from the CERN ALICE collaboration. They were carried out within the AliRoot framework using the slow simulations procedure described in the previous section. Low-, half-, and full multiplicity were considered with 7, 9, and 10 generated events respectively and the Kalman tracking procedure was applied to each particle in each event. Only primary pions and kaons were considered with a vertex cut of 100 μm from the geometrical interaction point. The generated events were analyzed to evaluate the transverse momentum distributions, the global (three detectors) detector efficiency, and the resolutions of the kinematic quantities, p_t , η, and ϕ.

9.4.1 Transverse Momentum Distribution

Figure 9.2 shows the p_t distribution of the reconstructed particles, black histogram. 74% of them reach the TRD, red histogram. 69% of the latter penetrate through the detector and leave it towards the ACB-outside region, green histogram, and less than 1% of those particles return to the TPC, blue histogram. The remainder of about 30% get stuck in the TRD.
Note that even particles with momenta below 200 MeV reach the TRD (2.5% of all low-p_t particles). This enhances the TRD contribution to the ALICE coverage of low-p_t physics.

9.4.2 Global Detector Efficiency in the ACB

The detector efficiency, ϵ, is determined by the ratio of the reconstructed tracks to the simulated ones within the pseudo rapidity acceptance of the ACB. A reduction of ϵ can be caused by two factors; i) the so-called *fake tracks*, where a track is rejected if it contains

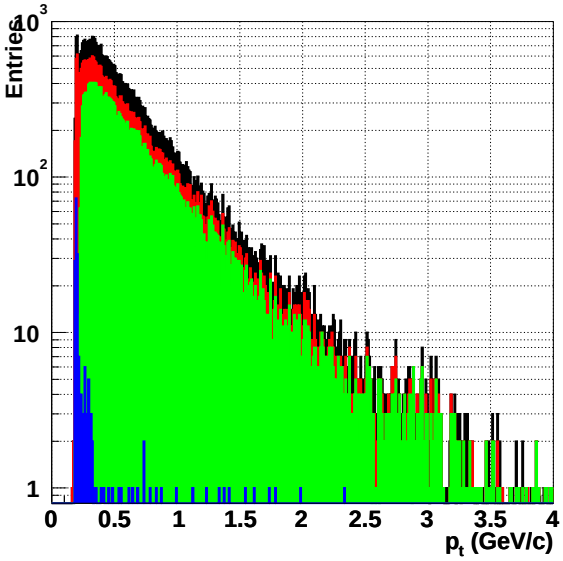

Figure 9.2: p_t distribution of reconstructed pions and kaons in the ACB, black. The red histogram represents the particles which reach the TRD. The green histogram contains the entries of particles which penetrate throughout the TRD and leave it towards regions outside the ACB and the blue histogram shows the particles which enter the TRD and leave it back towards the TPC. Also particles with $150 < p_t < 200$ MeV/c reach the TRD.

at least 10% of incorrectly assigned clusters. In the ACB there are about 5% of fake tracks at half multiplicity (integrated over all p_t values and ϕ- and η-acceptances). ii) Non active areas of the TRD and TPC between the 18 sectors in ϕ direction and between the TRD five sections in beam direction. However not all tracks in a non-active area are lost, some of them can be reconstructed. Low-p_t tracks, are inclined under the influence of the magnetic field. Therefore, only a track segment will be missed, where the track crosses the inactive area, see Figure 9.1.

The global detector efficiency is shown in Figure 9.3 for low-, half-, and full multiplicity, represented by the black, red, and green symbols respectively. In the left panel, ϵ is shown for the **back** tracking scenario which exhibits a slight reduction of ϵ with the multiplicity. Since data are only available for low and full multiplicity, the results of half multiplicity were extrapolated from those two, assuming a linear dependence of ϵ on the multiplicity[1].

In the right panel of Figure 9.3, ϵ is shown under the same conditions as in the left panel but with the **TRD-add-seeds** procedure. Here only half multiplicity data exist, therefor the curves for low and full multiplicity are reconstructed from the **back**-scenario data. The scaling factor is obtained from the half multiplicity data. The **TRD-add-seeds** scenario improves the efficiency by 8%-10%.
In the following discussion only the **TRD-add-seeds** scenario will be considered.

[1]This assumption is not quit correct. Especially in online analysis, as shown in [130] for the TRD, in stand-alone modus, the relation between ϵ and dN_{ch}/dy is only approximately linear. But since the ϵ deviation between low- and full multiplicity is small the linearity assumption is justified.

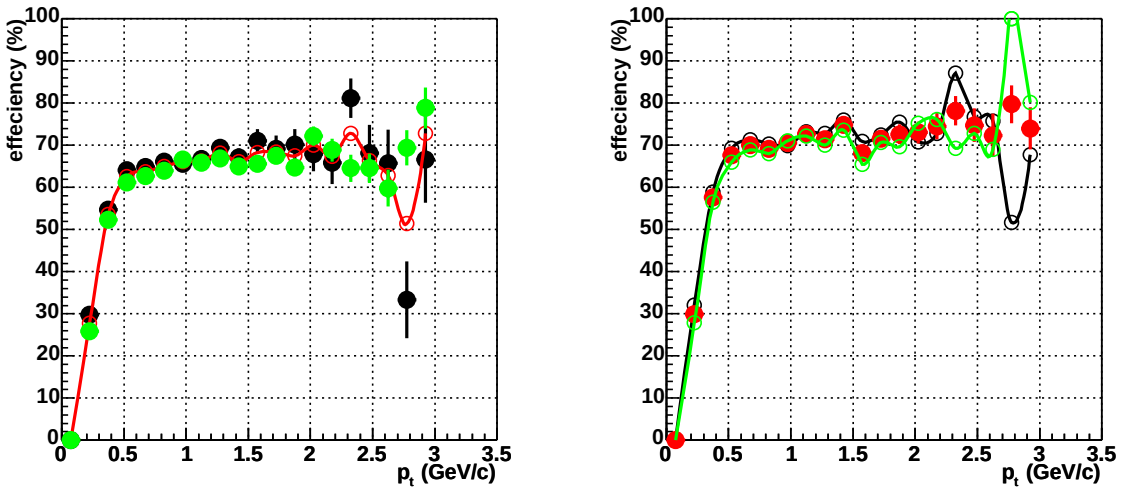

Figure 9.3: Global detector efficiency as a function of transverse momentum and the particle multiplicity per unit rapidity. Left panel: **back** scenario, the data for half multiplicity are extrapolated from the other two cases assuming linearity in $\epsilon = \epsilon(dN/dy)$. Right panel: **TRD-add-seeds** scenario, only the half multiplicity case is simulated, from which the other two cases are extrapolated relying on the results of the **back** scenario.

Due to the low statistics of the produced events, ϵ fluctuates strongly for transverse momenta above 2 GeV/c. Therefore, in the di-electron invariant mass simulations, it is consider to be constant for higher transverse momenta:

$$\epsilon(p_t) = const = \epsilon(p_t = 2 \text{ GeV}/c) \qquad : p_t > 2 \text{ GeV}/c.$$

This assumption obviously degrades the detector performance especially at the Quarkonia level but it also provides a safety factor.

In Figure 9.4 the global detector efficiency is shown as a function of ϕ (left panel) and η (right panel) for the three multiplicities. Conspicuous are the reductions of ϵ at the slits in ϕ caused by the TPC and TRD segmentation in ϕ and the TRD segmentation in η. Although only the TRD contributes to the second case, the reduction amounts to about 20%, which is larger by factor 2.4 than the first case where the efficiency reduction is only about 4%. The momentum of particles that reach the TRD within a ϕ-gap is usually large and so is the inclination radius, therefore the missing segment in the track is large and an inter-cluster matching falls. In addition, since the inclination surface is perpendicular to the beam direction, if a track is in an η-non-active area, the inclination keeps it within its surface and the track is lost, see the thick red track in Figure 9.1 which could be imagined to lay in a surface between two TRD sectors.

The LUTs (gained from pions) will be used to evaluate the detector response for electrons, where they are not necessarily valid. In [183] the global detector efficiency in the TPC and ITS for different particle species are compared. ϵ_{pion} is almost the same as $\epsilon_{electron}$ for transverse momenta lower than 1 GeV/c and higher than 3.5 GeV/c. In the intermediate

region ϵ_{pion} is lower than $\epsilon_{electron}$ by almost 10%, implying that the usage of pion-based simulation for the LUTs is not crucial and the results should be improved when using electron-based LUTs. However bremsstrahlung works in the opposite direction to this "improvement". Establishing LUTs with electrons is the first step to be done in the next simulation run.

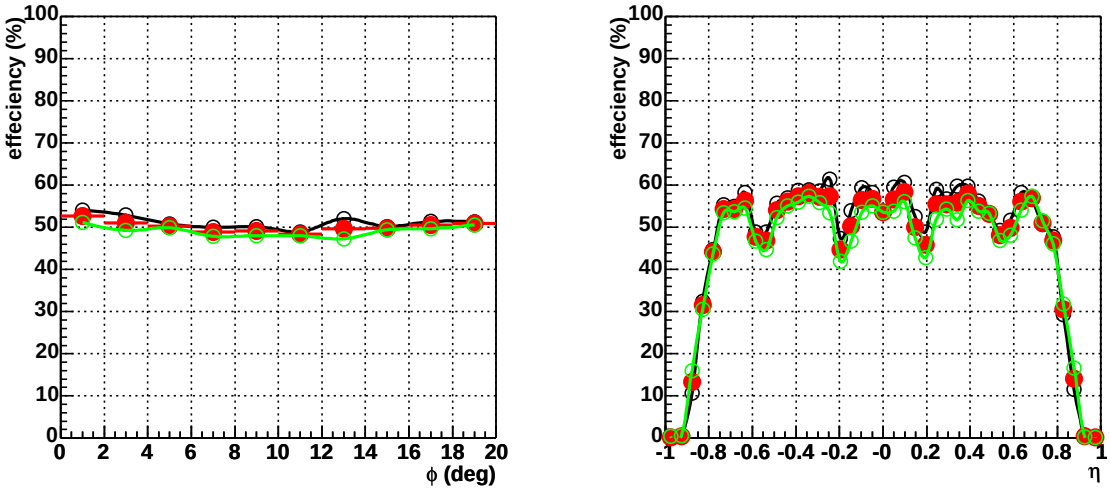

Figure 9.4: Global detector efficiency as a function of the azimuthal angle (left panel) and the pseudo rapidity (right panel) for the considered multiplicity cases.

9.4.3 Global Detector Resolutions in the ACB

The residuals Δp_t, $\Delta\phi$, and $\Delta\theta$ of the kinematics quantities [2] describe the distributions of the reconstructed values of each quantity reduced by the simulated (MC) ones. They are fitted with a Gaussian of which the parameters are stored in the data base of the LUTs.

In Figure 9.5 the distribution of Δp_t is shown. The results are integrated over the whole azimuth and polar angles within the ACB acceptance and a transverse momentum interval of 1 GeV/c < p_t <1.1 GeV/c. In a similar way the resolution of ϕ and θ are determined.

In the upper left panel of Figure 9.6, the p_t resolution is plotted as a function of p_t and the multiplicity. Due to the fluctuations above 1.8 GeV/c, the best fit on the data is a parabolic function with this point as upper limit. With the fit parameters, σ_{p_t} is extrapolated to higher momenta. The results are shown in the upper right panel. It is obvious that the parameterization overshoot the points at higher p_t values.

[2] The η resolution is calculated from the θ resolution in later steps during the fast simulation procedure, $\eta = -\log\tan(\theta/2)$.

In the lower right panel σ_{p_t}/p_t is shown as a function of p_t. Due to *multiple scattering*, this relation is relatively high at low-p_t values and it drops with higher p_t down to about 1% at $p_t = 1$ GeV/c where it takes a linear dependence on p_t for higher transverse momenta. Depending on th multiplicity, the resolution of a 3 GeV/c-particle is between 2% and 2.5 %.

Figure 9.7 shows the resolutions of ϕ and η in the same way as σ_{p_t}. In both cases the simulated resolutions can be described by a $1/p_t$-fit. In the ϕ case one reaches a resolution below 0.1 degree around $p_t = 1$ GeV/c which is improved to lower values for higher p_t. In the polar angle case the resolution reaches similar values at $p_t = 1$ GeV/c and improves only slightly with p_t. Both cases show only a slight dependence on the multiplicity.

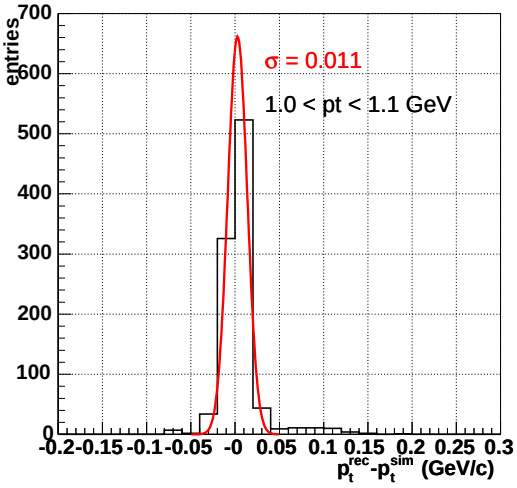

Figure 9.5: Δp_t distribution. The resolution is the of σ of the Gaussian fit.

The resolution of p_t exhibits only a slight dependence on ϕ and η as shown in the right upper and lower panel of Figure 9.8. The σ_{p_t} variation due to the slits in the detector is within 3 MeV/c and 4 MeV/c in the ϕ and the η case respectively. Therefore and, mainly due to the low statistics of the available slow simulation results, σ_{p_t} is considered to be constant as a function of ϕ and η. The same is true for the ϕ resolution as can be seen in the upper and lower middle panels of Figure 9.8. The θ resolution, right panels, shows only a slight dependence on η which is still however within 0.1 degree when going from mid rapidity to both outermost η values of -0.9 and 0.9 in the ACB acceptance. Therefore the ϕ and θ resolutions are also considered to be constant as functions of ϕ and η.

9.5 Particle Identification

The pion rejection in the ACB is the multiplicable combination of the TPC and TRD pion rejection capabilities. Measured data are available for the TRD which were discussed in Section 7.8.2 for electron identification efficiency of 90%. The measurements cover a momentum range up to 6 GeV/c. For higher momenta they are extrapolated, compare Figure 7.27. As a function of the particle momentum the TRD pion efficiency, π_{eff}^{TRD}, can be described by the parameterization:

$$\pi_{eff}^{TRD} = \left\{ \begin{array}{lll} 0.015197 - 0.002345 \cdot p, & : & p < 2 \text{ GeV}/c \\ 0.008082 + 0.001198 \cdot p, & : & p \geq 2 \text{ GeV}/c \end{array} \right\}. \quad (9.1)$$

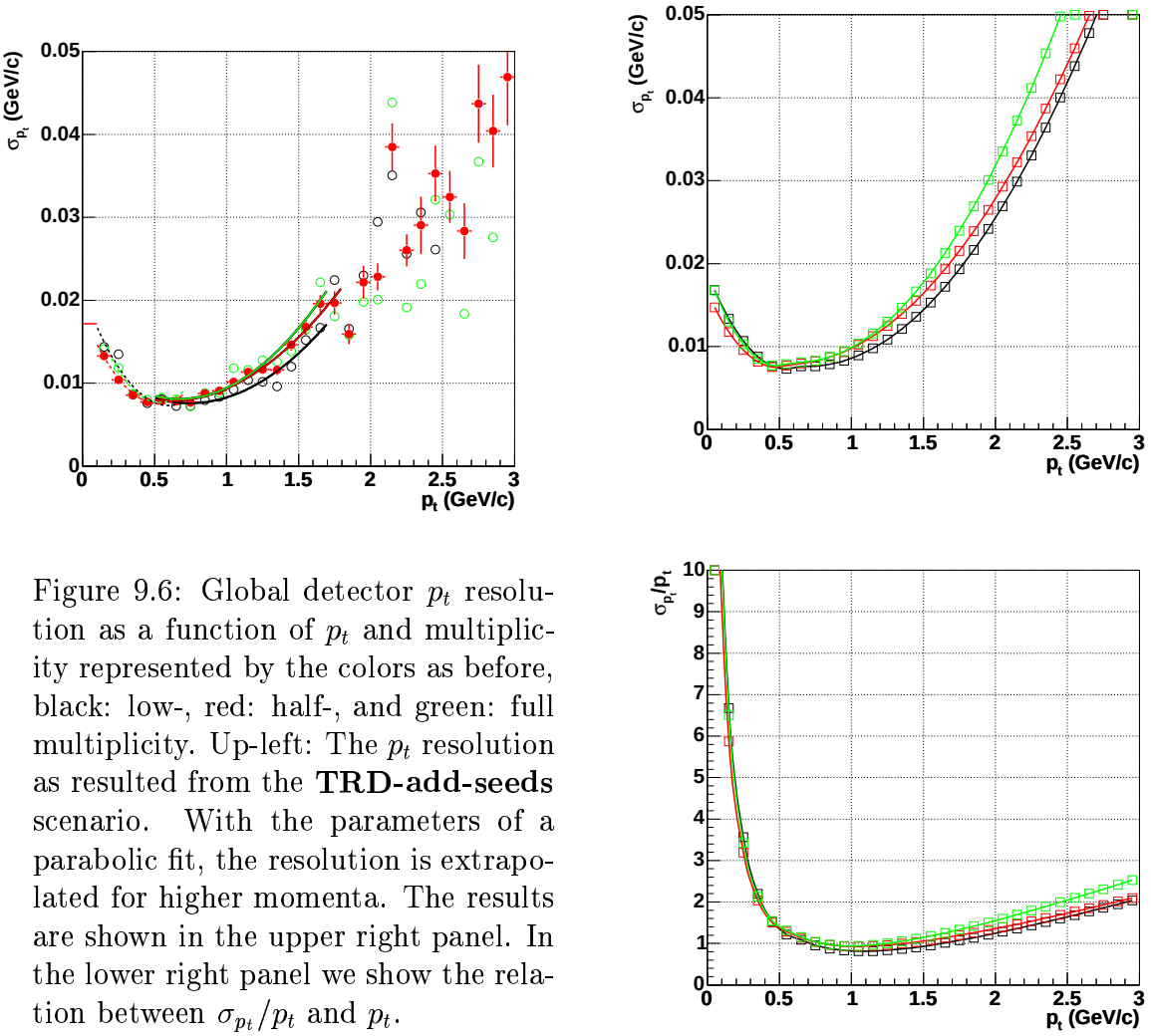

Figure 9.6: Global detector p_t resolution as a function of p_t and multiplicity represented by the colors as before, black: low-, red: half-, and green: full multiplicity. Up-left: The p_t resolution as resulted from the **TRD-add-seeds** scenario. With the parameters of a parabolic fit, the resolution is extrapolated for higher momenta. The results are shown in the upper right panel. In the lower right panel we show the relation between σ_{p_t}/p_t and p_t.

The results are achieved using the method of likelihood on integrated energy deposit. Using the method likelihood on energy deposit and position of the largest cluster found in the drift region, gives better results [130]. Employing neuronal network methods [184] delivers even better pion rejection capability. Nevertheless, sticking to the same strategy of considering worst case scenario to evaluate the detectors capability, the parameterization of Equation 9.1 is used in the fast simulation modus of the ACB.

In [130] it is shown that going from well isolated tracks, $(dN/dy = 0)$, to full multiplicity, the pion efficiency is deteriorated by factor 6 in online analysis. In the offline modus the deterioration factor is about 2 at full multiplicity. This study considers this factor for all multiplicities.

In the TPC one utilizes the energy deposit of particles in the drift gas, dE/dx, as briefly described in Section 3.1. The left panel of Figure 9.9 shows the dE/dx distributions for pions, kaons, protons and electrons as functions of the particle momentum. The distributions are calculated with a dE/dx resolution of 6.9% of the dE/dx value at a

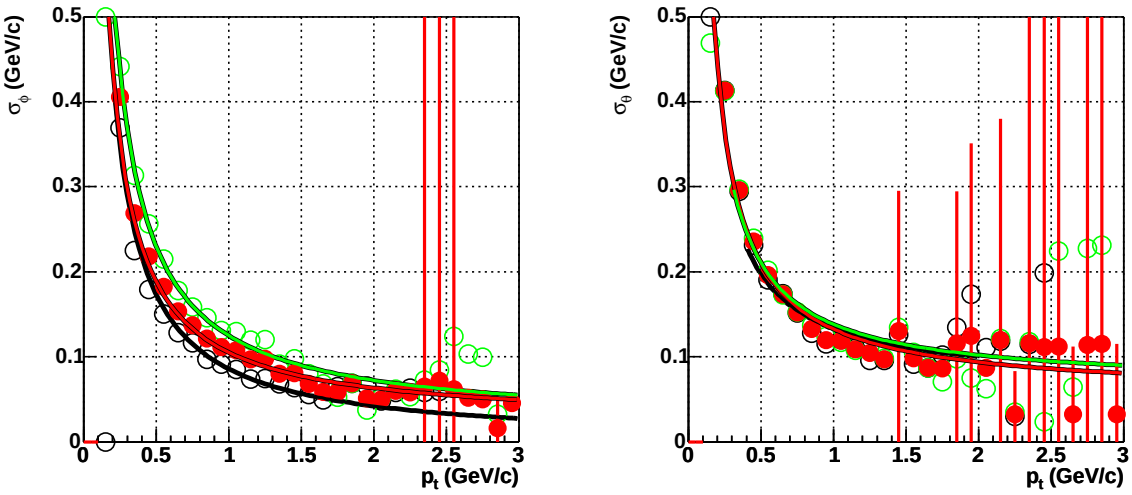

Figure 9.7: Global detector p_t resolution as a function of multiplicity and ϕ (left panel) and η (right panel).

given momentum corresponding to the resolution achieved in the ALICE TPC[5]. In general there are non-Gaussian contributions to the dE/dx distribution which deteriorate the TPC pion efficiency π_{eff}^{TPC}. Technics like the truncated mean of integrated energy deposit enable a reduction of the non-Gaussian contributions, but a pure Gaussian is only approximately achievable. For simplicity the dE/dx distributions in Figure 9.9 are calculated assuming a Gaussian shape. In order to avoid ideal case results in this study, many scenarios are studied including cases with a 10% dE/dx resolution.

The pions and electrons dE/dx distributions allow a reliable electron-pion separation within the momentum interval 200 MeV/$c < p <$ 2 GeV/c. However the figure considers an ideal situation, measured dE/dx as shown in Figure 3.1 are characterized by distribution which constricts the momentum interval and worsens the separation capability.
The figure contains also calculations for protons and kaons. The electron-kaon, and electron-proton rejection capabilities are better than that of the pions.

The upper panel of Figure 9.9 shows the calculated π_{eff}^{TPC} as a function of the particles momentum. A π_{eff}^{TPC} below 10^{-3} is not realistic and even this value approaches ideal cases especially with regards to the assumed Gaussian shape of the dE/dx distribution. Therefore the best achievable pion efficiency in the TPC, $\pi_{eff}^{TPCbest}$, is set to this value if it drops below it. In the following discussion this case is referred to as TPC1 scenario represented by the solid red line in the bottom panel of Figure 9.9.
To enable realistic studies under more realistic situations and worse case scenarios, cases with less sufficient π_{eff}^{TPC} are considered in the simulations. Thereby $\pi_{eff}^{TPCbest}$ takes values of $2 \cdot 10^{-3}$ and 10^{-2} corresponding, respectively, to the dashed (TPC2) and the doted red lines (TPC3) in the figure. Similar considerations are taken for a dE/dx resolution of 10%, TPC4, TPC5, and TPC6 corresponding to $\pi_{eff}^{TPCbest}$ of 10^{-3}, $2 \cdot 10^{-3}$, and 10^{-2}. These cases are represented by the green lines in the bottom panel of Figure 9.9.

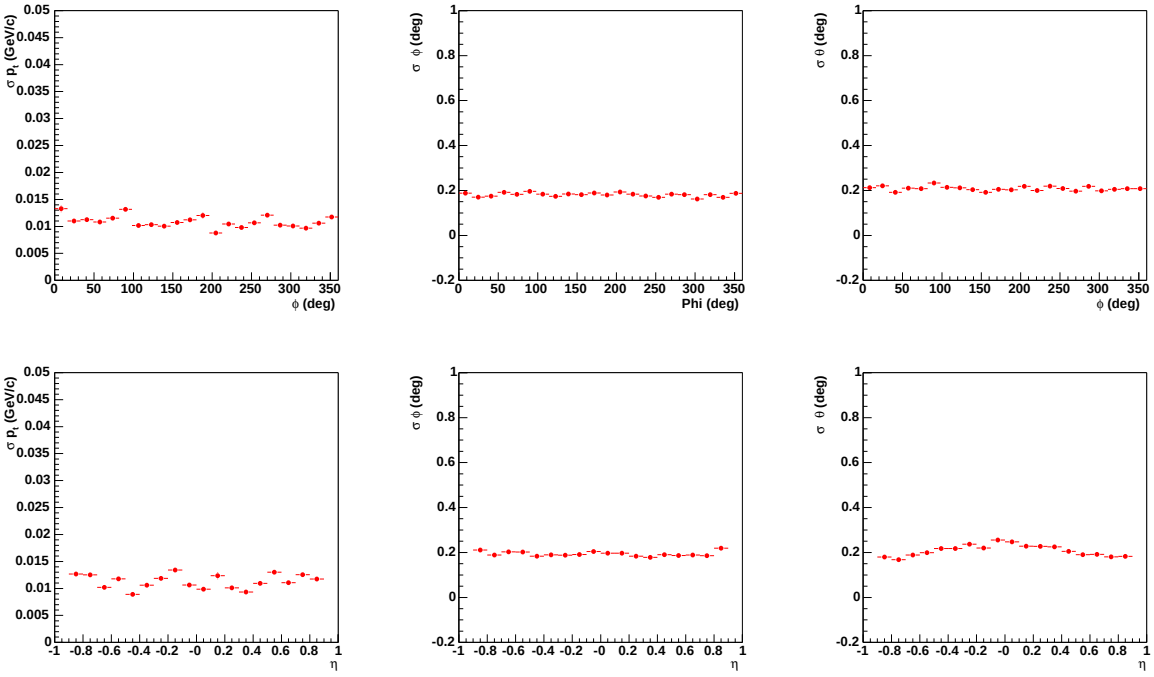

Figure 9.8: Global detector resolutions as functions of ϕ and η. None of the three resolutions depend seriously on these quantities. The data are simulated in the **TRD-add-seeds** scenario at half multiplicity.

9.6 Fast Simulation Package

The central barrel Fast Simulation Package (FSP) consists of six steps:

1. Rejection of 10% of the electrons and a large fraction of the pions according to the combined TPC and TRD pion efficiency as a function of their momentum.
2. Pseudo-rapidity cut, $|\eta| < 0.9$.
3. According to the particles transverse momentum and spatial location (η and ϕ), a decision is taken wether a particle is accepted or not in the detector space according to the detector efficiency LUT, Figure 9.3 and Figure 9.4.
4. Smearing the three kinematics quantities of each accepted particle according to the resolutions LUTs, Figures 9.6 and 9.7.
5. Transverse momentum cut.

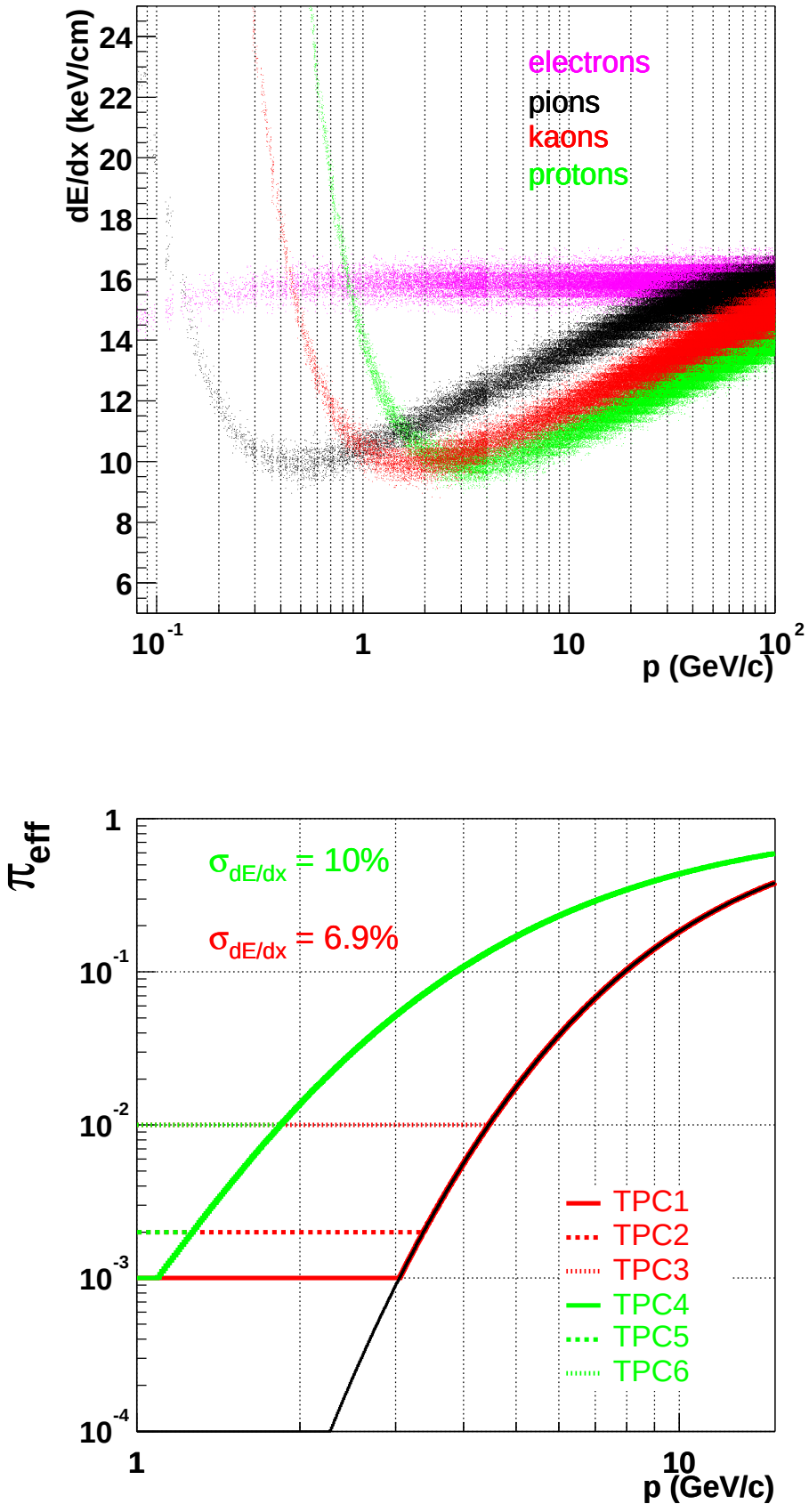

Figure 9.9: Upper panel: dE/dx distribution of electrons, pions, kaons, and protons. The distributions are Gaussian with $\sigma = 6.9\%$. Bottom panel: Pion efficiency at 90% electron identification efficiency for several TPC scenarios.

Chapter 10

Physics Performance of the ACB

10.1 Generators

Many processes contribute to the combinatorial background spectrum in the di-electron chanel. Dalitz processes, Drell-Yan process, open charm and open beauty semi-leptonic decays, mesons semi-leptonic and di-leptonic decays, conversion electrons generated from the particles interaction with the detector materials, and misidentified charged pions and kaons.
Many of these processes deliver electrons (positrons) at low transverse momenta. Therefore in Quarkonia studies, a p_t-cut is mandatory to eliminate the largest amount of the background. As shown in previous studies [9], and as will be justified below, a p_t-cut of 1 GeV/c is a suitable choice. This allows to exclude many electron sources which do not contribute to the background with such a p_t-cut. In this study only relevant sources are considered. These are the mis-identified charged pions[1], the **D** and **B** mesons semi-leptonic decays, and the electrons from Λ_c and Λ_c hyperons as well as their pion decay products.
Also those sources like the Dalitz and conversion, where a certain part of their e-daughters is still above the 1 GeV/c-cut, are not included. Their contribution is at the level of 2% [9].

The pions were generated by a parameterized HIJING model, which generates charged and neutral pions and kaons. The $c\bar{c}$ and $b\bar{b}$ were generated with PYTHIA, they decay in all **D** and **B** meson states respectively and Λ_c and Λ_b hyperons. The Quarkonia were generated with a PYTHIA-based AliRoot parameterization.

10.2 Generators Properties and Acceptance

p_t- and η-Distributions:
To make an overview on the p_t- and η-distributions of the Quarkonia, $5 \cdot 10^6$ particles

[1]Kaons and protons are considered to be well identified and separated from pions by the TPC and TOF detectors, see Figure 2.5.

of each family were generated according to a PYTHIA-based AliRoot parameterization. The generation was implement over a pseudo-rapidity range of $|\eta| < 10$, over the whole azimuth and a large momentum range ($0 \text{ GeV}/c < p < 999 \text{ GeV}/c$). The particles are forced to decay in the di-electron channel.

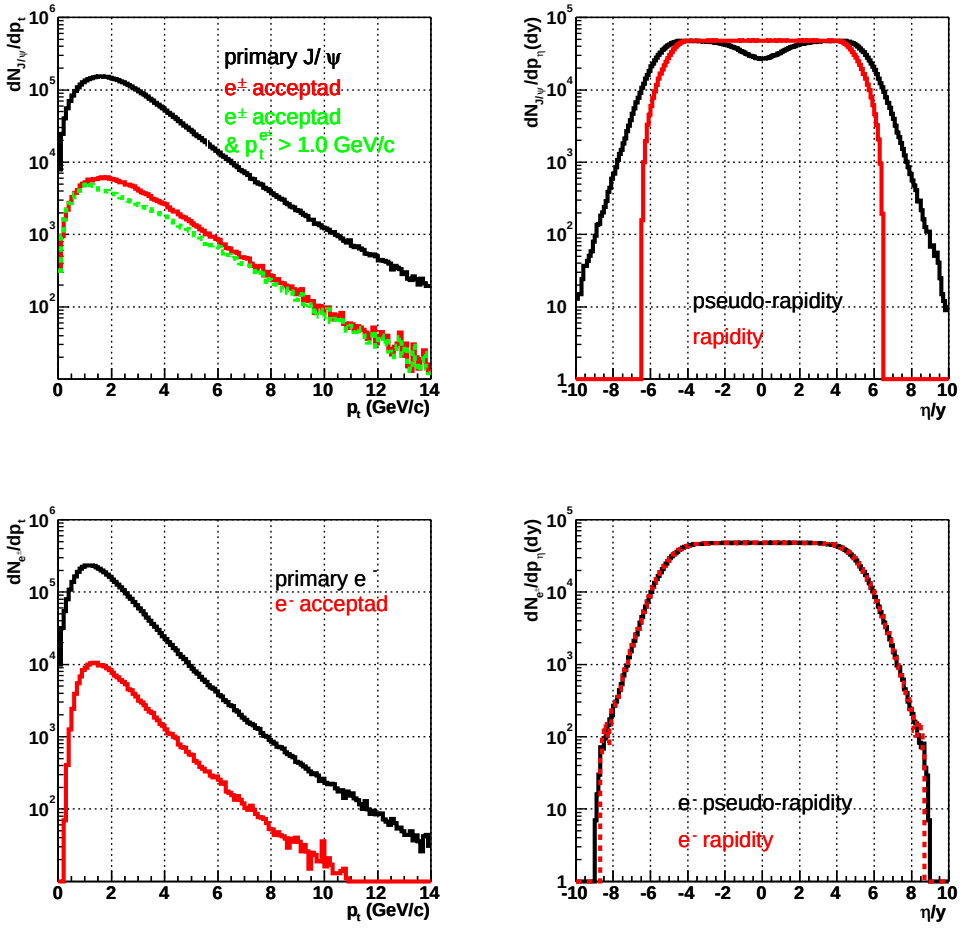

Figure 10.1: Up left: p_t-distributions of the generated J/ψ mesons. The black histogram shows the distribution of the primary particles. The red histogram shows the J/ψs of which the daughters are within detector acceptance at half multiplicity. The green histogram represents the p_t-distributions of the J/ψs of which both daughters are accepted and pass a p_t-cut of 1 GeV/c. The upper right panel shows the η- and y-distributions of the primary J/ψs. Bottom left: p_t-distributions of the primary J/ψ daughters (black) and those which are accepted (red). Bottom right: η- and y-distributions of the J/ψ decay electrons.

Figure 10.1 shows the kinematic quantities of the generated J/ψs. The upper left panel shows the p_t-distribution of the primary "generated" J/ψs, represented by the black histogram. Their average transverse momentum is about $\langle p_t^{J/\psi} \rangle = 2.578$ GeV/c. The red histogram shows those J/ψs of which both di-electron daughters are within detector

acceptance. In the following discussion, a particle is considered to be accepted if it is within the η-acceptance of the ACB **and** it passes the combined detector efficiency at a given multiplicity. The distributions discussed in this section were determined by using the detector efficiency at half multiplicity.
The green histogram shows those J/ψs of which both daughters are within acceptance, with a p_t larger than 1 GeV/c. After applying the combined pion efficiency of TPC3, see Figure 9.9, and TRD and a p_t-cut on single electrons of 1 GeV/c, only about 4.5% of the primary generated J/ψs can be detected and identified. From now on, the expression "p_t-cut" is related to single electrons or pions unless otherwise noted.

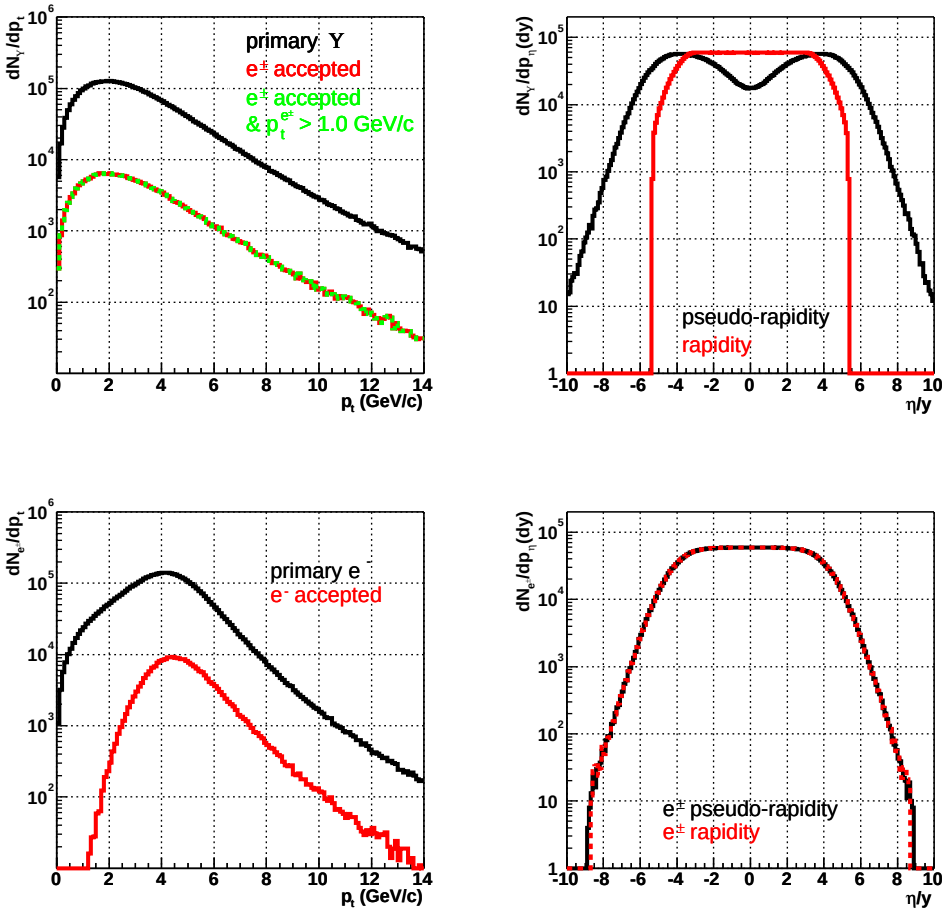

Figure 10.2: Up left: p_t-distributions of the generated Υ mesons. The black histogram shows the distribution of the primary particles. The red histogram shows the Υs of which the daughters are within detector acceptance at half multiplicity. The green histogram represents the p_t-distributions of the Υs of which both daughters are accepted and pass a p_t-cut of 1 GeV/c. The upper right panel shows the η- and y-distributions of the primary Υs. Bottom left: p_t-distributions of the primary Υ daughters (black) and those which are accepted (red). Bottom right: η- and y-distributions of the Υ decay electrons.

The upper right panel of Figure 10.1 shows the η- and y-distributions of the primary

J/ψs. They are distributed within a flat rapidity region of $|y| < 4$. For the ACB performance, invariant mass spectrum simulations, the J/ψs will be generated within this rapidity range.
The lower left panel of Figure 10.1 shows the p_t-distributions of the J/ψ decay electrons. The primary electrons (no cuts) have an average p_t of $\langle p_t{}^{J/\psi \to e^{\pm}} \rangle = 1.835$ GeV/c, black histogram. The red histogram shows the p_t-distribution of those daughters which are within the ACB acceptance. The lower right panel of the figure shows the η- and y-distributions of the J/ψ decay electrons.

Figure 10.2 shows the p_t-distribution of the Υs as described above in the J/ψ case (upper left panel) and the η- and y-distributions in the upper right panel. The generated Υs have an average transverse momentum of $\langle p_t^{\Upsilon} \rangle = 3.115$ GeV/c. They are distributed over a flat rapidity range of $|y| < 3$. Nevertheless for the invariant mass spectrum simulations they will be generated within a rapidity range of $|y| < 4$. This allows a large safety factor.

The lower left panel of Figure 10.2 shows the p_t-distribution of the Υ decay electrons. The primary electrons are represented by the black histogram. With an average p_t of about 4.111 GeV/c they can not be identified by any of the realistic TPC pion identification scenarios, see later. The majority of these electrons reach the TRD and pass through all of its six layers where they can be identified. The red histogram shows those electrons within acceptance. Their average p_t is 4.85 GeV/c, note that the distribution starts at a p_t of about 1 GeV/c. A p_t-cut at this level does not affect the Υ signal at all, but it eliminates a large fraction of the background as will be shown later.
The lower right panel shows the rapidity and the pseudo-rapidity distributions of the primary electrons of the Υ decays. After applying the acceptance conditions, the combined PID of TPC3 and TRD, and a p_t-cut of 1 GeV/c, only about 6.3% of the generated Υs are identified within acceptance.

The left panel of Figure 10.3 shows the p_t distributions of the **D** mesons (black) and the Λ_c baryons (red) which come from the generated $c\bar{c}$ pairs. The solid lines represent the distributions of the primary electrons with average transverse momenta of 0.463 GeV/c for the **D**s and 0.453 GeV/c for the Λ_cs. The dashed histograms of corresponding colors represent the electrons within acceptance.
The upper right panel of Figure 10.3 shows the corresponding histograms of the pions produced from the **D** and Λ_c decays. Their average transverse momenta are 0.440 GeV/c and 0.274 GeV/c respectively. The dashed histograms show the pions within the detector acceptance. The dotted histograms represent misidentified pions (within acceptance) after applying the pion efficiency of TPC3 and TRD. With a p_t-cut of 1 GeV/c, the combined pion efficiency rejects more than 99.99% of accepted pions.

The bottom row of Figure 10.3 shows the p_t-distributions of the electrons and pions from **B** and Λ_b decays which come from $b\bar{b}$ pairs. The average p_t of the electrons is 1.528 GeV/c in the **B** mesons case and 0.546 GeV/c in the Λ_b case. These values show that the largest contribution to the background comes from the semi-leptonic decays of the **B** mesons. The bottom right panel shows the pion distributions generated from the **B** and the Λ_b decays. Their average p_t are 0.557 GeV/c and 0.546 GeV/c respectively. With a p_t-

cut of 1 GeV/c, the combined pion efficiency of TPC3 and TRD, eliminates more than 99.9(99.99)% of the pions generated from the **B**s (Λ_bs).

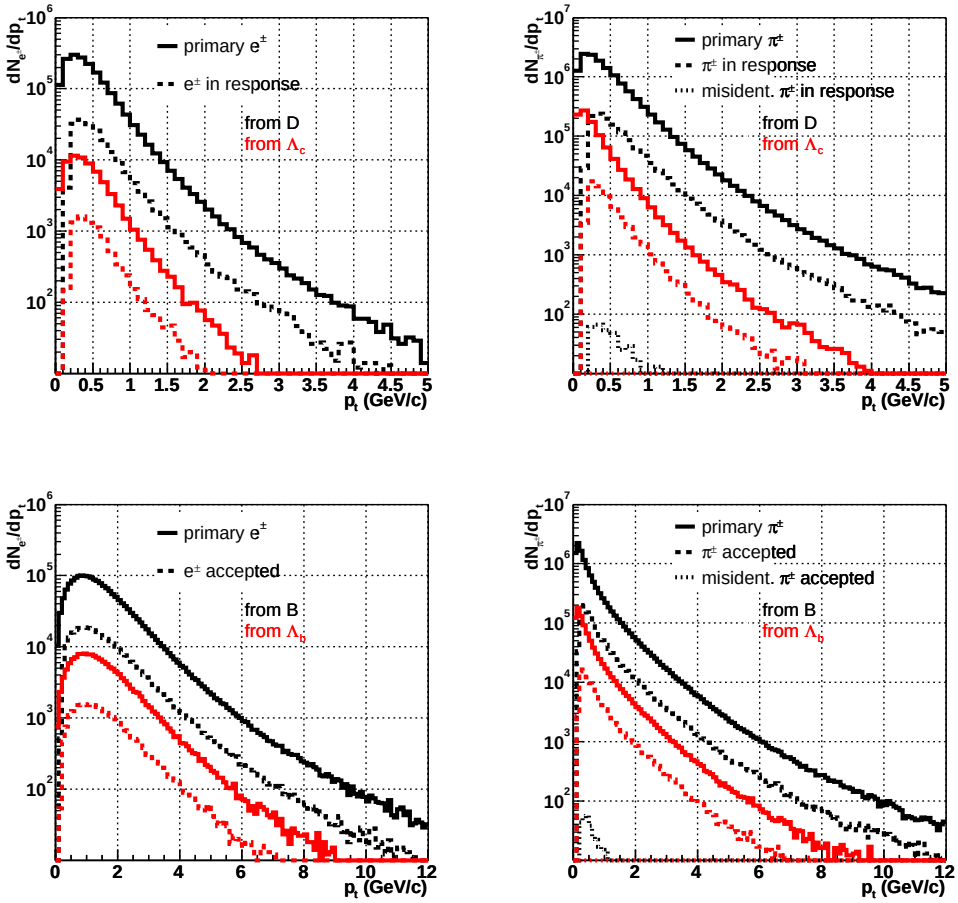

Figure 10.3: p_t-distributions of **D** and Λ_c electrons (up left) and pions (up right). The bottom row shows the corresponding p_t-distributions of the **B** and Λ_b decays. Solid: primary, dashed: within detector acceptance, and dotted misidentified pions.

Figure 10.4 shows the pions and kaons distributions which are generated from the underlying event with a multiplicity, dN_{ch}/dy=4000. The average p_t of the pions and kaons is 0.472 GeV/c and 0.67 GeV/c respectively. In each event there are about 8200 primary pions and 850 primary kaons. 0.12 pions and 0.016 ($< 4 \cdot 10^{-3}$%) kaons pass all cuts (including a p_t-cut of 1 GeV/c) and are misidentified according to the combined pion efficiency TRD3/TRD. The kaons are rejected according to the pion rejection capability of the detectors. The low number of surviving kaons justifies again their exclusion from the invariant mass simulations, protons are excluded as well.

p_t-Cut:
Figure 10.5 shows the survival probability of electrons and pions from the different back-

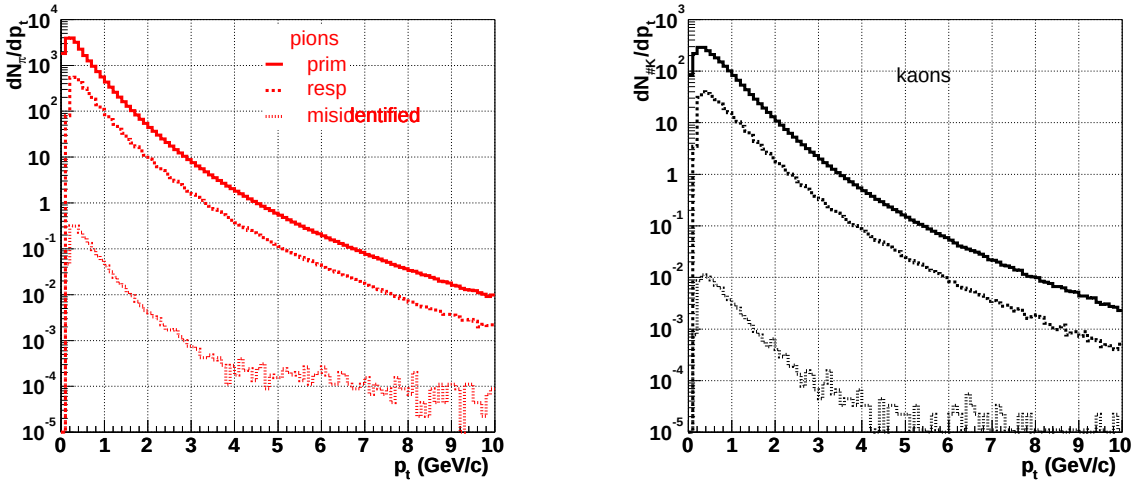

Figure 10.4: p_t-distributions of pions (left) and kaons (right) generated from the underlying event with a multiplicity of 4000. In average 0.12 pions per event pass all cuts and are misidentified. Assuming the kaon electron separation to be equal the pion electron separation capability, in average, 0.016 kaons per event pass all cuts and are misidentified.

ground sources considered in this study and the Quarkonia signals. The surviving probability for pions from the underlying event drops to 60% at a p_t-cut of 0.5 GeV/c, just where the J/ψ electrons decay products are still not affected by the cut. Apart from the **B** electron decay products where 95% of the electrons survive, the same reduction factor is achieved in the pions and electrons decay products of the other sources (D, Λ_c, Λ_b). The rejection of particles with p_t below 1 GeVc removes more than 80% of the pions from the underlying event and the pions and electrons from the **D** and Λ_c decay products. In the $b\bar{b}$ sector this cut removes more than 75% of the pions and 25% of the electrons products but only 10% of the J/ψ electrons are rejected. The Υdecay electrons are not affected by this cut and any cut up to 2 GeV/c. With these results a single electron p_t-cut of 1 GeV/c will be adopted in the performance simulations and a case study of the Υ sector will be held at p_t-cuts up to 2.5 GeV/c where effectively only the electrons from the **B** decay contribute to the background.

10.3 Simulation Environment

The fast simulation procedure of di-electron invariant mass spectrum is carried out under the following considerations:

1. **Detector response:**
   The LUTs are reconstructed within the following remarks:

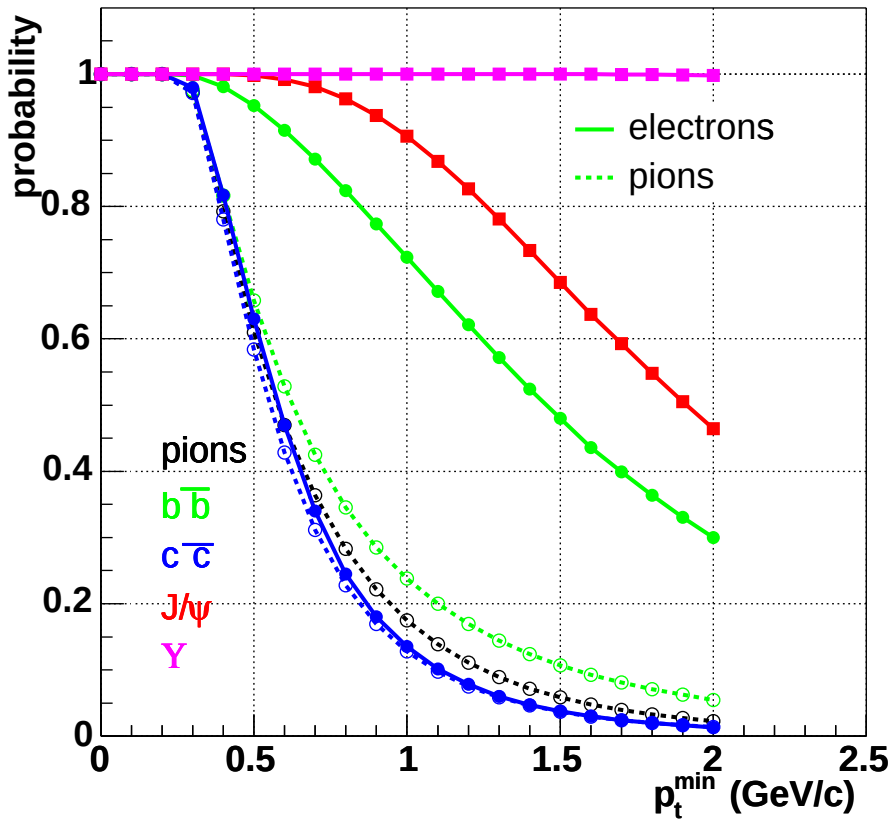

Figure 10.5: The survival probability of electrons and pions as a function of the lowest considered, single electron p_t. The results are achieved with particles within the ACB η acceptance and the detector response for half multiplicity.

- Magnetic field is 0.4 T.
- The statistics is not large enough for all multiplicities, especially at low multiplicity. Therefore the detector efficiency is to be understood as a lower limit and the resolutions are to be taken as upper limits. Meanwhile, improved tracking procedures have improved them significantly [185].
- The generated events contain only pions and kaons. The results will be used for di-electron spectrum analysis. This reduces the detection efficiency especially for p_t between 1 GeV/c and 3 GeV/c by about 10%.
- The data at low- and full multiplicity do not include the **TRD-add-seeds** step, therefore the results were reconstructed from the half multiplicity data where such simulations exist. The best fits to the resolutions do not describe the data well at high p_t.

2. **Particle identification:**

- Kaons are considered to be well identified in the TPC and TOF. Only pions

from underlying events as well as pions and electron pairs from the $c\bar{c}$ and $b\bar{b}$ decays can contaminate the reconstructed electrons and positrons.

3. **Included particles:**

   - 0.033 J/ψ particles and 0.0004 Υ are included in each event. They are generated with an AliRoot parameterization.
   - 115 $c\bar{c}$ pairs and 5 $b\bar{b}$ pairs are included in each event which are generated with PHYTIA.
   - Charged pions are generated with a HIJING model corresponding to the multiplicities 2000, 4000, and 8000.
   - Background sources with low-p_t electrons ($p_t < 1$ GeV/c) are not included. Also Dalitz and conversion electrons are not included. In [9] it is shown that their contributions to the background are below 2% as far as a p_t-cut of 1 GeV/c is considered.

4. **Nominal conditions:**
   If not specified, the simulations are carried out under the following conditions:

   - Low multiplicity.
   - η-cut, $< |0.9|$.
   - p_t-cut, > 1 GeV/c.

10.4 Qualitative Consideration of the Invariant Mass Spectra

For the Quarkonia signal analysis, 300 k underlying events were generated for each of the three considered multiplicities. Each event contains 115 $c\bar{c}$ and 5 $b\bar{b}$ pairs, and 0.033 J/ψ and $4 \cdot 10^{-4}$ Υ mesons, as calculated in Section 8.3. The invariant mass spectrum is calculated from electron pair candidates (standing for electron pairs and misidentified pions) after applying all cuts. The calculation has been carried out by combining each of the surviving electron candidates with each of the surviving positron candidates (*comb*inatorial).

To enhance the statistics, the electrons of each event were also combined with the positrons of the following nine events leading to a total of $3 \cdot 10^6$ analyzed events. This establishes a fraction of about $3.8 \cdot 10^{-4}$ of the total minimum bias event rate and $3.8 \cdot 10^{-3}$ of the central event rate within an ALICE year.

Figure 10.6 shows the invariant mass spectrum calculated under nominal conditions. The spectra represent the invariant mass as gained by applying the different TPC pion efficiency and dE/dx-resolution scenarios, TPC1 to TPC6, with the pion efficiency shown in Figure 9.9.

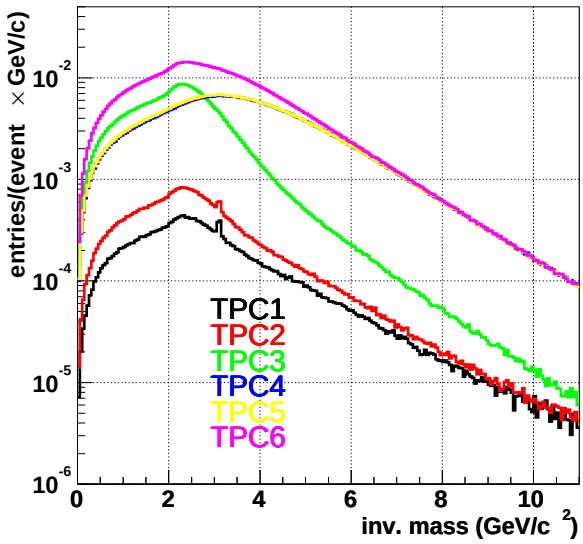

Figure 10.6: Invariant mass spectrum of electron pair candidates for all TPC scenarios without TRD pion rejection support. Results are achieved under nominal conditions. Only constricted access to the J/ψ region is achieved by TPC1 and TPC2 which consider optimistic pion efficiency. An access to the Υ region is not possible even under those optimistic scenarios.

The TPC1 scenario allows a good access to the J/ψ region as can be seen in the spectrum where the J/ψ resonance is visible. The same is true for the TPC2 scenario. However, TPC1 is a very optimistic case since it considers a pion efficiency of 10^{-3} for momenta below 3 GeV/c and therefore one can not rely on its achievement in reality. TPC2 is still an optimistic option but closer to realistic conditions.
Going to TPC3 and above, the resonance is overcasted by the background. None of the TPC scenarios allow an access to the Υ region. Therefore, it can already be stated that all TPC scenarios with pion efficiency worse than TPC2, will not be able to access any of the Quarkonia states significantly. Only TPC1 and TPC2 allow an access to the J/ψ family but not to the Υ.
Realistic TPC scenarios are located between TPC2 and TPC3, and therefore only these two cases will be discussed in the following unless otherwise noted.

The left panel of Figure 10.7 shows the invariant mass spectrum resulting from the combined pion rejection capability of TPC2. As in the experiment, the combinatorial spectrum is calculated by combining each surviving electron candidate with each surviving positron candidate. The calculation results in the dashed black histogram. The background distribution is calculated by the mix-event method resulting in the solid black histogram. A part from the J/ψ region, both histograms are not distinguishable. Although this is still an optimistic approach, especially because of the assumed Gaussian shape of the dE/dx distribution, it is obvious that the TPC is able to access the J/ψ family. However the spectrum lays by factor 6 above the J/ψ signal, which is computed directly from the surviving electron pairs coming from the primary J/ψs (blue peak). In the region of the Υ family, both spectra are by an order of magnitude higher than the Υ signal (purple peak).
Combining the TPC2 pion identification capability with that of the TRD, reduces the

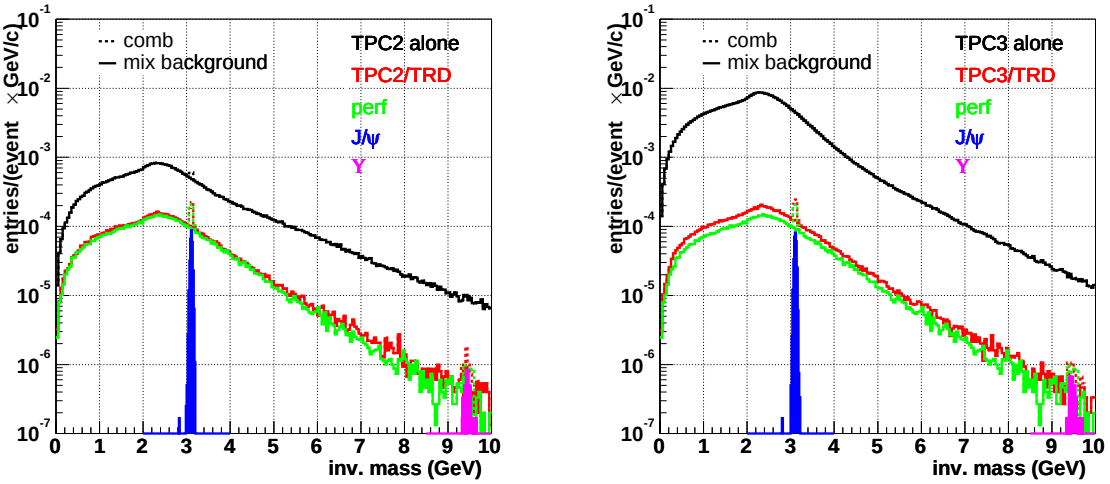

Figure 10.7: Invariant mass spectrum of di-electron candidates. The spectra are calculated under nominal conditions. Left panel: TPC2 scenario in stand alone modus and in combination with the TRD. Right panel: Same as in the left panel for the TPC3 scenario.

background by an order of magnitude in the J/ψ sector as can be seen by comparing the black histograms with the red ones. Low statistics cause numerical fluctuations in the spectrum above $m_{e^+e^-} = 7$ GeV/c^2. Nonetheless, the TRD contribution makes the Υ family accessible. The results of the combined electrons identification differs only slightly from the ideal case where a perfect pion identification is assumed[2] (*perf*, green histogram).

Going to the more realistic case of TPC3, results in a combinatorial distribution which stands by two orders of magnitude above the J/ψ and the Υ peaks as visible in the right panel of Figure 10.7. Also in this case only the TRD enables a reasonable distinction of both resonances.

As discussed above, worse scenarios of the TPC would obviously not be able to record Quarkonia signals by their own. It is to be verified, whether the TRD will be able to perform in the Υ region for worse case scenarios with a resolution of the energy loss distribution above 6.9%.
Figure 10.8 shows the calculated invariant mass spectrum under the same conditions as in Figure 10.6 but with applying the measured TRD pion efficiency in addition to that of the different TPC scenarios. The graphical representation of the spectrum is subdivided into two panels to illustrate the unambiguous accessibility to the Υ family enabled by the TRD for all TPC scenarios. In the following if not explicitly specified, the discussed TPC scenarios include the TRD pion efficiency.

[2]Note that the perfect identification scenario implies a total pion rejection at an electron efficiency of 90%. The background under the resonances comes from the surviving electrons, mostly, from the **B** semi-leptonic decays.

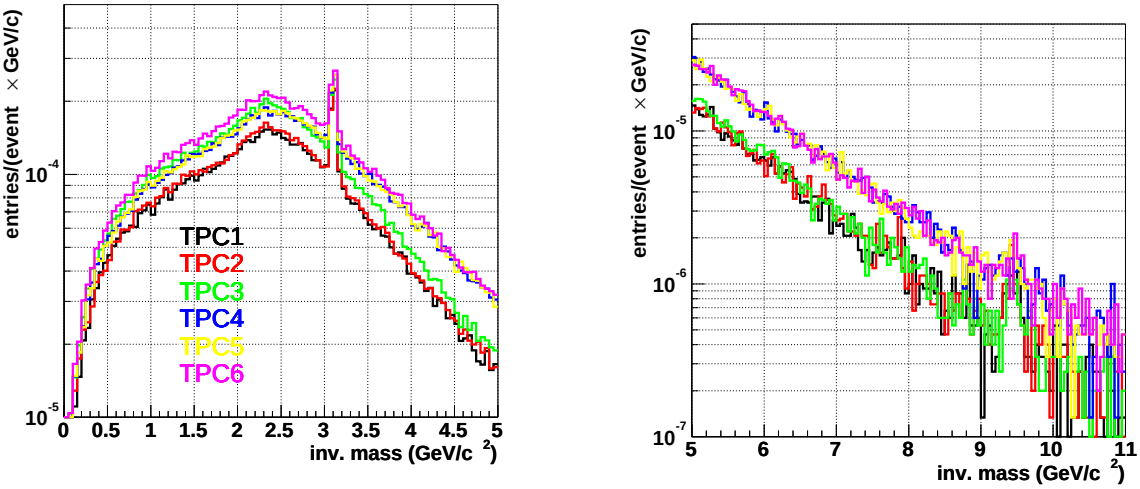

Figure 10.8: Same calculations as in Figure 10.6 with the TRD contribution to the pion efficiency. Both Quarkonia sectors become accessible even under the TPC worst-case pion efficiency and a dE/dx-resolution of 10%, TPC6. The graphical representation is subdivided into two panels for illustration purposes.

10.5 Resonances Resolution

Figure 10.9 shows the J/ψ and the Υ signals as achieved by the TRD and the TPC2 scenario (upper row) and TPC3 scenario (lower row). As in the experiment, the signal has been derived by subtracting the mixed event background from the combinatorial invariant mass distribution. Both combinations enable a resolution of about 26 MeV in the J/ψ sector and 76 MeV and 86 MeV in the Υ sector for the TPC2 and TPC3 respectively. These values are better than the anticipated values ($\sigma_{J\psi} \simeq 30$ MeV and $\sigma_{\Upsilon} \simeq 100$ MeV) such that the individual Quarkonia states can be solved.

	J/ψ		Υ	
	TPC2	TPC3	TPC2	TPC3
2000	26.1	27.4	75.6	86.4
4000	29.4	29.8	89.0	86.5
8000	33.4	33.6	111.9	76.7

Table 10.1: J/ψ and Υ resolutions at three multiplicities and the most realistic TPC scenario. The values are in MeV.

At half- and full multiplicities the resolutions are given in Table 10.1. For both TPC scenarios, the J/ψ resolution at half multiplicity is around the anticipated value and it is by about 11% higher at full multiplicity.
Due to spectrum fluctuation in the Υ region, the resonance fit flattens in some cases. Therefore the Υ resolution fluctuates such that only a trend statement can be made. Nevertheless, it is below 100 MeV/c^2 for low- and half multiplicity. At full multiplicity it will, however, not exceed the anticipated value by more than 12%. Recalling that the

parameterization of the global resolutions of the kinematic quantities are upper limits, the achieved resolutions are in a satisfying range even at full multiplicity and without making use of the improved tracking procedure [185].

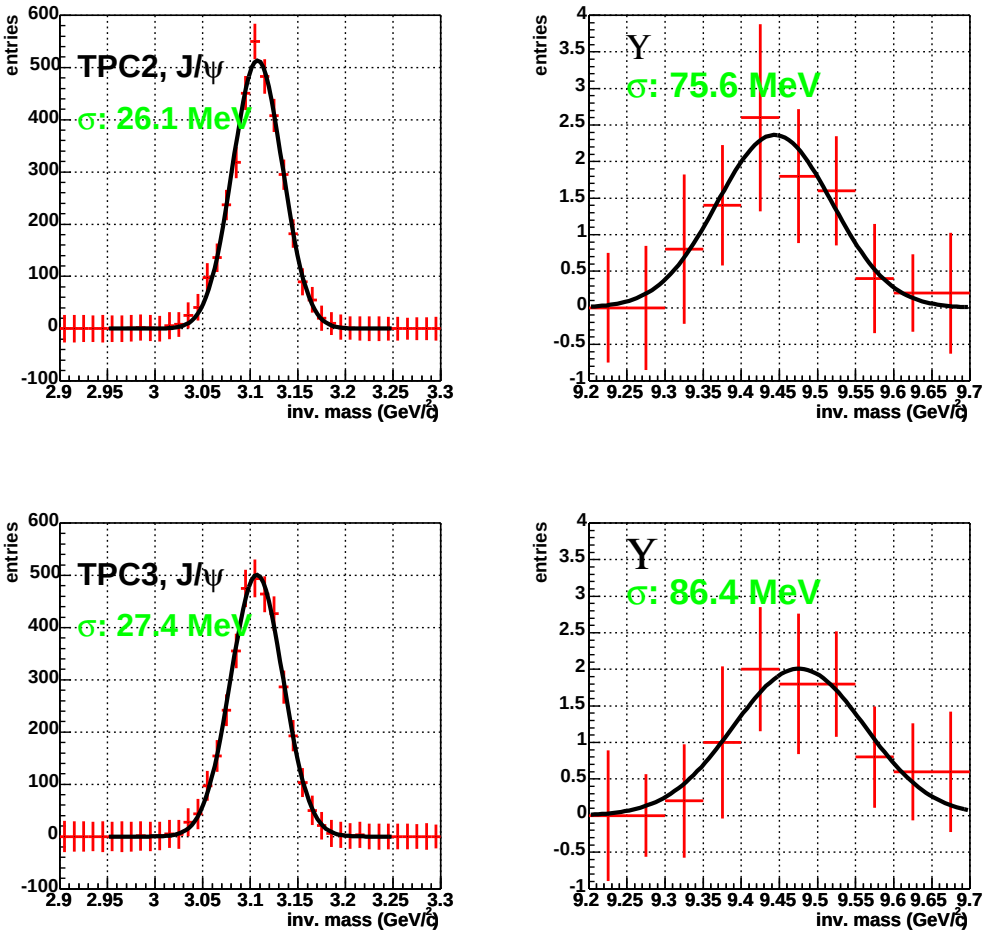

Figure 10.9: Upper row: The J/ψ signal (left) and the Υ signal (right) as achieved by the combination of TPC2 and TRD. The ACB enables a J/ψ resolution on the order of 26 MeV and an Υ resolution of about 76 MeV. The resolutions achieved by the TRD and the TPC3 scenario is on the same order, bottom row.

10.6 Calculation of the Signal

The signal and the background values are calculated by integrating the resonance peak and the background distribution between the mass values $m_Q - a \times \sigma_Q$ and $m_Q + a \times \sigma_Q$, where m_Q is the mean value of a Gaussian fit of the resonance and σ_Q its resolution.
The choice of the factor a influences the results and therefore it must be optimized. To evaluate its influence on the results of the signal-to-background ratio (S/B-ratio) and the significance, both quantities of the J/ψ signal are shown in Figure 10.10 as functions of

the factor a. The significance is defined as: $Signal/\sqrt{Signal + Background}$ for a fraction of $3.8 \cdot 10^{-3}$ from the ALICE year. It does not depend seriously on the integration range within the studied a interval. However, the best achieved S/B-ratio is at $a = 1.6$. Therefor this value is used in the signal and background calculation.

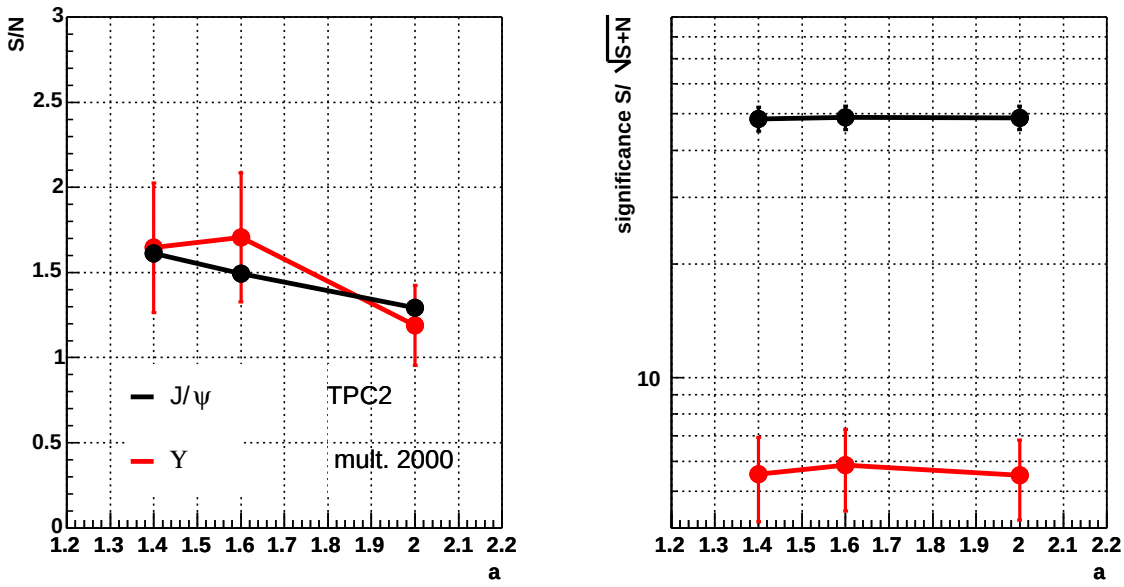

Figure 10.10: S/B-ratio (left) and significance (right) as functions of the signal integration window in units of the resonances resolutions.

10.7 Quantitative Consideration of the Invariant Mass Spectra

Figure 10.11 compares the S/B-ratio (left) and the significance (right) as functions of the pion efficiency (in terms of the TPC scenarios) with and without a TRD contribution at nominal cuts. Without TRD, dashed lines, the J/ψ S/B-ratio drops evanescent by more than 96%, when going from TPC1 to TPC3. This low S/B level continues for all other TPC scenarios with worse pion efficiency. The corresponding significance drops by almost 75% between TPC1 ($S/\sqrt{S+N} \simeq 38$) and TPC3 ($S/\sqrt{S+N} \simeq 10$) where it saturates. The same behavior is true for the Υ family with the difference that all the Υ S/B-ratios as well as the significance values are negligible.

With the TRD, solid line, the J/ψ S/B-ratio is enhanced by an order of magnitude for all TPC scenarios and the significance reaches values around 50 for TPC1-TPC3 and about

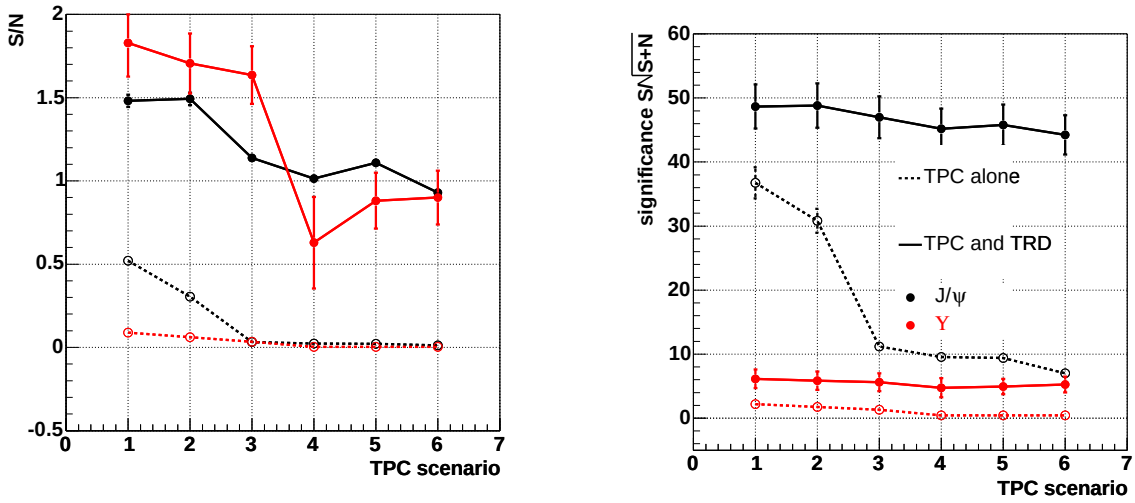

Figure 10.11: S/B-ratio (left) and significance (right) as functions of the TPC pion efficiency scenarios alone (dashed) and with the TRD support (solid). Going from TPC1 to TPC3, both the S/B-ratio and the significance of the J/ψ signal drop dramatically with the TPC alone scenarios and reach negligible values for worser TPC cases. The Υ signal is for all cases almost negligible. With the TRD the signals are improved by an order of magnitude and the significance is improved by factor 5 especially at TPC pion efficiency corresponding to TPC3 to TPC6.

45 for TPC4-TPC6. The Υ S/B-ratio is enhanced by factors larger than the J/ψ ratio. It reaches values between 1.6 and 1.8 for the TPC1-TPC3 with a significance of about 6. For the TPC4-TPC6 the Υ S/B-ratio reaches values around 0.9 with significance higher than 5. Note that the numerical fluctuation in the Υ region causes large errors. The signal at TPC4 does not follow the trend of the other values. However, in terms of the relatively low statistics, the value is compatible with the other values within its error bars.

Figure 10.12 relativizes the calculated S/B-ratios and the significance values to the ideal case of perfect pion identification for all TPC scenarios with (solid lines) and without TRD (dashed lines). The perfect S/B-ratios of the J/ψ and the Υ signals are, respectively about 1.44 and 2.13 with significance values of 48.86 and 6.1.
Without the TRD contribution the best case TPC scenario achieves rather 35% of the ideal S/B-ratio in the J/ψ region and less than 5% in the Υ region. Both vanish for worse cases. The significance is as good as 75% (J/ψ) and 35% (Υ) of the ideal case. With TPC2 (TPC3) the relative significance of the J/ψ is about 60% (20%) of the ideal case. For the Υ signal, the significance drops to 30% for TPC2 and to 10% for TPC3.
With the TRD, all values improve significantly. Realistic TPC scenarios (between TPC2 and TPC3), achieve a relative J/ψ S/B-ratio around 90% and an Υ S/B-ratio of about 75%. The achieved significance values are on the order of 90% of the ideal case for both Quarkonia regions. For worse TPC pion identification, the TRD enables a significance

larger than 80% of the ideal case

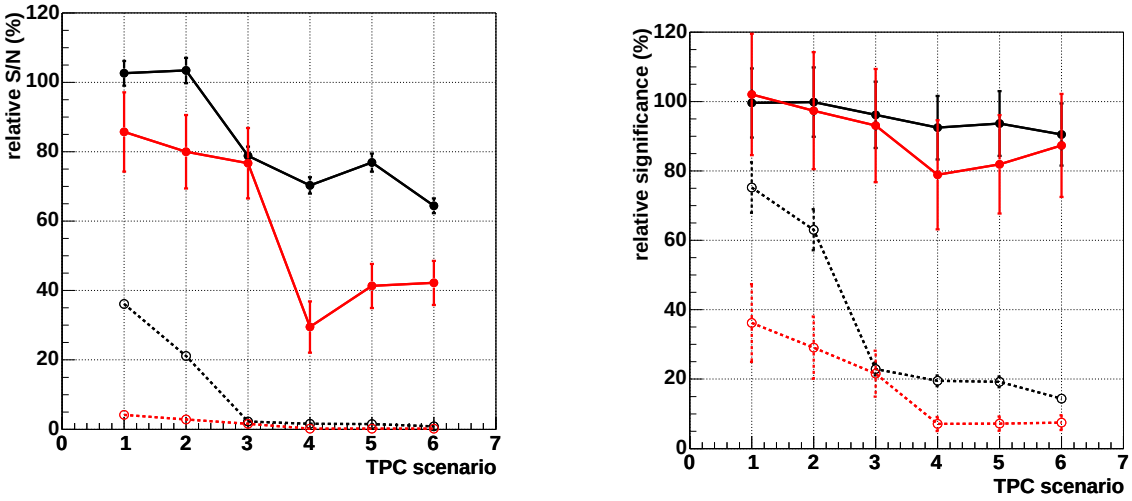

Figure 10.12: Relative S/B-ratio (left) and relative significance (right) as functions of the TPC pion efficiency. The quantities are related to the ideal case of perfect pion rejection.

The quantitative results discussed in this section, are in accordance with the qualitative discussion in the previous section and highlight, not only the necessity of the TRD as a sub-detector of the ALICE experiment, but they also show that the performance of the designed TRD is at a good level despite the worse case assumption like in the pion efficiency, detector efficiency, resolutions parameterization, and relatively low statistics. In connection with realistic cases of the TPC pion efficiency (TPC2 and TPC3), the detector enables unambiguous recording of Quarkonia signals with reasonable significant.

10.8 Significance and p_t-Cut

In Section 10.2 it was stated that a p_t-cut of 1 GeV/c eliminates a large fraction of the background. Figure 10.5 have shown that a p_t-cut at this level slightly deteriorates the J/ψ signal, but improves the Υ signal. The later is not affected even by p_t-cuts up to 2.5 GeV/c. It is to be verified, to which extend a given p_t-cut influences each signal.
The results of an extensive study of the Quarkonia signals are shown in Figure 10.13. The left panel shows the calculated S/B-ratio of both Quarkonia resonances as a function of the p_t-cut on the single electron candidates with TPC2 and TPC3. With TPC2, the ratio of the J/ψ resonance improves by factor 2 when going from a p_t-cut of 0.2 GeV/c to

1 GeV/c. At a cut of 2.5 GeV/c the increment factor is about 10. However, the significance of the signal (right panel of Figure 10.13) increases only in the region between a p_t-cut of 0.2 GeV/c and 0.8 GeV/c where it reaches its largest value and starts to drop. At a p_t-cut of 2.5 GeV/c its value is only as good as 30% of its largest one. This suggests that the best conditions to evaluate the J/ψ signal is given with the p_t-cut of 0.8 GeV/c. But, such a cut cancels the justification of excluding the Dalitz and the conversion electrons from the background. Their contributions exceed the 2% level [9] at this cut and they can not be neglected any more[3].

At low cuts, the resulting J/ψ S/B-ratio from the TPC3 scenario is worse than that of TPC2 by about 10%. At higher cuts both scenarios perform almost similar. Remember that both scenarios differ from each other only at low transverse momentum. At high momentum they are exactly similar. Therefor, within error bars, no difference is seen between the two scenarios in the S/B-ratio of the Υ resonance. The Υ S/B-ratio is constant up to a p_t-cut of 1.2 GeV/c and it is higher than the J/ψ ratio. Going to higher p_t-cuts the ratio increases by almost factor 2. Although it is relative much lower than in the J/ψ case, the Υ S/B-ratio is much more significant. Within error bars, the significance of the signal is constant at a value of about 6 for both TPC scenarios and all p_t-cuts.

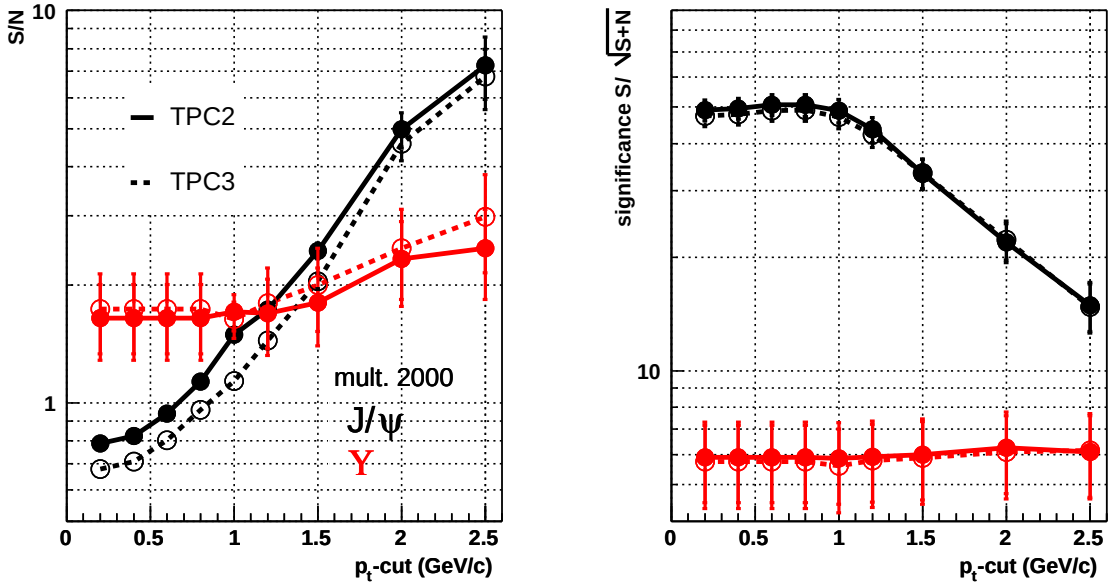

Figure 10.13: S/B-ratio (left) and significance (right) as functions the p_t-cut on single electron candidates. The J/ψ signal is only at low p_t-cuts significant. Within errors, the significance of the Υ signal is constant up to a p_t-cut of 2.5 GeV/c.

[3]Note that because of the exclusion of low-p_t contributions to the background, the statements made here are only significant in terms of relative comparison between the TPC scenarios. Only values achieved with p_t-cuts at or higher than 1 GeVc can make absolute statements.

10.9 Significance and Multiplicity

Apart from the resolutions of the resonances, the discussed results are valid for low multiplicity. Going to higher multiplicities reduces the S/B-ratios of both Quarkonia resonances. To allow a judgment on the reduction, the S/B-ratio and the significance are relativized to the ideal case of perfect pion-electron identification.

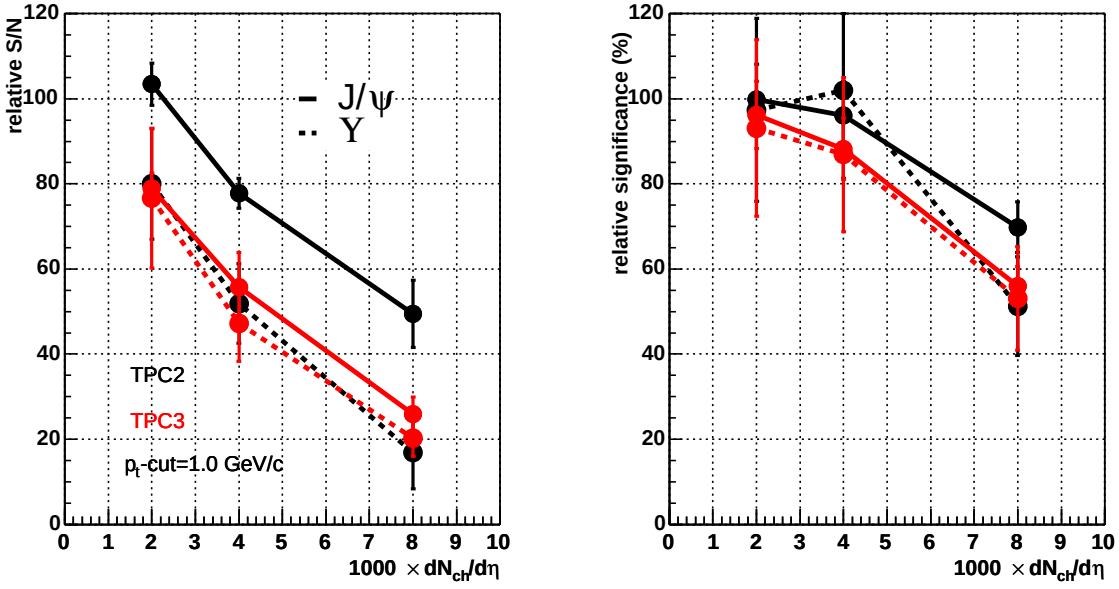

Figure 10.14: Relative S/B-ratio (left) and relative significance (right) as functions of the multiplicity for both TPC pion efficiency scenarios, TPC2 and TPC3. The quantities are related to the ideal case of perfect pion rejection. The significance is over 80% of the ideal case for multiplicities up to 5000. At higher multiplicities the significance is higher than 50% of the ideal case.

Figure 10.14 shows the relative S/B-ratio (left) and the relative significance (right) as functions of the multiplicity for both TPC scenarios: TPC2 and TPC3. Both Quarkonia signals are considered under nominal conditions. Within errors the TPC2 scenario performs almost perfect at low multiplicity for the J/ψ signal and about 80% of the ideal case for the Υ signal. At half multiplicity the ratio is reduced by about 20% (J/ψ) and 25% (Υ), translating in 80% and about 55% of the ideal case. At full multiplicity the J/ψ S/B-ratio evaluates about 50% and that of the Υ signal about 25% of the ideal case. With TPC3, the S/B results for the Υ signal are almost the same. For the J/ψ signal the S/B-ratio is about 80%, 75%, and 20% of the ideal case at low-, half-, and full multiplicity respectively. The difference in the J/ψ sector is again related with the difference between the two TPC scenarios at low transverse momentum. This is also seen in the results of

the Υ signals where no differences are expected.

Apart from the J/ψ relative significance with TPC2, the results of both resonances are above 90% of the ideal case at low-, and half multiplicity and about 60% at full multiplicity and with both TPC scenarios. The difference between the J/ψ values with both TPC scenarios holds, of course, also here. Note that the error bars are on the order of 20% in the Υ case.

Chapter 11

Conclusion

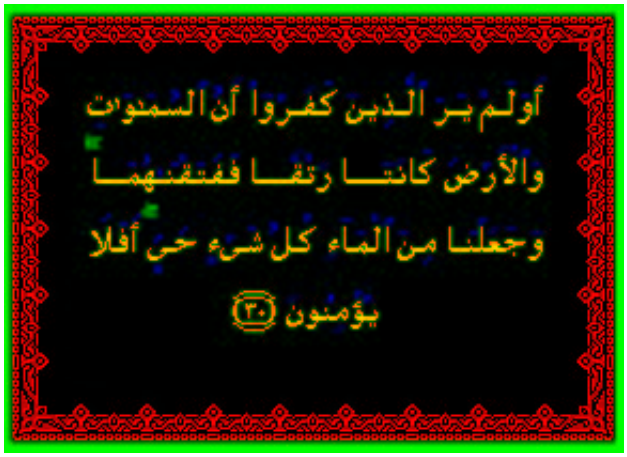

"Haben die Ungläubigen nicht gesehen, dass die Himmel und die Erde eine Einheit waren, die Wir dann zerteilten? Und Wir machten aus dem Wasser alles Lebendige. Wollen sie denn nicht glauben?"
Quran, Surah 21, Vers 30

None of the proposed QGP signatures in heavy-ion collisions is able to utterly evidence the existence of the deconfined state of matter. Beside the global observables and the hadronic signatures, the electromagnetic signatures offer a continuous access to the QGP. The Quarkonia di-electron channel is one of the most promising exposure of the existence of the deconfined plasma. The rareness of the produced Quarkonia in such collisions and their low di-electron branching ratios as well as the huge background at LHC energies, require an advanced electron identification and improved trigger on high-p_t electrons. In addition to improving the tracking capability of the ALICE Central Barrel (ACB), these

two points are the main motivation for adding the TRD to the family of the ALICE sub-detectors.

This thesis describes the development of the first real dimension TRD drift chamber from the first theoretical consideration until testing it on its tracking and particle identification performance. After the completion of tests on a prototype, the achieved pion efficiency results and those of position and angular resolutions were put in a fast simulations package to evaluate the physical capability of the TRD as constituent of the ACB.

With the programs MAGBOLTZ [136] and GARFIELD [137] the readout chamber and its drift gas mixture were simulated. The space limitation in the ACB and the saturation of the transition radiation, constrain the usage of xenon as the main component of the drift gas mixture, where a typical TR photon of 15 keV can be absorbed within 10 to 15 mm. The second component is CO_2 which was chosen to avoid flammability, reduce the diffusion and accelerates the gas mixture. The CO_2 content is 15%, which was fixed to keep the Lorentz angle within tolerances.
In this gas mixture the required drift velocity of 1.5 cm/μs is attained with a drift field of about 700 V/cm. With the drift distance of the 3 cm, this constrains the drift voltage to 2.1 kV. The smoothness of the drift field at the edges of the chamber volume and the control on the ions feed-back current are achieved with the voltage divider on the inner side of the chamber frame.
The required charge sharing on adjacent pads and the average pad width of 7.25 mm ascertain the amplification depth to 7 mm.
Due to gain variation the gas gain was chosen to be 3000, this gives an acceptable S/N-ratio and reduces the gas gain variation. With the wire gap in the amplification region this gain is attained with an amplification voltage of 1.5 kV. The electrostatical wire sagitta caused by this voltage are below 75 μm. The gain variation caused by this wire sag is below 6%. with the gain variation caused by the readout sandwich and the space charge effect the total gain variation is about within tolerances of 15%.
The anode wire pitch of 5 mm is a compromise between frame load and charge density on a wire length unit (space charge effect) as well as the position resolution of the detector. With two cathode wires per an anode wire the best possible compromise between frame load and ions feed back current in the drift region is attained.

With these specifications the first real dimension (largest) TRD chamber prototype was built from materials such that the total TRD depth is 15% of radiation length. The prototype was tested on its mechanical and electrostatical stability, and the stability of the recorded signal (gas gain variation).
The prototype exhibits a robust construction. Its frame holds a force up to 240 kg, which is more than 250% of the nominal force caused by the wire tension. The frame deformation is about 140 μm, the wire sag caused by such a deformation is negligible.

The deformations of the radiator under both, the wire tension and the overpressure in the chamber, is below 1 mm which does not affect the drift properties of the chamber. The readout sandwich concavity under the overpressure is about 210 μm. The correlated gain variation is, within errors, around the tolerated value of 15%.

The experience gained from the first prototype and the measured gain variation triggered addition investigations and lead to modifications in the construction of the readout sandwich. The addition of a thin honeycomb layer of 2 mm thickness adds to the sandwich stiffness. In addition, it has allowed to optimize the glue procedure and it ensures the flatness of the pad plane, such that the global gain variation is reduced down to 12%.

The second tests run was take with a beam of electrons and pions at momenta up to 6 GeV/c. They allowed detailed understanding of the detector components and their limitation. Detector physics parameters like drift velocity, space charge, gas gain, gas gain variation, as well as electronics components like noise and tail cancellation were evaluated. The agreement with simulated values and measurements with small prototype chambers show reliable detector performance.

The attained position resolution is on the order of 240 μm for pions at a signal-to-noise ratio of 30. For electrons this value is about 350 μm. The first value is considerably and the second is satisfying under the anticipated value of 400 μm. The angular resolutions at the same S/N-ratio are on the order of 0.75 degrees for pions and 1 degree for electrons.

Using the Likelihood pion-electron separation method the prototype is able to perform a pion efficiency of about 0.5. In a group with four small prototypes the attained pion efficiency is on the order of $2.2 \cdot 10^{-2}$. The anticipated value of 0.01 is attained by extrapolating the data for six chambers at particle momentum of 2 GeV/c. Better results are achievable when using the method of two dimensional likelihood on energy deposit (L-QX), or the application of the recently introduced *Neuronal Network Method*[184]. The agreement with simulations and achieving the anticipated value indicate a complete understanding and control on the detector.

The detector response of the TRD was evaluated within the ALICE Central Barrel (ACB), consisting of the detectors ITS, TPC, and TRD. The response study was carried out with charged pions in a magnetic field of 0.4 T. At a charged particles density per unit rapidity of 2000, the ACB reaches a total detection efficiency larger than 70% at transverse momenta above 0.5 GeVc. It enables a p_t-resolution of less than 1% at a p_t of 1 GeV/c and a value of about 3.5% at a p_t of 2.5 GeV/c. Both, the resolutions of the azimuthal angle ϕ and the polar angle θ are on the order of 0.1 degree at a p_t of 1 GeV/c.
Neither the detection efficiency nor the resolutions vary significantly when considering a multiplicity of 4000 and 8000. Discrepancies become visible at high particle momenta.

The average p_t of the J/ψ decay electrons is about 1.8 GeV/c and that of the Υ decay electrons is about 4.1 GeV/c. This allowed a p_t-cut of 1 GeV/c without loosing much of the J/ψ electrons and any of the Υ electrons, but to exclude many of the background resonance sources like ρ, ω, and ϕ mesons from the simulations. The main contributions to the background which are contained in the simulations are the underlying events and the open charm and open beauty.

As a part of the ACB, the TRD physics performance in the Quarkonia sector was extendly simulated using the project-oriented simulation environment AliRoot. A fast simulation package was developed to allow simulations with significant statistics without consuming time and computer power.

Under realistic TPC pion efficiency, the Quarkonia resonances are only accessible with the pion rejection contribution of the TRD. This capability holds on for TPC worse-scenario cases with a dE/dx resolution of 10% and a best pion efficiency of 0.01.

At charged particles multiplicity of $\mathrm{d}N_{ch}/\mathrm{d}y = 2000$ and a p_t-cut of 1 GeV/c, the three ACB detectors enable a signal-to-noise ratio of about 1.5 in the J/ψ region and 1.7 in the Υ region. This translates in about 90% of the ratios at the ideal case where pions are perfectly identified. The significance values of the signals under these conditions are on the order of 95% of the ideal case significance.
The resolution of the J/ψ and Υ resonances are below the anticipated values, which allows to resolve the individual resonance states.

The detectors performance is established for higher values of the multiplicity. At the highest possible multiplicity value of 8000, The S/N-ratios are on the order of 20% to 40% of the ideal case and the significance is on the order of 50%. Within tolerances, the resonances resolution are consistent with, or below the anticipated values.

11.1 Outlook

In detector physics, the results presented in this thesis have lead to the determination of some chamber parameters and some changes in others. The TRD is now in mass production stage.
The TRD pion efficiency will be measured in this years fall with six real dimension TRD chambers. This will refrains from extrapolating the results. After verifying that the detector is able to record Quarkonia with worse case pion efficiency, the results from other analysis methods like the L-QX and the Neuronal Network Method will be used in coming performance simulations.

In the physics performance sector, this thesis is the first study under realistic conditions and with measured detector particle separation capability. It is constrains to the Quarkonia sector, where there is still a lot to be done in the coming future. The next run has already started, it will take into account all restrictions and assumptions considered in this study.
New LUTs will be established with electrons kinematics and with high statistics to avoid extrapolations of the detector efficiency and resolutions in the high-p_t region. All values are expected to improve significantly.
The excluded sources of background like Dalitz decays and conversion electrons will be included.

The TRD contributes also to measurements of many other electronic decays, therefore other sectors like the open charm and open beauty will be studied. A vertex cut study is also planed to evaluate the capability of the ACB to separate primary and secondary J/ψs.

Finally, I wish I could contribute to the process of coming closer to an always debated particle, J/ψ. On which people do not even agree by settling its name.

Bibliography

[1] See for example F. Karsch, Lect. Notes Phys. **583** 209 (2002).

[2] *http://lhc-new-homepage.web.cern.ch/lhc-new-homepage/.*

[3] J. Schukraft, Pramana journal of physics, **57** 345 (2001).

[4] ALICE Collaboration, Technical Proposal, CERN/LHCC/95-71 (1995).

[5] ALICE Physics Performance Report (PPR), *http://alice.web.cern.ch/Alice/ppr/web/CurrentVersion.html.*

[6] T. Matsui and H. Satz, Phys. Lett. **B178**, 416 (1986).

[7] S. Digal, P. Petreczky, and H. Satz, Phys.Rev. **D64** 094015 (2001).

[8] G. Baur *et al.*, CMS Collaboration, CMS NOTE 2000/060, (2000).

[9] ALICE Collaboration, A Transition Radiation Detector, Technical Proposal, Addendum 2, CERN/LHCC/99-13.

[10] C.-Y. Wong Introduction to High-Energy Heavy-Ion Collisions, World Scientific, Singapore, (1994).

[11] F. Karsch, E. Laermann, and Peikert, arXiv:hep-lat/0305025 (2003).

[12] Douglas F. Brewer, Gauge Theories in Particle Physics, second edition, Adam Hilger, Bristol and Philadelphia (1989).

[13] A.C. Benvenuti *et al.* Phys. Lett. **B223**, 490 (1989).

[14] J. Friedman, Rev. Mod. Phys. **63**, 615 (1991.)

[15] R. Taylor, Rev. Mod. Phys. **63**, 573 (1991.)

[16] H. Kendall, Rev. Mod. Phys. **63**, 597 (1991.)

[17] G. Hansen *et al.*, Phys. Rev. Lett. **35**, 1609 (1975).

[18] S. Hahn, Nucl. Phys. **B74**, 12 (1999).

[19] J. C. Collins and M. J. Perry, Phys. Rev. Lett. **34**, 1353 (1975).

[20] I. R. Kenyon, Elementary Particle Physics (1987).

[21] K. Wilson, Phys. Rev. **D10**, 2445 (1974).

[22] J. Kogut Rev. Mod. Phys. **55**, 775 (1983).

[23] F. Karsch, E. Laermann, and Peikert, Nucl. Phys. **B605**, 579 (2001).

[24] A. A. Khan *et al.* Phys. Rev. **D63**, 034502 (2001).

[25] Z. Fodor and S. Katz, Nucl. Phys. B(Proc. Suppl.) **106**, 441 (2002).

[26] P. Forcrand and O. Philipsen, Nucl. Phys. **B642**, 290 (2002).

[27] C. R. Allton *et al.* Phys. Rev. **D66**, 074507 (2002).

[28] P. Forcrand and O. Philipsen, arXiv:hep-lat/0205016.

[29] D. Adamova *et al.*, CERES Collaburation, nucl-ex/0207008 (2002).

[30] Z. Fodor and S. Katz, hep-th/0402006.

[31] See *http://www.gsi.de/GSI-Future/cdr/.*

[32] P. Kolb, U. Heinz, nucl-th/0305084 (2003).

[33] P. Carruthers and M. Duong-Van, Phys. Rev. **D8**, 859 (1973).

[34] J. D. Bjørken, Phys. Rev., **D27**, 140 (1983).

[35] J. Y. Ollitrault, Phys. Rev. **D46**, 229 (1992).

[36] P. Braun-Munzinger and J. Stachel, Phys. Lett. **B490**, 196 (2000).

[37] M. Gazdzicki and M. I. Gorenstein, Phys. Rev. Lett. **83**, 4009 (1999).

[38] M. I. Gorenstein, A. P. Kostyuk, H. Stöcker, and W. Greiner, Phys. Lett. **B509**, 277 (2001).

[39] J.P. Blaizot Nucl. Phys. **A661**, 3c (1999).

[40] I. Tserruya, Indian Academy of Science, Vol. 60, No. 4, 577 (2003).

[41] E. L. Bratkovskaya, *et al.*, nucl-th/0401031 (2004).

[42] A. M. Poskanzer and S. A. Voloshin, Phys. Rev. **C58**, 1671 (1998).

[43] C. M. Hung and E. Shuryak, Phys. Rev. Lett. **75**, 4003 (1995).

[44] D. H. Rischke *et al.*, Heavy Ion Phys. **1**, 309 (1995).

[45] J. Barrette, *et al.*, Phys. Rev. **C 59**, 884 (1999).

[46] M. Agarwal *et al.*, WA98 Collaboration, Nucl. Phys. **A638**, 147 (1998).

[47] F. Ceretto *et al.*, CERES Collaboration Nucl. Phys. **A638**, 467 (1998).

[48] C. Alt *et al.*, NA49 Collaboration Phys. Rev. **C68**, 034903 (2003).

[49] G. Agakichiev *et al.*, CERES Collaboration Phys. Rev. Lett. **92**, 3 (2004).

[50] J. Adams *et al.*, STAR Collaboration Phys. Rev. Lett. **92**, 6 (2004).

[51] P. Kolb, J. Sollfrank, and Phys. Lett. **B459**, 667 (1999).

[52] J. Hofmann *et al.*, Phys. Rev. Lett. **36**, 88 (1976).

[53] C. Alt *et al.*, NA49 Collaboration Phys. Rev. **C**, in press, nucl-ex/0303001 (2004).

[54] H. Liu *et al.*, E895 Collaboration, Phys. Rev. Lett. **84**, 5488 (2000).

[55] X. N. Wang and M. Gyulassy, Phys. Rev. Lett. **86**, 3496 (2001).

[56] J. Barrette et al., the E814/E877 Collaboration, Phys. Rev. Lett. **70**, 2996 (1993).

[57] T. Anticic *et al.*, NA49 Collaboration Phys. Rev. **C 69**, 024902 (2004).

[58] K. Adcox *et al.*, PHENIX Collaboration Phys. Rev. Lett. **87**, 52301 (2001).

[59] M. Aggarwal *et al.*, WA98 Collaboration, Eur. Phys. J.**C 18**, 651 (2001).

[60] K. Adcox *et al.*, PHENIX Collaboration, Phys. Rev. Lett. **87**, 052301 (2001).

[61] P. Braun-Munzinger and J. Stachel, J. Phys. **G28**, 1971 (2002).

[62] P. Braun-Munzinger, J. Stachel, J. P. Wesssels, and N. Xu, Phys. Lett. **B344**, 43 (1994).

[63] P. Braun-Munzinger, I. Heppe and J. Stachel, Phys. Lett. **B465**, 15 (1999).

[64] J. Stachel, Nucl. Phys. **A610**, 509c (1996).

[65] P. Forcrand and O. Philipsen, arXiv:hep-lat/0205016.

[66] P. Braun-Munzinger, D. Magestro, K. Redlich and J. Stachel, Phys. Lett. **B518**, 41 (2001).

[67] R. Hagedorn, Riv. Nuovo Cimento **6**, 1 (1983).

[68] E.Schnedermann *et al.*, Phys. Rev. **C48**, 2462 (1993).

[69] D. Adamova *et al.*, CERES Collaburation, nucl-ex/0207008 (2002).

[70] CERES Collaburation, Nucl. Phys. **A714**, 124 (2003).

[71] D. Adamova, CERES Collaburation, Phys. Rev. Lett. **90**, 022301 (2003).

[72] C. Adler *et al.*, STAR Collaboration, Phys. Rev. Lett. **87**, 082301 (2001).

[73] K. Adcox *et al.*, PHENIX Collaboration Phys. Rev. Lett. **88**, 192302 (2002).

[74] D. H. Rischke and M. Gyulassy, Nucl. Phys. **A608**, 479c (1996).

[75] J. Rafelski and B. Müller, Phys. Rev. Lett. **48**, 1066 (1982).

[76] P. Koch *et al.*, Phys. Rep. **142**, 169 (1986).

[77] D. Kharzeev, E. Levin, and M. Nardi, hep-ph/0111315.

[78] E. Andersen *et al.*, Phys. Lett. **B449**, 401 (1999).

[79] L. Ahle, *et al.*, Phys. Lett. **B476**, 1 (2000).

[80] J. C. Dunlop and C. A. Ogilvie, Phys. Rev. **C61**, 031901 (2000).

[81] F. Antinori *et al.*, WA97 Collaburation, Eur. Phys. J. **C14**, 633 (2000).

[82] N. Carrer. NA57 Collaboration, Nucl. Phys. **A698**, 29 (2002).

[83] K. Rajagopal, Quark-Gluon Plasma 2, World Scientific, 1995.

[84] J. D. Bjørken, Acta Phys. Pol. **B23**, 637 (1992).

[85] F. Steffen, M. Thoma, Phys. Lett. **B510**, 98 (2001).

[86] J. Kapusta, P. Lichard and D. Seibert, Phys. Rev. **D44**, 2774 (1991).

[87] J. Alam, *et al.*, Phys Rep.**273**, 243 (1996).

[88] M. M. Aggarwal *et al.*, WA98 Collaboration, Phys Rev. Lett. **85**, 2595 (2000).

[89] D. Y. Peressounko and Y. E. Pokrovsky, (hep-ph/0009025) (2001).

[90] P. Huovinen, (hep-ph/0111052) (2001).

[91] T. Peitzmann, nucl-ex/0201003, (2002).

[92] M. Gyulassy, M. Plümer, Phys. Lett. **B 243**, 432 (1990).

[93] X.N. Wang, M. Gyulassy, Phys. Rev. Lett. **68**, 1480 (1992).

[94] M. Gyulassy, I. Vitev, X. N. Wang and B. W. Zhang, nucl-th/0302077 (2003).

[95] J. Harris *et al.*, STAR Collaboration, Nucl. Phys. **A698**, 64c (2002).

[96] K. Adcox *et al.*, PHENIX Collaboration Phys. Rev. Lett. **88**, 022301 (2002).

[97] E. Wang and X. N. Wang, Phys. Rev. **C64**, 034901 (2001).

[98] J. W. Cronin *et al.*, Phys. Rev. **D11**, 3105 (1975).

[99] D. d'Enterria, nucl-ex/0403055, submitted to Elsevier Science, (2004).

[100] M. M. Aggarwal *et al.*, WA98 Collaburation, Phys Rev. Lett. **81**, 4087 (1998).

[101] M. Asakawa, U. Heinz, B. Müller, Phys. Rev. Lett. **85**, 2072 (2000).

[102] S. Jeon and V. Koch, Phys. Rev. Lett. **85**, 2076 (2000).

[103] S. Jeon and V. Koch, arXiv:hep-ph/0304012 (2003)

[104] ATLAS Collaboration, Detector and Physics Performance, Technical Design Report, CERN/LHCC/99-15 (1999).

[105] CMS Collaboration, CMS TDR 6.1, CERN/LHCC/2000-38 (2000).

[106] LHCb Collaboration, CERN/LHCC/98-004 (1998).

[107] A. Andronic, P. Braun-Munzinger, K. Redlich, and J. Stachel, Phys. Lett. **B571**, 36 (2003).

[108] K. Kajantie, Nucl. Phys. **A715** 432 (2003).

[109] K.J. Eskola, K. Kajantie, P.V. Ruuskanen and K. Tuominen Nucl.Phys. **B570**, 379 (2000).

[110] U. Heinz and M. Jacob, nucl-th/0002042 (2000).

[111] K. Adcox *et al.*, Phys. Rev. Lett. **86**, 3500 (2001).

[112] H. Sorge, E. Shuryak, and I. Zahed, Phys. Rev. Lett. **79**, 2775 (1997).

[113] P. Braun-Munzinger and J. Stachel, Nucl. Phys. **A690**, 119 (2001).

[114] Y. Schutz, EPJdirect (2003).

[115] K. Schindl, LHC Performance Workshop, Charmonix XII, 3-8/03/2003.

[116] P. Giubellino, Nucl. Phys. **A715**, 441 (2003).

[117] Claus Grupen, Teilchendetektoren, Wissenschaftsverlag, Mannheim (1993).

[118] W. Blum and L. Rolandi, Particle Detection with Drift Chambers, Springer Verlag, Berlin, Heidelberg, New York, **ISBN** 3-540-56425-X, (1993).

[119] K.Hagiwara *et al.* Review of Particle Physics, Phys. Rev. D66 (2002).

[120] A. Andronic *et al.*, Nucl. Instr. Meth. **A519**, 508 (2004).

[121] B. Dolgoshein, Nucl. Instrum. Meth. **A326**, 434 (1993).

[122] C. Favuzzi, N. Giglietto, M. Mazziotta, and P. Spinelli, Transition radiation detectors for particle physics and astrophysics, della Societa italiana di Fisica, 5-6, (2001).

[123] V.M. Grichine, Parametrisation Models for X-ray Transition Radiation in GEANT4 Package. Computer Physics Communications, (2000).

[124] X. Artru, G.B. Yodh, and G. Mennessier, Phys. Rev., **D125**, 1289 (1975).

[125] G. M. Garbyan *et al.*, Zh. Eksp. Teor. Fiz. **66**, 552 (1974).

[126] G. M. Garbyan, L.A. Gevorgian and C. Yang, Nucl. Instr. Meth., **125**, 133 (1975).

[127] A. Andronic *et al.*, IEEE Trans. Nucl. Sc., vol. 48, 1259 (2001), nucl-ex/0102017.

[128] A. Andronic *et al.*, physics/0402043 (2003).

[129] A. Andronic *et al.*, Nucl. Instr. Meth., **A522**, 40 (2004).

[130] ALICE Collaboration, Transition Radiation Detector, Technical Design Report, CERN/LHCC/2001.

[131] R. Rapp and E. Shuryak, Phys. Lett. **B473**, 13 (2000).

[132] O. Busch Position Resolution wit prototypes of ALICE Transition Radiation Detector, Gesellschaft für Schwerionenforschung mbH, Dipl. (2002-01 June).

[133] ALICE Collaboration, Time Projection Chamber, Technical Design Report, CERN/LHCC/2000.

[134] W. Schmitz Cathode Pad Design for the CERES-TPC, Heidelberg (1998).

[135] O. Zaudtke, Diplomarbeit, Westfälische Wilhelms-Universität Münster,, Institut für Kernphysik, (2003).

[136] S. Biaggi Nucl. Instr. Meth. **A421**, 234 (1999).

[137] R. Veenhof, Nucl. Instr. Meth. **A419**, 726 (1998).
http://consult.cern.ch/writeup/garfield/.

[138] A. Andronic *et al.*, Nucl. Instrum. Meth. **A523**, 302 (2004).

[139] O. Busch, ALICE TRD Collaboration, Nucl.Instr.Meth. **A522**, 54 (2004).

[140] R. Veenhof, ALICE-INT-2003-029, (2003).

[141] E. Mathieson, Nucl. Instr. Meth. **A270**, 602 (1988).

[142] *http://www.josef-graef.de/baeume/rkn_i.html.*

[143] A. Andronic *et al.*, Nucl. Instr. Meth. **A498**, 143 (2003).

[144] http://www-w2k.gsi.de/daq/.

[145] M. Gutfleisch, Digitals Frontend und Preprozessor im TRAP1-Chip des TRD-Triggers für das ALICE-Experiment am LHC (CERN), Kirchhoff-Institut für Physik Heidelberg, (2002).

[146] G. Domokos and J. I. Goldman, Phys. Rev. **D23**, 203 (1981).

[147] CERES Collaburation, G. Agakichiev *et al.*, Phys. Rev. Lett. **75**, 1272 (1995).

[148] CERES Collaburation, G. Agakichiev *et al.*, Eur. Phys. J. **C 4**, 231 (1998).

[149] CERES Collaburation, G. Agakichiev *et al.*, Phys. Lett. **B 422**, 405 (1998).

[150] CERES Collaburation, B. Lenkeit *et al.*, Nucl. Phys. **A 661**, 23c (1999).

[151] Wessels *et al.*, Nucl. Phys. **A715**, 262c (2003).

[152] G. Brown, M. Rho, Phys Rep.**363**, 85 (2002).

[153] R. Rapp, J. Wambach, Eur Phys. J. **A6**, 415 (1999).

[154] CERES Collaburation, Phys. Rev. Lett. **91**, 4 (2003).

[155] A. Angelis *et al.*, HELIOS/3 Collaboration, Eur. Phys. J. **C13**, 433 (2000).

[156] M. Abereu *et al.*, NA38/50 Collaboration, Eur. Phys. J. **C14**, 443 (2000).

[157] C. Wong and Z. Wang, Phys. Lett. **B4167**, 50 (1996).

[158] M. I. Gorenstein, A. P. Kostyuk, H. Stöcker, and W. Greiner, J. Phys. **G27**, L47 (2001).

[159] M. I. Gorenstein, A. P. Kostyuk, and W. Greiner, Phys. Lett. **B519**, 207 (2001).

[160] NA60 Collaboration, Internal Note 2003-001, (2003).

[161] P. Petreczky, S. Datta, K. Karsch, and I. Wetzorke, hep-lat/0309012.

[162] M.C. Abreu *et al.* (NA50 Collab.), Phys. Lett. **B450**, 456 (1999).

[163] M. Asakawa and T. Hatsuda, Phys. Rev. Lett. **90**, 012001 (2004).

[164] C. Gerschel and J. Hüfner, Z. Phys. **C56**, 171 (1992).

[165] P. Braun-Munzinger, K. Redlich, and J. Stachel, nucl-th/0304013 (2003).

[166] M.C. Abreu *et al.* (NA50 Collab.), Phys. Lett. **B477**, 28 (2000).

[167] A. Andronic and P. Braun-Munzinger, hep-ph/0402291 (2004).

[168] S. Adler *et al.* PHENIX Collab., nucl-ex/0305030 (2003).

[169] R. Thews, M. Schrödter, and J. Rafelski, Phys. Rev. **C63**, 054905 (2001).

[170] R. Thews and J. Rafelski, Nucl. Phys. **A698**, 575 (2002).

[171] L. Grandchamp and R. Rapp, Phys. Lett. **B523**, 60 (2001).

[172] LHC Study Group, Report No. CERN/AC/95-05 (1995).
http://lhc.web.cern.ch/lhc.

[173] The CDF Collaboration, Fermilab-Conf-94/136-E, hep-ex/9412013.G. Baur *et al.*, CMS Collaboration, CMS NOTE 2000/060, (2000).

[174] F. Abe *et al.*, (CDF Collab.), Phys. Rev. Lett. 75 4358 (1995).

[175] C. Baglin *et al.*, (NA38 Collab.) Phys. Lett. **B270**, 105 (1991).
D.M. Adle *et al.*, (E772 Collab.), Phys. Rev. Lett. 66 133 (1991).

[176] N. Carrer and A. Dainese, ALICE-INT-2003-019 v.3 (2003).

[177] AliRoot, *http://AliSoft.cern.ch/offline/.*

[178] GEANT 3.21 Package, CERN Program Library W5013.

[179] *http://wwwasd.web.cern.ch/wwwasd/geant4/geant4.html*

[180] PYTHIA Physics and Manual. T. Sjstrand and L. Lnnblad [hep-ph/0108264].
http://www.thep.lu.se/tf2/staff/torbjorn/Pythia.html.

[181] P. Billior, S. Quian, Nucl. Instr. and Meth. **A294**, 219 (1990).

[182] B. Batyuna, Yu. Belikov, K. Safarik,, Internal Note /Pat ALICE/97-24 (1997).

[183] A. Dainese and N. Carrer, ALICE-INT-2003-011 (2003).

[184] Alexander Wilk, Elektronen-Pionen-Seperation im ALICE TRD, Diplomarbeit, Westfälische Wilhelms-Universität Münster,, Institut für Kernphysik, (2004).

[185] M. Ivanove, ALICE CERN-Group, private comonication.

List of Figures

1 The ALICE detector vii
2 The ALICE space frame ix

2.1 Energy density as a function of the temperature in QCD calculations. . . . 17
2.2 QCD phase boundary in the temperature-chemical potential plane. 18
2.3 Sketch of the dynamical evolution in a heavy ion collision. 21
2.4 Charged particle multiplicity as a function of beam energy. 34
2.5 Particle identification capabilities of the ALICE central detectors. 42

3.1 Energy deposit in in multi-hadron events. 44
3.2 Pions energy deposit in a Xe/CO_2 mixture. 45
3.3 Sketch of transition radiation production. 46
3.4 Energy distribution of transition radiation of a single interface. 48
3.5 Energy distribution of transition radiation of a single interface and a single foil. 49
3.6 A sketch of a MWPC chamber. 53

4.1 Pion efficiency for different TRDs as a function of the detector depth . . . 58
4.2 A cross section a long the TRD chamber. 62
4.3 Wire geometry in a TRD module. 64
4.4 TR yield from three different materials. 66
4.5 Sketch of an ALICE TRD module. 67
4.6 Sketch of the TRD front-end electronics. 69

5.1 Absorption length of photons in Xe, Kr, and Ar. 81
5.2 Drift velocity for different Xe/CO_2 gas mixtures. 82
5.3 Lorentz angle leads to an error in angular reconstruction. 83
5.4 Lorentz angle as a function of the drift field and the CO_2 content in the chamber. 84

5.5 Longitudinal and transverse diffusion, electron attachment, and Townsend coefficients in Xe/CO_2 (85:15). 86
5.6 Simulated pad response function. 89
5.7 Townsend coefficient for several Xe/CO_2 gas mixtures. 91
5.8 Gas gain as a function of the drift voltage. 92
5.9 Gas gain as a function of the number of cathode wires per anode wire and the wire pitch. 93
5.10 Electrostatic force acting on the anode wires as a function of displacement of the wire. 95
5.11 Electrostatical anode and cathode wire sagitta as functions of the anode wire voltage. 96
5.12 Cathode and anode wire sagitta as functions of the corresponding wire tension. 97
5.13 Anode wire sag as a function of the anode wire pitch. 98
5.14 Relative signal as a function of the drift time and gas gain. 101
5.15 Relative gas gain as a function of the pad plane deflection and the total wire sag. 102
5.16 Anode and cathode wire sagitta as a function of the corresponding wire diameter. 103
5.17 Equipotential lines in the chamber. 104
5.18 Electric field as a function of z and y. 105
5.19 Sketch of the voltage divider. 106
5.20 Ion drift paths away from an anode wire. and ion fraction on the cathodes. 107
5.21 Charge fraction which is induced on the different electrodes. 108
5.22 Electron drift lines from a track. 109
5.23 Drift time as a function of z and drift time distribution. 109

6.1 Photographic of the chamber with stretched spring scales. 112
6.2 Deflection in the mid-point of the read-out sandwich and the resulting gain variation. 114
6.3 Schematic illustration of the deflections in the read-out sandwich and the radiator. 114
6.4 Deflection in the mid-point of the radiator. 115
6.5 Frame binding under the influence of the wire tension. 116
6.6 Field cage current as a function of drift voltage. 117
6.7 Gas gain as a function of the anode voltage. 118
6.8 Gas gain along the chamber length and width. and the overall gain variation.119

7.1 Schematic of the test setup, not to scale. 122
7.2 Correlated Cherenkov - Pb-glass signals. 122
7.3 Average pulse height of electrons and pions as function of the drift time. . 123
7.4 Average pulse height as a function of the drift voltage. 124
7.5 Measured drift velocity. 125
7.6 Two examples of pulse heights integrated over all pads in the drift region. . 126
7.7 Influence of the filter on the pulse height and the reconstructed angles. . . 127
7.8 Angular and position distributions. 128
7.9 Signal and noise distributions. 129
7.10 Noise on each of the eight readout pads. 130
7.11 One event signal and displacement. 131
7.12 Signal-to-noise ration as a function of U_a. 131
7.13 Measured PRF with pad width $W = 8.25$ mm. 132
7.14 The average number of the reconstructed points in a track. 133
7.15 Position resolution as function of S/N ratio. 134
7.16 Angular resolution as function of S/N ratio. 135
7.17 Pulse height as a function of the anode voltage. 136
7.18 $1000 \times Q_{ratio}$ and Q_{sum} as functions of U_a. 136
7.19 Measured gas gain as a function of U_a. 137
7.20 Electrons to pions signal ratios as a function of the drift position. 138
7.21 Electron and pion energy deposit distributions. 139
7.22 The ratio of pions and electrons in different chambers. 140
7.23 TR yield in DC5 as function of beam momentum. 141
7.24 Probability distributions. 142
7.25 Pion efficiency as a function of the beam momentum. 143
7.26 Pion efficiency of the combined small chambers. 144
7.27 Pion efficiency as a function of detector depth. 145
7.28 Pion efficiency as a function of the beam momentum extrapolated from five to six layers. 146

8.1 Schematic di-electron invariant mass spectrum. 150
8.2 J/ψ suppression. 153
8.3 Binary collisions as a function of the collision geometry. 155
8.4 Multiplicity distribution and J/ψ differential yield. 157

9.1 The tracks of a Pb-Pb event in the ALICE central barrel. 162

9.2 p_t distribution of reconstructed pions and kaons in the ACB. 164
9.3 Detector efficiency in the ACB as a function of transverse momentum. . . . 165
9.4 Detector efficiency of the ACB as a function of ϕ and η. 166
9.5 Δp_t distribution. 167
9.6 Detector p_t resolution of the ACB as a function of p_t. 168
9.7 Detector p_t resolution of the ACB as a function of ϕ and η. 169
9.8 Detector resolutions of the ACB as functions of ϕ and η. 170
9.9 Energy deposit distribution and the TPC pion rejection capability. 171

10.1 p_t, η-, and y-distributions of J/ψ and its decay electrons. 174
10.2 p_t, η-, and y-distributions of $\Upsilon$and its decay electrons. 175
10.3 p_t-distributions of **D** and **B** mesons, Λ_c and Λ_b hyperons and their decay pions and electrons. 177
10.4 p_t-distributions of pions and kaons. 178
10.5 The survival probability of electrons and pions as a function of p_t-cut. . . . 179
10.6 Invariant mass spectrum of electron pair candidates for all TPC scenarios without TRD pion rejection support. 181
10.7 Invariant mass spectrum of di-electron candidates with TPC2 and TPC3. . 182
10.8 Same calculations as in Figure 10.6 with the TRD contribution. 183
10.9 Quarkonia signals. 184
10.10S/B-ratio and significance as function of the integration interval. 185
10.11S/B-ratio and significance as functions of the TPC pion efficiency. 186
10.12Relative S/B-ratio and relative significance as functions of the TPC pion efficiency. 187
10.13S/B-ratio and significance as functions the p_t-cut. 188
10.14Relative S/B-ratio and relative significance as functions of the multiplicity. 189

List of Tables

2.1 Extrapolation of particle production from pp to AA 35

3.1 Ionization and excitation energies of Xe, Ar, and CO_2. 55

4.1 Requirements and tolerances put on the TRD readout chamber. 60
4.2 Radiation length X_0 of the materials used in the TRD. 61
4.3 Parameters of the wire grids in a TRD module. 65
4.4 Abstract of the TRD parameters 71

5.1 Parameters of the ALICE TRD read out chamber. 76
5.2 Electron Attachment, longitudinal and transversal diffusion coefficients, Lorentz angle, and drift fields for different Xe/CO_2 mixtures. 87
5.3 Geometrical parameters and voltages in the chamber. 92
5.4 Updated Table 5.3. 100

8.1 Quarkonium masses, radii and dissociation temperatures. 152

10.1 J/ψ and Υ resolutions. 183

Dank

Nach vier Jahren Beschäftigung mit dieser Arbeit wei"s ich, dass sie ohne die gro"szügige Hilfe vieler Menchen und das Verständnis vieler anderen, nicht zu schaffen war. Diesen allen möchte ich aus ganzem Herzen danken.
Meiner Familie, meinen Kollegen in Heidelberg, an der GSI und in Frankfurt, meinen Freunden und nicht zuletzt Barbara.